Xiaoli Li *Editor*

Signal Processing in Neuroscience

Springer

Signal Processing in Neuroscience

Xiaoli Li
Editor

Signal Processing in Neuroscience

Springer

Editor
Xiaoli Li
State Key Laboratory of Cognitive
Neuroscience and Learning
Beijing Normal University
Beijing, China

ISBN 978-981-10-1821-3 ISBN 978-981-10-1822-0 (eBook)
DOI 10.1007/978-981-10-1822-0

Library of Congress Control Number: 2016951459

Printed on acid-free paper

This Springer imprint is published by Springer Nature
The registered company is Springer Science+Business Media Singapore Pte Ltd.

Contents

Chapter 1
Brief History and Development of Electrophysiological Recording Techniques in Neuroscience

Zhuo Huang

1.1 The Brief History of Bioelectrical Investigation

The bioelectrical investigation began with Luigi Galvani and Alessandro Volta in the 1700s. In 1786, Luigi Galvani, an Italian professor of medicine, showed that the frog muscle could be made to twitch when the leg of a dead frog was cut by a metal knife. Galvani thought that the muscles of the frog must contain electricity. However, Alessandro Volta repeated Galvani's experiments and believed that the electricity was generated by the metal cable which Galvani used to connect nerves and muscles in his experiments. Volta was right. To prove his idea, Volta invented the voltaic pile, which was the first electrical battery that could continuously provide an electrical current to a circuit. He demonstrated that the animal electricity did not come from the muscle in its pelvis but was a physical phenomenon caused by rubbing frog skin (Bresadola 1998). In the following decades, scientists began to ask how the sensory information is transmitted by electrical signals. The first attempt to answer this question was the theory of "law of specific nerve energies" which was proposed by Johannes Peter Müller in 1835. In this doctrine, Müller thought that the nature of a sensory stimulus is defined by the pathway over which the sensory information is carried and neurons which do not localized to this pathway are not responsible for this information processing (Norrsell et al. 1999). In support of this view, Hermann von Helmholtz provided evidence that cells at different locations along the cochlear spiral are sensitive to different frequencies of sound (Helmholtz 1885). These findings from the late nineteenth century form our current understanding about the nervous system. Nowadays when we are trying to figure out how information is processed in the cortex, where an array of neurons decodes

Z. Huang (✉)
State Key Laboratory of Natural and Biomimetic Drugs, Department of Molecular and Cellular Pharmacology, School of Pharmaceutical Sciences, Peking University Health Science Center, Beijing 100191, China
e-mail: huangz@hsc.pku.edu.cn

X. Li (eds.), *Signal Processing in Neuroscience*, DOI 10.1007/978-981-10-1822-0_1

incoming stimuli according to the values of different component features, we are reminded of Helmholtz' work, who found that the array of auditory nerve fibers would decompose sound into its component frequencies.

To examine the idea of Helmholtz and Müller about neuronal coding of sensory information, it is required that direct recording of electrical activity from a single neuron, not just additive effect of bundle of nerve fibers. However, in those years, the electrical signals from a single neuron were too small to record. To pick up these small signals, in 1917 Lucas at Cambridge University using vacuum tube built an instrument which allowed the recoding of microvolt electrical signals in bandwidths of several kilohertz. Luckily, Edgar Adrian, an English electrophysiologist and recipient of the 1932 Nobel Prize for Physiology, used this instrument and revealed much of what we know to this day about the principles of neuronal coding. Adrian's experiments revealed three fundamental facts about neural code (Hodgkin 1889). Firstly, Adrian demonstrated that individual sensory neurons fire all-or-none action potentials in response to external stimuli although the all-or-none firing law had already been established for muscle and neurons. This finding, however, provides first evidence that individual sensory neurons only provide a series of spikes for the brain to process. Secondly, Adrian found that in response to a static stimulus, the rate of spiking increases as the stimulus becomes stronger. The rate, or frequency, of spikes implies the intensity of the stimulus. Thirdly, he discovered that if a static stimulus is continued for a long time, the spike rate begins to decline, which is normally called adaptation. Adrian believed this physiological phenomenon is corresponding to the perception phenomena wherein the constant stimuli are gradually ignored.

Additionally, Haldan Keffer Hartline, an American physiologist and corecipient with George Wald and Ragnar Granit of the 1967 Nobel Prize in Physiology or Medicine, investigated the response of single neuron from the compound eyes of the horseshoe crab. Apart from reproducing Adrian's results about the rate coding, Hartline recorded the electrical impulses from a single optic nerve fiber which is activated by light stimulation and demonstrated that photoreceptor cells in the eye are interconnected in such a way that when one is stimulated, other neighboring cells are depressed, thus increasing the contrast in the light patterns and contributing to the contrast enhancement. Therefore, Hartline provided a detailed description of how photoreceptors and nerve fibers work in the retina and how simple retinal mechanisms constitute vital steps in the integration of visual information. The concept of feature selectivity was clearly proposed by Horace Basil Barlow in 1935, who is a British visual neuroscientist. Barlow recorded electrical activities from retinal ganglion cells in the frog and showed that the response of these cells to a spot of light at first grows with the area of the spot, but then declines if the spot exceeds a critical size. The particular region of the sensory space that can affect the activity of a neuron is called the receptive field of that cell. The receptive field is "center surrounded": spots within a small region excite the cell, but spots just outside this region inhibit the cell (Barlow 1953a, b). Later on, the importance of feature selectivity was strongly supported by the observations of Hubel and Wiesel (1962). They found that many cells in cat visual cortex are selective not only for

size of objects but also for their orientation. In Hubel and Wiesel's experiments, they showed that neighboring neurons are normally correlated to neighboring orientations, so that feature selectivity is mapped over the surface of the cortex (Hubel and Wiesel 1977). Furthermore, the notion of feature selectivity was also demonstrated by the findings of O'Keefe and his colleagues. In pioneering studies that were recognized by a Nobel Prize in 2014, O'Keefe discovered "place cells" in the hippocampus (O'Keefe and Dostrovsky 1971; O'Keefe 1976; O'Keefe and Conway 1978). In his early investigations, O'Keefe and Dostrovsky using single-unit electrodes identified specific cells within the hippocampus in the freely moving rat that fired only in the fixed location within an open field or maze. They referred to these cells as "place cells" and coined the complementary neologism "place field" to describe the specific location in the environment where the cell selectively fires. The firing field is very stable over days and months once established, and place field is established reasonably quickly on the order of a few minutes to one hour (Tanila et al. 1997; Lever et al. 2002). Then, do the idea of rate cording, feature selectivity, and cortical mapping tell us what we want to know about the neural code? Are there other coding strategies which neurons use to interpret the external stimuli? Actually, these previous ideas leave an open question of whether other features of the spike train carry meaningful information, and indeed this question has been central to many discussions of neural cording. In the following section, several classical recording strategies for measuring the neuronal activity will be discussed.

1.2 What Is Spike Train?

Spike train is normally referred to as a series of discrete action potentials from a neuron taken as a time series, sometimes referred to as temporal coding. This string of neuronal firing may be generated spontaneously or in response to some external stimuli. Spike train is a language in which the external world is encoded into our brains, the language the brain uses for its internal communication, and the language it talks to outside world.

To understand what spike is and how the spike train is generated, we need to clarify how bioelectrical signals and neuronal action potentials are produced. Bioelectrical signals are generated by ion channels and ion transporter proteins (ion pumps) on neuronal membranes. Ion channels are the ion-permeable membrane proteins. They open and close in response to specific stimuli and selectively pass ions such as sodium, potassium, calcium, etc., through the impermeable cell membrane. The ions flow across the membrane that generates bioelectrical signals. There are two distinctive features of ion channels that differentiate them from ion pumps. First, the rate of ion transport through the ion channel is very high (normally more than 100 ions per second). Second, ions pass through ion channels down their electrochemical gradient; thus this process does not require any help of metabolic energy, whereas ion transporter proteins do require energy to move ions across a plasma membrane against their concentration gradient (Hille 2001).

Like other typical membrane proteins, mRNAs of ion channels are transcribed in nuclei, and channels are synthesized in ribosome and inserted into the membrane of the endoplasmic reticulum. Then following the posttranslational modification including glycosylation, phosphorylation, and ubiquitination, the channels are inserted into targeted membranes. They have many features of signaling proteins. Ion channels have a variety of conformational states such as open, close, inactivation, and desensitization states. Ion channels are typically subdivided into two categories according to their way to activate the channels. The largest superfamily of ion channels is opened by changes in membrane potential; thus they are called voltage-gated ion channels, while several families of ion channels are gated by extracellular ligands and they are called ligand-gated ion channels (Hille 2001).

Human brain has almost 100 billion neurons, and some of these neurons communicate with each other in such a highly structured manner as to form neural networks. To understand neural networks, it is necessary to understand how individual neurons are interconnected. A neuron is a specialized cell that has four morphological defined regions: the cell body, dendrites, axons, and axonal terminals. The cell body is normally called soma, which contains the nucleus and is responsible for the protein synthesis and cell metabolism. A neuron usually has multiple branched projections (dendrites) from the soma, which serve as the main apparatus for receiving input into the neuron from other nerve cells. The soma also gives rise to the axon, which is capable of integrating all inhibitory and excitatory synaptic inputs, generating all-or-none action potentials and transmitting the messages to axonal terminals. The axonal terminals are distal terminations of the branches of an axon. The neurotransmitters are packaged into tiny, bubble-like compartments known as vesicles in axonal terminals. Presynaptic neurons normally send their axons to dendrites of postsynaptic neurons, which are the region where one neuron receives connections from other neurons. The connections between neurons are not continuous but contiguous. The gaps between two neurons are called *synapses*. The axon terminals of presynaptic neurons release excitatory or inhibitory synaptic transmitter; commonly they are glutamate or GABA in the brain, respectively. In neocortex, GABA mainly controls the excitability of local microcircuit, whereas glutamate is responsible for transmitting the information between neurons. The synaptic transmission is electrochemical in nature. In excitatory synaptic transmission, presynaptic neurons release excitatory transmitter, glutamate, into synaptic cleft. The glutamate binds its inotropic receptors, AMPA, NMDA, or kainite, and thus produces excitatory postsynaptic potentials *(EPSP)*. Neuronal dendrites from a single neuron received thousands of EPSP, which are temporally synchronized and summated. The summarized EPSP propagates along the dendrites to axon initial segment to initiate the all-or-none action potential (spike). Individual neurons receive thousands of synaptic input and continuously generate series of action potentials, which are called *spike trains*.

1.3 The Measurement of Bioelectrical Signals

To investigate the significance of bioelectrical signals in the brain, the reliable recording strategies for assessing the electrical properties of biological cells and tissues are highly appreciated. In the past century, various electrophysiological recording techniques were developed for measuring the voltage change or electrical current on a wide variety of scales from single ion channel proteins to whole organs. In general, the recording techniques are divided into two categories: intracellular recording and extracellular recording. The *intracellular recording* technique usually requires small electrode (micrometer in tip diameter) and inserts the tip into a single cell, which allows us to make direct measurement of intracellular electrical activity of a single neuron. The commonly used approaches for intracellular recording include *voltage clamp*, *current clamp*, *patch-clamp*, *and sharp electrode techniques* (Sakmann and Neher 1995). Oppositely, for *extracellular recording* techniques, the electrode tip is left in the continuity with the extracellular space. If the tip is small enough, such a configuration allows indirect observation and recording of action potentials from a single cell, which is termed *single-unit recording*. Depending on the preparation and precise placement, an extracellular configuration may pick up the activity of several nearby cells simultaneously, and this is termed *multi-unit recording*. As electrode size increases, the resolving power decreases. Larger electrodes are sensitive only to the net activity of many cells, termed *local field potentials*. Still larger electrodes, such as uninsulated needles and surface electrodes used by clinical and surgical neurophysiologists, are sensitive only to certain types of synchronous activity within populations of cells numbering in the millions, such as *electrocorticography* (*EcoG*) and *electroencephalography* (*EEG*).

1.4 Single-unit and Multi-unit Recording and Their Applications in Measuring Brain Activities

As discussed above, if microelectrode tip is small enough (usually 3–10 μm in diameter), the spike activity (action potentials) of a single neurons can be isolated when the electrode is placed close to the neuron's soma or axon. The microelectrode is primarily a glass micropipette or metal microelectrode made of platinum or tungsten (Boulton 1990). The single-unit recordings are widely used in cognitive science, where it allows us to study the relationship between a neuron's activities in response to various forms of sensory stimuli and behavior. For example, with single-unit recording technique, the firing rate of single neurons in medial entorhinal cortex has been shown to tightly correlate with the rodent's spatial locations (Hafting et al. 2005).

However, the main disadvantage of this technique is to maintain the recording electrode in place for long duration because the amplitude of the recorded spike is very sensitive to electrode position. This is especially true when the single-

unit recording is carrying on in a free-moving animal. Additionally, a major challenge today is to successfully record the simultaneous activities from as many neurons as possible because the complex behavior function requires the dynamics of large neural networks which is composed of thousands of neurons. This is made possible by the development of microelectronics' microfabrication technologies. It now becomes possible to build high-density microelectrode arrays containing several hundreds of microelectrodes. This microelectrode theoretically allows us to simultaneously record dozens or hundreds of neurons in various preparations although many channels in the microelectrode don't record "good quality signals" (Van Dijck and Van Hulle 2014).

Based on the single-unit technique, if the electrode tip increases slightly, then the electrode might record the summed synaptic voltages and action potentials from several neurons surrounding the recording tip (Bishop and O'Leary 1942; Lorente de No 1947). This type of recording is called *multi-unit recording* and is often used in conscious animals to record changes in the activity in a discrete brain area during normal activity. Recordings from one or more such electrodes that are closely spaced can be used to identify the number of cells around it as well as which of the spikes come from which cell. This process is called *spike sorting* and is suitable in areas where there are identified types of cells with well-defined spike characteristics. Nevertheless, multi-unit recording is less sensitive to electrode placement than single-unit recording, thus making it difficult to isolate contributions of individual neurons.

1.5 Local Field Potentials

Local field potentials (LFPs) are electrical potentials recorded in the extracellular space of brain tissue, usually with a wide variety of electrodes (metal, silicon, or glass micropipettes). Such recordings were first made in animals over 140 years ago (Caton 1875) and became an increasingly important tool both in the fields of neuroscience research and medical diagnosis. LFP is different from the electroencephalography (EEG), which is recorded at the surface of the scalp with macro-electrodes. It is also different from the electrocorticography (EcoG, which is also called intracranial electroencephalography), which is recorded from the surface of the brain using large subdural electrodes, while LFPs are recorded in depth, from within the brain tissue. The spatial scale of sampling from LFP is larger than multi-unit recording, but is relatively local because the LFP signals can be very different from the signals recorded from 1 mm or a few hundred microns away (Nauhaus et al. 2009; Katzner et al. 2009).

What is the origin of LFP signals? Early studies supported a "circus movement theory," which proposed that the frequency of the LFP oscillations was generated by traveling electrical pulses along loops of neural network. In contrast, Bremer showed that action potentials have a limited contribution to the LFP and the oscillation of the membrane potential of neurons plays an important role in the generation

of the LFP (Bremer 1938, 1949). In 1951, Eccles proposed that postsynaptic potentials which are generated by synchronized excitation of neuron's dendrites are involved in the LFP activities (Eccles 1951). Later on, several evidences confirmed a close correspondence between the LFP activity and synaptic potentials (Creutzfeldt et al. 1966a, b; Klee et al. 1965). Recently, other neural sources such as inhibitory synaptic inputs (Hasenstaub et al. 2005) and subthreshold membrane properties (Kamondi et al. 1998) have also been found to considerably contribute to the LFP. Additionally, calcium-activated potassium currents also play an important role in the LFP generation (Buzsaki 2002). In summary, LFPs reflect the macroscopic and net synaptic inputs, as well as net result of local signal processing in certain brain area, while the multi-unit recordings most likely represent a weighted sum of the extracellular action potentials of all neurons within a sphere of approximately 140–300 μm radius surrounding the exposed tip of the electrode (Gray et al. 1995; Henze et al. 2000). It is usually assumed that LFPs integrate signals from a larger area than that of multi-unit recordings.

The reason for the fact that action potentials have a limited contribution to the LFP activities is due to strong frequency-filtering properties of cortical tissue. High-frequency signals (greater than 100 Hz), such as that produced by action potentials, are strongly filtered and attenuated, while low-frequency events, such as synaptic potentials, attenuate less with distance. Consequently, the action potentials only can be recorded by electrodes placed adjacent to the recorded cell, while synaptic events may propagate over large distances in extracellular space and be recordable as far as on the surface of the scalp, where they contribute to the generation of the EEG signals.

1.6 Electroencephalography (EEG)

Since Hans Berger made the first human EEG recording in 1924, the EEG technique has gradually become the most frequently used tools to study human brain. The electroencephalogram (EEG) is an electrical signal recorded from perhaps 20–256 electrodes attached to the human scalp. Each scalp electrode records electrical activity at very large scales which is generated by almost ten million neurons in the cortical layer. When compared to LFP, single-unit and multi-unit recordings, EEG recording is completely noninvasive, thus making it an ideal neuroimaging method that is routinely used in clinical applications as well as in neurophysiological research. There are, however, several disadvantages of EEG recording technique. First of all, the spatial resolution for EEG recording is very poor and it is impossible to use it for localization of electrical activities. Second, EEG merely records the signals originating from the superficial layer of the cortex. Third, the signal to noise ratio of EEG recording is poor. Therefore, a complicated data analysis and relatively large number of subjects are needed to obtain the useful information from EEG recording.

EEG signals are commonly subdivided into different frequency bands, whose properties and functional significance have recently drawn increased attention in neuroscience research field. These bands are typically referred to as delta (1–4 Hz), theta (4–8 Hz), alpha (8–12 Hz), beta (12–30 Hz), and gamma (greater than 30 Hz) (Basar 1980; Steriade 1991). The classification is based on the strong correlation of each band with a distinct behavioral state (Wang 2010). Delta band is the frequency range up to 4 Hz. It tends to be the highest in amplitude and the slowest waves. It is seen normally in adults in slow-wave sleep and in babies. Theta is the frequency range from 4 to 7 Hz. Theta is seen normally in young children. It may also be seen in drowsiness or arousal in older children and adults. Alpha is the frequency range from 7 to 14 Hz. Hans Berger named the first rhythmic EEG activity he saw as the "alpha wave." It emerges with closing of the eyes and with relaxation and attenuates with eye opening or mental exertion. Beta is the frequency range from 15 to about 30 Hz. Beta activity is closely linked to motor behavior and is generally attenuated during active movements. Low amplitude beta with multiple and varying frequencies is often associated with active, busy, or anxious thinking and active concentration. Rhythmic beta with a dominant set of frequencies is associated with various pathologies and drug effects. Gamma is the frequency range from approximately 30 to 100 Hz. Gamma rhythms are thought to represent binding of different populations of neurons together into a network for the purpose of carrying out a certain cognitive or motor function.

Early studies have been performed to understand the origin of the EEG signals and demonstrated a close correspondence between EEG activity and synaptic potentials (Creutzfeldt et al. 1966a, b; Klee et al. 1965), indicating that the population EPSP and IPSP of cortical neurons are major components of the EEG signal. Current view is the surface EEG signal reflects synchronized afferent or efferent activity of cells in a certain brain area (Eccles 1951). Therefore, neural synchrony is the key in explaining differences of electrical activities between those observed at the local level (LFP, multi-unit recording, EcoG) and those at the more global level (EEG) (Wennberg et al. 2011). The implication is that the scalp EEG is not merely a highly smoothed version of intracranial data, and it contains different kinds of information about neocortical dynamics which are not necessarily observable in intracranial recordings.

References

Barlow HB. Summation and inhibition in the frog's retina. J Physiol. 1953a;119:69–88.

Barlow HB. Action potentials from the frog's retina. J Physiol. 1953b;119:58–68.

Basar E. EEG-brain dynamics: relation between EEG and brain evoked potentials. Amsterdam: Elsevier/North-Holland Biomedical Pr.; 1980.

Bishop GH, O' Leary JL. Factors determining the form of the potential record in the vicinity of the synapses of the dorsal nucleus of the lateral geniculate body. J Cell Comp. 1942;19, 16.

Boulton AA. Neurophysiological techniques: applications to neural systems. Clifton: Humana Press; 1990.

Bremer F. L'activité électrique de l'écorce cérébrale. Actualités Scientifiques et Industrielles. 1938;658:44.
Bremer F. Considérations sur l'origine et la nature des "ondes" cérébrales. Electroencephalogr Clin Neurophysiol. 1949;1:17.
Bresadola M. Medicine and science in the life of Luigi Galvani (1737–1798). Brain Res Bull. 1998;46:367–80.
Buzsaki G. Theta oscillations in the hippocampus. Neuron. 2002;33:325–40.
Caton R. The electric currents of the brain. Br Med J. 1875;2.
Creutzfeldt OD, Watanabe S, Lux HD. Relations between EEG phenomena and potentials of single cortical cells. I. Evoked responses after thalamic and erpicortical stimulation. Electroencephalogr Clin Neurophysiol. 1966a;20:1–18.
Creutzfeldt OD, Watanabe S, Lux HD. Relations between EEG phenomena and potentials of single cortical cells. II. Spontaneous and convulsoid activity. Electroencephalogr Clin Neurophysiol. 1966b;20:19–37.
Eccles JC. Interpretation of action potentials evoked in the cerebral cortex. Electroencephalogr Clin Neurophysiol. 1951;3:449–64.
Gray CM, Maldonado PE, Wilson M, McNaughton B. Tetrodes markedly improve the reliability and yield of multiple single-unit isolation from multi-unit recordings in cat striate cortex. J Neurosci Methods. 1995;63:43–54.
Hafting T, Fyhn M, Molden S, Moser MB, Moser EI. Microstructure of a spatial map in the entorhinal cortex. Nature. 2005;436:801–6. doi:10.1038/nature03721.
Hasenstaub A, et al. Inhibitory postsynaptic potentials carry synchronized frequency information in active cortical networks. Neuron. 2005;47:423–35. doi:10.1016/j.neuron.2005.06.016.
Helmholtz HV. On the sensations of tone as a physiological basis for the theory of music (trans: Ellis AJ). 2nd ed. London: Longmans, Green, and Co.; 1885. p. 44. Retrieved 2010-10-12
Henze DA, et al. Intracellular features predicted by extracellular recordings in the hippocampus in vivo. J Neurophysiol. 2000;84:390–400.
Hille B. Ion channels of excitable membranes. Sunderland: Sinauer Associates; 2001.
Hodgkin A. Edgar Douglas Adrian, Baron Adrian of Cambridge, 30 November 1889–4 August 1977. Biographical Mem Fellows Roy Soc. Roy Soc (Great Britain). 1979;25:1–73.
Hubel DH, Wiesel TN. Receptive fields, binocular interaction and functional architecture in the cat's visual cortex. J Physiol. 1962;160:106–54.
Hubel D, Wiesel TN. Ferrier lecture. Functional architecture of macaque monkey visual cortex. Proc R Soc Lond Ser B Biol Sci. 1977;198:1–59.
Kamondi A, Acsady L, Wang XJ, Buzsaki G. Theta oscillations in somata and dendrites of hippocampal pyramidal cells in vivo: activity-dependent phase-precession of action potentials. Hippocampus. 1998;8:244–61. doi:10.1002/(SICI)1098-1063(1998)8:3<244::AID-HIPO7>3.0.CO;2-J.
Katzner S, et al. Local origin of field potentials in visual cortex. Neuron. 2009;61:35–41. doi:10.1016/j.neuron.2008.11.016.
Klee MR, Offenloch K, Tigges J. Cross-correlation analysis of electroencephalographic potentials and slow membrane transients. New York: Science; 1965. 147:519–21.
Lever C, Wills T, Cacucci F, Burgess N, O'Keefe J. Long-term plasticity in hippocampal place-cell representation of environmental geometry. Nature. 2002;416:90–4. doi:10.1038/416090a.
Lorente de No R. Action potentials of the motorneurones of the hypoglossus nucleus. J Cell Comp Physiol. 1947;81.
Nauhaus I, Busse L, Carandini M, Ringach DL. Stimulus contrast modulates functional connectivity in visual cortex. Nat Neurosci. 2009;12:70–6. doi:10.1038/nn.2232.
Norrsell U, Finger S, Lajonchere C. Cutaneous sensory spots and the "law of specific nerve energies": history and development of ideas. Brain Res Bull. 1999;48:457–65.
O'Keefe J. Place units in the hippocampus of the freely moving rat. Exp Neurol. 1976;51:78–109.
O'Keefe J, Conway DH. Hippocampal place units in the freely moving rat: why they fire where they fire. Exp Brain Res. 1978;31:573–90.

O'Keefe J, Dostrovsky J. The hippocampus as a spatial map. Preliminary evidence from unit activity in the freely-moving rat. Brain Res. 1971;34:171–5.

Sakmann B, Neher E, editors. Single-channel recording. New York: Springer; 1995.

Steriade M. Alertness, quiet sleep, dreaming, in cerebral cortex. New York: Plenum Press; 1991.

Tanila H, Sipila P, Shapiro M, Eichenbaum H. Brain aging: impaired coding of novel environmental cues. J Neurosci. 1997;17:5167–74.

Van Dijck G, Van Hulle MM. Review of machine learning and signal processing techniques for automated electrode selection in high-density microelectrode arrays. Biomedizinische Technik Biomed Eng. 2014;59:323–33. doi:10.1515/bmt-2013-0037.

Wang XJ. Neurophysiological and computational principles of cortical rhythms in cognition. Physiol Rev. 2010;90:1195–268. doi:10.1152/physrev.00035.2008.

Wennberg R, Valiante T, Cheyne D. EEG and MEG in mesial temporal lobe epilepsy: where do the spikes really come from? Clin Neurophysiol. 2011;122:1295–313. doi:10.1016/j.clinph.2010.11.019.

Chapter 2
Adaptive Spike Sorting with a Gaussian Mixture Model

Zheng Li

2.1 Introduction

This chapter presents a method for adaptive spike sorting: variational Bayesian Gaussian mixture (VBGM) adaptive spike sorting. We also present the nonadaptive spike sorting method upon which it is based, expectation–maximization on a Gaussian mixture model, so as to ease the reader into the adaptive case. We then show the results of some experiments on synthetic as well as real neural data to demonstrate the utility of VBGM adaptive spike sorting. This chapter is not meant as an overview of spike sorting methods and challenges in general. Some reviews of spike sorting can be found in Lewicki (1998), Sahani (1999), and Gibson et al. (2012).

Spike sorting is an important step in the processing of signals recorded from electrodes implanted into the extracellular space next to neurons. Such electrodes record changes in extracellular currents due to action potentials in these nearby neurons. These action potentials are manifested as spikes in the voltage versus time graph and hence are commonly called spikes. For many neuroscience investigations and other applications of neural recording, ideally, the activity of a single neuron is isolated from the activity of others. Thus, some method must be applied to distinguish the spikes of one neuron from the spikes of other neurons.

Due to differences in neuron morphology and relative position and orientation between electrode and neuron, different neurons tend to exhibit spikes with different shapes, i.e., different waveforms in the voltage versus time curve. The differences in the spike shapes allow the registration of spikes to different neurons using this

Z. Li (✉)
State Key Laboratory of Cognitive Neuroscience and Learning & IDG/McGovern Institute for Brain Research, Beijing Normal University, Beijing 100875, China

Center for Collaboration and Innovation in Brain and Learning Sciences, Beijing Normal University, Beijing 100875, China
e-mail: lz@bnu.edu.cn

X. Li (eds.), *Signal Processing in Neuroscience*, DOI 10.1007/978-981-10-1822-0_2

information. This process is called spike sorting. Unfortunately, spike shapes are contaminated by noise from the recording system and from background neural activity, which is the summation of action potentials and sub-threshold electrical activity from neurons in the vicinity. Such noise can make spikes from different neurons difficult to distinguish or can make spikes from the same neuron appear different at different times. Under low noise conditions, relatively simple spike sorting methods will perform sufficiently accurately for most research needs. This is particularly true in neuroscience as experiments are often carried out over many repeated trials, averaging out the effect of noise. However, in applications such as brain–machine interfaces for the real-time control of prosthetics, the luxury of repeated trials is not available.

In some applications, signals are acquired over long time periods. A problem that arises when signals are collected over hours or longer is that the spike shapes of neurons may change, due to micro-movements in the electrode relative to neurons. To sustain spike sorting accuracy, adjustments must be made to the parameters of the spike sorting method to adapt to these changes in spike shapes.

There has been prior work in adapting to changes in spike shapes. Some examples are Bar-Hillel et al. (2006), Wolf and Burdick (2008), Gasthaus et al. (2009), Calabrese and Paninski (2011), and Paraskevopoulou et al. (2014). In this chapter, we present a method which can probabilistically track changing spike shapes, spike noise distributions, and baseline firing rates in a computationally efficient manner.

2.2 Problem Statement

We start by describing more precisely what we mean by the spike sorting problem. In the following we will work with the data from one electrode at a time. Multiple electrodes can be processed independently in parallel using the same method. We do not specifically address the processing of data from tetrodes or stereotrodes here, though our adaptive algorithm is equally applicable. We assume that segments of the voltage versus time curve (time series) which contain action potentials of nearby neurons have been identified by some spike detection method. The most common method is to set a threshold on the voltage and cut out a time window around each threshold crossing. These time windows of the time series comprise our input data: many instances of putative spikes.

More precisely, our data consists of N vectors $\widehat{\mathrm{w}}_{1\ldots N} \propto R^l$, where each vector is the voltage in a time window, length l, containing a putative action potential. Since these windows of data may contain noise instead of an actual spike, we sometimes call them waveforms. We assume the elements of these vectors are real-valued voltages, though in actual implementations they are often stored as integer outputs from the analog-to-digital converters of recording hardware, for memory and bandwidth savings. The problem of spike sorting can be divided into two phases: an offline phase and an online phase. Some practitioners only need to perform

the offline phase, since all their data analysis is performed offline. However, our adaptive spike sorting is aimed primarily at the online phase.

During the offline phase of spike sorting, N waveforms comprise the input. The task is to cluster these waveform inputs into one of K groups, each of which hopefully corresponds to a single neuron. Hence, offline spike sorting is often synonymous with clustering. In practice, the practitioner cannot be sure of whether similar spikes come from one neuron, so the term "unit" is used instead of neuron. Also, there is often one or more groups which are called "multiunits," a designation for groups containing spikes which are too noisy to be further separated but are likely to contain spikes from multiple neurons (inferred from refractory violations or other hints). Also, some practitioners designate a group which holds all noise waveforms: those which were mistakenly detected as spikes by the spike detection method. Note that this clustering is generally considered to be unsupervised. However, practitioners may use other sources of information to assist in this endeavor, such as neuron refractory or encoding patterns (Ventura 2009). The number of clusters K is unknown but generally a number less than 5 for most electrode hardware (exceptions are stereotrodes and tetrodes). The output of offline spike sorting is a label for each input waveform. Note that, absent simultaneous intracellular recordings (e.g., Harris et al., 2000), there is no gold standard to measure the accuracy of this clustering. However, some practitioners may use metrics such as presence of refractory violations, separation between clusters, or signal-to-noise ratio to support the assertion that a group corresponds to a "well-isolated single unit."

During the online phase of spike sorting, waveforms arrive as they are detected by the spike detector and must be assigned to one of the K groups in real time. Standard methods do not perform clustering during the online phase, but rather classification. Usually, a model of spike waveform shape is used. This model describes what shape a waveform from a neuron is expected to be. The model parameters are fitted using the groups found during the offline phase. Then, this model and its parameters are used to classify each new waveform, giving it a label as the output of the algorithm. In standard practice, the parameters are static, thus assuming that the spike shape to neuron mapping is not changing.

For adaptive spike sorting, the problem is expanded. We not only need a label for the incoming waveform, but we need to update the parameters of our spike sorting model to adapt to any changes which the incoming waveform may tell us. An alternate formulation is to decouple the classification and model updates, so that classification occurs in real time as new waveforms arrive, but updates occur asynchronously and periodically, working on batches of the latest waveforms.

Thinking about this alternative formulation, we may notice a resemblance to the offline phase of spike sorting, except that instead of performing clustering de novo, we can perform clustering with some prior information—the previous estimates of the model parameters. It is precisely this line of thought which is the basis of our adaptive spike sorting method. However, before describing the adaptive method, we first describe the model and static spike sorting algorithm upon which it is based.

2.3 Spike Sorting with a Gaussian Mixture Model

One well-known probabilistic model used for spike sorting is the Gaussian mixture model (GMM), also called the mixture of Gaussians (MoG). In this model, each recorded instance of an action potential has a shape that is the archetypical shape for the unit plus normally distributed noise. The parameters for this normal distribution are specific to each unit and unchanging. Waveforms from multiple units are recorded on a channel, so the set of all waveforms is a mixture of K normal distributions, where K is the number of units. The archetypical shape for each unit is the center (mean) of the distribution for that unit. Since some units may have higher firing rate than others, the proportion of spikes from different units may be nonuniform; thus, the mixture is also described by mixing coefficients—relative frequencies of units, expressed as a probability.

When we use "shape," we mean a feature vector of numbers describing the shape in a concrete way. How we compute this feature vector is beyond the scope of this chapter. The most common way is to use principal components analysis to reduce dimensionality to a small number. For the remainder of this exposition, we assume we have some way to generate features, though our method is independent of exactly how. The dimension of the feature vector is typically small (about 2 to 3), both for visualization purposes and to make parameter estimation more reliable.

To make the above description precise, let us define a feature generator function g, and $\mathrm{g}(\widehat{\mathrm{w}})$ is the d-dimensional column vector of features generated from waveform $\widehat{\mathrm{w}}$. If the waveform is from unit k, the mixture model describes the features of a waveform $\mathrm{g}(\widehat{\mathrm{w}})$ as having distribution

$$\mathrm{g}(\widehat{\mathrm{w}}) \sim N\left(\widehat{\mathrm{m}}_k, \mathbf{P}_k^{-1}\right), \tag{2.1}$$

where N is a d-dimensional multivariate normal distribution, $\widehat{\mathrm{m}}_k$ is the d-dimensional mean vector for unit k (a column vector), and $\mathbf{P}_k$ is the $\mathrm{d} \times \mathrm{d}$ precision matrix (inverse of the covariance matrix) for unit k. The mean vector describes the archetypical shape, and the precision matrix describes the amount of noise, or how spread out in feature space the instances of waveforms from this unit are. Notational note: we use hats to indicate vectors and bold to indicate matrices.

If we want to draw a random sample from this mixture model, we first randomly decide which unit to draw from, using the mixing coefficients $\pi_{1\ldots K}$ as probabilities:

$$k \sim \mathrm{Cat}\left(\pi_{1\ldots K}\right). \tag{2.2}$$

Here, Cat is a categorical distribution, with category probabilities specified by the mixing coefficients $\pi_{1\ldots K}$, which are nonnegative and sum to one. Once we have chosen the unit (k), we draw randomly from the normal distribution, $N\left(\widehat{\mathrm{m}}_k, \mathbf{P}_k^{-1}\right)$. The output is the feature vector $\mathrm{g}(\widehat{\mathrm{w}})$ of a waveform of random identity and shape corrupted by random noise.

If we know the parameters of the model and want to know the identity of a given spike, we can compute and compare probabilities. That is, we first compute the probability of the spike coming from the first unit. We do this by computing the probability of the waveform shape given the first unit's center (archetypical shape) and noise distribution, i.e., we evaluate the probability density function of the normal distribution given the parameters of the first unit at the shape of the waveform. Next, we account for the relative frequencies of the units by multiplying the probability by the mixing coefficient of the unit. This gives us the unnormalized probability of the spike coming from this unit. More precisely, with $k = 1$, we compute

$$\mathrm{UP}\left(\mathrm{g}(\widehat{\mathrm{w}}), k\right) = \pi_k N\left(\mathrm{g}\left(\widehat{\mathrm{w}}\right) | \widehat{\mathrm{m}}_k, \mathbf{P}_k^{-1}\right). \tag{2.3}$$

We remember this $\mathrm{UP}\left(\mathrm{g}\left(\widehat{\mathrm{w}}\right), 1\right)$. Then, we compute the unnormalized probability of the spike coming from the second unit (set $k = 2$), and so on, until we have probabilities from each unit. Finally, we pick the unit with the highest unnormalized probability. This gives us the maximum probability estimate of the spike identity. We use this procedure during online spike sorting with a GMM.

Sometimes we need the normalized probability of the spike belonging to a unit. To compute it, we normalize the unnormalized probabilities so that they sum to one:

$$Pr\left(\eta\left(\widehat{\mathrm{w}}\right) = i \,|\widehat{\mathrm{w}}, \pi_{1\ldots K}, \widehat{\mathrm{m}}_{1\ldots K}, \mathbf{P}_{1\ldots K}\right) = \frac{\mathrm{UP}\left(\mathrm{g}(\widehat{\mathrm{w}}), i\right)}{\sum_{k=1}^{K} \mathrm{UP}\left(\mathrm{g}(\widehat{\mathrm{w}}), k\right)}. \tag{2.4}$$

Here, $\eta(\widehat{\mathrm{w}})$ is the identity of the unit which generated waveform $\widehat{\mathrm{w}}$. Let us next look at how to set the model parameters when we know the identity of each waveform in a dataset. We gather all the waveforms belonging to unit k and set the normal distribution parameters by computing the sample mean and sample covariance:

$$\widehat{\mathrm{m}}_{\mathrm{k}} = \frac{1}{\mathrm{n}_k} \sum_{\eta(\widehat{\mathrm{w}})=k} \mathrm{g}\left(\widehat{\mathrm{w}}\right), \tag{2.5}$$

$$\mathbf{P}_k^{-1} = \frac{1}{\mathrm{n}_k - 1} \sum_{\eta(\widehat{\mathrm{w}})=k} \left(\mathrm{g}\left(\widehat{\mathrm{w}}\right) - \widehat{\mathrm{m}}_k\right)\left(\mathrm{g}\left(\widehat{\mathrm{w}}\right) - \widehat{\mathrm{m}}_k\right)^{\mathrm{T}}, \tag{2.6}$$

where n_k is the number of waveforms belonging to unit k. To set the mixing coefficients, we find the sample proportion of waveforms belonging to each unit:

$$\pi_k = \frac{\mathrm{n}_k}{N}. \tag{2.7}$$

2.4 Clustering with the Expectation–Maximization Algorithm

During offline spike sorting, we need to find the model parameters $\pi_{1\ldots K}, \widehat{\mathrm{m}}_{1\ldots K}, \mathbf{P}_{1\ldots K}$ when given a set of waveforms $\widehat{\mathrm{w}}_{1\ldots N}$, as well as find the identity of each waveform. At first glance this may seem an impossible problem, since the model parameters are needed to compute the unit identities, but the identities are needed to compute the model parameters. However, the well-known expectation–maximization (EM) algorithm (Dempster et al. 1977) finds a solution, which in our case corresponds to a clustering of the data. This solution is a local maxima of the incomplete-data likelihood, which is

$$\mathrm{L} = \prod_{i=1}^{N} \sum_{k=1}^{K} \mathrm{UP}\left(\mathrm{g}(\widehat{\mathrm{w}}_i), k\right). \tag{2.8}$$

Note that this likelihood is incomplete because it is calculated without the labels.

The EM algorithm is often used with GMMs to perform clustering. We sketch the algorithm before going into specifics. First, cluster parameters are initialized using some scheme. This may be random or based on the output of a simpler clustering algorithm, such as k-means. Then, in the expectation step, the probability of each data point belonging to each cluster is computed using the parameters. These probabilities are called responsibilities, because they tell us how "responsible" the cluster is for that data point. Then, in the maximization step, the cluster parameters are updated. This is performed using the responsibilities as "soft" labels. For example, if a waveform belongs to unit A with 20 % probability, during the mean computation, it is included in the summation with a 20 % weight. Also, instead of contributing a count of 1 to $\mathrm{n_A}$, a contribution of 0.2 is used. The idea is that, when the label is not confident, the cluster parameter estimation should reflect this. Next, the incomplete-data likelihood is calculated. Then the process iterates between the expectation and maximization steps. Each step uses the values computed in the other step. This process continues until the incomplete-data likelihood no longer increases, which indicates convergence to a local maxima. In practice, iterations are stopped when improvement is smaller than a percentage threshold.

Now let us look at the equations. In the expectation step, we compute responsibilities $\mathrm{r}_{i,k}$ for each waveform i and for each cluster k:

$$\mathrm{r}_{i,k} \leftarrow Pr\left(\eta\left(\widehat{\mathrm{w}}_i\right) = k \,|\widehat{\mathrm{w}}_i, \pi_{1\ldots K}, \widehat{\mathrm{m}}_{1\ldots K}, \mathbf{P}_{1\ldots K}\right), \tag{2.9}$$

where the probability is as we defined it previously. We use an arrow instead of an equals sign to indicate an assignment.

In the maximization step, we first compute the statistic n_k for each cluster k:

$$\mathrm{n}_k = \sum_{i=1}^{N} \mathrm{r}_{i,k}\,. \tag{2.10}$$

Then, we compute the new cluster parameters, for each cluster k:

$$\widehat{\mathrm{m}}_k \leftarrow \frac{1}{\mathrm{n}_k} \sum_{i=1}^{N} \mathrm{r}_{i,k} \cdot \mathrm{g}\left(\widehat{\mathrm{w}}_i\right), \tag{2.11}$$

$$\mathbf{P}_k^{-1} \leftarrow \frac{1}{\mathrm{n}_k} \sum_{i=1}^{N} \mathrm{r}_{i,k} \cdot \left(\mathrm{g}\left(\widehat{\mathrm{w}}_i\right) - \widehat{\mathrm{m}}_k\right) \left(\mathrm{g}\left(\widehat{\mathrm{w}}_i\right) - \widehat{\mathrm{m}}_k\right)^{\mathrm{T}}. \tag{2.12}$$

Lastly, we compute the mixing coefficient for each cluster k:

$$\pi_k \leftarrow \frac{\mathrm{n}_k}{N}. \tag{2.13}$$

In practice, the expectation–maximization algorithm is fairly sensitive to the initialization, as it only converges to a local maxima. Time permitting, multiple restarts are advisable. The best clustering can be chosen by the highest incomplete-data likelihood. Another consideration is the need to pick the number of clusters K. There are many answers to the question of how to pick K, with varying sophistication and effectiveness. However, since the number of units on a channel is generally limited, fairly simple procedures such as trying multiple values of K and comparing solutions by penalized likelihood work fairly well. We will not discuss this problem further.

2.5 Gaussian Mixture Models and Adaptive Spike Sorting

Now we are ready to attack the problem of adaptive spike sorting using the Gaussian mixture model. We assume that we have already performed spike sorting offline on older data and so have some initial cluster parameters in hand. The problem becomes how to perform classification of waveforms online, while at the same time updating the clustering parameters to track changes in the units' archetypical spike shapes, noise distributions, and firing rates.

Let us think about this problem in one particular way to gain insight. We can assume that the new spikes are classified in real time without considering changes in clustering parameters, and then, periodically, we perform a parameter update. During this parameter update, we use the spikes which have been recorded since the last parameter update. We also have the labels generated by online spike sorting. Now, we are in a similar situation as the maximization step in the EM algorithm: we have data and labels and need parameters. We can then set the clustering parameters using the statistics calculated on the new batch of data. This is equivalent to performing one iteration of the EM algorithm, using the previous clustering parameters as initialization.

While this approach may work, it suffers from some drawbacks. The primary drawback is that, if the batch of data is small, the parameter estimates may be

unreliable. Also, one can criticize the algorithm as throwing away information, by only using the old parameters as initialization. Even though the old parameters initialize the EM iteration—they provide the labels—they do not in any other way constrain the final parameter estimates, which are entirely dependent on the new batch of data. If we make some assumptions about how spike shapes change over time, for example, that they change slowly and smoothly, then we can use the old parameters to inform the new parameter estimates.

Another possible criticism of this one-iteration approach is that the updated sorting parameters may change the labeling, which in turn may change the sorting parameters. This is ignored if only one iteration is performed. What if we perform more than one iteration of EM? In that case, the labels of the data might change. Since online classification has already been performed, this new information is wasted. What if we perform EM until convergence on each new waveform as it arrives? This would allow us to use the label computed based upon the updated parameters. However, if we do this with EM, we run into the problem of parameter estimates based on too little data.

Considering the above, one reasonable suggestion is to incorporate the previous spike sorting parameters during the computation of the new parameters in some manner. This would mitigate the problem of insufficient data, reduce the impact of noise in our estimates, and allow prior information contained in the previous parameters to inform our new parameters. Instead of completely new parameter estimates, the parameters would be *updated.* The question becomes how best to accomplish this scheme.

One approach may be to update the parameters using a moving average. We may store a set amount of past data and weigh data based upon its age. Or, to be more memory efficient, we can avoid storing data by using a stateful moving average, such as an exponentially weighted moving average. The state can be the parameters or the statistics we use to compute the parameters. While these approaches can work, they provide no assurances of optimality.

A more elegant and principled approach is to use a Bayesian probabilistic framework. We treat the parameters as random variables instead of point values. The distribution of the random variables represents our uncertainty about their values. Then, we can update our distributions for the parameters using Bayes' rule, which combines prior information (in our case, past parameter estimates) with new observations (new incoming waveforms) to compute posterior estimates (updated parameter estimates). The storing and calculation of uncertainty is crucial to this paradigm, because the amount of uncertainty tells us how best to combine different sources of information (prior information, new observations).

In the following, we present an adaptive spike sorting algorithm based on the GMM which performs Bayesian updates of the GMM parameters. We use probability distributions to represent the parameters of the GMM, so that the full model is a hierarchical model, with hyperparameters specifying the distributions of the GMM parameters. The algorithm operates on the hyperparameters during updates. The algorithm is an example of variational Bayesian inference, so we call it variational Bayesian Gaussian mixture adaptive spike sorting. In the next section, we specify the hierarchical model.

2.6 Hierarchical Model for GMM Parameters

The hierarchical Bayesian Gaussian mixture model and variational Bayesian clustering algorithm presented here can be found in Bishop (2006), which also presents an exposition on variational Bayesian inference. We apply the model and algorithm for adaptive spike sorting. This approach has been applied to other problems, for example, to the problem of speaker identification by Gauvain and Lee (1991). We refer to the general inference algorithm presented by Bishop as variational Bayes on Gaussian mixtures (VBGM) clustering and our application of it to adaptive spike sorting as VBGM adaptive spike sorting. We first discuss some preliminaries.

The three kinds of parameters we need to consider are mean vectors, precision matrices, and mixing coefficients. Each kind of parameter has a different form, best represented by a different distribution. We chose distributions for these parameters so that they are conjugate to the normal and categorical distributions they parameterize. This is a special property linking distributions which allows for efficient inference and storage of parameters.

For example, the parameter of distribution X on some data is a real number x. Say we model x as a random variable, with a distribution Y with parameter y. Say we start with some prior information on x, i.e., a prior distribution Y with known value of y, and observe some instances of data drawn from X. We can then update the distribution Y using Bayes rule to get a posterior distribution Y′. For arbitrary pairs of distributions X and Y, the posterior distribution Y′ will have a different form from Y, i.e., come from a different family of distributions. Furthermore, it is very likely that Y′ will not have a closed-form representation. However, if we choose Y so that it is conjugate to X, then the posterior distribution Y′ is guaranteed to be from the same distribution family as Y, differing only in the parameter value (y).

Thus, when we choose a distribution for the parameter ("prior distribution") which is conjugate to the distribution it parameterizes (the "likelihood"), we only need to work with and store the hyperparameters (y in the above example). We need not worry about the form of the distribution changing. Using conjugate priors allows closed-form solutions to Bayesian inference on parameters and is one of the key elements of the variational Bayesian approach. Admittedly, only using conjugate priors limits our ability to express prior beliefs; however, conjugate priors are in some sense "natural" as distributions for parameters—the hyperparameter updates that they entail are fairly intuitive and reasonable.

Now we are ready to specify the hierarchical model. The cluster parameters for a unit k, the mean vector $\widehat{\mathrm{m}}$ and precision matrix $\mathbf{P}$, are modeled as random variables which together form a normal-Wishart distribution:

$$\{\widehat{\mathrm{m}}_k, \mathbf{P}_k\} \sim N(\widehat{\mathrm{m}}_k | \widehat{\theta}_k, (\beta_k \mathbf{P}_k)^{-1}) W(\mathbf{P}_k | \mathbf{W}_k, \mathrm{v}_k),$$

where $\widehat{\theta}_k$, β_k, W_k, and v_k are hyperparameters. The hyperparameter $\widehat{\theta}_k$, a d-dimensional column vector, is analogous to the mean vector $\widehat{\mathrm{m}}$. It specifies the center of the distribution for the archetypical shape, and since the distribution

is normal, the maximum probability value and the expectation for $\widehat{\mathrm{m}}_k$ is $\widehat{\theta}_k$. The hyperparameter β_k, a scalar, acts like a count of the amount of data seen so far. The hyperparameter W_k, a matrix of size $\mathrm{d} \times \mathrm{d}$ called the scale matrix, is analogous to (the inverse of) the sum of squared differences matrix when computing a covariance. The hyperparameter v_k, a scalar, is analogous to the number of data when computing a covariance and is called the degrees of freedom. The expectation of the Wishart distribution is precisely the product of these two hyperparameters, which is analogous to computing the sample precision of a data set. Hence, it is intuitively satisfying that the Wishart distribution is the conjugate prior for the precision parameter of a normal distribution. The distributions on the mean and precision are linked (modeled jointly) because their uncertainties naturally covary. However, distributions are assumed to be independent between clusters.

The mixing coefficients $\pi_{1\ldots K}$ are modeled as having a Dirichlet distribution:

$$\pi_{1\ldots K} \sim \mathrm{D}\left(\alpha_{1\ldots K}\right), \tag{2.14}$$

where $\alpha_{1\ldots K}$ are scalar hyperparameters. They can be understood as observed counts, i.e., if we observe 10 spikes of unit A, 20 of unit B, and 30 of unit C, then $\alpha_{\mathrm{A}} = 10$, $\alpha_{\mathrm{B}} = 20$, and $\alpha_{\mathrm{C}} = 30$ would be the parameters of the Dirichlet distribution of the mixing coefficients considering only these data. If we add more observations, we simply add the counts for each unit to the corresponding α hyperparameters (if we assume old data is as good as new data). In this sense the Dirichlet distribution is an intuitively satisfying conjugate prior to the parameters of the categorical distribution. Note that there is one Dirichlet distribution for all the mixing coefficients.

2.7 Parameter Updates

We now consider how to update the cluster parameters and mixing coefficients. We assume that we have prior distributions for the cluster parameters and mixing coefficients, as represented by values of their hyperparameters. We assume we have as input a batch of N new waveforms, which includes the case of one new waveform.

The variational Bayes iterations are similar to EM iterations, with steps that are repeated until convergence. In the algorithm, we initialize the hyperparameters to their previous values (i.e., from the previous update or from the initial spike sorting). Some equations require the previous hyperparameters, since we need to know the prior, so we also use a tilde ($\sim$) to indicate the previous hyperparameters.

Like the expectation step of the EM algorithm on GMMs, we start with the computation of responsibilities. The equation is different from the evaluation of the normal probability density function and multiplication by the mixing coefficients, because now the normal distribution's parameters and the mixing coefficients are

distributions themselves. We redefine the responsibility as the expectation of the waveform's identity over the parameters' distributions. Due to conjugacy, this expectation is available in closed form. For all units k and all waveforms i, we compute:

$$\mathrm{r}_{k,i} \leftarrow \frac{1}{\mathrm{Z}_i} \exp\left\{ \langle \ln \pi_k \rangle + \frac{1}{2} \langle \ln |\mathbf{P}_k| \rangle - \frac{d}{2} \ln (2\pi) \right. \\ \left. -\frac{1}{2} \left(\frac{d}{\beta_k} + \mathrm{v}_k \left(\mathrm{g}\left(\widehat{\mathrm{w}}_i\right) - \widehat{\theta}_k \right)^{\mathrm{T}} \mathbf{W}_k \left(\mathrm{g}\left(\widehat{\mathrm{w}}_i\right) - \widehat{\theta}_k \right) \right) \right\}, \tag{2.15}$$

where Z_i is a normalizing constant to make all responsibilities for waveform i sum to one, d is the dimensionality of the features, and π without subscript is the natural constant. The terms with angled brackets $\langle \ \rangle$ mean the expectations of the expressions within them and are defined below:

$$\langle \ln \pi_k \rangle = \psi\left(\alpha_k\right) - \psi\left(\sum_{j=1}^{K} \alpha_j \right), \tag{2.16}$$

$$\langle \ln |\mathbf{P}_k| \rangle = d \ln 2 + \ln |\mathbf{W}_k| + \sum_{j=1}^{d} \psi\left(\frac{\mathrm{v}_k + 1 - j}{2} \right). \tag{2.17}$$

Here, ψ () is the digamma function and $|\mathrm{W}_k|$ is the determinant of W_k.

After the entire procedure has converged, the responsibilities can be used to find the classifier output of the online spike sorting algorithm. If we need a hard label for each waveform, we can choose the unit with the highest responsibility. If we need a confidence measure, we can use the responsibility values directly, since they are probabilities.

Now we move on to the cluster parameter update, analogous to the maximization step of EM on GMMs. We want to update the hyperparameters to reflect the changes to the parameters' distributions due to the new data observations. The equations for updating the hyperparameters can be derived by applying Bayes' rule—that is, adding (in log space) the probability density functions of the prior distributions (distributions on parameters) with the probability density functions of the likelihood (distributions on data). Then, one must carefully rearrange the terms in the resulting sums, so that the formulas mimic the structure of the probability density function of the prior distribution. Once this is complete, one can see that the posterior distribution is from the same distribution family but with different parameters, following the conjugacy property. Then, performing some algebra gives the expressions for the new hyperparameters in terms of the old hyperparameters and some statistics on the data. This is a somewhat tedious process, so we skip the derivation steps and present the update equations below.

To update the cluster parameters, execute the following for each cluster k:

$$\beta_k \leftarrow \widetilde{\beta}_k + \mathrm{n}_k,$$

$$\widehat{\theta}_k \leftarrow \frac{1}{\widetilde{\beta}_k + \mathrm{n}_k}\left(\widetilde{\beta}_k \widetilde{\theta}_k + \mathrm{n}_k \bar{\mathrm{s}}_k\right),$$

$$\mathrm{v}_k \leftarrow \widetilde{\mathrm{v}}_k + \mathrm{n}_k,$$

$$\mathbf{W}_k^{-1} \leftarrow \tilde{\mathbf{W}}_k^{-1} + \mathrm{n}_k \mathbf{S}_k + \frac{\tilde{\beta}_k \mathrm{n}_k}{\tilde{\beta}_k + \mathrm{n}_k}\left(\bar{\mathrm{s}}_k - \tilde{\theta}_k\right)\left(\bar{\mathrm{s}}_k - \tilde{\theta}_k\right)^{\mathrm{T}}. \tag{2.18}$$

Again, tilde signs over variables indicate prior values. The statistics n_k, $\bar{\mathrm{s}}_k$ (d-dimensional column vector), and S_k ($\mathrm{d} \times \mathrm{d}$ matrix) are defined as:

$$\mathrm{n}_k = \sum_{i=1}^{N} \mathrm{r}_{k,i},$$

$$\bar{\mathrm{s}}_k = \frac{1}{\mathrm{n}_k} \sum_{i=1}^{N} \mathrm{r}_{k,i}\ \mathrm{g}\left(\widehat{\mathrm{w}}_i\right),$$

$$\mathbf{S}_k = \frac{1}{\mathrm{n}_k} \sum_{i=1}^{N} \mathrm{r}_{k,i}\ \left(\mathrm{g}\left(\widehat{\mathrm{w}}_i\right) - \bar{\mathrm{s}}_k\right)\left(\mathrm{g}\left(\widehat{\mathrm{w}}_i\right) - \bar{\mathrm{s}}_k\right)^{\mathrm{T}}. \tag{2.19}$$

Note the resemblance to the equations which calculate the count, mean, and covariance matrix for EM. The contribution of the new data, summarized by these statistics, is combined with the prior knowledge encoded in the old hyperparameters in intuitive ways. For β_k, which acts like a count of the amount of data used to estimate the archetypical spike shape, the update is to add the count of the waveforms for which the cluster is responsible. For $\widehat{\theta}_k$, the center of the distribution for the archetypical spike shape, we do a weighted mean between the old center $\widetilde{\theta}_k$, weighted by the previous count $\widetilde{\beta}_k$, and the center of the new data $\bar{\mathrm{s}}_k$, weighted by the amount of new data n_k. The update for W_k is somewhat more complex. We perform the update on the inverse of the matrix, which is analogous to the sum of squared differences matrix in a covariance calculation. We can understand it as adding the previous sum of squared differences ($\tilde{\mathrm{W}}_k^{-1}$) to the sum of squared differences of the new data ($\mathrm{n}_k \mathrm{S}_k$), and then adding a term that accounts for the difference in the mean used when doing the calculations for the sum of squared differences in the new data and prior.

To update the hyperparameters defining the distribution for the mixing coefficients, for all k, do:

$$\alpha_k \leftarrow \widetilde{\alpha}_k + \mathrm{n}_k. \tag{2.20}$$

This can be easily understood as observing more instances of data belonging to each cluster.

The responsibilities should be recomputed after updating each set of hyperparameters. That means, after the cluster parameter update, responsibilities should be recomputed before performing the mixing coefficient update. Thus, an example order of computation is as follows: responsibilities, cluster parameters, responsibilities, mixing coefficients, and then repeat.

2.8 Detecting Convergence

The responsibility computation and the hyperparameter update steps are repeated until convergence, similar to EM. However, we determine convergence by calculating a different value, which takes into account the distributions on the parameters. This value is the variational lower bound, which we denote with B. It can be shown that maximizing this lower bound minimizes the Kullback–Leibler divergence between the inferred joint posterior on the parameters and the true joint posterior (Bishop 2006). The lower bound, when carefully calculated, can also serve as a diagnostic tool, because it should not decrease during any hyperparameter update step.

The lower bound has many terms, so for the sake of clarity we break it into four main contributors:

$$\mathrm{B} = \mathrm{B}_d + \mathrm{B}_r + \mathrm{B}_\pi + \mathrm{B}_{m,\mathrm{P}}. \tag{2.21}$$

B_d is the contribution from the data:

$$\mathrm{B}_d = \frac{1}{2}\sum_{k=1}^{\mathrm{K}} \mathrm{n}_k \left\{ \langle \ln |\mathbf{P}_k| \rangle - \frac{d}{\beta_k} - \mathrm{v}_k \mathrm{tr}\left(\mathbf{S}_k \mathbf{W}_k\right) \right.$$
$$\left. - \mathrm{v}_k \left(\bar{\mathrm{s}}_k - \widehat{\theta}_k\right)^{\mathrm{T}} \mathbf{W}_k \left(\bar{\mathrm{s}}_k - \widehat{\theta}_k\right) - d \ln (2\pi) \right\}, \tag{2.22}$$

where tr() is the trace operator. B_r is the contribution from the responsibilities:

$$\mathrm{B}_r = \sum_{i=1}^{N}\sum_{k=1}^{K} \mathrm{r}_{k,i} \left(\langle \ln \pi_k \rangle - \ln \mathrm{r}_{k,i} \right). \tag{2.23}$$

B_π is the contribution from the mixing coefficients:

$$\mathrm{B}_\pi = \ln \Gamma\left(\sum_{k=1}^{K} \tilde{\alpha}_k\right) - \sum_{k=1}^{K} \ln \Gamma\left(\tilde{\alpha}_k\right) - \ln \Gamma\left(\sum_{k=1}^{K} \alpha_k\right)$$
$$+ \sum_{k=1}^{K} \ln \Gamma\left(\alpha_k\right) + \sum_{k=1}^{K} \left(\tilde{\alpha}_k - \alpha_k\right) \langle \ln \pi_k \rangle, \tag{2.24}$$

where $\Gamma()$ is the gamma function. $\mathrm{B}_{m,\mathrm{P}}$ is the contribution from the cluster parameters:

$$\begin{aligned}\mathrm{B}_{m,\mathrm{P}} =& \frac{1}{2}\sum_{\mathrm{k}=1}^{K} d\left(\ln\tilde{\beta}_k - \ln\beta_k\right) - d\left(\frac{\tilde{\beta}_k - \beta_k}{\beta_k}\right) - \tilde{\beta}_k \mathrm{v}_k \left(\widehat{\theta}_k - \tilde{\theta}_k\right)^{\mathrm{T}} \mathbf{W}_k \left(\widehat{\theta}_k - \tilde{\theta}_k\right) \\ & - \tilde{\mathrm{v}}_k \left|\tilde{\mathrm{W}}_k\right| + \mathrm{v}_k \left|\mathbf{W}_k\right| - (d\ln 2)\left(\tilde{\mathrm{v}}_k - \mathrm{v}_k\right) - 2\left(\sum_{j=1}^{d} \ln\Gamma\left(\frac{\tilde{\mathrm{v}}_k + 1 - j}{2}\right)\right) \\ & + 2\left(\sum_{j=1}^{d} \ln\Gamma\left(\frac{\mathrm{v}_k + 1 - j}{2}\right)\right) + \left(\tilde{\mathrm{v}}_k - \mathrm{v}_k\right)\langle\ln|\mathbf{P}_k|\rangle - \mathrm{v}_k\left(\mathrm{tr}\left(\tilde{\mathrm{W}}_k^{-1}\mathbf{W}_k\right) - d\right).\end{aligned} \tag{2.25}$$

For more information about the lower bound, see Bishop (2006).

In practice, the lower bound calculation can be slow and difficult to implement correctly. As a substitute, one may look at the change in the posterior hyperparameters and stop when the change is smaller than some arbitrary, unitless threshold. The lower bound essentially implements the principled way to do this: the threshold is in terms of probability, thus allowing the contributions of different hyperparameters to be added together in a meaningful way. Alternatively, one can iterate a predetermined number of times or until some quota of execution time is spent, with the possibility of larger approximation error.

2.9 Transition Model for Parameters

The variational Bayesian clustering method we have described thus far combines new information from newly observed data with prior information to update clustering, as well as assigns labels to the new data. We repeat this procedure each time new data arrives. This accumulates information about the clustering parameters, making them more and more certain. In other words, the distributions for the clustering parameters become more and more narrow, and the parameter updates, all else being equal, become smaller and smaller over time.

This is not exactly what we want from an adaptive algorithm. The reason we want adaptation is that we assume the parameters are changing over time. Therefore, if we accumulate information, we are giving undue influence to old data. To use an analogy, in a moving average, we either discount old data or only take the average within a time window so that only recent data are included. If the average was over all data seen so far, it would not be adaptive, but rather more accurately described as accumulating information or sequential estimation.

Thus, we need some way of discounting old information. This is equivalent to making the distributions for the clustering parameters wider or less certain. For those

familiar with Kalman filtering, we are essentially tracking the clustering parameters, and we need to define a transition model for them. This model is called a transition model because it characterizes how the parameters transition from the previous time step (previous run of adaptive clustering) to the current time step.

We need some way to say mathematically that our knowledge of the parameters are becoming less certain over time, since we assume they are changing. However, we do not wish this transition model to change the expectations of the clustering parameters. In other words, we only want to change the width of the distributions and not their center locations. Their center locations will be updated during the VBGM clustering procedure. We use the following updates to express such a transition model, for all k:

$$\widetilde{\beta}_k^{-1} \leftarrow \beta_k^{-1} + \mathrm{c}_1,$$

$$\widetilde{\mathrm{v}}_k \leftarrow \mathrm{v}_k \cdot \mathrm{c}_2,$$

$$\tilde{\mathbf{W}}_k \leftarrow \mathbf{W}_k / \mathrm{c}_2,$$

$$\tilde{\alpha}_\mathrm{k} \leftarrow \alpha_\mathrm{k} \cdot \mathrm{c}_3,$$

where $0 \leq \mathrm{c}_1$, $0 < \mathrm{c}_2 \leq 1$, and $0 < \mathrm{c}_3 \leq 1$ are constants. Note that the right-hand sides have posterior hyperparameter values from the previous update, and the left-hand sides have prior hyperparameter values for the next update.

The update for β_k is somewhat like the effect of a random walk (zero-mean normally distributed additive noise) upon a random variable with a normal distribution. For v_k and α_k, we chose updates in this manner because these hyperparameters act like counts of data observed so far. The update shrinks this count by a fraction, in a manner analogous to an exponentially weighted moving average. The update to W_k is necessary to keep the same P_k value in expectation. The three constants may need different values, as they represent different aspects of change: c_1 represents how fast the archetypical spike shape is changing (larger means faster), c_2 represents how fast the noise distribution is changing (smaller means faster), and c_3 represents how fast the mixing coefficients, or relative firing rates, are changing (smaller means faster).

The optimal values of the constants depend on the actual rate of change of the spike shapes and the time duration between updates. We do not address how to find the optimal values here, and in our experiments they are chosen by hand. If we had labels for the waveform identities, we may use methods from the field of system identification to pick these values. However, true spike sorting labels are unlikely to be available in practice, so some guesswork and tweaking on the part of the practitioner is probably required.

The transition model should be executed whenever time passes. In practice, this means executing it once before each run of the VBGM clustering. The constants will need to be adjusted to reflect the amount of time which has elapsed since

the previous clustering, if clustering occurs at varying intervals. When performing adaptive spike sorting in batch mode, i.e., when working with many spikes at once, we are approximating the transition. That is, since the spikes in the batch likely occurred at different times, rigorously, they should be clustered one at a time, in order, with transitions between each using values of c_1, c_2, and c_3 corresponding to the time elapsed since the previous spike. However, this may be too cumbersome, and since spike shapes do not change on the order of seconds, it is probably unnecessary to do a transition more often than once a minute.

2.10 Initial Spike Sorting

Variational Bayesian inference on Gaussian mixtures can be used for initial or offline spike sorting as well. In fact, this is a convenient way to generate hyperparameters for input to the first update. For this purpose, a set of hyperparameters, encoding some reasonable prior knowledge on the clustering parameters, or encoding ignorance, is needed to initialize the algorithm. Then the variational inference proceeds as described above.

For our experiments on synthetic and real neural data, we use the following initialization, for all k:

$$\widetilde{\theta}_k \sim N\left(0, 25 \cdot \mathbf{I}\right),$$

$$\widetilde{\beta}_k = 10,$$

$$\tilde{\mathbf{W}}_k = 10 \cdot \mathbf{I},$$

$$\widetilde{\nu}_k = \mathrm{d} + 2,$$

$$\widetilde{\alpha}_k = 1,$$

where I is the $\mathrm{d} \times \mathrm{d}$ identity matrix. Note that $\widetilde{\theta}_k$ is randomly drawn from a multivariate normal distribution. This prevents different clusters from having the same prior, a situation which may lead to degenerate clustering results. The hyperparameters $\widetilde{\beta}_k$, $\widetilde{\nu}_k$, and $\widetilde{\alpha}_k$, which are larger when more data has been observed, are set to small initial values, to encode weak prior beliefs on the archetypical spike shapes and mixing coefficients. As long as $\widetilde{\beta}_k$, $\widetilde{\nu}_k$, and $\widetilde{\alpha}_k$ are sufficiently small, the exact values for $\widetilde{\theta}_k$, $\tilde{\mathrm{W}}_k$, and $\tilde{\alpha}_k$ are not important, since the data will easily overrule the prior.

VBGM clustering can be used in offline spike sorting in general. When using carefully chosen priors, one may avoid some problems encountered with EM on GMM clustering, such as degenerate clusters or clusters with unlikely shapes or mixing coefficients.

2.11 Experiments on Synthetic Data

We next demonstrate the utility of the VBGM adaptive spike sorting approach on synthetic data. We test on synthetic data first since we can generate data to our liking. We perform a series of three experiments, with increasingly more challenging changes to track.

The synthetic data are not based on spike shapes, but generic data points drawn from a Gaussian mixture model with time-varying parameters. We used two dimensions for the data, to ease visualization. All our synthetic experiments use three components, and we assume that the algorithm knows K=3. In each experiment, an initial clustering is performed on a static training data set. Then updates are performed on sequential batches of non-stationary data.

Experiment 2.1
In the first experiment, we test the ability of the VBGM adaptive spike sorting method to track changing spike shapes only, without changes in noise distribution or mixing coefficients. To generate the data, we set the mixing coefficients $\pi_1 = 0.3$, $\pi_2 = 0.3$, and $\pi_3 = 0.4$. The cluster covariance matrices were $\mathrm{P}_1^{-1} = \mathrm{I}$, $\mathrm{P}_2^{-1} = 2 \cdot \mathrm{I}$, and $\mathrm{P}_3^{-1} = 0.5 \cdot \mathrm{I}$. Each cluster mean parameter is a function of the time t:

$$\widehat{\mathrm{m}}_1(t) = \left(2 - \frac{2t}{10000}, 4 - \frac{2t}{10000}\right),$$

$$\widehat{\mathrm{m}}_2(t) = \left(3 + \frac{2t}{10000}, -1 + \frac{2t}{10000}\right),$$

$$\widehat{\mathrm{m}}_3(t) = \left(-0.5 + \frac{3t}{10000}, 2 - \frac{2t}{10000}\right).$$

The cluster means change roughly two standard deviations in each axis over the duration of the experiment. To perform the initial clustering, we drew one thousand points with t=0. This acted as static training data. Then we drew 10,000 points with t increasing from 1 to 10,000 and tested the adaptive clustering on this data. The data were processed in batches of 1000 consecutive points.

We performed initial clustering using the initialization from the previous section. For the transition model on the clustering parameters, we set $\mathrm{c}_1 = 0.01$ and $\mathrm{c}_2 = \mathrm{c}_3 = 1$. Figure 2.1 shows several plots of the results. In each of the first ten panels, we show the data in two dimensions so that clusters can be seen. Each panel corresponds to a run of VBGM adaptive spike sorting on a batch of 1000 data points. The last two panels show one dimension versus all time, to illustrate the drift in the clusters more clearly. The coloring of the points indicates true cluster membership (for visualization only, this was not given to the algorithm). To keep the plots as simple as possible, we do not show the label output of VBGM adaptive spike sorting. The magenta X marks the true centers of the clusters in the first ten panels. Since each panel spanned 1000 time points, and the centers drifted continuously, we

show the cluster center at the midpoint of the time window included in the panel. The magenta lines in the last two panels indicate the true cluster centers versus time. The posterior cluster center and cluster standard deviation as found by VBGM adaptive spike sorting are indicated by the black + sign and ellipse in the first ten panels. In the last two panels, the black lines indicate the posterior cluster centers. Note that the black lines are piecewise linear interpolations of the posterior mean values found in the batches. We can see that the VBGM adaptive spike sorting was able to follow the changes in cluster means very well.

Experiment 2.2
For the second experiment on synthetic data, we increased the rate of change of the cluster centers. We also made the clusters move closer to each other. The centers were defined as:

$$\widehat{\mathrm{m}}_1(t) = \left(2 + \frac{3t}{10000}, 4 - \frac{3t}{10000}\right),$$

$$\widehat{\mathrm{m}}_2(t) = \left(3 - \frac{2t}{10000}, -1 + \frac{3t}{10000}\right),$$

$$\widehat{\mathrm{m}}_3(t) = \left(-0.5, 2 - \frac{4t}{10000}\right).$$

The cluster means change about three standard deviations in each axis over the course of 10,000 time points. All other parameters were the same as Experiment 2.1.

The results of Experiment 2.2 are shown in Fig. 2.2. The layout of the figure is similar to that of Fig. 2.1. For Experiment 2.2, tracking was mostly successful but less accurate than in Experiment 2.1. Due to the proximity of the green and red clusters, the tracking of both was affected, with the largest error during time points 7001–8000. However, as seen in the plots of Dimension 1 and Dimension 2 versus time, the adaptive clustering started to recover near the end of the 10,000 time steps.

Experiment 2.3
In the third experiment on synthetic data, we set the cluster means, the cluster precisions, and the mixing coefficients to vary over time:

$$\widehat{\mathrm{m}}_1(t) = \left(2 + \frac{3t}{50000}, 4 - \frac{3t}{50000}\right),$$

$$\widehat{\mathrm{m}}_2(t) = \left(3 - \frac{2t}{50000}, -1 + \frac{3t}{50000}\right),$$

$$\widehat{\mathrm{m}}_3(t) = \left(-0.5, 2 - \frac{4t}{50000}\right),$$

$$\mathbf{P}_1^{-1}(t) = \begin{bmatrix} 1 & \frac{-0.7t}{50000} \\ \frac{-0.7t}{50000} & 1 \end{bmatrix},$$

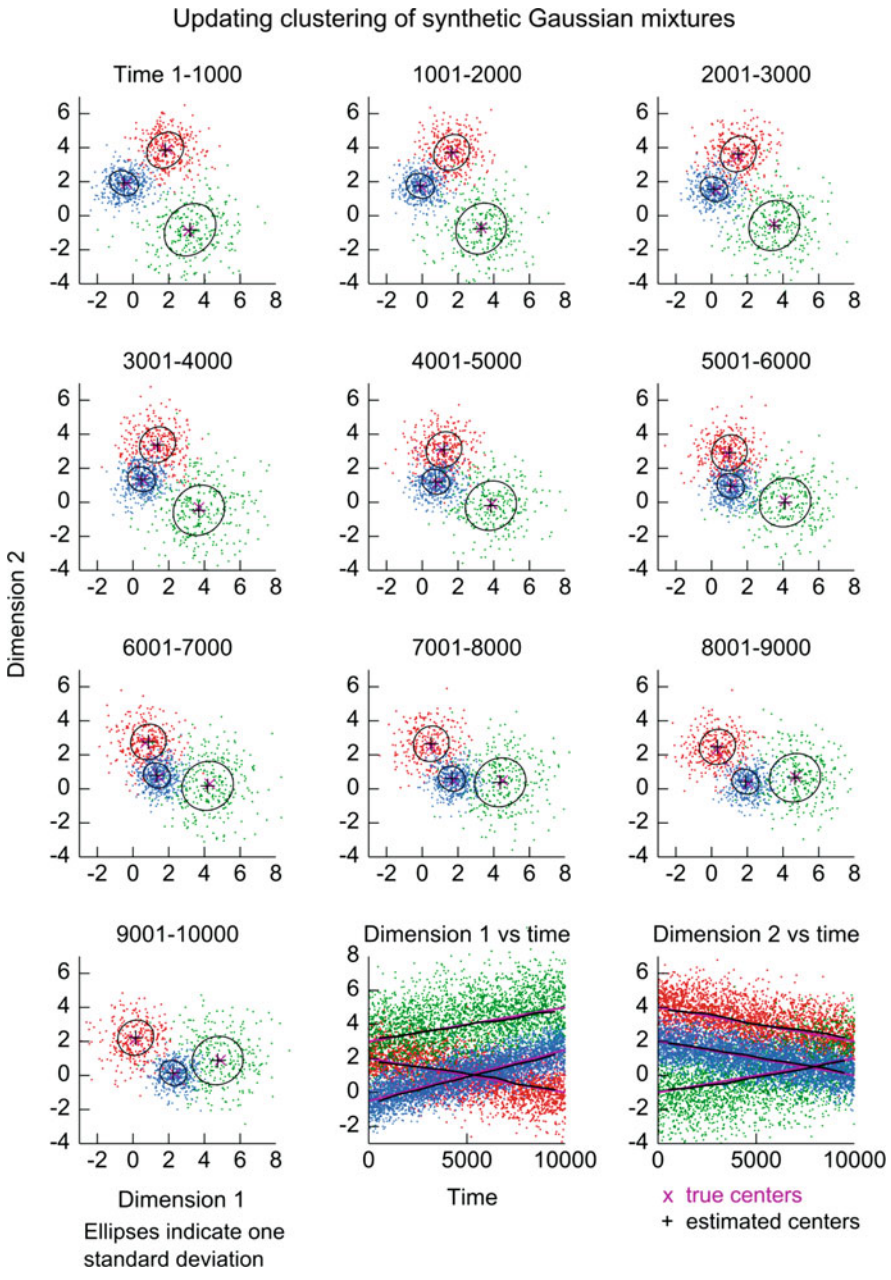

Fig. 2.1 VBGM adaptive spike sorting on synthetic data, Experiment 2.1. Only means of clusters changed. First ten panels show clustering results on each batch. Last two panels show one dimension versus time

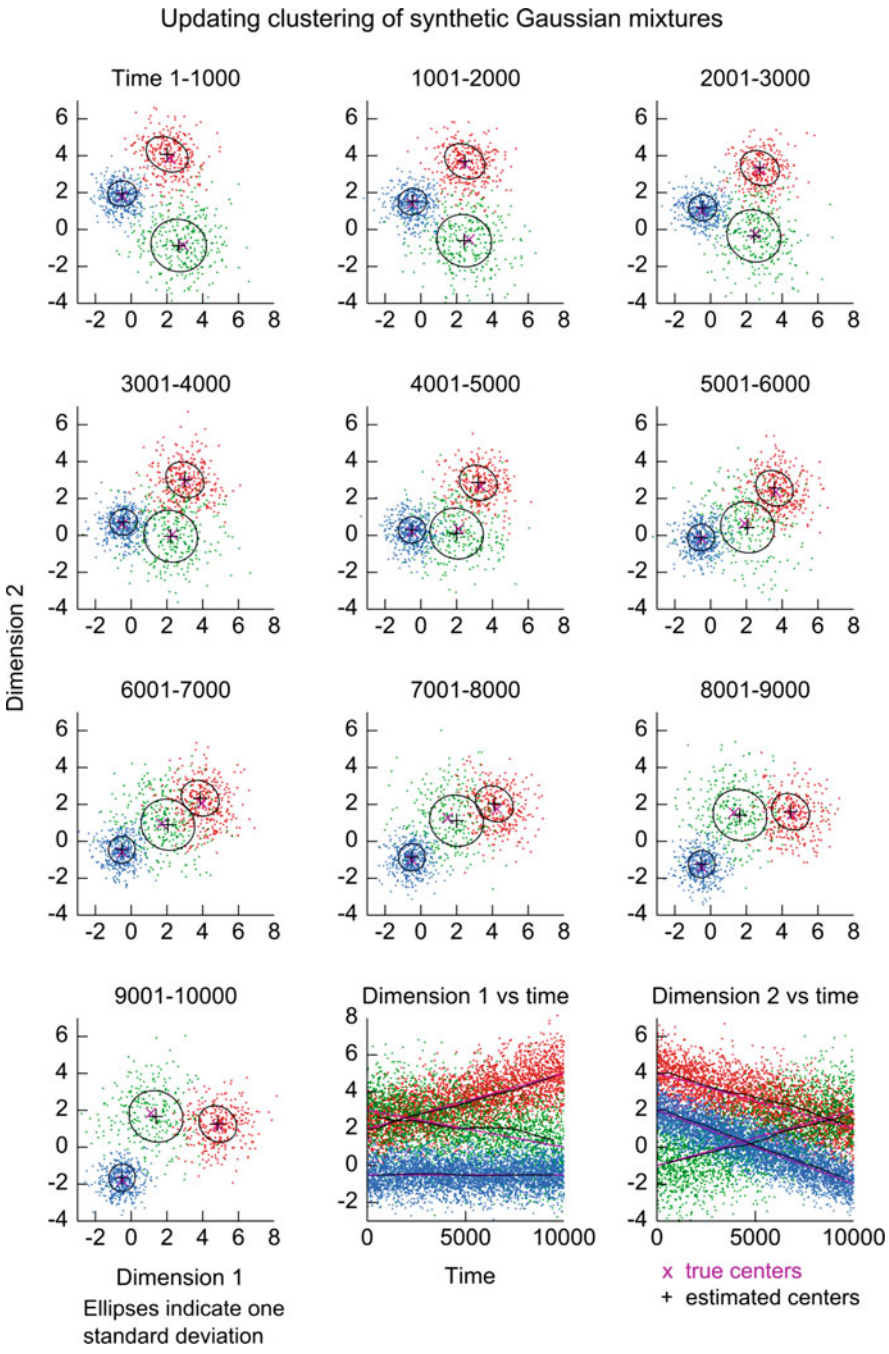

Fig. 2.2 VBGM adaptive spike sorting on synthetic data, Experiment 2.2. Means of clusters changed more quickly than in Experiment 2.1. First ten panels show clustering results on each batch. Last two panels show one dimension versus time

$$\mathbf{P}_2^{-1}(t) = \begin{bmatrix} 2 + \frac{t}{50000} & 0 \\ 0 & 2 + \frac{t}{50000} \end{bmatrix},$$

$$\mathbf{P}_3^{-1}(t) = \begin{bmatrix} 0.5 & \frac{0.3t}{50000} \\ \frac{0.3t}{50000} & 0.5 \end{bmatrix},$$

$$\pi_1(t) = 0.3 + \frac{0.2t}{50000},$$

$$\pi_2(t) = 0.3 - \frac{0.1t}{50000},$$

$$\pi_3(t) = 0.4 - \frac{0.1t}{50000}\ .$$

We also increased the number of data points to 50,000, since more data is needed to track the simultaneously changing parameters. The cluster means change about three standard deviations in this experiment. The change in mixing coefficients is 0.2 for one cluster and 0.1 for the two others. For the transition model on parameters, we used $c_1 = 0.01$, $c_2 = 0.99$, and $c_3 = 0.5$. Adaptive clustering was performed on batches of 5000 data points.

Figure 2.3 shows the results of Experiment 2.3, using the same layout as before, except that 5000 points are depicted in each of the first ten panels. Also, magenta ellipses have been added to show the true cluster standard deviations. VBGM adaptive spike sorting performed fairly well in terms of cluster means, comparable to Experiment 2.2. The tracking of cluster precisions was poorer: the final one-standard-deviation ellipses were less elongated than the true ellipses for the blue and red clusters. This was likely because c_2 was too large. In terms of mixing coefficients, accuracy was also fairly good. The (expectations of the) mixing coefficients from the initial clustering were $\pi_1 = 0.2906$, $\pi_2 = 0.3021$, and $\pi_3 = 0.4073$, very close to the true mixing coefficients at t=0. After processing all data, the (expectations of the) final mixing coefficients were $\pi_1 = 0.4640$, $\pi_2 = 0.2132$, and $\pi_3 = 0.3228$. The inferred mixing coefficients slightly lag behind the true mixing coefficients. This is understandable, since the algorithm operates in batch mode.

2.12 Experiments on Real Neural Data

The experiments on synthetic data showed that the VBGM adaptive spike sorting algorithm can track changes in synthetic data fairly well. Next we test our method on real neural data.

The data were acquired from a Rhesus monkey (*Macaca mulatta*) in the laboratory of Miguel Nicolelis at Duke University. The data were recorded from

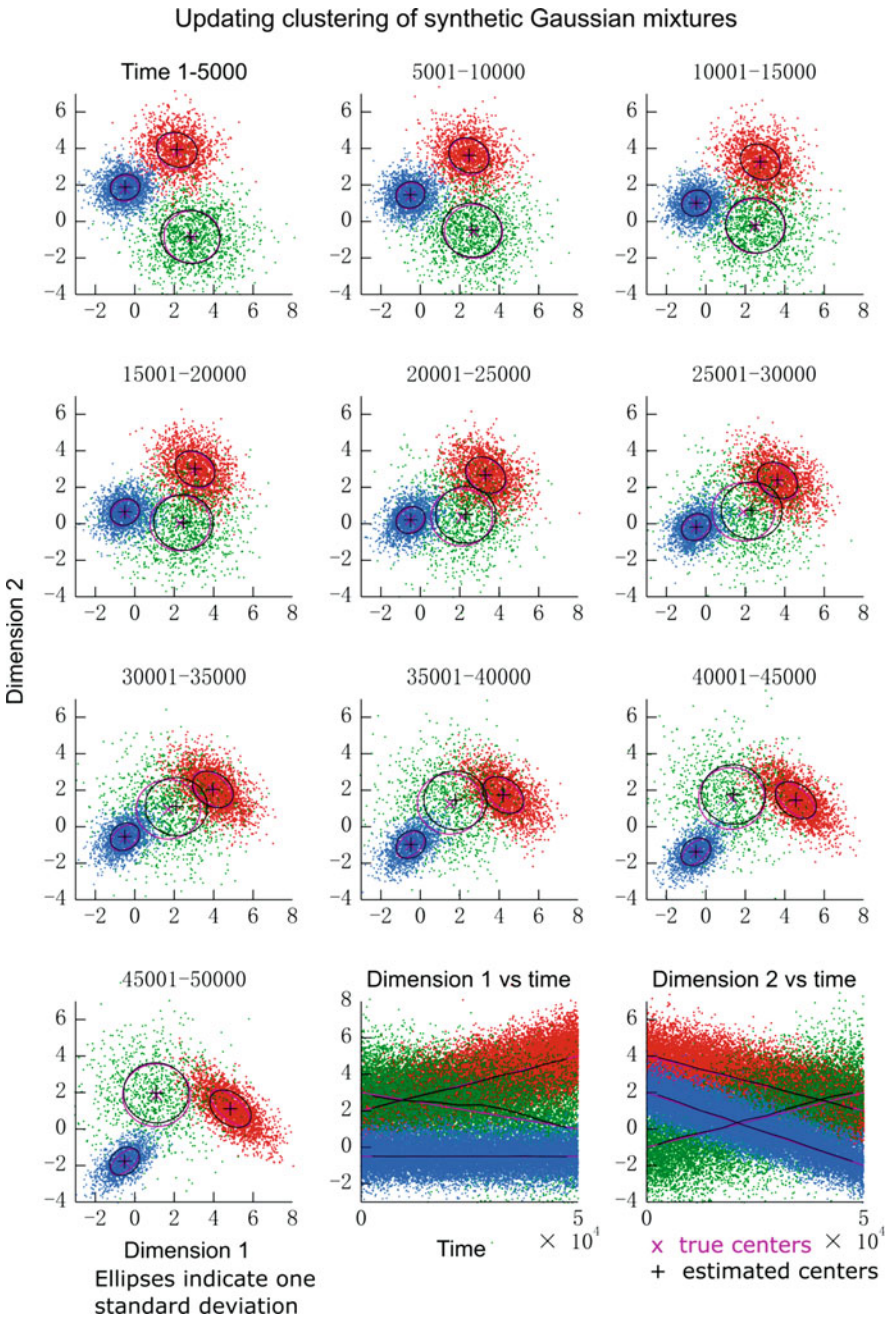

Fig. 2.3 VBGM adaptive spike sorting on synthetic data, Experiment 2.3. All parameters changed. First ten panels show clustering results on each batch. Last two panels show one dimension versus time

motor-related cortical areas using chronically implanted microwire electrode arrays (for methods, see Li et al. 2009, monkey C). Electrodes were made of stainless steel or tungsten and approximately 50 micron in diameter. Electrodes were grouped into pairs which had 300 micron differences in length. Electrodes were positioned in a uniform grid where adjacent pairs were separated by 1 mm. The electrodes in each pair were separated by a large enough distance in depth so that they were unlikely to record from the same neurons; thus, we do not process them as stereotrodes. The data were recorded using a Plexon Inc. Multichannel Acquisition Processor.

The unstable recordings at the start and end of sessions were discarded. We only processed waveforms which crossed an experimenter-set voltage threshold for spike detection. Putative noise waveforms were culled by template matching against a database of noise shapes observed in that recording setup. Also, waveforms which saturated the analog-to-digital converter for more than 10 % of the waveform window were culled. After these preprocessing steps, we removed the labels obtained from online spike sorting using the Plexon hardware. We divided the spikes into six consecutive blocks, with an approximately equal number of spikes in each block.

We used two feature dimensions for input, to be similar to the experiments on synthetic data and to make visualization easy. We first computed the time derivative of each waveform. Then we performed principal components analysis using data in the first block. We used the two largest principal components to project all data down to two dimensions. We then scaled the features to have standard deviation of approximately two, so as to be similar to the synthetic data.

The number of clusters K was set by hand. We used constants $c_1 = 0.01$ and $c_2 = c_3 = 1$, also set by hand. Initial spike sorting was performed on the first block, using the initialization previously described, then VBGM adaptive spike sorting was applied sequentially to the remaining five blocks.

Results of adaptive spike sorting on three different channels are shown in Figs. 2.4, 2.5, and 2.6. These channels had data spanning 23, 24, and 35 min, respectively. The black + signs and ellipses indicate means and standard deviations. In the sixth panel, the initial mean and standard deviation are shown in red for comparison. The bottom panels show spike shapes of each unit to illustrate the change in actual waveform shape, instead of feature values. The mean initial and final spike shapes are shown in red and black, respectively. For calculating the mean shapes, responsibilities were used to weigh the mean calculation, similar to the maximization step of EM. We can see that the VBGM adaptive spike sorting could track the slowly changing spike shapes. In Fig. 2.6, there is substantial change in spike shape over the course of 35 min.

2.13 Discussion

The experiments on neural data show that VBGM adaptive spike sorting can track changing spike shapes when conditions are favorable. That is, when the clusters are fairly well separated. Tracking accuracy is expected to deteriorate if clusters are

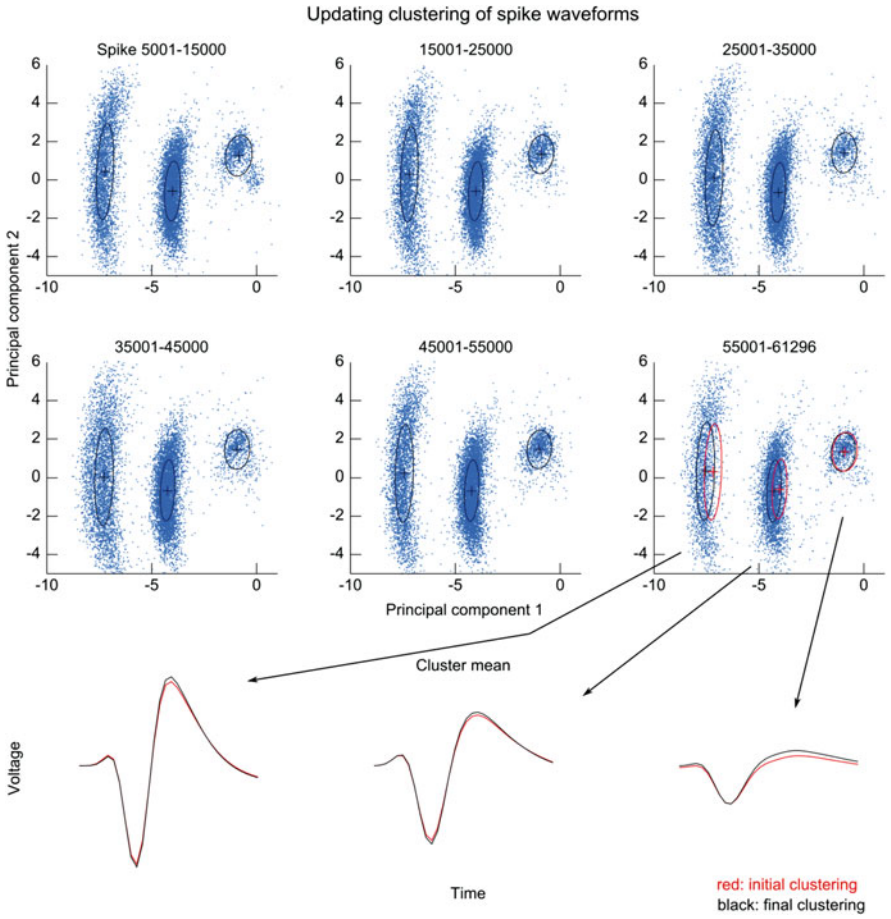

Fig. 2.4 VBGM adaptive spike sorting on neural data from cortex of Rhesus monkey, example 1. First six panels show clustering on each batch. Last three panels show mean waveform shape comparison. Data shown spans 23 min

close together in feature space, as seen in the second experiment on synthetic data. If true labels or labels with high confidence from some other source are available, they can be used to make tracking of parameters more accurate. There are also likely to be some heuristics which can improve tracking performance, by leveraging knowledge about the biology.

In general, adaptive spike sorting is an ill-posed problem. Given only the spike shape data, we cannot distinguish an outlier due to noise from a data point reflecting a sudden change in the underlying biology. However, we can define a probabilistic model on the entire system and, by assuming the model is correct, trust in the most probable explanation. In this approach, the probability of the deviation from expected spike shape arising from noise would be weighed against the probability of

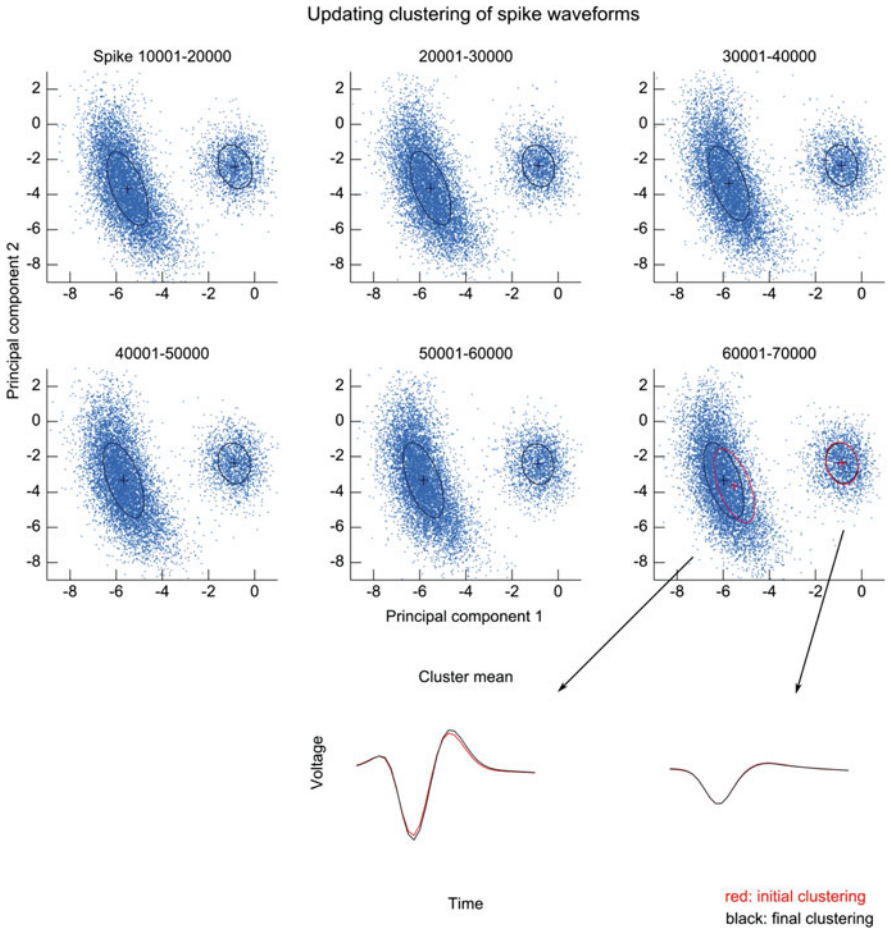

Fig. 2.5 VBGM adaptive spike sorting on neural data from cortex of Rhesus monkey, example 2. First six panels show clustering on each batch. Last two panels show mean waveform shape comparison. Data shown spans 24 min

the underlying system changing, as defined by the transition model on parameters. This is what we do in our adaptive spike sorting solution.

A consideration for adaptive spike sorting is the computational cost of the algorithm, since it must process data in real time. Using batch mode for parameter updates, asynchronous with real-time classification for spike labels, gives two benefits: amortization of some of the fixed computational costs and likely better CPU cache performance. However, it still requires that data be processed faster than it arrives, on average.

In our experiments, we used a moderately optimized MATLAB implementation of VBGM clustering on a desktop personal computer with an Intel Core i7 class

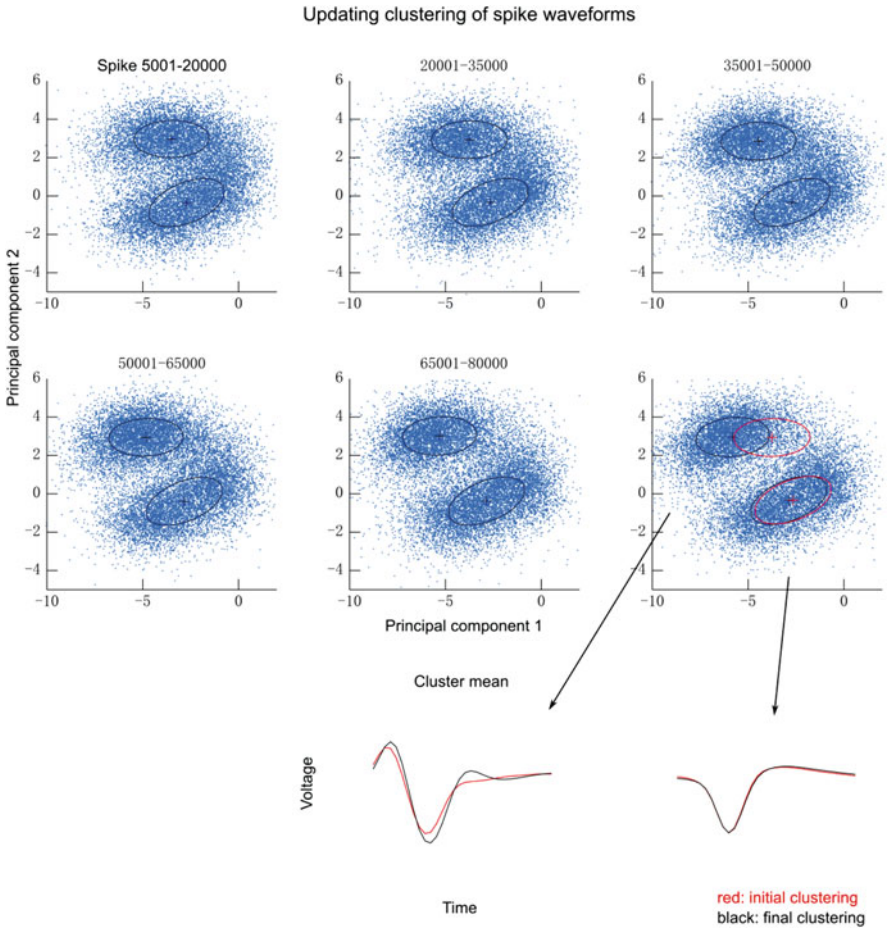

Fig. 2.6 VBGM adaptive spike sorting on neural data from cortex of Rhesus monkey, example 3. First six panels show clustering on each batch. Last two panels show mean waveform shape comparison. Data shown spans 35 min

processor. Initial clustering of 15,000 data points used less than 2 s. Runs of the VBGM adaptive spike sorting on batches of data (also 15,000 data points) took less than 0.25 s each. During the updates, convergence was quicker due to prior information.

Execution speed is expected to be heavily dependent on the feature dimensionality d, though for spike sorting, dimensionality much higher than three is seldom seen. Complexity analysis of the computations shows that the slowest steps (computing $r_{k,i}$ and $\mathbf{S}_k$) have time complexity $O\left(NKd^2\right)$, while overall, the complexity of one VBGM clustering iteration is $O\left(NKd^2 + Kd^3\right)$. The cubic term comes from the inverse in the update for $\mathbf{W}_k^{-1}$. The number of iterations per run

largely depends on the prior, and our above results suggest the number of iterations is low (<10) during adaptation.

If we were to use our current MATLAB implementation to perform adaptive spike sorting on individual spikes as they arrive, the execution rate would be about 220 Hz, where each event is processing one new spike. This value was found while processing 10,000 data points in succession with 2 clusters and 2 feature dimensions. Note that this value is far lower than the >60 KHz execution rate of batch-mode operation, indicating that much of the computation during single spike adaptation is independent of the amount of data. This execution speed is fast enough for one to a few channels of recordings. With a well-optimized C/C++ implementation, speed should be at least an order of magnitude faster. If the VBGM clustering algorithm stops iterating when available execution time runs out, the clustering results would be biased toward the prior, since it is the initialization. This is a fairly safe failure condition, which makes stop-on-time-limit a potential implementation strategy.

The VBGM adaptive spike sorting method compares most closely with the work of Wolf and Burdick (2008). Their algorithm uses the previous clustering result as initialization in a Bayesian extension of EM. However, they do not place strong priors on the cluster covariances and mixing coefficients; they use diffuse priors instead. Their algorithm also handles loss and discovery of neurons and models noise outliers. The work of Calabrese and Paninski (2011) is also similar to ours in some ways. They use a mixture of Kalman filters to track changing archetypical spike shapes. They also add a mechanism for modeling refractory. The sophisticated hierarchical model of Gasthaus et al. (2009) elegantly handles loss and discovery of neurons, as well as neural refractory. They use a particle filter to perform inference on this model.

In summary, we have presented an adaptive spike sorting method which uses Bayesian inference to track slow drifts in spike shape, noise distribution, and relative firing rate. The method is computationally efficient and can successfully track changes in real neural data. However, future work can improve this approach by adding a method to handle discovery and loss of neurons and a method for choosing transition model parameters intelligently.

References

Bar-Hillel A, Spiro A, Stark E. Spike sorting: Bayesian clustering of non-stationary data. J Neurosci Methods. 2006;157(2):303–16.

Bishop CM. Pattern recognition and machine learning. New York: Springer; 2006.

Calabrese A, Paninski L. Kalman filter mixture model for spike sorting of non-stationary data. J Neurosci Methods. 2011;196(1):159–69.

Dempster AP, Laird NM, Rubin DB. Maximum likelihood from incomplete data via the EM algorithm. J R Stat Soc Ser B (Methodol). 1977;39(1):1–38.

Gasthaus J, Wood F, Görür D, Teh YW. Dependent Dirichlet process spike sorting. In: Advances in neural information processing systems 22. Cambridge: MIT Press; 2009.

Gauvain JL, Lee CH. Bayesian learning of Gaussian mixture densities for hidden Markov models. In: DARPA speech and natural language workshop.Harriman; 1991. p. 272–277.
Gibson S, Judy JW, Markovic D. Spike sorting. IEEE Signal Process Mag. 2012;29:124–43.
Harris KD, Henze DA, Csicsvari J, Hirase H, Buzsaki G. Accuracy of tetrode spike separation as determined by simultaneous intracellular and extracellular measurements. J Neurophysiol. 2000;84(1):401–14.
Lewicki MS. A review of methods for spike sorting: the detection and classification of neural action potentials. Netw Comput Neural Syst. 1998;9(4):53–78.
Li Z, O'Doherty JE, Hanson TL, Lebedev MA, Henriquez CS, Nicolelis MAL. Unscented Kalman filter for brain-machine interfaces. PLoS One. 2009;4(7):e6243.
Paraskevopoulou SE, Wu D, Eftekhar A, Constandinou TG. Hierarchical Adaptive Means (HAM) clustering for hardware-efficient, unsupervised and real-time spike sorting. J Neurosci Methods. 2014;235:145–56.
Sahani M. Latent variable models for neural data analysis. Ph. D. thesis, California Institute of Technology; 1999.
Ventura V. Automatic spike sorting using tuning information. Neural Comput. 2009;21:2466–501.
Wolf MT, Burdick JW. Bayesian clustering and tracking of neuronal signals for autonomous neural interfaces. In CDC 2008. 47th IEEE conference on decision and control; 2008. pp. 1992–1999.

Chapter 3
Causality of Spike Trains Based on Entropy

Zhaohui Li and Xiaoli Li

3.1 Introduction

Over the past decades, most studies by means of spike trains have focused on the understanding of the neural coding (de Charms and Zador 2000; Nemenman et al. 2008; Ohiorhenuan et al. 2010; Pouget et al. 2000). It is of great interest to find out how neurons process and transmit information, which is a foundational issue for understanding the function of neuronal circuits and systems (Averbeck et al. 2006; Cessac et al. 2010). To this end, simultaneous recording of multiple single neurons was employed, including multielectrode arrays (Dickey et al. 2009; Kandagor et al. 2010), multiple single electrodes (Fries et al. 2001), optical imaging (Sasaki et al. 2006; Takahashi et al. 2007; Zochowski et al. 2000), etc. By using the recorded spike trains, it is possible to study the interaction among neurons and their relationships within neural systems and then quantify the neural network's structural information to investigate the neural coding. Analysis of spike trains can give functional information such as the coupling strength and direction (Averbeck et al. 2006; Brown et al. 2004; Cessac et al. 2010; Salinas and Sejnowski 2001).

Most analytical methods concentrate on the strength of pairwise connections, i.e., the degree of similarity or dissimilarity between two spike trains, including the cost-based metric (Victor and Purpura 1997; Victor and Purpura 1996), the van Rossum distance (van Rossum 2001), correlation-based methods (Haas and White 2002;

Z. Li (✉)
School of Information Science and Engineering, Yanshan University, Qinhuangdao 066004, China
e-mail: lizhaohui@ysu.edu.cn

X. Li (✉)
State Key Laboratory of Cognitive Neuroscience and Learning & IDG/McGovern Institute for Brain Research, Beijing Normal University, Beijing 100875, China

Center for Collaboration and Innovation in Brain and Learning Sciences, Beijing Normal University, Beijing 100875, China
e-mail: xiaoli@bnu.edu.cn

X. Li (eds.), *Signal Processing in Neuroscience*, DOI 10.1007/978-981-10-1822-0_3

Schreiber et al. 2003), event synchronization method (Quian Quiroga et al. 2002), and the ISI-distance (Kreuz et al. 2007). These methods have been successfully used to find the temporal similar pattern of the spike trains (Fellous et al. 2004; Narayan et al. 2006; Wang et al. 2007). However, above methods are symmetric, and thus they can't capture the causal relationship between spike trains. To obtain the causal relationship between the spike trains, Granger causality and information theory-based causality were proposed. Granger causality method evaluates the coupling directions by determining whether the information of a neuronal series is useful in forecasting (Chen et al. 2004; Ding et al. 2006; Havlicek et al. 2010; Kamiński et al. 2001; Seth 2005, 2010). In recent years, Granger causality has been used to estimate the coupling direction in spike trains (Krumin and Shoham 2010; Nedungadi et al. 2009). But it has two disadvantages: requirement of stationarity and reliance on second-order statistics (Nedungadi et al. 2009). Other methods for estimating the causality between neural series based on the information theory are conditional mutual information (Palu et al. 2001; Palu and Stefanovska 2003), transfer entropy (Schreiber 2000; Vicente et al. 2011), and permutation entropy (Bandt and Pompe 2002; Olofsen et al. 2008). The details on these methods can be found in Hlavkov Schindler et al. (2007). At present, to estimate the causality between two spike trains, two main methods, causal entropy (Waddell et al. 2007) and transfer entropy (Gourévitch and Eggermont 2007), were applied. The causal entropy (CE) is a time-adaptive approach to detect the asymmetries in the relative inter-spike intervals between neuronal pairs. The transfer entropy (TE) quantifies the fraction of information in the past of a neuron flowed to the future of another neuron.

In this chapter, we address an information theory-based approach, which is referred to as permutation conditional mutual information (PCMI), to extract the causality between spike trains recorded from a pair of neurons. The permutation entropy and conditional mutual information have been used to analyze neural signals (Li et al. 2007, 2008, 2010; Salvador et al. 2010; Vejmelka and Palus 2008). Recently, the two methods have been integrated together, named as PCMI, to evaluate the directionality index between two cardiorespiratory series (Bahraminasab et al. 2008) and to estimate the coupling direction between two neuronal populations (Li and Ouyang 2010). In this chapter, we intend to estimate the coupling direction between the spike trains by means of PCMI.

3.2 Entropy in Spike Trains

3.2.1 Conditional Mutual Information

The spike trains are series of the occurrence of action potentials recorded from individual neurons, and each spike train can then be represented as a series of impulse functions:

$$S(t) = \sum_{i=1}^{W} \delta\left(t - t_i\right) \tag{3.1}$$

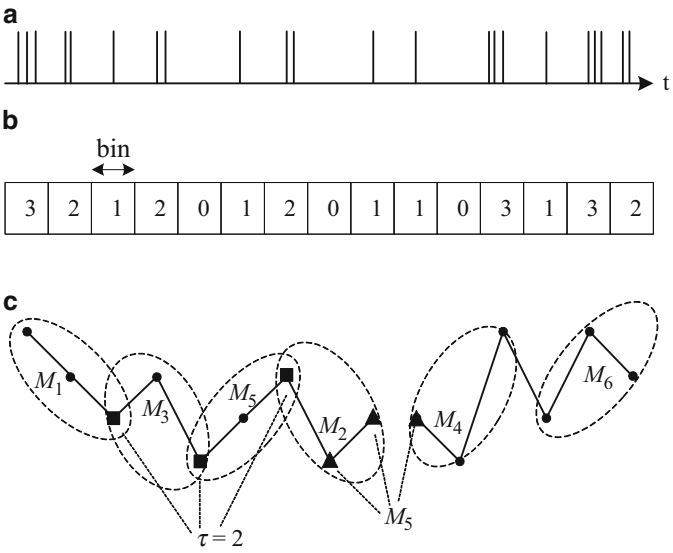

Fig. 3.1 Extraction of motifs from a simulated spike train. (**a**) A simulated spike train. (**b**) Discretize the spike train by adding spikes in each bin. (**c**) Motifs contained in the discretized sequence (order: $m = 3$, so $3! = 6$ different motifs), including "slopes" (M_1 and M_5), "peaks" (M_2 and M_4), and "troughs" (M_3 and M_6). The numbers indicate six different motifs which are defined identical to Li and Ouyang (Li and Ouyang 2010)

where $t_1 \cdots t_W$ are the spike times and W denotes the number of spikes. In order to analyze with PCMI, a temporal resolution Δ (i.e., the bin size) is employed to discretize a spike train to a sequence of integers $N = \{N_1, N_2, \ldots, N_n\}$ (Shlens et al. 2007; Strong et al. 1998), where each integer N_i ($i = 1, 2, \ldots, n$, $n = T/\Delta$ is the total number of time steps within the recorded time interval of length T) denotes the number of spikes occurred in each bin. The scheme is illustrated in Fig. 3.1a, b. Less spikes will fall into a bin with the decrease of bins. If Δ is equal to the sampling period of the spike train, the sequence will become a binary one.

Like electroencephalogram (EEG) and local field potential (LFP), the discretized spike trains may generally present as a fluctuation over time. The motifs (i.e., ordinal patterns, defined in Olofsen et al. (2008) and denoted as M in this chapter) embedded in the fluctuations may provide the causal information between two spike trains. According to the definition of permutation entropy (Bandt and Pompe 2002), the number of total motifs is equal to the factorial of the order (i.e., the number of data points in each motif). For example, there are six different motifs when order $m = 3$, including "slopes," "peaks," and "troughs," which are illustrated in Fig. 3.1c. The order m is an important parameter in the PCMI algorithm, and how to choose its value will be discussed in the following section. It should be noted that there is a little difference in the sorting method in discretized spike trains compared with the method in EEG or LFP. The values in the fragment of continuous EEG or LFP signal

have a continuous distribution; equal values are neglected and only unequal ones are considered for simplicity (Bandt and Pompe 2002). However, in the discretized spike trains, the equal values can't be simply neglected. Otherwise, the temporal patterns contained in spike trains will be destroyed severely by the removal of equal values. To solve this problem, the approach employed in this chapter contains the following step: two equal values for sorting $N_i = N_j$ and $i < j$ are treated as $N_i < N_j$, i.e., an ascending pattern. As shown in Fig. 3.1c, the ordinal pattern that is composed of three data points denoted as solid triangles is classified as M_5.

Another important parameter is the lag τ in PCMI. The lag is the number of sample points spanned by each section of the motif (Olofsen et al. 2008). The motifs under $\tau = 1$ and $\tau = 2$ are illustrated in Fig. 3.1c. The motifs inside the ellipses are of lag $\tau = 1$, and the motif indicated by the solid squares is of lag $\tau = 2$. The effect of lag τ on the result of PCMI in the discretized spike trains will be addressed in the following section. Now, the probability of occurrence of each motif can be calculated as $p(M_i) = f(M_i) / (n - (m-1)\tau)$, where $f(M_i)$, $i \in (1 : m!)$ denotes the frequency of M_i in the discretized spike trains and n is the length of the discretized spike trains.

On the basis of the permutation analysis, the probability distribution functions, the joint probability functions, and the conditional probability functions of two discretized spike trains can be obtained, and then the conditional mutual information can be calculated. Let S_X and S_Y be two spike trains recorded from two neurons. Their corresponding discretized sequences are $X = \{x_n\}$ and $Y = \{y_n\}$, respectively. The marginal probability distribution functions of X and Y are denoted as $p(x)$ and $p(y)$, respectively; the joint probability function of X and Y is denoted as $p(x, y)$. Then, the entropy of X and Y can be defined as (Thomas and Cover 1991)

$$H(X) = -\sum_{x \in X} p(x) \log p(x), \tag{3.2}$$

and

$$H(Y) = -\sum_{y \in Y} p(y) \log p(y). \tag{3.3}$$

The joint entropy $H(X, Y)$ of X and Y is given by

$$H(X, Y) = -\sum_{x \in X} \sum_{y \in Y} p(x, y) \log p(x, y). \tag{3.4}$$

The conditional entropy $H(X|Y)$ of X given Y is defined as

$$H(X|Y) = -\sum_{x \in X} \sum_{y \in Y} p(x, y) \log p(x|y). \tag{3.5}$$

Then, the common information contained in both X and Y can be evaluated by the mutual information:

$$I(X;Y) = H(X) + H(Y) - H(X,Y). \tag{3.6}$$

To infer the causal relationship, i.e., the directionality of the coupling between X and Y, the conditional mutual information (CMI, i.e., the PCMI in this chapter) may be employed to estimate the "net" information about the future of one process contained within the other process. The PCMI between X and Y can be calculated by the following equations (Li and Ouyang 2010; Palu et al. 2001; Palu and Stefanovska 2003):

$$I^{\delta}_{X\to Y} = I(X;Y_{\delta}|Y) = H(X|Y) + H(Y_{\delta}|Y) - H(X,Y_{\delta}|Y) \tag{3.7}$$

and

$$I^{\delta}_{Y\to X} = I(Y;X_{\delta}|X) = H(Y|X) + H(X_{\delta}|X) - H(Y,X_{\delta}|X), \tag{3.8}$$

where X_{δ} (Y_{δ}) is the future δ steps ahead of the process $X(Y)$. The main procedure of the algorithm to detect the coupling direction is as follows:

1. Find the maximum value in $I^{\delta}_{X\to Y}$ and $I^{\delta}_{Y\to X}$, then denoted as $I^{\eta}_{X\to Y}$ and $I^{\eta}_{Y\to X}$.
2. Similar to Rosenblum et al. (2002) and Schnupp et al. (2006), the directionality index between X and Y is defined as

$$D^{P}_{X\to Y} = \left(\frac{I^{\eta}_{X\to Y} - I^{\eta}_{Y\to X}}{I^{\eta}_{X\to Y} + I^{\eta}_{Y\to X}}\right). \tag{3.9}$$

Since both $I^{\eta}_{X\to Y}$ and $I^{\eta}_{Y\to X}$ are confined in the interval [0 1], the value of $D^{P}_{X\to Y}$ (D^{P}: the directionality index of PCMI) ranges from -1 to 1. $D^{P}_{X\to Y} > 0$ means that S_X drives S_Y, and $D^{P}_{X\to Y} < 0$ means that S_Y drives S_X.

3.2.2 Transfer Entropy

The transfer entropy can estimate the information transferred from one neuron to another neuron (Gourévitch and Eggermont 2007). Let $\left[t \quad t+\tau_f\right]$ and $\left[t-\tau_p \quad t\right]$ denote the upcoming time interval and past time interval, respectively, and X^F, X^P and Y^F, Y^P are the number of spikes of S_X and S_Y (S_X and S_Y denote two spike trains) falling in the two intervals; then the transfer entropy from S_X to S_Y is defined as

$$\varphi_{X\to Y} = I\left(Y^F;X^P|Y^P\right) = H\left(Y^F|Y^P\right) - H\left(Y^F|X^P,Y^P\right). \tag{3.10}$$

To reduce the bias caused by the surrogate data that generated by randomly shuffling the inter-spike intervals, the normalized transfer entropy (NTE) is defined as

$$\psi_{X\to Y} = \frac{\varphi_{X\to Y} - \varphi_{X\to Y}^{\text{shuffled}}}{H\left(Y^F|Y^P\right)}. \tag{3.11}$$

There is no causality between two spike trains, when the NTE is less than zero. To restrict the NTE in the interval [0 1], we set up $\psi = 0$ if $\psi < 0$. The directionality index $D_{X\to Y}^T$ (D^T: the directionality index of TE) is defined as

$$D_{X\to Y}^T = \left(\frac{\psi_{X\to Y} - \psi_{Y\to X}}{\psi_{X\to Y} + \psi_{Y\to X}}\right) \in [-1 \quad 1]. \tag{3.12}$$

The $D_{X\to Y}^T$ is greater than 0 if the spike train S_X drives the spike train S_Y; if the $D_{X\to Y}^T$ is less than 0, that means the spike train S_X is driven by the spike train S_Y; if the $D_{X\to Y}^T$ is about 0, there is no causal relationship between the two spike trains.

3.2.3 Causal Entropy

The causal entropy is an information theory method to estimate the causal relationship between two spike trains (Dzakpasu and Zochowski 2005; Waddell et al. 2007). The method is based on the variations of the distribution of inter-spike intervals in S_X and S_Y. The detail of the algorithm can be found in Waddell et al. (2007). Herein, the $\xi_{X\to Y}$ and $\xi_{Y\to X}$ are denoted as the causal entropies between S_X and S_Y. The normalized directionality index of CE is defined as

$$D_{X\to Y}^C = -\frac{\xi_{X\to Y} - \xi_{Y\to X}}{\xi_{X\to Y} + \xi_{Y\to X}} \in [-1 \quad 1] \tag{3.13}$$

where $D_{X\to Y}^C$ (D^C: the directionality index of CE) has the same meaning as the $D_{X\to Y}^T$.

3.3 Izhikevich Model for Spike Trains

In this chapter, the Izhikevich neuronal model is employed for the simulation analysis to evaluate the performance of the methods. The Izhikevich neuronal model combines the biological plausibility of Hodgkin-Huxley-type dynamics and the computational efficiency of integrate-and-fire neurons; this simple model can generate the rich behavior of biological neurons, including spiking, bursting, and mixed mode firing patterns (Izhikevich 2003).

The Izhikevich neuronal model contains two variables: v and u. v is the membrane potential of the neuron and u is a membrane recovery variable; the model is below:

$$v' = 0.04v^2 + 5v + 140 - u + I, \tag{3.14}$$

$$u' = a\,(bv - u) \tag{3.15}$$

with the auxiliary after-spike resetting

$$\text{if } v \geq 30 \text{ mv, then } \begin{cases} v \leftarrow c \\ u \leftarrow u + d, \end{cases} \tag{3.16}$$

where I is the synaptic current or injected DC current. The parameter a describes the time scale of u, b describes the sensitivity of u to subthreshold fluctuations in v, c describes the spike reset values of v, and d describes the spike reset value of u. These parameters are set as $a = 0.02$, $b = 0.2$, $c = -65$ mv, $d = 2$. The injected current I is set as a normally distributed random Gaussian variable. The causality between two neurons is obtained in such a way the output of the first neuron (neuron 1) is fed into the second neuron (neuron 2) with a time delay (denoted as "d_I"). The coupling strength is determined by a proportion R which means how many percents of the output of neuron 1 are injected into neuron 2. The larger the proportion, the stronger the coupling between the two neurons.

3.4 Characterization and Comparison of the Causality

3.4.1 Parameter Choices in PCMI

In the PCMI algorithm, four different parameters (i.e., Δ, τ, order, and δ) should be firstly considered before its application. The effect of these parameter selections on the performance of the PCMI is discussed by the Izhikevich neuronal model. Given $R = 0.5$, $d_I = 25$ ms, and the spike train length 50s, two spike trains are generated:

1. The temporal resolution Δ. The Δ is the bin size that is used to discretize spike trains. The Δ ranges from 1 to 30 ms with a step of 1 ms. Figure 3.2 plots the directionality index estimated by the PCMI with order $m = 2$ and $m = 3$, respectively. For $m = 2$, it can estimate the coupling direction when $\Delta < 15$ ms; while $m = 3$, when Δ is larger than 10 ms, the coupling direction cannot be found. The underlying reason is that the larger Δ destroys the inherent permutation patterns contained in the two spike trains; however the smaller the Δ, the more accurate permutation information can be obtained. In this chapter, it is recommended that the Δ is set as the sample period of the spike train, namely, $\Delta = 1$ ms.

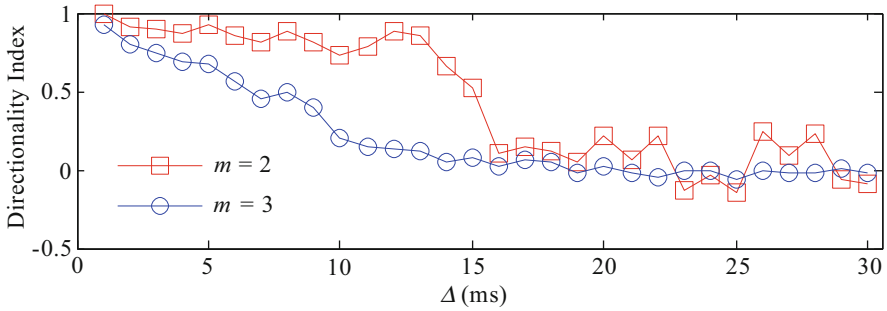

Fig. 3.2 Directionality indexes for different bins

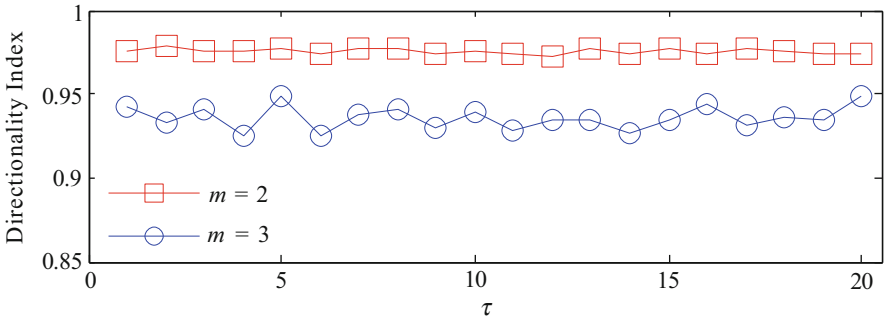

Fig. 3.3 Directionality indexes for different lags

2. The lag τ. The lag is the number of data points between the adjacent two points in the motifs. Figure 3.3 shows the directionality index at the different lags with $m = 2$ and $m = 3$; it is found that the different lags can give similar results for the two orders. In Shelhamer (2007), an autocorrelation function (ACF) of a signal can be employed to determine the lag τ. In this chapter, we found the lag τ determined by the ACF is always one, so the $\tau = 1$ is selected in this simulation analysis.
3. The order m. The order denotes the number of data points included in the motif. The length of data is at least greater than $m! * m! * m!$ points to obtain a reliable result of PCMI, for example, $m = 4$ means we need 13,824 data points (Li and Ouyang 2010). In this chapter, there are only 0 s and 1 s in the binary sequences; when $m = 2$ (ascending and descending ordinal patterns), the permutation patterns of the series can be fully described. As can be seen in Figs. 3.2 and 3.3, $m = 2$ is an appropriate selection for the calculation of PCMI.
4. The δ. It is noted that the δ cannot be less than the order m in PCMI (Bahraminasab et al. 2008). And the δ is associated with the delay time, which will be discussed in the following section. Thus, the δ should be larger than the maximal delay between two spike trains for investigating the causality at all delay times.

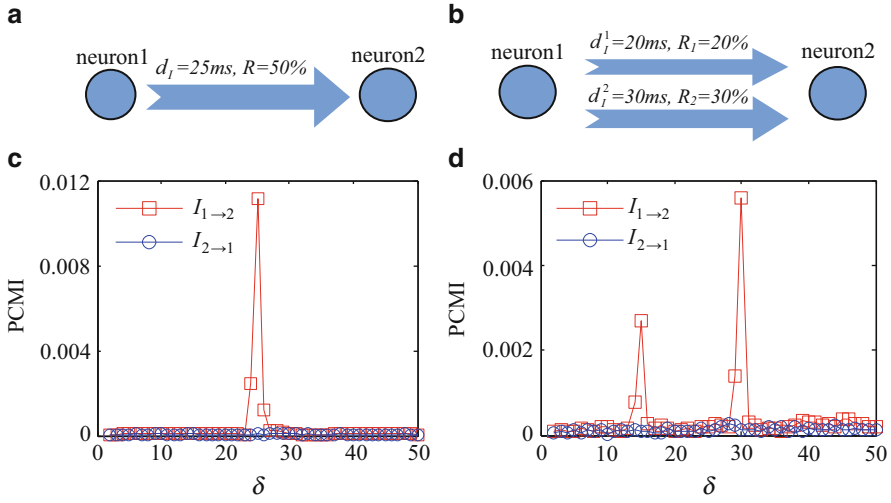

Fig. 3.4 The PCMI estimate for the Izhikevich neuronal models. (**a**) Model I_1: one delay of 25 ms between neuron 1 and neuron 2, 50 % of the output of neuron 1 is injected into neuron 2. (**b**) Model I_2: two different delays of 15 ms and 30 ms between neuron 1 and neuron 2, 20 % and 30 % of the output of neuron 1 associated each delay is injected into neuron 2. (**c** and **d**) The PCMI estimate between neuron 1 and neuron 2 ($I_{1\to2}$ and $I_{2\to1}$) with different δ values for model I_1 and model I_2

3.4.2 Comparison of Simulation Results

Firstly, the capability of PCMI for charactering the causal relationship is demonstrated by the Izhikevich neuronal model. Model I_1 and model I_2 are constructed and shown in Fig. 3.4a, b, respectively. In model I_1, $R = 50$ % and $d_I = 25$ ms, two spike trains of 10s are generated with the causality from neuron 1 to neuron 2. In model I_2, the coupling direction is the same as model I_1 but the strength is composed of two fractions: $R_1 = 20$ % with $d_I^1 = 15$ ms and $R_2 = 30$ % with $d_I^2 = 30$ ms. The reason for the usage of the model I_2 is that the coupling between neurons may involve multiple pathways that vary in their conduction delays (Swadlow et al. 1978). For both models, we use $\Delta = 1$ ms to discretize the two spike trains and $m = 2$, $\tau = 1$, and $\delta = 2 : 50$ to calculate the PCMI. Figure 3.4c, d plots the PCMI values between neuron 1 and neuron 2 ($I_{1\to2}$ and $I_{2\to1}$) with different δ values for model I_1 and model I_2, respectively. Obviously, there is a peak of $I_{1\to2}$ corresponding to every delay time in the two models, which is indicated by the product of δ and Δ (e.g., $\delta = 25$ and $\Delta = 1$ ms for 25 ms delay). In fact, Δ identifies the resolution of the delay times. Moreover, the value of $I_{1\to2}$ is proportional to the coupling strength, as can be observed in Fig. 3.4d. On the other hand, the $I_{2\to1}$ stays closely to 0 due to the absence of causality from neuron 2 and neuron 1. The estimated directionality indexes for the two models reflect the coupling direction exactly.

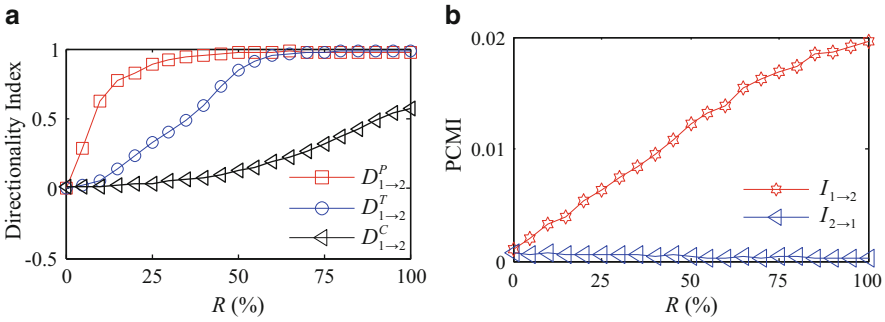

Fig. 3.5 Directionality index and PCMI values for different coupling strength. (**a**) Directionality index estimated by PCMI, TE, and CE for the Izhikevich neuronal model ($D^P_{1\to2}$, $D^T_{1\to2}$, and $D^C_{1\to2}$), respectively. (**b**) PCMI values ($I_{1\to2}$ and $I_{2\to1}$) for different coupling strength

Secondly, to compare with the PCMI, the TE and CE methods are carried out with the same simulations. As mentioned in the previous section, the PCMI, TE, and CE are all parameter-dependent methods. We set the parameters of the three methods as follows: $\delta = 2 : 50$ for PCMI; $\tau_f = 1 : 50$ ms and $\tau_p = 1 : 50$ ms for TE; 10 bins of size 5 ms for CE. The comparison is carried out in three aspects:

1. Variation of directionality index with the coupling strength

In the Izhikevich neuronal model, the parameter R which reflects the coupling strength ranges from 0 to 100 % with a step of 5 %. Spike trains for neuron 1 and neuron 2 are simulated with the causality from neuron 1 to neuron 2 and a delay time of 10 ms. These spike trains are of 10s length. As can be seen in Fig. 3.5a, it is clear that the PCMI and TE are superior to the CE at identifying the coupling direction. As far as PCMI and TE are concerned, the advantage of the PCMI is that it can determine the coupling direction with more reliability and robustness for the weak coupling. Figure 3.5b plots the PCMI values for different coupling strengths. In the direction from neuron 1 to neuron 2, the PCMI estimate is proportional to R. On the other hand, the PCMI estimate is always close to 0 because there is no causality between the two neurons in the opposite direction.

2. The effect of spike train duration on the directionality index estimation

Since the three methods for comparison in this chapter all depend on the statistical calculation, it is necessary to investigate the effect of the duration of spike trains on the directionality index estimation. Given $d_I = 10$ ms, two neurons are generated with the driving direction from neuron 1 to neuron 2. Figure 3.6a, b plots the directionality index estimated by the PCMI, TE, and CE for two different coupling strengths: $R = 10\,\%$ and $R = 30\,\%$. In Fig. 3.6a, with the increase of duration, the directionality index of PCMI increases with small fluctuations and then becomes stationary. In comparison, the directionality index of TE is not suitable for estimating the directionality index because of the large fluctuations and the small

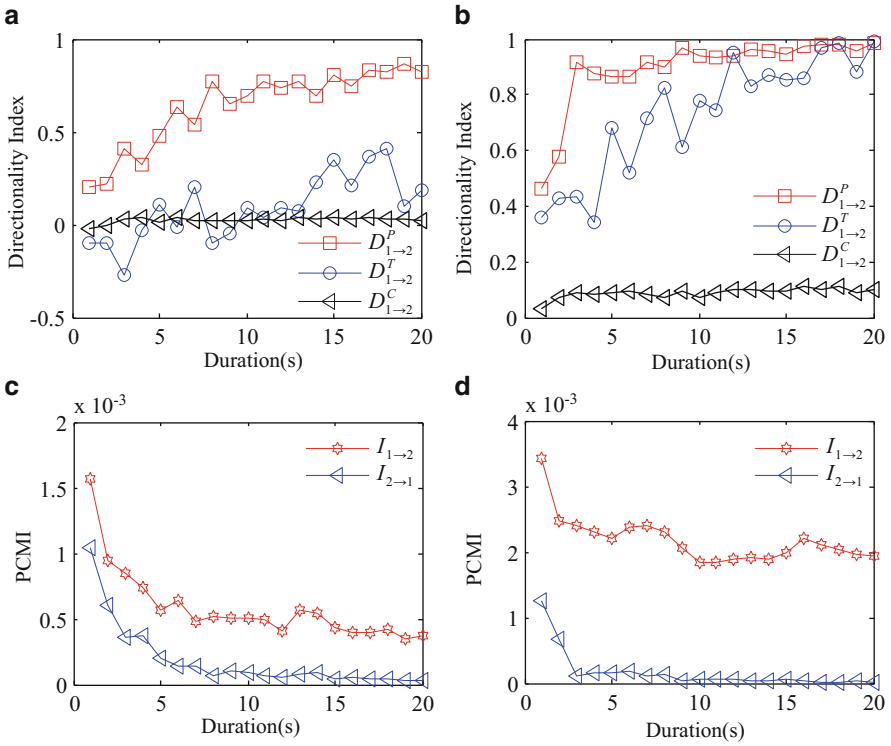

Fig. 3.6 Effect of spike train duration on the directionality index and PCMI values for the Izhikevich neuronal model. (**a** and **b**) Directionality index estimated by the PCMI, TE, and CE($D^P_{1\to2}$, $D^T_{1\to2}$, and $D^C_{1\to2}$) for $R = 10\,\%$ and $R = 30\,\%$. (**c** and **d**) PCMI values ($I_{1\to2}$ and $I_{2\to1}$) with different durations for $R = 10\%$ and $R = 30\,\%$

directionality index. As can be seen in Fig. 3.6b, the behavior of PCMI and TE are similar, but the PCMI is still superior to the TE, especially when the spike trains duration is less than 10s. In both of the cases, compared with PCMI and TE, the directionality index of the CE does not change obviously with the spike train duration, but it is not very efficient to evaluate the coupling detection. The effect of spike train duration on the PCMI values for the two coupling strengths are described in Fig. 3.6c, d. It was found that that there is a significant decrease for $R = 10\,\%$. On the other hand, for the coupling strength $R = 30\,\%$, the PCMI value almost does not vary with the spike train durations.

3. The robustness of directionality index

Three types of noise are considered in this chapter: the jitter noise corresponding to a shift in time of the spikes in spike trains, the missing spikes corresponding to the random deletion of spikes in spike trains, and the extra spikes corresponding to the random insertion of independent spikes in spike trains. The jitter noise may

appear in stochastic biological processes such as synaptic transmission and spike propagation in a neural network. The missing and extra spikes arise as spurious points in the spike trains, primarily caused by spikes which are not fired by the recorded neuron, but by other external processes involving the discharges of other neurons, errors in the spike sorting procedure, electrical artifacts, etc. (Asai and Villa 2008; Schreiber et al. 2003).

For the Izhikevich neuronal model, neuron 1 drives neuron 2 with a delay time of 10 ms. The simulated spike trains are of 10s length. The effect of noise on the directionality index estimation is evaluated by the models of two different coupling strengths: $R = 10\,\%$ and $R = 30\,\%$.

a) Jitter noise. The jitter noise is added to the spike trains via shifting every spike in each spike train by a time normally distributed in an interval. From the simulation results for the Izhikevich neuronal model which are shown in Fig. 3.7a, b, it can be observed that the performances of PCMI and TE to resist jitter noise are very

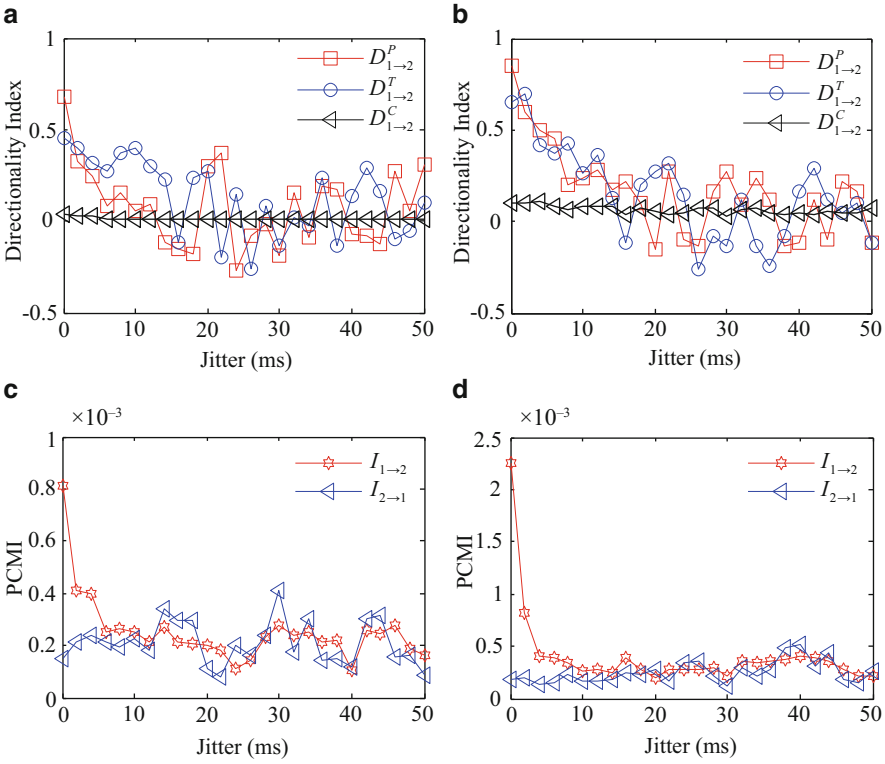

Fig. 3.7 Effect of jitter noise on the directionality index and PCMI values for the Izhikevich neuronal model. (**a** and **b**) The robustness of directionality index estimated by the PCMI, TE, and CE ($D^P_{1\to2}$, $D^T_{1\to2}$, and $D^C_{1\to2}$) against jitter noise for $R = 10\%$ and $R = 30\,\%$. (**c** and **d**) The variation of PCMI values ($I_{1\to2}$ and $I_{2\to1}$) with different jitters for $R = 10\%$ and $R = 30\,\%$

close to each other. However, they can only resist small jitter noise. But the CE cannot resist against the jitter noise. In Fig. 3.7c, d, the PCMI estimate from neuron 1 to neuron 2 ($I_{1\to 2}$) is greatly influenced by the jitter noise which leads to the poor ability of identifying the coupling direction.

b) Missing spikes. The amount of missing spikes is quantified by the percentage of randomly deleted spikes in each spike train. The simulation results for the directionality index are shown in Fig. 3.8a, b. For the coupling strength $R = 10\,\%$, the directionality index estimated by the PCMI decreases with the increasing number of missing spikes. The directionality index of TE fluctuates dramatically and the directionality index of CE stays around zero. For the coupling strength $R = 30\,\%$, the effect of the missing spikes on the PCMI and CE are not significant, but the directionality index of TE decreases significantly. Figure 3.8c, d plots the variation of PCMI values with the missing spikes. With the increase of missing spikes, $I_{1\to 2}$ decreases significantly and $I_{2\to 1}$ increases very slightly. But $I_{1\to 2}$ is always larger than $I_{2\to 1}$ which ensures a correct estimation of the coupling direction.

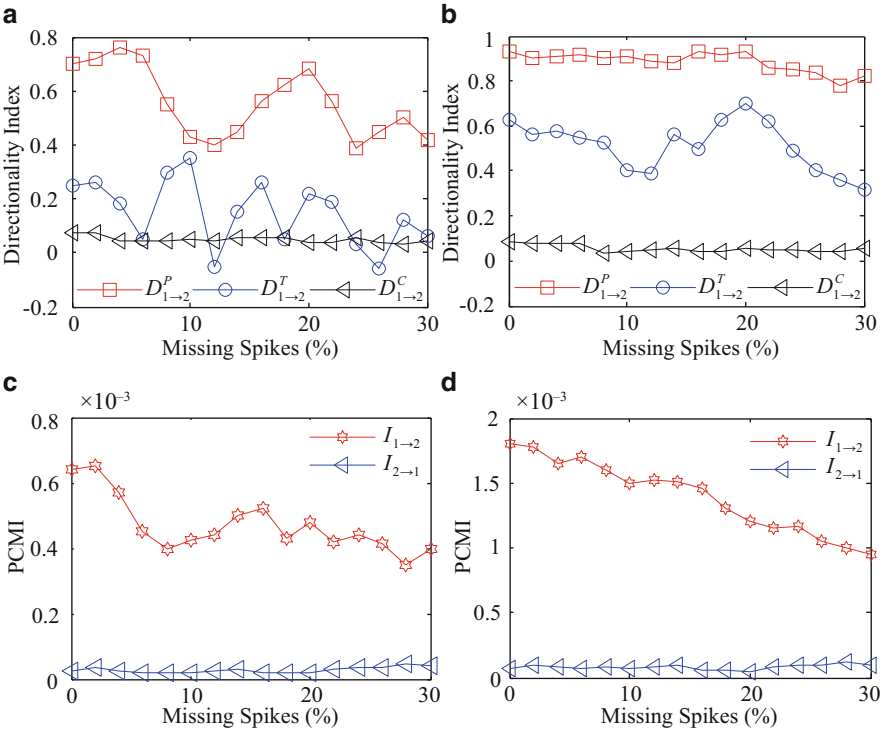

Fig. 3.8 Effect of missing spikes on the directionality index and PCMI values for the Izhikevich neuronal model. (**a** and **b**) The robustness of directionality index estimated by the PCMI, TE, and CE ($D^P_{1\to 2}$, $D^T_{1\to 2}$, and $D^C_{1\to 2}$) against jitter noise for $R = 10\%$ and $R = 30\,\%$. (**c** and **d**) The variation of PCMI values ($I_{1\to 2}$ and $I_{2\to 1}$) with different jitters for $R = 10\,\%$ and $R = 30\,\%$

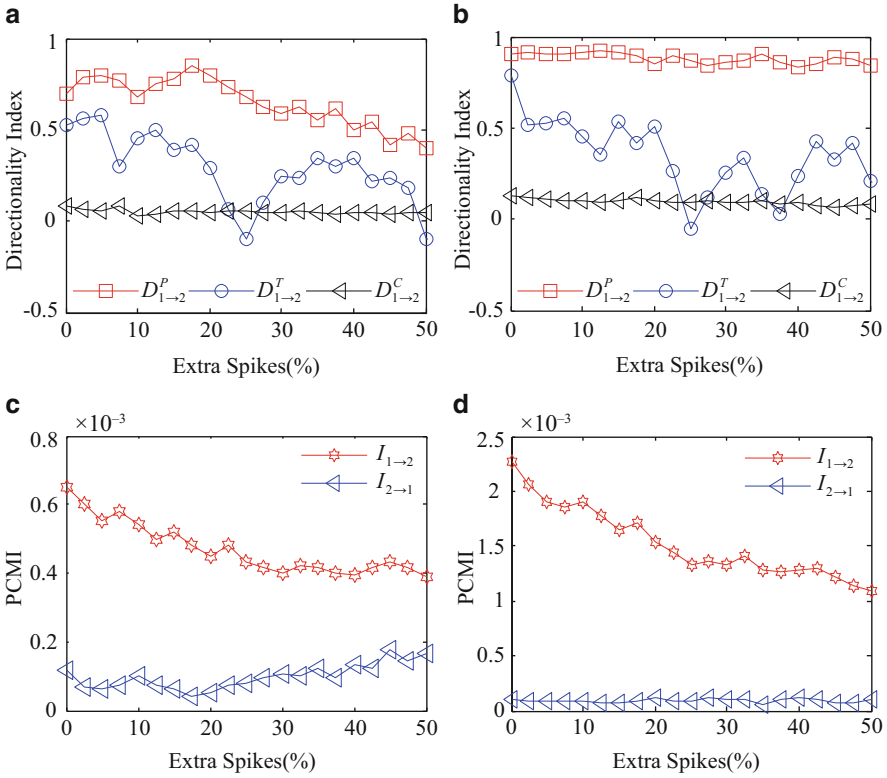

Fig. 3.9 Effect of extra spikes on the directionality index and PCMI values for the Izhikevich neuronal model. (**a** and **b**) The robustness of directionality index estimated by the PCMI, TE, and CE ($D^P_{1\to2}$, $D^T_{1\to2}$, and $D^C_{1\to2}$) against jitter noise for $R = 10\%$ and $R = 30\,\%$. (**c** and **d**) The variation of PCMI values ($I_{1\to2}$ and $I_{2\to1}$) with different jitters for $R = 10\%$ and $R = 30\,\%$

c) Extra spikes. The amount of extra spikes is quantified by the percentage of randomly inserted independent spikes in each spike train. Figure 3.9a, b shows the estimation of directionality index by the PCMI, the TE, and the CE as a function of extra spikes. For the coupling strength $R = 10\,\%$, the extra spikes make the directionality index of PCMI decrease to about 0.4 when the number of the extra noisy spikes is equal to the half of original spikes number. But the PCMI is still capable of estimating the coupling direction. On the other hand, the TE is not suitable for estimating the coupling direction due to its uncertain results, and the CE is not appropriate because of its approximate zero values. For the coupling strength $R = 30\,\%$, the directionality index of the TE and CE are both influenced severally by the extra spike noise. However, there is only a small decrease for the PCMI with the increasing of the noisy spikes. As can be seen in Fig. 3.9c, d, there is variation of the PCMI values because of the extra spikes, but this does not alter the result about the coupling direction, which is similar to the case of missing spikes.

3.5 Conclusions

Characterizing the connections between individual neurons is essential for the better understanding of neural coding. In this chapter, the PCMI method is introduced to identify the causal relationships (information flow) between two spike trains. To assess the performance of the measure, a series of simulations were performed by means of the Izhikevich neuronal model. The simulation results shows that the PCMI method can be applied for the analysis of causality between neurons by spike trains. In comparison with the TE and CE methods, the advantages of the PCMI can be summarized in the following. (1) The PCMI can detect the interaction delays between two spike trains, even if there is a wide distribution of the delay times due to the multiple pathways that connect two neurons. The interaction delays are indicated by the product of δ and Δ, and the resolution is determined by Δ. (2) The PCMI method is able to estimate the directionality index reliably for the weak coupling strength (e.g., $R = 10\,\%$ for the Izhikevich neuronal model) between spike trains, but the TE and CE methods are not suitable in this case because of the dramatical fluctuations and small values of the directionality index, respectively. For the stronger coupling strength (e.g., $R = 30\,\%$ for the Izhikevich neuronal model), the three methods are able to identify the directionality index, but the PCMI is better than the TE and CE at identifying the coupling direction for short spike trains. (3) The PCMI is more robust to the noise in spike trains than the TE and CE, particularly for the missing and extra spikes. The underlying reason is that the PCMI is based on the ordinal patterns contained in the spike trains; thus the missing or extra spikes cannot severely destroy the inherent ordinal patterns, particularly when there is a stronger coupling strength between two spike trains. On the other hand, because the TE is calculated in terms of the number of spikes in time intervals and the CE is computed by means of the relative inter-spike intervals between a pair of spike trains, therefore they are influenced greatly by the missing and extra spikes. In summary, the PCMI method can give the quantification of the directionality index and the detection of temporal dynamics between two interacting spike trains.

References

Asai Y, Villa AE. Reconstruction of underlying nonlinear deterministic dynamics embedded in noisy spike trains. J Biol Phys. 2008;34:325–40.

Averbeck BB, Latham PE, Pouget A. Neural correlations, population coding and computation. Nat Rev Neurosci. 2006;7:358–66.

Bahraminasab A, Ghasemi F, Stefanovska A, McClintock P, Kantz H. Direction of coupling from phases of interacting oscillators: a permutation information approach. Phys Rev Lett. 2008;100:84101.

Bandt C, Pompe B. Permutation entropy: a natural complexity measure for time series. Phys Rev Lett. 2002;88:174102.

Brown E, Kass R, Mitra P. Multiple neural spike train data analysis: state-of-the-art and future challenges. Nat Neurosci. 2004;7:456–61.

Cessac B, Paugam-Moisy H, Viéville T. Overview of facts and issues about neural coding by spikes. J Physiol Paris. 2010;104:5–18.

Chen Y, Rangarajan G, Feng J, Ding M. Analyzing multiple nonlinear time series with extended Granger causality. Phys Lett A. 2004;324:26–35.
deCharms RC, Zador A. Neural representation and the cortical code. Annu Rev Neurosci. 2000;23:613–47.
Dickey AS, Suminski A, Amit Y, Hatsopoulos NG. Single-unit stability using chronically implanted multielectrode arrays. J Neurophysiol. 2009;102:1331–9.
Ding M, Chen Y, Bressler S. Granger causality: basic theory and application to neuroscience 2006; Arxiv preprint q-bio/0608035.
Dzakpasu R, Zochowski M. Discriminating differing types of synchrony in neural systems. Physica D Nonlinear Phenomena. 2005;208:115–22.
Fellous JM, Tiesinga PH, Thomas PJ, Sejnowski TJ. Discovering spike patterns in neuronal responses. J Neurosci. 2004;24:2989–3001.
Fries P, Neuenschwander S, Engel AK, Goebel R, Singer W. Rapid feature selective neuronal synchronization through correlated latency shifting. Nat Neurosci. 2001;4:194–200.
Gourévitch B, Eggermont J. Evaluating information transfer between auditory cortical neurons. J Neurophysiol. 2007;97:2533–43.
Haas JS, White JA. Frequency selectivity of layer II stellate cells in the medial entorhinal cortex. J Neurophysiol. 2002;88:2422–9.
Havlicek M, Jan J, Brazdil M, Calhoun VD. Dynamic Granger causality based on Kalman filter for evaluation of functional network connectivity in fMRI data. Neuroimage. 2010;53:65–77.
Hlavkov Schindler K, Palus M, Vejmelka M, Bhattacharya J. Causality detection based on information-theoretic approaches in time series analysis. Phys Rep. 2007;441:1–46.
Izhikevich EM. Simple model of spiking neurons. IEEE Trans Neural Netw. 2003;14:1569–72.
Kamiński M, Ding M, Truccolo W, Bressler S. Evaluating causal relations in neural systems: Granger causality, directed transfer function and statistical assessment of significance. Biol Cybern. 2001;85:145–57.
Kandagor V, Cela CJ, Sanders CA, Greenbaum E, Lazzi G, Humayun MS, Zhou DM, Castro R, Gaikwad S, Little J. Spatial characterization of electric potentials generated by pulsed microelectrode arrays. Conf Proc IEEE Eng Med Biol Soc. 2010;1:6243–6.
Kreuz T, Haas JS, Morelli A, Abarbanel HDI, Politi A. Measuring spike train synchrony. J Neurosci Methods. 2007;165:151–61.
Krumin M, Shoham S. Multivariate autoregressive modeling and granger causality analysis of multiple spike trains. Comput Intell Neurosci. 2010;752428.
Li X, Ouyang G. Estimating coupling direction between neuronal populations with permutation conditional mutual information. Neuroimage. 2010;52:497–507.
Li X, Ouyang G, Richards DA. Predictability analysis of absence seizures with permutation entropy. Epilepsy Res. 2007;77:70–4.
Li X, Cui S, Voss LJ. Using permutation entropy to measure the electroencephalographic effects of sevoflurane. Anesthesiology. 2008;109:448–56.
Li D, Li X, Liang Z, Voss LJ, Sleigh JW. Multiscale permutation entropy analysis of EEG recordings during sevoflurane anesthesia. J Neural Eng. 2010;7:046010.
Narayan R, Grana G, Sen K. Distinct time scales in cortical discrimination of natural sounds in songbirds. J Neurophysiol. 2006;96:252–8.
Nedungadi AG, Rangarajan G, Jain N, Ding M. Analyzing multiple spike trains with nonparametric granger causality. J Comput Neurosci. 2009;27:55–64.
Nemenman I, Lewen GD, Bialek W, de Ruyter van Steveninck RR. Neural coding of natural stimuli: information at sub-millisecond resolution. PLoS Comput Biol. 2008;4:e1000025.
Ohiorhenuan IE, Mechler F, Purpura KP, Schmid AM, Hu Q, Victor JD. Sparse coding and high-order correlations in fine-scale cortical networks. Nature. 2010;466:617–21.
Olofsen E, Sleigh JW, Dahan A. Permutation entropy of the electroencephalogram: a measure of anaesthetic drug effect. Br J Anaesth. 2008;101:810–21.
Palu M, Stefanovska A. Direction of coupling from phases of interacting oscillators: an information-theoretic approach. Phys Rev E. 2003;67:55201.

Palu M, Komárek V, Hrncír Z, Stěrbová K. Synchronization as adjustment of information rates: detection from bivariate time series. Phys Rev E. 2001;63:46211.
Pouget A, Dayan P, Zemel R. Information processing with population codes. Nat Rev Neurosci. 2000;1:125–32.
Quian Quiroga R, Kreuz T, Grassberger P. Event synchronization: a simple and fast method to measure synchronicity and time delay patterns. Phys Rev E Stat Nonlin Soft Matter Phys. 2002;66:041904.
Rosenblum MG, Cimponeriu L, Bezerianos A, Patzak A, Mrowka R. Identification of coupling direction: application to cardiorespiratory interaction. Phys Rev E Stat Nonlin Soft Matter Phys. 2002;65:041909.
Salinas E, Sejnowski T. Correlated neuronal activity and the flow of neural information. Nat Rev Neurosci. 2001;2:539–50.
Salvador R, Anguera M, Gomar JJ, Bullmore ET, Pomarol-Clotet E. Conditional mutual information maps as descriptors of net connectivity levels in the brain. Front Neuroinform. 2010;4:115.
Sasaki T, Kimura R, Tsukamoto M, Matsuki N, Ikegaya Y. Integrative spike dynamics of rat CA1 neurons: a multineuronal imaging study. J Physiol. 2006;574:195–208.
Schnupp JW, Hall TM, Kokelaar RF, Ahmed B. Plasticity of temporal pattern codes for vocalization stimuli in primary auditory cortex. J Neurosci. 2006;26:4785–95.
Schreiber T. Measuring information transfer. Phys Rev Lett. 2000;85:461–4.
Schreiber S, Fellous JM, Whitmer D, Tiesinga P, Sejnowski TJ. A new correlation-based measure of spike timing reliability. Neurocomputing. 2003;52–54:925–31.
Seth AK. Causal connectivity of evolved neural networks during behavior. Network. 2005;16:35–54.
Seth AK. A MATLAB toolbox for Granger causal connectivity analysis. J Neurosci Methods. 2010;186:262–73.
Shelhamer M. Nonlinear dynamics in physiology: a state-space approach. Singapore: World Scientific Pub Co Inc.; 2007.
Shlens J, Kennel MB, Abarbanel HD, Chichilnisky EJ. Estimating information rates with confidence intervals in neural spike trains. Neural Comput. 2007;19:1683–719.
Strong S, Koberle R, de Ruyter van Steveninck R, Bialek W. Entropy and information in neural spike trains. Phys Rev Lett. 1998;80:197–200.
Swadlow HA, Rosene DL, Waxman SG. Characteristics of interhemispheric impulse conduction between prelunate gyri of the rhesus monkey. Exp Brain Res. 1978;33:455–67.
Takahashi N, Sasaki T, Usami A, Matsuki N, Ikegaya Y. Watching neuronal circuit dynamics through functional multineuron calcium imaging (fMCI). Neurosci Res. 2007;58:219–25.
Thomas J, Cover T. Elements of information theory. New York: Wiley-Interscience; 1991.
van Rossum MC. A novel spike distance. Neural Comput. 2001;13:751–63.
Vejmelka M, Palus M. Inferring the directionality of coupling with conditional mutual information. Phys Rev E Stat Nonlin Soft Matter Phys. 2008;77:026214.
Vicente R, Wibral M, Lindner M, Pipa G. Transfer entropy- a model-free measure of effective connectivity for the neurosciences. J Comput Neurosci. 2011;30:45–67.
Victor JD, Purpura KP. Nature and precision of temporal coding in visual cortex: a metric-space analysis. J Neurophysiol. 1996;76:1310–26.
Victor J, Purpura K. Metric-space analysis of spike trains: theory, algorithms and application. Netw Comput Neural Syst. 1997;8:127–64.
Waddell J, Dzakpasu R, Booth V, Riley B, Reasor J, Poe G, Zochowski M. Causal entropies–A measure for determining changes in the temporal organization of neural systems. J Neurosci Methods. 2007;162:320–32.
Wang L, Narayan R, Grana G, Shamir M, Sen K. Cortical discrimination of complex natural stimuli: can single neurons match behavior? J Neurosci. 2007;27:582–9.
Zochowski M, Cohen LB, Fuhrmann G, Kleinfeld D. Distributed and partially separate pools of neurons are correlated with two different components of the gill-withdrawal reflex in Aplysia. J Neurosci. 2000;20:8485–92.

Chapter 4
Quantification of Spike-LFP Synchronization

Zhaohui Li and Xiaoli Li

4.1 Introduction

The advent of multielectrode arrays makes it possible to simultaneously record the spiking activity of multiple neurons and neural ensembles, which offers an important avenue to investigate fundamental issues about the neural coding (Galashan et al. 2011; Stafford et al. 2009). The resulting voltage signals are generally separated into two types: one is the spikes or action potentials, which are fired by neurons and identified by high-pass filtering, detecting, and sorting, and another is the local field potentials (LFPs), which are the total synaptic current in the neuronal circuit and obtained by low-pass filtering the original wideband signal (Mizuseki et al. 2009; Perelman and Ginosar 2007). The interaction between the spikes of single neurons, i.e., spike trains, and the ongoing LFP oscillations is becoming a hot topic in neuroscience, because it allows us to study how the activities of individual neurons are related to those of the larger-scale networks in which they are embedded. Its significance has been shown to be associated with high-level brain functions, such as attention (Chalk et al. 2010; Fries et al. 2001), memory (Harris et al. 2002; Le Van Quyen et al. 2008; Lee et al. 2005), motor task (Courtemanche et al. 2002; Hagan et al. 2012; van Wingerden et al. 2010), and sensory processing (Eggermont and Smith 1995; Fries et al. 1997; Pienkowski and Eggermont 2011 Xu et al. 2012).

Z. Li
School of Information Science and Engineering, Yanshan University, Qinhuangdao 066004, China
e-mail: lizhaohui@ysu.edu.cn

X. Li (✉)
State Key Laboratory of Cognitive Neuroscience and Learning & IDG/McGovern Institute for Brain Research, Beijing Normal University, Beijing 100875, China

Center for Collaboration and Innovation in Brain and Learning Sciences, Beijing Normal University, Beijing 100875, China
e-mail: xiaoli@bnu.edu.cn

X. Li (eds.), *Signal Processing in Neuroscience*, DOI 10.1007/978-981-10-1822-0_4

4.2 Spike Field Coherence

4.2.1 Spike-Triggered Average and Spike Field Coherence

A typical method for studying spike-LFP interaction is the spike field coherence (SFC), which measures synchronization between spike trains and LFPs as a function of frequency and takes values between 0 % (complete lack of synchronization) and 100 % (complete synchronization) (Fries et al. 2001; Fries et al. 1997). The SFC can be used to describe the strength of synchronization between spike times and a particular phase of the LFP oscillation at a certain frequency. It has been employed to investigate the memory formation in humans (Rutishauser et al. 2010), the neural mechanism of visual attention in macaque monkeys (Chalk et al. 2010; Fries et al. 2001), the stimulus-specific synchronization in primary visual cortex of awake-behaving cats (Siegel and Konig 2003), and other brain functions (Fries et al. 2002; Issa and Wang 2011; Lewandowski and Schmidt 2011; Tiesinga et al. 2004; Wang et al. 2011). An important advantage of the SFC is that it is independent on the LFP power and spike rate (Fries et al. 2001).

The SFC is a function of frequency and obtained by computing the ratio of power spectrum of the spike-triggered average (STA) over the average of power spectrum of the LFP fractions (Fries et al. 1997). Thus, the SFC is independent on the LFP power and spike rate (Fries et al. 2001). Suppose that the spike train of a neuron is denoted as $S = [s_1, s_2, \ldots s_m]$, where m is the spike number. $V = [v_1, v_2, \ldots v_m]$ is the set of LFP segments, where v_i is the samples of the LFP signal in the window $[s_i - T/2,\ \ s_i + T/2]$. Here, T is the duration of the window. The STA is constructed by averaging the LFP fractions within windows that centered on the spikes. Then, the power spectrum of STA (PSTA) is defined as

$$\mathrm{PSTA} = \Psi\left(\frac{1}{m}\sum_{i=1}^{m} v_i\right), \tag{4.1}$$

where Ψ denotes the operation for calculating the power spectrum. Next, to describe the power of every frequency component in the LFP segments that used to construct the STA, i.e., v_i with $i = 1, 2, \ldots, m$, the average power spectrum of v_i (spike-triggered power spectrum or STP) is (Fries et al. 1997; Rutishauser et al. 2010)

$$\mathrm{STP} = \frac{1}{m}\sum_{i=1}^{m} [\Psi\,(v_i)]. \tag{4.2}$$

Then, the SFC is defined as [17]

$$\mathrm{SFC} = \frac{\mathrm{PSTA}}{\mathrm{STP}} \times 100\%. \tag{4.3}$$

The STP and PSTA can be computed with many methods. For instance, multitaper analysis is a powerful and robust method to estimate single-trial spectrum (Jarvis

and Mitra 2001), which can be performed by using the Chronux toolbox (Bokil et al. 2010). The multitaper method is employed in this chapter for spectrum analysis of the simulated and experimentally recorded LFP signals.

4.2.2 Bursty Spike Trains and Weighted Spike Field Coherence

The SFC reflects the synchronization between spike trains and LFPs at different frequencies. However, it does not work well for bursty spike trains and LFPs at high frequency band, which will be shown in the following section. A burst can be defined as a temporary increase in the firing rate of spikes from the background activity (Cocatre-Zilgien and Delcomyn 1992; Palm 1981; Robin et al. 2009). As the mechanism for generating bursts is mentioned, it is commonly accepted that small depolarization keeps the cell silent, moderate depolarization makes the cell fire single spikes, and large depolarization causes the cell to discharge in burst mode. Thus, bursts code the same neural information as single spikes but with higher reliability (Harris et al. 2001; Lisman 1997). With this understanding, the first spike in each burst is selected and used to represent the burst as event (Kepecs and Lisman 2003; Swadlow and Gusev 2001).

When all spikes in the bursts are used to calculate the coherence, this operation will decrease the SFC values even if there is strong phase-locked synchronization between bursty spike trains and LFPs at high frequency band. To overcome this drawback, an improvement for the algorithm of SFC is introduced in this chapter. That is, multiple copies of the first spike in each burst are used to compute the SFC. The number of the copies is determined by the number of spikes per burst. Since this is analogous to the process of weight, the modified approach is referred to as weighted spike field coherence (WSFC). To evaluate the performance of this method, it is applied to both simulation data and real neurobiological signals recorded in the hippocampus of rats.

The WSFC method allows only the first spike in every burst enter into the computation of PSTA and STP. To emphasize the difference between single spikes and bursts, multiple copies of the first spikes in bursts are used. In this way, the first spike timing represents the occurrence of the burst, and the weighting procedure (multiple copies of the first spike) reflects the properties of the burst. Then, the WSFC is defined as

$$\mathrm{WSFC} = \frac{\mathrm{PWSTA}}{\mathrm{WSTP}} \times 100\,\%, \tag{4.4}$$

where the PWSTA is the power spectrum of weighted STA and the WSTP denotes the weighted spike-triggered power spectrum of LFP. The “weighted” means that the LFP segments around the first spikes in bursts are reused in the calculation of STA and STP, and the “weight” is related to the spike number per burst. The main difference between the two methods is that WSFC uses the first spike in burst

multiple times rather than all the spikes used by SFC. An important advantage of this operation is that it can remove the influence of the second and later spikes in bursts on the computation of SFC. In other words, the WSFC method is immune to the effect of burst.

Similar to the SFC, the WSFC is a population method and cannot be calculated for single spikes. It suffers from the effect of spike count used in the computation as well. Thus, it is necessary to minimize or avoid the bias raised by the amount of spikes. Two measures may be adopted. One is to use enough spikes (>50 generally) to calculate the WSFC. Another is to ensure that the spike counts in different conditions are equal. In addition, two parameters should be identified before calculating the SFC and WSFC. First, the traces of LFP to construct the STA are set to be 960 ms in the simulations, with the aim of examining low frequencies. For the real data in this study, a relatively short window of 480 ms is used focusing on the gamma band frequencies. To summarize, the window length is selected depending on the following principle: long enough to make reliable estimate for the power spectrum and relatively short to represent the dynamics of LFP signal in the desired band. Next, in the simulations, the spectrum is estimated by using multitaper method with a time-bandwidth product of four and seven tapers, resulting in a spectral resolution (half bandwidth) of 4.2 Hz. In the analysis of real data, due to the short window of 480 ms, we use a time-bandwidth product of three and five tapers in order to get a relatively smaller spectral resolution of 6.25 Hz. It means that we should choose an appropriate time-bandwidth product and taper count to make a good compromise between the spectral resolution and the benefit of the spectral estimate.

4.2.3 Simulation and Application

4.2.3.1 Simulation Results

To simulate the real extracellular recoding, the LFP signal is generated by summing multiple sine waves with different frequencies, amplitudes, and phases (Rutishauser et al. 2010). The frequencies range from 1 Hz to 100 Hz with a step of 1 Hz, focusing on the LFP in gamma band and below. The amplitudes of the components are inversely proportional to their frequencies. The phases are randomly selected from $[0\ \ 2\pi]$. In addition, a white Gaussian noise with the signal-to-noise ratio of 3 dB is added to the composite oscillation. Thus, the generated artificial LFP signal follows the 1/f power distribution. The phase-locked spikes that fired by simulated individual neurons locate at a certain phase of the underlying oscillation and skip cycles at random, while the non-phase-locked spikes occur randomly. The simulated bursts consist of two to six spikes. The interspike intervals (ISIs) in the bursts range from 3 to 10 ms. The amount of the burst is quantified by burst index, which is defined as the ratio of spikes in bursts to all spikes (Mizuseki et al. 2011, 2012). To avoid the bias caused by the number of spikes (Fell et al. 2001; Grasse and Moxon 2010), 200 spikes are generated for each realization.

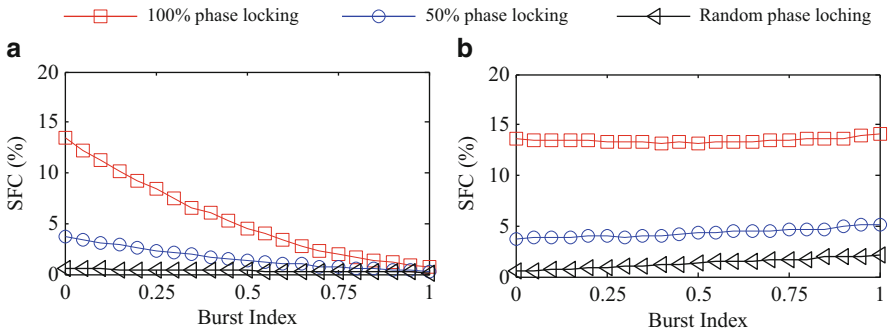

Fig. 4.1 The SFC between bursty spike train and LFP for different phase-locked cases. (**a**) Spikes or bursts are phased locked to 50-Hz component. (**b**) Spikes or bursts are phased locked to 5-Hz component

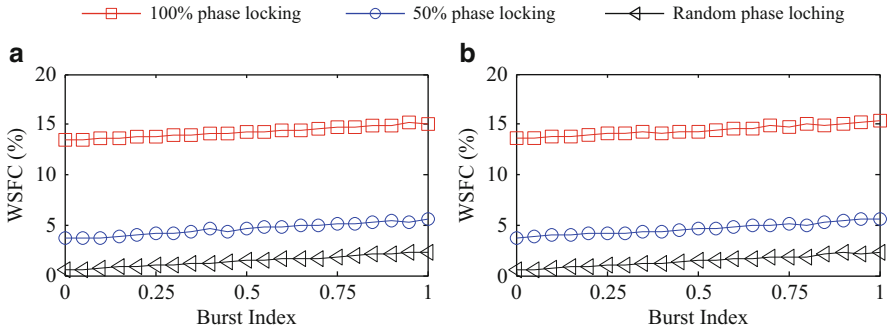

Fig. 4.2 The WSFC between bursty spike train and LFP for different phase-locked cases. (**a**) The phase locking is represented between spikes or bursts and 50-Hz component. (**b**) The phase locking is represented between spikes or bursts and 5-Hz component

By using the simulated LFP signal, the effect of bursts in spike trains on the calculation of SFC and WSFC is investigated, and the advantage of WSFC for estimating the coherence between bursty spike trains and LFPs is demonstrated. The SFC and WSFC are calculated in three cases: 100 % spikes are locked to a certain phase of specified components (e.g., 50 Hz and 5 Hz) in the simulated LFP signal (100 % phase locked), 50 % spikes are phased locked (50 % phase locked), and spikes are fired randomly (non-phase locked), where the spikes include single spikes and first spikes in bursts. The mean values of SFC and WSFC at the two frequencies versus the burst indexes are plotted in Figs. 4.1 and 4.2. For the 50-Hz component, the SFC is strongly reduced by the bursts that occurred in spike trains for both 100 % and 50 % phase-locked cases, while it keeps at the chance level for the random phase locking, as shown in Fig. 4.1a. It means that the bursts do not lead to spurious increase of the SFC for random spikes, but can severely reduce the SFC values for spikes phase locked to high-frequency components. For

the 5-Hz component, the decrease of the SFC also presents in the 100 % and 50 % phase-locked cases, but with smaller amplitude. However, the SFC increases a little for the random phase locking, as illustrated in Fig. 4.1b. It implies that the bursts exert relatively small effect on the SFC estimate for spikes phase locked to low-frequency components. All simulations are implemented by using 200 spikes, which means that the decrease of the SFC is indeed caused by the location rather than the amount of spikes.

On the other hand, the WSFC method using the first spikes effectively eliminates this influence caused by bursts for both low and high frequencies. Due to the reuse of first spikes in bursts, the amplitude of the STA gets larger as a function of the number of bursts involved. Consequently, the WSFC presents a slight increase with the increasing of bursts in spike trains, as shown in Fig. 4.2a, b. However, the relative difference in WSFC between conditions almost remains the same, which is meaningful for the comparison between different phase-locked cases.

Furthermore, the influence of the bursts at different frequencies is examined. The given nine frequencies are as follows: 5 Hz in theta band, 10 Hz in alpha band, 20 Hz in beta band, and 30 Hz, 40 Hz, 50 Hz, 60 Hz, 70 Hz, and 80 Hz in gamma band. The single spikes and first spikes in bursts are presumed to fire exactly at a certain phase of these component oscillations. The influence is quantified by the coefficient of variation (CV) of the SFC or WSFC magnitudes for different burst indexes. As shown in Fig. 4.3a, b, the SFC between spike trains and LFPs in gamma frequency band is prone to be affected by the bursts for 100 % and 50 % phase-locked cases. Whereas for the low frequencies, e.g., 5 Hz and 10 Hz, the bursts in spike trains exert very little effect on the computation of SFC, on the other hand, the WSFC has a relatively more robust performance for both high and low frequencies. The effect of bursts under the random phase locking is illustrated in Fig. 4.3c. The SFC and WSFC measure performs similarly to each other. Although the variation of WSFC is relatively large, it does not imply a reduction of the WSFC performance. As explained before, these variations are represented in different locked conditions with similar increasing tendencies, providing a reliable comparison of the coherence between different conditions. This is also demonstrated by the values of CV in different phase-locked cases. The lower degree of the phase locking, the smaller mean of the WSFC at different burst indexes and the larger CVs for frequencies take

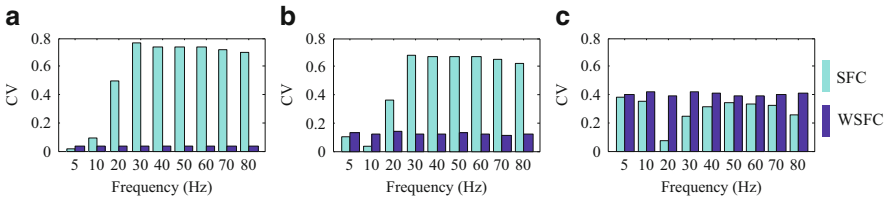

Fig. 4.3 Effect of burst on the SFC and the WSFC when spikes or bursts phase locked to different frequency components. (**a**) 100 % phase locking. (**b**) 50 % phase locking. (**c**) Random phase locking

on. To summarize, the WSFC is an efficient tool to reveal the coherence between spike trains and LFPs, particularly in high frequency band.

4.2.3.2 Application to Real Data

The data set consists of simultaneous recordings of cells in layer CA1 of the right dorsal hippocampus of three Long-Evans rats, which were implanted with a 4-shank or 8-shank silicon probe. After recovery from surgery (about 1 week) and training (at least 3 days), the physiological signals were recorded during the open field tasks in which the rats chased randomly dispersed drops of water or pieces of Froot Loops on an elevated square platform. The signals were amplified (1000x), band-pass filtered (1 Hz–5 kHz), and sampled continuously at 20 kHz. Then, the LFPs were down-sampled to 1250 Hz. The offline spike sorting was performed automatically. The details about the behavioral experiment and data collection can be found in (Mizuseki et al. 2009). A subset of the data set is analyzed in this study (in particular, ec013.527 at http://crcns.org/data-sets/hc/hc-2).

In hippocampus, gamma frequency oscillations (30–80 Hz) have been suggested to underlie various cognitive functions, such as attention selection (Bauer et al. 2006; Fries et al. 2001), memory (Fell et al. 2001; Howard et al. 2003; van Vugt et al. 2010), and sensory perception (Colgin et al. 2009; Muzzio et al. 2009). Moreover, it has been reported that the firing patterns of pyramidal cells in hippocampus are significantly phase locked to gamma oscillations in behaving rats (Colgin et al. 2009; Csicsvari et al. 2003; Senior et al. 2008). Here, we examine that whether this phase locking can be characterized by the WSFC and SFC methods. In the recordings of the data set used in this study, the pyramidal cells exhibit firing patterns of single spikes and complex spike bursts. A segment ($150 \sim 400$ s) of the recordings used for the analysis of coherence is shown in Fig. 4.4a, b, containing the gamma band LFP signal and the neuronal activity (neuron 37 in the selected data set).

In order to preserve the timing relationship between spikes and LFP, the gamma band-pass filtering is performed digitally with zero-phase shift using the EEGLAB toolbox (Delorme and Makeig 2004). Then, we estimate the WSFC and SFC as a function of time (sliding window of 10s advanced in steps of 5 s), respectively. A series of two or more consecutive spikes with <10-ms ISIs is considered as a burst in this study (Mizuseki et al. 2011; Senior et al. 2008). Figure 4.4c shows the burst index in every window. To guarantee sufficient statistical power, we select the windows containing at least 50 single spikes and bursts for the calculation of coherence (Rutishauser et al. 2010). For statistical purposes, the results are converted to z-scores. The surrogate spike trains are created by perturbing every spike with a random time in a window of 30 ms around the original spikes. The statistical significance is set conservatively at $z > 1.96$ for the level $p < 0.05$. In Fig. 4.4d, e, the z-transformed WSFC and SFC are plotted versus time, respectively, and the horizontal line indicates the significant level. Obviously, the traditional method, i.e., SFC which uses all spikes in bursts, fails to descript the phase locking

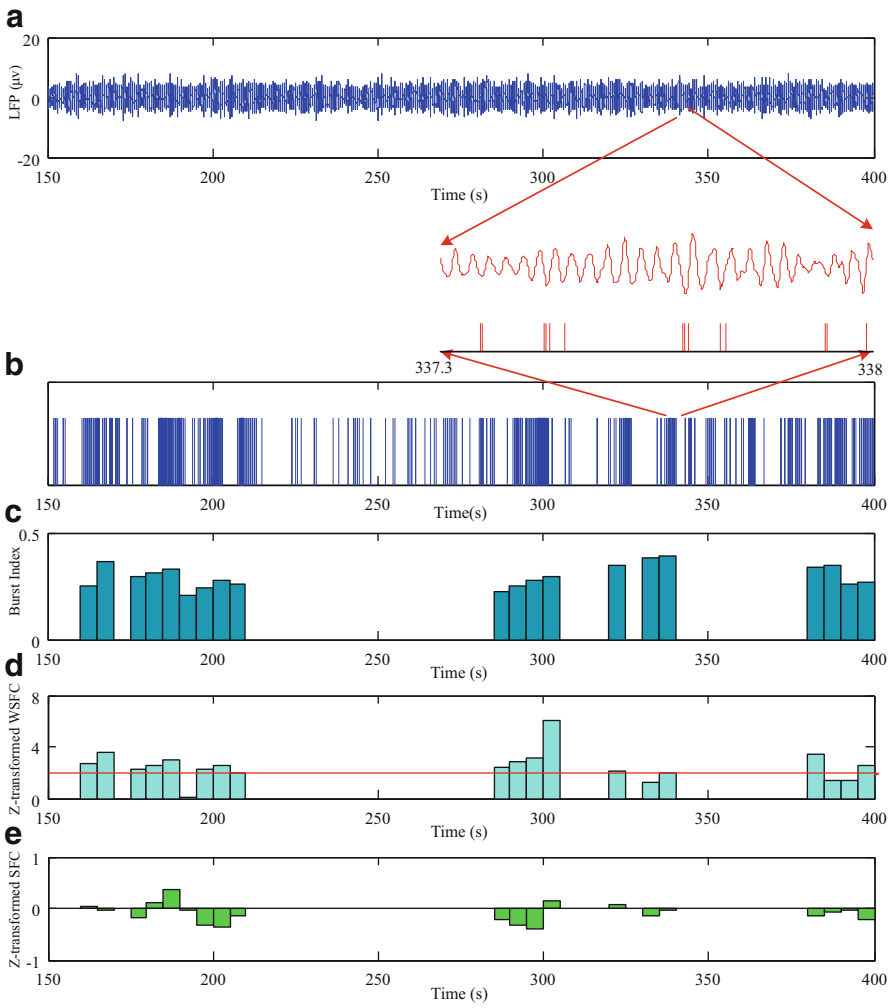

Fig. 4.4 The WSFC and SFC applied to real data. (**a**) A segment of the recorded LFP signal. (**b**) Spiking activities of neuron 37 in the segment. *Vertical lines* indicate the occurrence of spikes fired by the neuron. (**c**) Burst index for windows with >50 spikes. (**d**) Z-transformed WSFC for each selected window. The *red horizontal line* indicates the significant level of $p < 0.05$. (**e**) Z-transformed SFC for each selected window. The coherence in the two plots (*d*) and (*e*) is obtained by using the average of the WSFC and SFC within gamma band, respectively

between the spike train and LFP in gamma band, while the modified method, i.e., WSFC which utilizes the copies of first spikes in bursts, characterizes this relationship effectively. We also found similar results for other data sets, which further demonstrate the performance of WSFC to uncover the relationship between activities of pyramidal cells in hippocampus and LFP in gamma band; the results for other data sets are shown in the supporting document.

4.3 Spike-Triggered Correlation Matrix Synchronization

Spikes and LFP are acquired from the signal recorded by a microelectrode. The former are fired by neurons and identified by high-pass filtering, detection, and sorting. The latter reflects the total effects of the synaptic currents in the neuronal circuit and is obtained by low-pass filtering the original wideband signal. Several rhythms of LFP are generated through inhibitory networks that produce periodic fluctuations in the intracellular potential of the target postsynaptic neurons such that the excitability of these neurons varies within one period of the rhythm, which can be used to synchronize the spiking of neurons (Buzsaki and Wang 2012; Ray 2014). Also, it is reported that spikes can be inferred from LFP in the primary visual cortex of monkeys (Rasch et al. 2008). Furthermore, LFP is thought to mainly reflect the summed transmembrane currents flowing through the neurons within a local region around the microelectrode tip (Buzsaki et al. 2012; Reimann et al. 2013), and its phase is widely adopted to characterize the spike-LFP synchronization (Colgin et al. 2009; Csicsvari et al. 2003; Fries et al. 2001). In view of the above considerations, we suggest that a specific variation of LFP phase causes an individual neuron to fire spikes and consequently generate the spike-LFP synchronization.

4.3.1 Correlation Matrix and Spike-LFP Synchronization

Several spike-LFP synchronization measures have been introduced in the past few years, e.g., the phase histogram (Csicsvari et al. 2003), phase locking (Colgin et al. 2009), spike field coherence (Fries et al. 2001), and coherency (Pesaran et al. 2002). However, these measures are dependent upon the total number of spikes, which renders comparison of spike-LFP synchronization across experimental contexts difficult. Often, different experimental conditions yield substantially different numbers of spikes. Thus, it is necessary and urgent to develop an unbiased measure for characterizing the synchronization between spikes and LFP. In 2010, a circular statistics, pairwise phase consistency (PPC), has been proposed. It is a bias-free and consistent estimator of spike-LFP synchronization (Vinck et al. 2010). Unfortunately, as shown below, the performance of PPC severely deteriorates in the presence of spike noise. In this chapter, we present a new measure for estimating spike-LFP synchronization, which is independent of the total number of spikes and robust against spike noise. The main idea of the method is to take LFP segments centered on each spike (spike-triggered LFPs) as multichannel signals and calculate the index of spike-LFP synchronization by constructing a correlation matrix. Thus, this method is referred to as spike-triggered correlation matrix synchronization (SCMS).

Suppose that the spike train (i.e., a series of spikes) fired by a neuron is denoted as $S = [s_1, s_2, \ldots s_n]$, where s_i $(i = 1, 2, \ldots, n)$ is the spiking time and n is the number of spikes. $V = [v_1, v_2, \ldots v_n]$ is the set of LFP segments, where v_i $(i = 1, 2, \ldots, n)$ denotes the samples of the LFP signal in the time window $[s_i - T/2,\ \ s_i + T/2]$

and T is the duration of the LFP segments. First, extract the instantaneous phase of every LFP segment by Hilbert transform. For a signal $v(t)$, the analytic signal $\zeta(t)$ is a complex function of time, and it is defined as

$$\zeta(t) = v(t) + j\tilde{v}(t) = A(t)e^{j\phi(t)}, \tag{4.5}$$

where the function $\tilde{v}(t)$ is the Hilbert transform of $v(t)$:

$$v(t) = \frac{1}{\pi}\text{P.V.} \cdot \int_{-\infty}^{+\infty} \frac{v(t)}{t-\tau}\, d\tau. \tag{4.6}$$

P.V. indicates that the integral is taken in the sense of Cauchy principal value (Rosenblum et al. 1996). Thus, the instantaneous phase $\phi_i(t)$ of LFP segment $v_i(t)$ is obtained. Second, construct the correlation matrix $\mathbf{C}$ by calculating the phase-locking value (PLV) between pairs of LFP segments, i.e.,

$$c_{ij} = \left| \frac{1}{N} \sum_{k=1}^{N} e^{j\left(\phi_i(t_k) - \phi_j(t_k)\right)} \right|, \tag{4.7}$$

where N denotes the number of samples in the time window and $\mathbf{C}$ is a real symmetric matrix. Then, the eigenvalue decomposition of $\mathbf{C}$ is given by

$$C\, u_i = \lambda_i u_i, \tag{4.8}$$

where λ_i are the eigenvalues, with $\lambda_1 \geq \lambda_2 \geq \cdots \geq \lambda_n$, and u_i are the eigenvectors corresponding to λ_i. Finally, in order to obtain a normalized value of spike-LFP synchronization which is independent of the number of spikes, we randomize all spike-triggered LFP segments to compute a surrogate correlation matrix $\mathbf{R}$ (Li et al. 2007). The surrogate data is generated by randomly shuffling the order of the original signals (Theiler et al. 1992). Similarly, we can obtain the ordered eigenvalues of matrix $\mathbf{R}$. Repeating this randomization and computation M times (we select $M = 100$ in this work), the mean and standard deviation (SD) of the maximum eigenvalues are denoted as $\overline{\lambda}_1'$ and s_1, respectively. Then, the normalized spike-LFP synchronization can be computed by the following equation:

$$\eta = \begin{cases} \left(\lambda_1 - \overline{\lambda}_1'\right) / \left(n - \overline{\lambda}_1'\right) & \text{if } \lambda_1 > \left(\overline{\lambda}_1' + K \times s_1\right) \\ 0 & \text{otherwise} \end{cases}, \tag{4.9}$$

where K is a constant that determines the threshold and $K = 3$ is selected for 99 % confidence intervals (Li et al. 2007).

The reason for the choice of the maximum eigenvalue (λ_1 and $\overline{\lambda}_1'$) is in the following. Li et al. noted that when multichannel signals are acquired from a local region, the first synchronization index, which corresponds to the maximum eigenvalue, is appropriate for indicating the global synchronization (Li et al. 2007). Moreover, as spikes and LFP are recorded by the same microelectrode, the spike-

triggered LFPs can be considered as signals from one region of synchronization. Thus, it is justifiable to use the first synchronization index to characterize the spike-LFP synchronization.

In the SCMS algorithm, a parameter (i.e., the window length of the LFP segments) should be determined before its application. It is possible that there are other spikes immediately before or after a specific spike. These spikes may alter the frequency and phase of the LFP (Zanos et al. 2011). This supports the selection of a short window. However, the algorithm uses the similarity of the variation in LFP phase as the mechanism for the calculation of spike-LFP synchronization. Consequently, a longer window improves the accuracy of the similarity calculation. Considering this trade-off, we used a window of 20 ms in the analysis of simulated and real data.

4.3.2 Simulation and Application

4.3.2.1 Simulation Results

To test the properties of the algorithm, simulated LFP was generated by summing multiple sine waves with different frequencies, amplitudes, and phases (Rutishauser et al. 2010). The frequencies ranged from 1 to 100 Hz with a step of 1 Hz, thereby focusing on the LFP in the gamma band and below. The amplitudes of the components were inversely proportional to their frequencies. The phases were randomly selected from $[0\ 2\pi]$. Synchronized spikes fired by simulated individual neurons were located at a certain phase of the summed LFP waveform. These simulated neurons skipped cycles at random. The total number of synchronized spikes was denoted by ϑ_p. Additionally, non-synchronized spikes occurred randomly, and their amount was denoted by ϑ_n. The strength of spike-LFP synchronization was determined by the ratio $R = \vartheta_p / (\vartheta_p + \vartheta_n)$, e.g., $R = 1$ implies perfect synchronization and $R = 0$ indicates complete non-synchronization.

First, the effect of the total number of spikes on the algorithm's output was investigated. The number of spikes ranged from 10 to 100 with a step of 5. The strength of simulated spike-LFP synchronization was set to 0.25, 0.5, or 0.75. Figure 4.5 shows the mean value of the SCMS output for different numbers of spikes, with 100 realizations for each number. As can be seen, the SCMS output almost does not change with the sample size. This property is of crucial importance when making comparisons between different experimental conditions.

Second, the robustness of the SCMS method against noise in the spike trains was studied. Three types of noise were considered: jitter noise (a shift of spiking time), missing spikes (false negatives), and extra spikes (false positives). Jitter noise may appear in stochastic biological processes, such as synaptic transmission and spike propagation in a neural network. The noise due to missing and extra spikes is primarily caused by external processes such as the firing of other neurons, errors in the spike sorting procedure, and electrical artifacts (Asai and Villa 2008). We compare the SCMS method with the pairwise phase consistency (PPC) method.

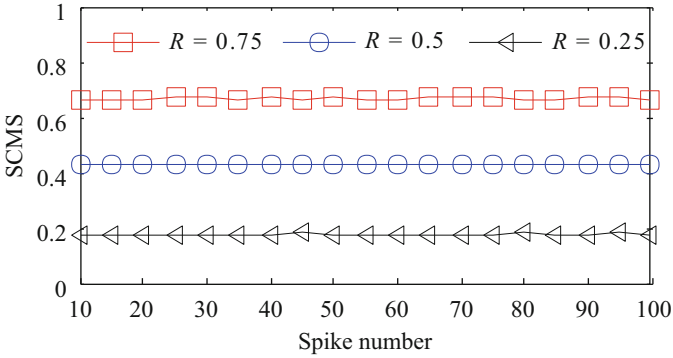

Fig. 4.5 Effect of the total number of spikes on the output of the SCMS method

Jitter noise was added to the spike trains via shifting every spike by a time normally distributed in an interval. The strength of jitter noise was quantified by the interval length. The number of spikes in the simulation was set to 50. As shown in Fig. 4.6a, b, both the SCMS and the PPC are affected by jitter noise, and their output values decrease as the interval of jitter increases. However, the output of SCMS decreases more slowly compared to that of PPC. Moreover, we are still able to visually distinguish between the different levels of spike-LFP synchronization in the SCMS output even as the jitter interval grows to 20 ms. In contrast, it becomes difficult to observe a clear distinction between different levels of synchronization by looking at the PPC output when the interval is larger than 5 ms. Once the data acquisition procedures, recording system, and the spike detection method have been determined, the jitter noise of different neurons is about the same in scale. Thus, when comparing the spike-LFP synchronization between different experimental conditions or between different pairs of neurons and LFP signals, the SCMS measure is able to provide more significant results.

Noise due to extra spikes was quantified by the number of independent spikes randomly inserted into spike trains. In the simulation, the original number of spikes was 20, and the number of extra spikes ranged from 2 to 30 with a step of 2. As shown in Fig. 4.6c, d, the SCMS and PPC outputs decrease with the number of extra spikes. Due to the random insertion of independent spikes, the strength of the simulated spike-LFP synchronization reduces, and consequently the two outputs decrease. It is difficult to distinguish between different synchronization strengths by looking at the output of the PPC method when a large amount of extra spikes is present. In comparison, the output of the SCMS method indicates differences between the synchronization levels for even the largest amount of extra spikes.

The noise due to missed spikes was quantified by the number of randomly deleted spikes. In the simulation, the original number of spikes was 50, and the number of missed spikes ranged from 2 to 30, with a step of 2. Figure 4.6e, f show that the two methods are basically unaffected by the number of missed spikes. That is to say, they are robust against the noise due to missed spikes. The underlying reason is that the

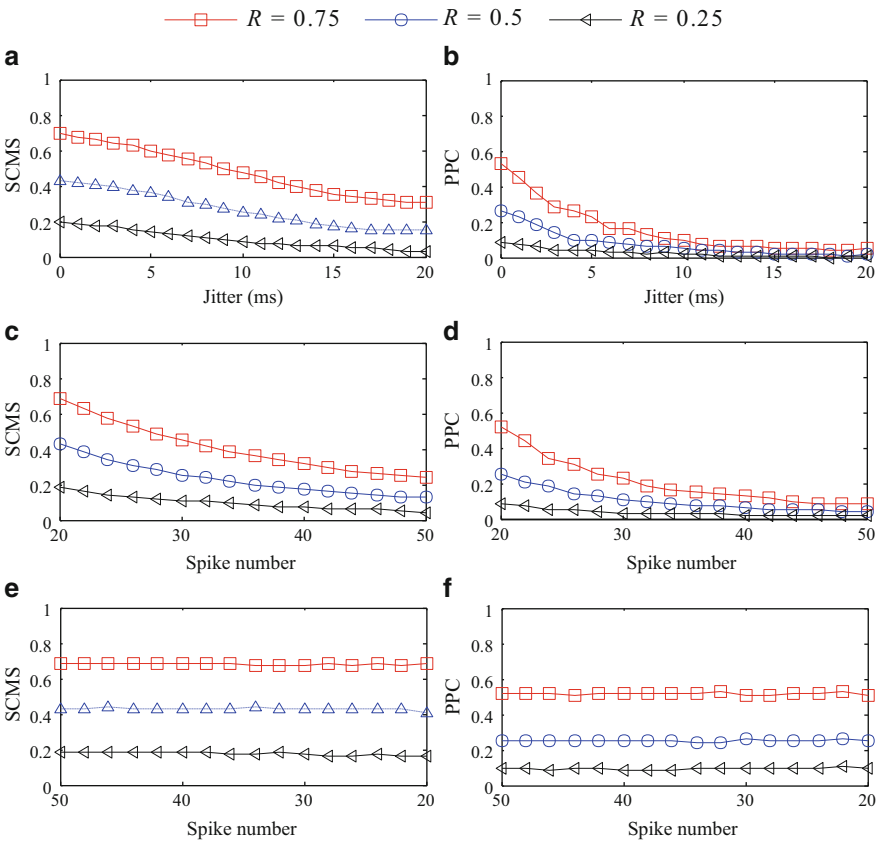

Fig. 4.6 Effect of noise in the spike trains on SCMS and PPC. The simulated spike-LFP synchronization strength was 0.25, 0.5, or 0.75. There were 100 realizations for each strength. (**a**) Mean SCMS output and (**b**) mean PPC output as a function of jitter noise. (**c**) Mean SCMS output and (**d**) mean PPC output versus the number of extra spikes. (**e**) Mean SCMS output and (**f**) mean PPC output versus the number of missed spikes

random deletion of spikes does not alter the strength of spike-LFP synchronization, but just reduce the total number of spikes. Since the two methods are not biased by the total number of spikes, they are both resistant to noise arising from missed spikes.

4.3.2.2 Application to Real Data

In this section, the SCMS method was applied to data recorded from rhesus monkey. All procedures were conducted in compliance with the National Institutes of Health Guide for the Care and Use of Laboratory Animals and were approved by the

Institutional Animal Care and Use Committee of Beijing Normal University. Data was recorded from a male adult monkey (*Macaca mulatta*). After the animal had been trained in a simple fixation task, a 6×8 multielectrode array (with electrode length of 0.5–0.6 mm, interelectrode spacing of 0.4 mm, and typical electrode impedances of a few hundred kiloohms at 1 kHz; Blackrock Microsystems) was implanted into V1 corresponding to eccentricities between 2.0° and 5.0° in the lower visual field. LFP and spike data were recorded at 30 kHz using a 128-channel acquisition system (Cerebus; Blackrock Microsystems). Visual stimuli were generated by a stimulus generator (ViSaGe; Cambridge Research Systems) on a 22-in. CRT monitor (Iiyama Vision Master Pro 514) at a viewing distance of 100 cm. Drifting sinusoidal gratings (99 % contrast; spatial frequency, 2 cycle/deg; temporal frequency, 4 Hz) were displayed within a circular patch of 4° visual angle in diameter, covering the visual field locations of all recording sites. The gratings drifted in different directions between 0 and 360°, in 22.5° steps in a pseudorandom order. The stimulus was presented for 2 s and repeated eight times.

To identify spikes fired by neurons, the recorded signals were filtered with a band-pass filter of 300–3000 Hz. Then, spikes were detected using a threshold method (Quiroga et al. 2004). We did not use spike sorting in this work. Due to the robustness of the method against noise in spike trains, it was not necessary to implement spike sorting in the data preprocessing. For LFPs, the recorded signals were filtered with a band-pass filter of 30–80 Hz, because our concentration was on the synchronization between spikes and LFPs in the gamma band. To preserve the phase relationship between spikes and LFP, gamma band-pass filtering was performed digitally with a zero-phase shift using the EEGLAB toolbox (Delorme and Makeig 2004).

Orientation selectivity is an emergent property of neurons in the primary visual cortex (V1) (Hubel and Wiesel 1962, 1968). Most studies focused on the response of individual neurons to investigate the mechanisms of this selectivity (Priebe and Ferster 2012; Ringach et al. 1997; Shapley et al. 2003). Neuronal oscillations in the gamma band (30–80 Hz) have been suggested to play a central role in feature binding or establishing channels for neural communication (Ray and Maunsell 2010). With increasing interest in and popularity of LFP analysis, oscillations in LFP gamma band have been used to study orientation selectivity (Berens et al. 2008; Xing et al. 2012). In this chapter, we examined whether the spike-LFP synchronization exhibits orientation selectivity in macaque V1 by using the SCMS method. Orientation selectivity based on spike-LFP synchronization is quantified by circular variance (CV), which is a global measure of the shape of the orientation tuning curve and defined as (Batschelet 1981)

$$\Gamma = 1 - \frac{\left|\sum_k r_k \exp\left(i2\theta_k\right)\right|}{\sum_k r_k}, \tag{4.10}$$

where r_k denotes the mean spike-LFP synchronization in response to a drifting grating with angle θ_k. The angles θ_k spanned the range from 0 to 360 ° with

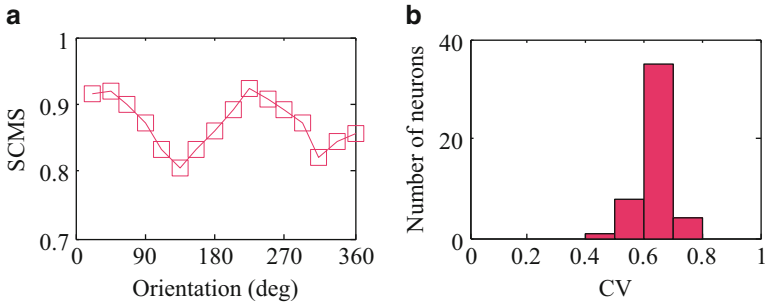

Fig. 4.7 Application of SCMS to data recorded from the visual cortex of a rhesus monkey. (**a**) The orientation tuning curve, calculated using spike-LFP synchronization as a substitute for firing rate, of a neuron (electrode #17) in V1. (**b**) The histogram of circular variance (CV) values, quantifying significance of orientation selectivity, of the 48 recorded neurons from V1

equally spaced intervals (22.5 ° in this work). According to circular statistics, $\Gamma < 0.9$ means that the orientation selectivity of a neuron to the drifting grating is significant. Figure 4.7a shows the tuning curve based on spike-LFP synchronization of a neuron in V1. Clearly, two troughs can be observed and the tuning curve shows a regular pattern as a function of the orientation. This means that the spike-LFP synchronization of this neuron is sensitive to the orientations of the drifting gratings. As shown in Fig. 4.7b, the CV of all 48 recorded neurons in V1 is less than 0.8, and the great majority (75 %) is located in the range from 0.6 to 0.7. This implies that the recorded neurons' spike-LFP synchronization exhibits significant orientation selectivity.

4.4 Conclusion

In this chapter, we introduced two methods to estimate the synchronization between the spiking activity of individual neurons and the LFP of neural ensembles. The WSFC is a correcting measure of a widely used SFC method which underestimates the coherence between bursty spike trains and LFPs, especially in high frequency band. The WSFC method allows only the first spike in every burst to enter into the calculating procedure, aiming to eliminate the influence of the other spikes. Moreover, it utilizes multiple copies of the first spike to highlight the difference between single spike and burst. This "weighting" operation preserves the inherent characteristic of burst, i.e., series of spikes raised by a large depolarization. Both simulation and experimental results show that the WSFC method performs better than SFC for investigating the relationship between bursty spike trains and high frequency band LFPs. Also, it can be used to analyze any spike trains and LFPs. Furthermore, a potential application of the WSFC is to study whether bursts enhance

the coherence between spike trains and LFPs. Briefly, the WSFC is a promising method to uncover details of the neural coding.

Moreover, we introduced a new method, spike-triggered correlation matrix synchronization (SCMS), for characterizing the synchronization between spike trains and rhythms present in LFP. We demonstrated that the SCMS is not sensitive to the total number of spikes in the calculation. In addition, it is superior to another unbiased measure (PPC) in resisting spike noise arising from jitter and extra spikes. Thus, the SCMS is a promising measure for estimating spike-LFP synchronization. By applying the SCMS method to neuronal data recorded from macaque primary visual cortex, we demonstrate that spike-LFP synchronization can be used to explore the mechanism of orientation selectivity.

References

Asai Y, Villa AE. Reconstruction of underlying nonlinear deterministic dynamics embedded in noisy spike trains. J Biol Phys. 2008;34:325–40.

Batschelet E. Circular statistics in biology. London: Academic; 1981.

Bauer M, Oostenveld R, Peeters M, Fries P. Tactile spatial attention enhances gamma-band activity in somatosensory cortex and reduces low-frequency activity in parieto-occipital areas. J Neurosci. 2006;26:490–501.

Berens P, Keliris GA, Ecker AS, Logothetis NK, Tolias AS. Comparing the feature selectivity of the gamma-band of the local field potential and the underlying spiking activity in primate visual cortex. Front Syst Neurosci. 2008;2:2.

Bokil H, Andrews P, Kulkarni JE, Mehta S, Mitra PP. Chronux: a platform for analyzing neural signals. J Neurosci Methods. 2010;192:146–51.

Buzsaki G, Wang XJ. Mechanisms of gamma oscillations. Annu Rev Neurosci. 2012;35:203–25.

Buzsaki G, Anastassiou CA, Koch C. The origin of extracellular fields and currents – EEG, ECoG, LFP and spikes. Nat Rev Neurosci. 2012;13:407–20.

Chalk M, Herrero JL, Gieselmann MA, Delicato LS, Gotthardt S, Thiele A. Attention reduces stimulus-driven gamma frequency oscillations and spike field coherence in V1. Neuron. 2010;66:114–25.

Cocatre-Zilgien JH, Delcomyn F. Identification of bursts in spike trains. J Neurosci Methods. 1992;41:19–30.

Colgin LL, Denninger T, Fyhn M, Hafting T, Bonnevie T, Jensen O, Moser MB, Moser EI. Frequency of gamma oscillations routes flow of information in the hippocampus. Nature. 2009;462:353–7.

Courtemanche R, Pellerin JP, Lamarre Y. Local field potential oscillations in primate cerebellar cortex: modulation during active and passive expectancy. J Neurophysiol. 2002;88:771–82.

Csicsvari J, Jamieson B, Wise KD, Buzsaki G. Mechanisms of gamma oscillations in the hippocampus of the behaving rat. Neuron. 2003;37:311–22.

Delorme A, Makeig S. EEGLAB: an open source toolbox for analysis of single-trial EEG dynamics including independent component analysis. J Neurosci Methods. 2004;134:9–21.

Eggermont JJ, Smith GM. Synchrony between single-unit activity and local field potentials in relation to periodicity coding in primary auditory cortex. J Neurophysiol. 1995;73:227–45.

Fell J, Klaver P, Lehnertz K, Grunwald T, Schaller C, Elger CE, Fernandez G. Human memory formation is accompanied by rhinal-hippocampal coupling and decoupling. Nat Neurosci. 2001;4:1259–64.

Fries P, Roelfsema PR, Engel AK, Konig P, Singer W. Synchronization of oscillatory responses in visual cortex correlates with perception in interocular rivalry. Proc Natl Acad Sci U S A. 1997;94:12699–704.
Fries P, Reynolds JH, Rorie AE, Desimone R. Modulation of oscillatory neuronal synchronization by selective visual attention. Science. 2001;291:1560–3.
Fries P, Schroder JH, Roelfsema PR, Singer W, Engel AK. Oscillatory neuronal synchronization in primary visual cortex as a correlate of stimulus selection. J Neurosci. 2002;22:3739–54.
Galashan FO, Rempel HC, Meyer A, Gruber-Dujardin E, Kreiter AK, Wegener D. A new type of recording chamber with an easy-to-exchange microdrive array for chronic recordings in macaque monkeys. J Neurophysiol. 2011;105:3092–105.
Grasse DW, Moxon KA. Correcting the bias of spike field coherence estimators due to a finite number of spikes. J Neurophysiol. 2010;104:548–58.
Hagan MA, Dean HL, Pesaran B. Spike-field activity in parietal area LIP during coordinated reach and saccade movements. J Neurophysiol. 2012;107:1275–90.
Harris KD, Hirase H, Leinekugel X, Henze DA, Buzsáki G. Temporal interaction between single spikes and complex spike bursts in hippocampal pyramidal cells. Neuron. 2001;32:141–9.
Harris KD, Henze DA, Hirase H, Leinekugel X, Dragoi G, Czurko A, Buzsaki G. Spike train dynamics predicts theta-related phase precession in hippocampal pyramidal cells. Nature. 2002;417:738–41.
Howard MW, Rizzuto DS, Caplan JB, Madsen JR, Lisman J, Aschenbrenner-Scheibe R, Schulze-Bonhage A, Kahana MJ. Gamma oscillations correlate with working memory load in humans. Cereb Cortex. 2003;13:1369–74.
Hubel DH, Wiesel TN. Receptive fields, binocular interaction and functional architecture in the cat's visual cortex. J Physiol. 1962;160:106–54.
Hubel DH, Wiesel TN. Receptive fields and functional architecture of monkey striate cortex. J Physiol. 1968;195:215–43.
Issa EB, Wang X. Altered neural responses to sounds in primate primary auditory cortex during slow-wave sleep. J Neurosci. 2011;31:2965–73.
Jarvis MR, Mitra PP. Sampling properties of the spectrum and coherency of sequences of action potentials. Neural Comput. 2001;13:717–49.
Kepecs A, Lisman J. Information encoding and computation with spikes and bursts. Network. 2003;14:103–18.
Le Van Quyen M, Bragin A, Staba R, Crepon B, Wilson CL, Engel Jr J. Cell type-specific firing during ripple oscillations in the hippocampal formation of humans. J Neurosci. 2008;28:6104–10.
Lee H, Simpson GV, Logothetis NK, Rainer G. Phase locking of single neuron activity to theta oscillations during working memory in monkey extrastriate visual cortex. Neuron. 2005;45:147–56.
Lewandowski BC, Schmidt M. Short bouts of vocalization induce long-lasting fast gamma oscillations in a sensorimotor nucleus. J Neurosci. 2011;31:13936–48.
Li X, Cui D, Jiruska P, Fox JE, Yao X, Jefferys JG. Synchronization measurement of multiple neuronal populations. J Neurophysiol. 2007;98:3341–8.
Lisman JE. Bursts as a unit of neural information: making unreliable synapses reliable. Trends Neurosci. 1997;20:38–43.
Mizuseki K, Sirota A, Pastalkova E, Buzsaki G. Theta oscillations provide temporal windows for local circuit computation in the entorhinal-hippocampal loop. Neuron. 2009;64:267–80.
Mizuseki K, Diba K, Pastalkova E, Buzsaki G. Hippocampal CA1 pyramidal cells form functionally distinct sublayers. Nat Neurosci. 2011;14:1174–81.
Mizuseki K, Royer S, Diba K, Buzsaki G. Activity dynamics and behavioral correlates of CA3 and CA1 hippocampal pyramidal neurons. Hippocampus. 2012;22:1659–80.
Muzzio IA, Levita L, Kulkarni J, Monaco J, Kentros C, Stead M, Abbott LF, Kandel ER. Attention enhances the retrieval and stability of visuospatial and olfactory representations in the dorsal hippocampus. PLoS Biol. 2009;7:e1000140.
Palm G. Evidence, information, and surprise. Biol Cybern. 1981;42:57–68.

Perelman Y, Ginosar R. An integrated system for multichannel neuronal recording with spike/LFP separation, integrated A/D conversion and threshold detection. IEEE Trans Biomed Eng. 2007;54:130–7.
Pesaran B, Pezaris J, Sahani M, Mitra P, Andersen R. Temporal structure in neuronal activity during working memory in macaque parietal cortex. Nat Neurosci. 2002;5:805–11.
Pienkowski M, Eggermont JJ. Sound frequency representation in primary auditory cortex is level tolerant for moderately loud, complex sounds. J Neurophysiol. 2011;106:1016–27.
Priebe NJ, Ferster D. Mechanisms of neuronal computation in mammalian visual cortex. Neuron. 2012;75:194–208.
Quiroga RQ, Nadasdy Z, Ben-Shaul Y. Unsupervised spike detection and sorting with wavelets and superparamagnetic clustering. Neural Comput. 2004;16:1661–87.
Rasch MJ, Gretton A, Murayama Y, Maass W, Logothetis NK. Inferring spike trains from local field potentials. J Neurophysiol. 2008;99:1461–76.
Ray S. Challenges in the quantification and interpretation of spike-LFP relationships. Curr Opin Neurobiol. 2014;31C:111–18.
Ray S, Maunsell JH. Differences in gamma frequencies across visual cortex restrict their possible use in computation. Neuron. 2010;67:885–96.
Reimann MW, Anastassiou CA, Perin R, Hill SL, Markram H, Koch C. A biophysically detailed model of neocortical local field potentials predicts the critical role of active membrane currents. Neuron. 2013;79:375–90.
Ringach DL, Hawken MJ, Shapley R. Dynamics of orientation tuning in macaque primary visual cortex. Nature. 1997;387:281–4.
Robin K, Maurice N, Degos B, Deniau JM, Martinerie J, Pezard L. Assessment of bursting activity and interspike intervals variability: a case study for methodological comparison. J Neurosci Methods. 2009;179:142–9.
Rosenblum MG, Pikovsky AS, Kurths J. Phase synchronization of chaotic oscillators. Phys Rev Lett. 1996;76:1804–7.
Rutishauser U, Ross IB, Mamelak AN, Schuman EM. Human memory strength is predicted by theta-frequency phase-locking of single neurons. Nature. 2010;464:903–7.
Schwartz AB. Cortical neural prosthetics. Annu Rev Neurosci. 2004;27:487–507.
Senior TJ, Huxter JR, Allen K, O'Neill J, Csicsvari J. Gamma oscillatory firing reveals distinct populations of pyramidal cells in the CA1 region of the hippocampus. J Neurosci. 2008;28:2274–86.
Shapley R, Hawken M, Ringach DL. Dynamics of orientation selectivity in the primary visual cortex and the importance of cortical inhibition. Neuron. 2003;38:689–99.
Siegel M, Konig P. A functional gamma-band defined by stimulus-dependent synchronization in area 18 of awake behaving cats. J Neurosci. 2003;23:4251–60.
Stafford BK, Sher A, Litke AM, Feldheim DA. Spatial-temporal patterns of retinal waves underlying activity-dependent refinement of retinofugal projections. Neuron. 2009;64:200–12.
Swadlow HA, Gusev AG. The impact of 'bursting' thalamic impulses at a neocortical synapse. Nat Neurosci. 2001;4:402–8.
Theiler J, Eubank S, Longtin A, Galdrikian B, Doyne Farmer J. Testing for nonlinearity in time series: the method of surrogate data. Physica D Nonlinear Phenomena. 1992;58:77–94.
Tiesinga PH, Fellous JM, Salinas E, Jose JV, Sejnowski TJ. Inhibitory synchrony as a mechanism for attentional gain modulation. J Physiol Paris. 2004;98:296–314.
van Vugt MK, Schulze-Bonhage A, Litt B, Brandt A, Kahana MJ. Hippocampal gamma oscillations increase with memory load. J Neurosci. 2010;30:2694–9.
van Wingerden M, Vinck M, Lankelma JV, Pennartz CM. Learning-associated gamma-band phase-locking of action-outcome selective neurons in orbitofrontal cortex. J Neurosci. 2010;30:10025–38.
Vinck M, van Wingerden M, Womelsdorf T, Fries P, Pennartz CM. The pairwise phase consistency: a bias-free measure of rhythmic neuronal synchronization. Neuroimage. 2010;51:112–22.
Wang Y, Iliescu BF, Ma J, Josic K, Dragoi V. Adaptive changes in neuronal synchronization in macaque V4. J Neurosci. 2011;31:13204–13.

Xing D, Shen Y, Burns S, Yeh CI, Shapley R, Li W. Stochastic generation of gamma-band activity in primary visual cortex of awake and anesthetized monkeys. J Neurosci. 2012;32:13873–80a.

Xu S, Jiang W, Poo MM, Dan Y. Activity recall in a visual cortical ensemble. Nat Neurosci. 2012;15:449–55.

Zanos TP, Mineault PJ, Pack CC. Removal of spurious correlations between spikes and local field potentials. J Neurophysiol. 2011;105:474–86.

Chapter 5
Artifact Removal in EEG Recordings

Ke Zeng and Xiaoli Li

5.1 Introduction

EEG is the neurophysiologic measurement of the electrical activity of the brain recorded through electrodes placed on the scalp. As it may provide insight into the functional structure and dynamics of the brain, EEG signals play a vital role in brain research. Clinical practices have extensively relied on E analysis to diagnose brain diseases such as the seizure disorders, head injuries, degenerative diseases, and metabolic disturbances. However, as a result of directly recording from electrodes placed on the scalp, EEG traces are prone to contamination of artifacts from various sources such as scalp muscles, eyeblinks, sweating, and instrumentation noises. These artifacts will inevitably introduce severe bias to the data interpretation or even completely overwhelm the EEG waves (Fatourechi et al. 2007). The common clinical practice is to cut the entire neural data segment affected by known artifacts, which will lead to a relevant information loss (Cassani et al. 2014). There exists a pressing need for an approach that is able to remove the artifacts in EEG recording to the most and to avoid loss or disruption of the structural information when achieving the former goal.

Numerous attempts have been performed to tackle this grand research challenge. The independent component analysis (ICA)-based methods are dominant for automatic artifact rejection (James and Gibson 2003). ICA is a blind source separation (BSS) technique which extracts statistical sources, i.e., independent components, from the raw multivariate recordings. ICA separates artifacts and concentrates them into the corresponding independent components, and those can be easily canceled

K. Zeng • X. Li (✉)
State Key Laboratory of Cognitive Neuroscience and Learning & IDG/McGovern Institute for Brain Research, Beijing Normal University, Beijing 100875, China

Center for Collaboration and Innovation in Brain and Learning Sciences, Beijing Normal University, Beijing 100875, China
e-mail: zengke2009@gmail.com; xiaoli@bnu.edu.cn

X. Li (eds.), *Signal Processing in Neuroscience*, DOI 10.1007/978-981-10-1822-0_5

afterwards. When there are less channels than sources, ICA by its nature cannot guarantee an efficient separation of the artifacts from the neural components, and useful information may be lost (Hyvärinen et al. 2001; Eriksson and Koivunen 2004). Furthermore, the effectiveness of ICA also depends on the length of the data segment under processing. That is, the data segment should be long enough to adapt to the number of channels (over-complete ICA), normally in an exponential manner.

To overcome the limitation with the ICA-based methods, wavelet transform has been proposed to assist ICA for improving the performance of denoising (Castellanos and Makarov 2006; Mammone et al. 2012). In general, these "wavelet-ICA" methods use wavelet transform to decompose the data of each channel into multiple predefined frequency sub-bands, such as delta, theta, alpha, and beta sub-bands. ICA then applies to these components in different frequency sub-bands to extract the sources. When the wavelet transform performs an n-level decomposition of the original data, an extended dataset forms with a size n times of the original data. The extended dataset contains more "channels" than the original data and satisfies the condition of applying ICA. However, wavelet transform is a linear algorithm which demands the data to be decomposed should be linear and stationary, while the neural data are typical nonlinear and nonstationary, such as EEG. A common disadvantage of data decomposition by wavelet is that the temporal patterns of data, such as instantaneous amplitude and phase/frequency, cannot be accurately estimated. Moreover, wavelet decomposition splits up data at each sub-band by the means of predefined corresponding time-invariant filters, thereby precluding the possibility of adapting the decomposition to the local variation of the oscillation. There exists a lack of accuracy in the decomposition of nonlinear and nonstationary neural data with wavelet; thus, the separation of artifact sources with ICA may not be reliable (Mijović et al. 2010; Sweeney et al. 2013).

It is critical to ensure that the decomposed data components still accurately reflect the characteristics of the original neural data. In other words, the decomposition approach should adapt to the data's nonlinearity and nonstationarity. Ensemble empirical mode decomposition (EEMD) has proved effective in exploring the structure of neural data (Wu and Huang 2009). The EEMD method can break down a complicated signal without a basic function into a series of oscillatory intrinsic mode functions (IMFs) embedded in the original data. This method is data-driven, which can decompose nonlinear and nonstationary data without a priori knowledge. EEMD also excels in its resistance to noises, which make it a natural candidate for processing noisy neural data. This study established an approach upon EEMD and ICA for artifact rejection of multivariate neural data, namely, EEMD-ICA (Zeng et al. 2014). The approach employs EEMD to decompose data into intrinsic mode functions (IMFs), and those IMFs possibly containing artifacts will be identified and selected. ICA then concentrates the artifacts hidden in the selected IMFs into the target sources, which will be automatically captured and eventually rejected.

To evaluate the performance of the proposed approach, EEMD-ICA had been tested against two dominant methods in terms of artifact rejection, i.e., the classical ICA (Delorme et al. 2007) and the automatic wavelet ICA (AWICA) methods (Mammone et al. 2012). Two batches of experiments on artifact removal had been

performed using semi-simulated data and real-life epileptic EEG data, respectively. In the first batch of experiments, four types of common artifacts (i.e., eyeblink, muscle noise, discontinuity, and white noise) in EEG were simulated and mixed with resting-state EEG to construct semi-simulated data. Results indicated that the proposed approach continuously outperforms the counterparts in terms of both normalized mean square error (NMSE) and structure similarity (SSIM) (Wang and Bovik 2009; Zhang et al. 2013). The superiority of the proposed method becomes even greater with the decrease of SNR in all cases, e.g., the SSIM of the EEMD-ICA can almost double that of AWICA and triple that of ICA. The second batch of experiments aimed to investigate the effects of the alternative approaches on dynamic characteristics of EEG containing absence seizures (absence EEG). Multi-scale permutation entropy (MPE) (proposed in our previous work (Ouyang et al. 2013)) had been calculated to measure the dynamic characteristics of absence EEG during seizure-free, pre-seizure, and seizure states and to classify the three seizure states via linear discriminant analysis (LDA). The raw absence EEG might contain intensive artifacts, which would severely affect the accuracy of classification. Prior to the MPE feature extraction, the three methods were applied to the raw EEG data for artifact rejection. Using the manually selected dataset as a reference (with a classification accuracy of 89.7 % obtained), the EEMD-ICA approach performed the best for classifying the three states (87.4 %, about 4.1 % and 8.7 % higher than that of AWICA and ICA, respectively).

The remainder of this paper is organized as follows: Section 5.2 gives a comprehensive review of the main methods proposed for removing artifacts from the EEG and a brief introduction to the design of the proposed EEMD-ICA approach. Section 5.3 compares EEMD-ICA approach with alternative approaches handling semi-simulated dataset. Section 5.4 presents the results for analyzing absence EEG after artifact removal with approaches. Section 5.5 concludes the paper with a summary.

5.2 Denoising Methods

In this section, we will provide a comprehensive overview of methods used for artifact removal in EEG recordings and then give a brief introduction to the design of EEMD-ICA approach. For each method, we not only account for its principle in the removal of EEG artifact but also highlight its advantages and disadvantages. Furthermore, we also refer to the extension of the methods if there exist.

5.2.1 Regression Methods

Regression methods are the most frequently used EEG artifact removal methods up to the mid-1990s, especially for electrooculography (EOG) artifact reduction

(Gratton et al. 1983). The premise condition of regression methods is that one or more reference channels are available and properly represent all artifact waveforms. Regression methods can be used either in the time or frequency domain to estimate the influence of the reference waveforms on the signal of interest. Regression methods assume that each EEG channel is a linear and time-invariant superposition of interesting source signal and a fraction of the source artifact represented by the reference channels. Formally, this is given as follows:

$$\boldsymbol{x}_i = \boldsymbol{s}_i + \sum_{j=1}^{N} \alpha_j * \boldsymbol{r}_j \tag{5.1}$$

where $\boldsymbol{x}_i$ and $\boldsymbol{s}_i$ are the observed EEG and desired EEG from channel i, respectively, $\boldsymbol{r}_j$ is the jth reference channel, and α_j is the corresponding jth fraction coefficient. Regression methods estimate fraction coefficients α_j of all the reference channels for each EEG channel. Artifact removal is then performed by subtracting the regressed portions of the reference waveforms from each EEG channel, resulting in an estimation of artifact-free EEG.

Due to their simplicity and reduced computational demands, regression methods have been widely used. Application of this method for artifact removal in EEG suffers the following two deficits. The main drawback of regression methods is the bidirectional contamination, which refers to the brain signals being measured in the reference channels such as EOG channels. If artifact removals directly use the regression methods and do not take bidirectional contamination in account, certain cerebral information of interest would be inevitably canceled in the subtraction procedure. To alleviate the effect of bidirectional contamination, the simplest way is to filter out the brain signal in the reference channels, as the artifact signal often focuses in some special channel such as EOG (1–4 Hz) (Romero et al. 2008). The other disadvantage of regression methods is that they need one or more reference channels, which limits their application mainly in EOG and ECG. Due to this deficient, regression methods have been replaced by more sophisticated algorithms in the real application. However, regression methods are still used as the "gold-standard" technique when comparing the performance among different EEG artifact removal methods.

5.2.2 Filtering Methods

Simple low-pass, band-pass, or high-pass filtering represents the classical filtering methods for artifact removal in EEG. However, they are only effective when there is no overlap between the frequency bands of signal of interesting and artifacts. As it is known that spectral overlap is common for typical artifact recorded along with the EEG, application of these classical filtering methods for removing EEG artifacts would therefore inevitably lose certain cerebral information of interest. To overcome this deficiency, numerous advanced filtering methods were introduced to adapt their

filter parameters following some optimization criteria. In this section, we briefly describe three main advanced filtering methods: adaptive filtering, Wiener filtering, and Bayes filtering.

1. Adaptive filtering. Adaptive filtering operates under the assumption that the desired signal and artifacts are uncorrelated. The filter generates a signal correlated with artifact signals from reference channels, and then the estimated desired signal is the subtraction from observed signal (Diniz 2008). The most prevalent algorithm employed in adaptive filtering is the least mean squares (LMS), which is linear in complexity and convergence. To model the contamination of the artifact on the EEG activity, LMS iteratively adjusts a vector of weights ($\boldsymbol{w}$) by

$$\widehat{\boldsymbol{s}}(n) = \boldsymbol{x}(n) - \boldsymbol{w}^T(n)\boldsymbol{r}(n) \tag{5.2}$$

$$\boldsymbol{w}\,(n+1) = \boldsymbol{w}(n) + 2\mu\widehat{\boldsymbol{s}}(n)\boldsymbol{r}(n) \tag{5.3}$$

where $\hat{\boldsymbol{s}}(n)$ and $\boldsymbol{x}(n)$ are the estimated of desired signal and the observed signal, respectively, $\boldsymbol{r}$ is the reference channel, and μ controls the rate of adaption. The weight $\boldsymbol{w}$ continues to adapt until the generated artifact $\boldsymbol{w}_n^T\boldsymbol{r}$, which is correlated with the provided reference, has been minimized.

In the adapting filtering methods, the choice of the artifact reference is key to the proper functioning of the algorithm (Daly et al. 2013). Though both adaptive filtering and regression methods need reference channels in artifact removal in EEG, the former has some advantage over the latter as the weights used to modeling artifacts in regression methods should be constant (Romero et al. 2009). The adaptive filter is easy to implement and can be operated online and without preprocessing or calibration, but the requirement of additional reference channel can add the complexity of the hardware system and limit its real application.

2. Wiener filtering. Wiener filtering is another parametric technique used for artifact removal in EEG. The Wiener filtering is based on a statistical approach, which does not require external reference signals. Wiener filtering produces a linear time-invariant filter to minimize the mean square error between the desired signals and their estimated desired signals (Izzetoglu et al. 2005). The minimization is performed using the power spectral densities (PSDs) of the observed signal and the artifacts. For most practical application, these PSDs are generally not available a priori and must be estimated from measurements.

The necessity for calibration prior to usage and inability to run in real time are the disadvantages of Wiener filter compared with the adaptive filter. However, it eliminates the requirement for additional sensors to recording reference signals in the adaptive filter. In addition, once properly calibrated, it even can achieve a better performance with respect to the adaptive filter.

3. Bayes filtering. Bayes filtering is a probabilistic method estimating a given systems state from available noisy observed signal. The assumption of Bayes

filtering is that the dynamic system is Markov, meaning that the current state variables contain all the relevant information about the system (Fox et al. 2003). Bayes filters are performed with predictor–corrector processes. The predictor uses a time update model to estimate the process state at a given time, and then the corrector utilizes a measurement model to evaluate the relationship between the observed data and the internal state.

Bayes filters are not directly implementable due to their intractable computation, while they can be approximated through Kalman filters (Morbidi et al. 2008) and particle filters (Candy 2009). These approaches can overcome both the limitations of adaptive filtering and Wiener filtering. Like Wiener filtering, the Bayes filter methods do not require additional sensors to record reference signals. However, unlike the Wiener filtering, Bayes filtering can be employed in real-time applications and does not need calibration prior to usage.

5.2.3 Blind Source Separation Methods

Blind source separation (BSS) is a wide class of algorithms with the goal of estimating sources from a mixing system without the aid of information about the mixing process (Comon and Jutten C. Handbook of blind source separation. Academic Press 2010). A linear mixing system can be expressed as

$$\mathbf{X} = \mathbf{AS} \tag{5.4}$$

where $X=[x1, \ldots, xq]T$ is the observations, $S=[s1, \ldots, sp]T$ is the sources, and A is a $[q \times p]$ mixing matrix. As only the observations X are known, the BSS technique is used to generate an unmixing matrix to determine the original sources.

$$\widehat{\mathbf{s}} = \mathbf{WX} \tag{5.5}$$

where $\widehat{s}$ is the estimation of the original sources and W is the $[q \times p]$ unmixing matrix W. In the BSS methods, all EEG channels are simultaneously exploited to estimate the source signals, and EEG artifacts removal is performed in the transformation domain; the artifact-free EEG is then obtained by applying the inverse transformation to the corrected components. As BSS is an unsupervised learning process, no additional reference signal is required.

There are lots of different algorithms available to perform BSS, including principal component analysis (PCA) (Ille et al. 2002), independent component analysis (ICA) (Hyvarinen et al. 2001), and canonical correlation analysis (CCA) (De Clercq et al. 2006) described in the following. Each algorithm performs matrix factorization to implement BSS with some particular assumptions about the signals, such as independence for ICA. The choice of the optimum algorithm to employ depends on a priori knowledge of the signal. Some of the most common BSS algorithms employed in research are described as follows.

1. PCA. PCA uses an orthogonal transformation to convert a set of observations of possibly correlated variables into a set of values of linearly uncorrelated variables called principal components. The orthogonal transformation is defined in such a way that the first principal component has the largest possible variance, which means accounting for as much of the variability in the data as possible, and each succeeding component in turn has the highest variance possible under the constraint that it is orthogonal to all the preceding components. PCA can be done by eigenvalue decomposition of a data covariance (or correlation) matrix or singular value decomposition of a data matrix, usually after normalizing or Z-scores the data matrix for each variable.

PCA is a second-order algorithm and is therefore strongly influenced by amplitude. It is shown that PCA performed well for EEG artifact removal only when the amplitude of the artifact was greater than that of interesting signal. And when the amplitude of artifact was similar or less than that of interesting signal, other BSS methods obtain better performance. In addition, the greatest problem of PCA is that the assumption of orthogonality in both temporal and spatial between neural activity and typical artifacts does not generally hold. Hence, PCA is often unable to separate some artifactual components from brain signals. In fact, PCA is often used just as a whitening step of ICA, since artifacts and brain signals are better modeled as independent rather than orthogonal.

2. ICA. ICA is a typical technique which extracts statistical sources, i.e., independent components, from the raw multivariate recordings. ICA separates artifacts and concentrates them into the corresponding independent components, and those can be easily canceled afterwards. And the artifact-free EEG is reconstructed by inverse ICA with desired signal source. There are a lot of algorithms used to determine the independent components. Some of the most commonly employed are FastICA, JADE, Infomax, and SOBI. The approach of each algorithm to estimating independence is different: FastICA maximizes the magnitude of the kurtosis or the neg-entropy of the component distributions; Infomax estimates the component probability distributions; SOBI takes advantage of temporal correlations in the source activities; and the JADE algorithm maximizes the kurtosis of the component distributions through a joint diagonalization of the fourth-order cumulants.

ICA, as a nonparametric algorithm, has a major advantage over some other parametric algorithms (such as adaptive filtering), and no priori information (such as reference signals) is required for the algorithm to function. One of the major limitations of ICA is the requirement for the independent sources to be non-Gaussian. ICA can obtain an estimate of the sources if the sources are non-Gaussian. Unfortunately, a component is generally not known to be Gaussian or non-Gaussian a priori. The EEG data are commonly whitened by PCA before the computation of the ICA to cancel the correlation between the signals and reduce the dimensionality of the data. In addition, when there are less channels than sources, ICA by its nature cannot guarantee an efficient separation of the artifacts from the neural components, and useful information may be lost.

3. CCA. CCA is another typical BSS method for the source separation of mixed signals. To solve the BSS problem, CCA assumes the sources to be maximally autocorrelated and mutually uncorrelated. In terms of seeking uncorrelated sources, CCA uses a weaker condition than statistical independent sought by ICA. In addition, ICA does not consider temporal correlations and can return the same solution no matter how the samples are arranged in time. To address this problem, CCA extracts uncorrelated sources that have maximum spatial or temporal correlation within each source.

As ICA employs statistical independence to separate the sources, it only can isolate those artifacts with stereotyped scalp topographies, but not those artifacts without (such as muscle artifacts). However, CCA performs well for both stereotyped and non-stereotyped artifacts by considering temporal correlations. Moreover, it is also noted that the CCA method always returns the same components ordered by autocorrelation with a given dataset, and the last few components with lower autocorrelation are often corresponding to the artifact sources. In addition, the CCA method adopts second-order statistics (SOS) rather than high-order statistics (HOS) to extract components; hence, CCA algorithm performed better relative to ICA in terms of computational complexity by at least an order of magnitude and can be used for online EEG artifact removal.

5.2.4 Source Decomposition Methods

In addition to separating artifact components simultaneously using all the EEG channels by the BSS methods, there are also lots of additional algorithms devised to estimate artifact component from just a single channel. Such algorithms directly decompose each individual channel into basic waveforms that represent either signal of interesting or the artifact component. The principle based on these algorithms is that source signal (either the signal or artifact) can be represented by a single decomposition unit, such as certain wavelet basis for the wavelet transform or an intrinsic mode function (IMF) for empirical mode decomposition. As the personal healthcare devices desire for minimal instrumentation (less sensors) and low operational complexity, these algorithms are utilized more frequently in this domain:

1. Wavelets transform. The wavelet transform (WT) has been used for artifact removal in EEG recordings since the early 1990s. The WT is defined as the inner product of the signal with the time shifted and scaled wavelet functions. The wavelet transform coefficients at some scale represent the similarity of the signal to be decomposed with the wavelet at that scale. The discrete wavelet transform (DWT) is most often used for wavelet denoising, and the goal of DWT is to isolate the artifact in both time and frequency in order to minimize the impact of the artifact removal process on the rest of the neural signal. DWT computes two sets of coefficients: approximation coefficients and detail coefficients, which are

obtained by convolving signal with a series of low-pass filters for approximation and high-pass filters detail.

Wavelet denoising operates in three steps: (1) decompose the signal into a number of levels, 2) threshold the wavelet coefficients, and (3) reconstruct EEG data from artifact-free components. EEG artifact removal based on the wavelet transform depends on that the sources of interest and artifacts will not be decomposed in the same wavelet basis. As the accurate separation of the signal and noise depends on the wavelet basis and its similarity to the source signal to be preserved, the mother wavelet and the decomposition level are critical for the design of wavelet denoising. The strategy of selecting a wavelet is that the shape of wavelet and the transient of interest should be matched. As to decomposition level, the artifact will be diluted across frequency bands for too deep decomposition, leading it difficult to isolate in time, and the artifact will not be isolated in frequency for too little decomposition, causing neural data to be unnecessarily lost in the thresholding process. The proper level of decomposition depends in large part on artifact type and the sampling frequency of the data. When the artifacts to be removed include many types, a strategy of multilevel wavelet decomposition may be used (Kelly et al. 2011). The choice of threshold in the second step also needs to be carefully made. In general, there are two strategies for threshold setting: hard and soft threshold. It is known that soft threshold has large bias in the denoised signal resulting in under correction of artifacts. On the other hand, hard threshold produces large variance and induces artifact itself when there is a spike-like transient artifact. So good threshold should be trade-off between soft and hard thresholds in terms of artifact removal and signal distortion, such as adaptive thresholding (Krishnaveni et al. 2006).

Although DWT shows to be an interesting tool for EEG artifact removal, there are many limits for the real application. One of the most typical cases is that the DWT is unable to separate artifacts completely which overlap with signal of interesting in the spectral domain, such as EMG artifact embedded on an EEG signal. In 2011, synchrosqueezed wavelet transform (SWT) (Daubechies et al. 2011), a combination of wavelet analysis and reallocation method, has been proposed as a novel adaptive decomposition tool for signals. This method introduces a precise mathematical definition for a class of functions that can be viewed as a superposition of a reasonably small number of approximately harmonic components. And experiments show that SWT does indeed succeed in decomposing arbitrary oscillatory components. Hence, SWT may be a potential interesting tool to achieve better EEG artifact removal performance relative to WT.

2. Empirical mode decomposition. The EMD was proposed as a new signal decomposition method for nonlinear and nonstationary data (Huang et al. 1998). The EMD method can decompose any complicated signal into a collection of oscillatory modes, called intrinsic mode functions (IMFs), which represent fast to slow oscillations in the signal. EMD sequentially decomposes N IMFs by a sifting process such that $x(t) = \sum_{i=1}^{N} imf_i(t) + r_n(t)$ where rn is the residual of signal. Each IMF should satisfy two conditions: (1) over the full length of each IMF, the number of maxima and the number of zero crossings must be the same

or differ by 1 at the most; (2) at any point of each IMF, the envelope defined by the mean value of the maxima and the minima must be zero.

In the EMD denoising, thresholds also need to be selected for EEG artifact removal (Kopsinis and McLaughlin 2009). The first strategy for thresholds setting is to judge whether a specific IMF contains signal of interesting or noise. The key to this strategy is that the artifacts can be represented by one or more IMFs. The second strategy is just a direct application of wavelet thresholding in the EMD denoising such as hard and soft thresholding. This is because the EMD can also be interpreted as a dyadic filter bank although this filter bank structure is by no means predetermined and fixed as in wavelet decomposition. A wavelet-like threshold directly applying to IMFs can bring catastrophic consequences for the continuity of the reconstructed signal. This is because the processed IMF with some thresholds would be against to the definition of IMF. However, it is possible to guess if the interval between two zero crossings is noise dominant or signal dominant based on the single extrema that correspond to this interval. Hence, the third strategy is to adapt threshold for EMD characteristics which is referred to as EMD interval thresholding.

IMF in the EMD is introduced based on the local properties of the signal, which eliminate the need for spurious harmonics to represent nonlinear and nonstationary signals. Therefore EMD would outperform DWT in the case of handling oscillatory signals, such as EEG. Additionally, EMD is a data-driven method rather than relying on a predefined linear basis as the wavelet does, which enables it to deal with very local variations of nonlinear and nonstationary EEG. EMD also has been criticized due to its sensitivity to noise and susceptibility to interference from mode mixing, which means a single IMF including oscillations of dramatically disparate scales. When mode mixing occurs, an IMF would contain different physical processes in a mode, suggesting a lack of accuracy in the decomposition between the signal of interesting and the noise. To address the pitfalls, EMD method has recently evolved to ensemble empirical mode decomposition (EEMD) (Wu and Huang 2009), which consists of sifting an ensemble of white noise-added signal (data) and treats the mean as the final IMF. EEMD utilizes the full advantage of the statistical characteristics of white noise to perturb the signal in its true solution neighborhood. As the EEMD demands repetitive processing of many trials of the noise-added signals, the EEMD-based method is intensive in computing. A parallelized EEMD method has been developed using general-purpose computing on the graphics processing unit (GPGPU), namely, G-EEMD (Chen et al. 2010), which paves the way of EEMD in practice.

5.2.5 EEMD-ICA Method

The design of the EEMD-ICA approach (Zeng et al. 2014) is illustrated in Fig. 5.1. The approach operates in five stages: (1) decomposition of neural data, (2) selection

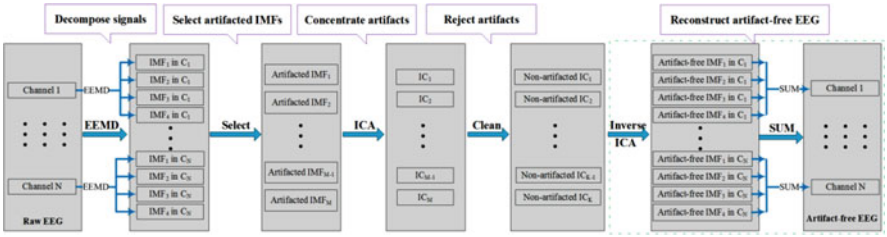

Fig. 5.1 Block diagram of EEMD-ICA framework for artifact rejection of multivariate neural data. This framework consists of five blocks: (1) decomposition of neural data, (2) selection of IMFs with artifacts, (3) concentration of artifacts, (4) artifact rejection, and (5) reconstruction of "artifact-free" neural data. Each channel neural data is first decomposed into four IMFs in this diagram. The artifact IMFs are then selected from the IMFs dataset and passed into ICA. The artifacts in the selected IMFs can be concentrated into a few independent components. The artifact components then can be identified by means of quantitative measures and rejected afterwards. The artifact-free neural data is eventually reconstructed via the inverse ICA

of IMFs with artifacts, (3) concentration of artifacts, (4) artifact rejection, and (5) reconstruction of the "artifact-free" neural data. In the first stage, EEMD was used to decompose each data channel into a series of embedded IMFs. In the second stage, the IMF containing artifacts will be automatically selected. In the third stage, ICA concentrates the artifact contents dispersing in multiple IMFs into a few components. In the fourth stage, the artifact components are automatically identified by means of a quantitative measure and rejected. Finally, the artifact-free EEG dataset is reconstructed in two steps: inverse ICA and summing up every group of denoised IMFs corresponding to the same data channel.

EEMD-ICA approach utilized both the EEMD and ICA to separate artifact from EEG recordings. The EEMD is unable to remove artifacts which overlap with EEG in the spectral domain, and ICA by its nature cannot guarantee an efficient separation when the number of channels is less than that of sources. The EEMD-ICA combines the positive aspects of both independent algorithms to overcome some of their individual shortcomings. And this combined method can even be used for single-channel EEG recordings due to the EEMD creating multidimensional data from a single-channel EEG measurement. To remove the artifact in EEG, a strategy of coarse-to-fine detection was used. Once the IMFs are obtained by the EEMD, the artifactual IMFs should be identified for further processing. This intends to refine the ICA's processing of the subset of IMFs. In this study, entropy and kurtosis are referred to for detecting the components containing artifacts:

(a) Entropy. Most artifacts are typically "unusual" time courses in the sense that they appear as transient or unexpected events. The outliers generated by these events would enhance the randomness or the uncertainty of the neural data. Then entropy, a natural measure to quantifying the degree of randomness, is particularly appealing as an indicator to detect the IMFs containing artifacts (Hild et al. 2006). To estimate the entropy of each IMF, all of the probability

density functions (pdf) of data values in each IMF were first computed. The entropy (E) of the ith IMF (IMFi) can be then computed as follows:

$$E(i) = -\sum_{x \in IMF_i} pdf(x) \log\left(pdf(x)\right) \tag{5.6}$$

where pdf(x) is the probability of the value x in the probability distribution in IMFi. The entropy was computed for all of the decomposed IMFs.

(b) Kurtosis. The entropy measure can be used to identify transient or unexpected artifacts, while some other artifacts, such as blinks and discontinuity, are typically characterized by a peaky distribution of potential values and can be detected based on their unusual peakyness. The kurtosis (or the fourth-order cumulant) of the activity values in IMFs applies to quantify the peakyness (Delorme et al. 2007). For each IMF, its kurtosis K conforms to the following equations:

$$K = m_4 - 3m_2^2 \tag{5.7}$$

$$m_n = E\left\{(x - m_1)^n\right\} \tag{5.8}$$

where *mn* is the nth central moment of all activity values of the IMF and m1 is the mean value and E is the expectancy function.

The two measures were first normalized to zero mean and unit standard deviation. Then, those components (IMFs or independent components) whose entropy or kurtosis exceeds the corresponding thresholds were marked as artifact components. In the coarse process of artifact removal, the choices of the two thresholds were not too strict, and low thresholds will be better, which can reject IMFs obviously corresponding to interesting neural signal and retain enough data channels for the ICA. However, thresholds in the fine process will be more rigorous and higher to guarantee accurate selection of artifact independent components.

5.3 Simulation

As EEG data are generally noisy, artifact rejection is crucial for EEG preprocessing. It has long been a grand research challenge for an approach which is able (1) to remove the artifacts to the most and (2) to avoid loss or disruption of the structural information at the same time; thus the risk of introducing bias to EEG interpretation may be minimized. To achieve this goal, we proposed an approach upon EEMD and ICA for artifact removal in EEG recordings, namely, EEMD-ICA. The approach was tested against the classical ICA (Delorme et al. 2007) and the automatic wavelet ICA (AWICA) methods (Mammone et al. 2012), which were dominant methods for artifact rejection. The classical ICA separated artifacts and concentrated them

into the corresponding independent components for rejection afterwards. AWICA first used wavelet transform to decompose raw data of each channel into multiple frequency sub-bands and then applied ICA to the decomposed data to separate the artifacts for rejection at the end. In order to evaluate the effectiveness of the proposed approach in handling EEG data possibly with intensive noises, experiments on artifact removal had been performed using semi-simulated data mixed with a variety of noises.

5.3.1 Data Simulation

The test data is a resting-state EEG, which was recorded at a sampling rate of 256 Hz using an 8-electrode scalp montage. There were two electrodes located in the frontal area, the central area, the tempo-parietal area, and in the occipital area, respectively. Fifty epochs of 10 s "clean" data were selected by experts as background EEG to construct semi-simulated data.

In this study, four types of artifacts were simulated to represent the noises commonly observed in EEG according to (Delorme et al. 2007). Those include (a) eyeblink, (b) discontinuity, (c) muscle noise, and (d) white noise as illustrated in Fig. 5.2. Eyeblinks and muscle artifacts were modeled using random noise band-pass filter (FIR) between 1 and 3 Hz and between 20 and 60 Hz, respectively. Electrical shift artifacts were implemented as discontinuities. Finally, unfiltered random Gaussian noises were used to simulate the white noise.

To construct the semi-simulated EEG, the modeled artifacts were added to the "clean" EEG as follows: (1) the modeled eyeblinks and muscle noises were projected to all electrodes with varying intensities, and (2) the discontinuity and white

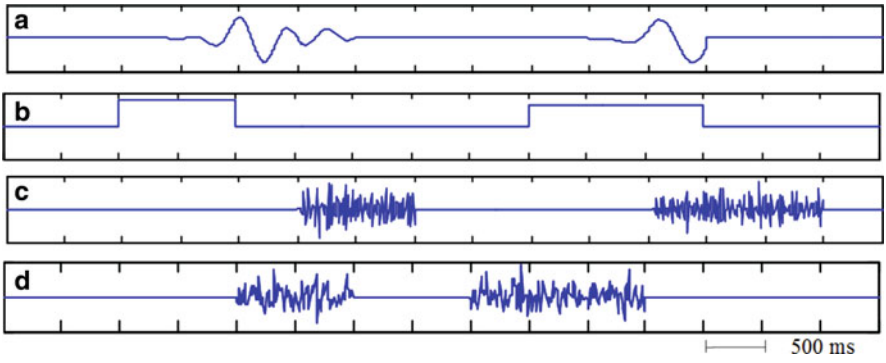

Fig. 5.2 Four types of simulated artifacts introduced into actual EEG. (**a**) Low-frequency events (1–3 Hz) modeling eyeblink artifacts, (**b**) signal discontinuities modeling the electrical shift artifacts, (**c**) transient high-frequency events (20–60 Hz) modeling muscle artifacts, and (**d**) unfiltered random Gaussian noises modeling the white noise

noises were added to data channels randomly selected. As eyeblinks significantly affected the EEG in the frontal area, the scalp topography of modeled eyeblinks in each projection was set with high gains (>80 %) at the most frontal electrodes and low gains (<20 %) at the rest electrodes. The projection of modeled muscle noises mainly concentrated at temporal electrodes (>95 %) as these electrodes were liable to the muscle noises. The discontinuity and white noises manifested no spatial characteristics, and those were added to randomly selected channels.

In general, SNR could affect the performance of noise removal methods. This simulation study investigated the performance of the three approaches with data of a range of SNRs (from 0.1 to 1.5). For each type artifact, 50 modeled artifacts in each SNR level were projected to the 50 epochs of "clean" EEG data, respectively. And the performance of artifact rejection methods was calculated as the average of the 50 simulation trials.

5.3.2 Performance Metrics

The goal of artifact rejection is to restore the artifact-free state of the semi-simulated EEG contaminated by artifacts. Two performance metrics are proposed to quantify an artifact rejection approach's ability of rejecting artifacts. That is, how "clean" the resulted data is after artifact rejection:

(a) Normalized Mean Square Error (NMSE). NMSE is the most commonly used metric for quantifying performance of signal processing, which can be defined as follows:

$$NMSE = \frac{\|x - \widehat{x}\|_2^2}{\|x\|_2^2} \tag{5.9}$$

where x is the original artifact-free data and $\widehat{x}$ is the corresponding data reconstructed from the artifactual signal.

(b) Structure Similarity (SSIM). SSIM (Wang and Bovik 2009) is the second metric. SSIM for the original signal x and its reconstructed data $\widehat{x}$ conforms to the following formula:

$$S(x, \widehat{x}) = \left(\frac{2\mu_x \mu_{\widehat{x}}}{\mu_x^2 + \mu_{\widehat{x}}^2}\right) \cdot \left(\frac{2\sigma_x \sigma_{\widehat{x}}}{\sigma_x^2 + \sigma_{\widehat{x}}^2}\right) \cdot \left(\frac{\sigma_{x\widehat{x}}}{\sigma_x \sigma_{\widehat{x}}}\right) \tag{5.10}$$

where μ_x and $\mu_{\widehat{x}}$ are the local sample means of x and $\widehat{x}$, respectively; σ_x and $\sigma_{\widehat{x}}$ are the local sample standard deviations of x and $\widehat{x}$, respectively; and $\sigma_{x\widehat{x}}$ is the sample cross correlation of x and $\widehat{x}$ after removing their means. SSIM is bounded: $-1 \leq S(x, \widehat{x}) \leq 1$, the maximum value $S(x, \widehat{x}) = 1$ may be achieved only if $x = \widehat{x}$. The higher the SSIM is, the better the quality of recovery is.

5.3.3 Parameter Settings

The FastICA (Hyvärinen 1999) was chosen as a representative ICA method as it was the fastest implementation of ICA. The mother wavelet adopted in the AWICA approach was db4, which denoted a maximally flat-frequency response. The decomposition level was set to 5 as the EEG (sample rate 256 Hz) can be separated into the five ranges of the major EEG rhythms: delta 1–4 Hz, theta 4–8 Hz, alpha 8–14 Hz, beta 14–32 Hz, and gamma 32–64 Hz, 64–128 Hz. In the context of the EEMD-ICA approach, the number of IMFs was set to six in order to keep consistence with the AWICA. The ratio of the standard deviation of the added noise in EEMD is set to 0.1.

5.3.4 Results and Discussions

The results for every approach against the four types of artifacts are presented in Fig. 5.3. The MMSE and SSIM values are the average of 50 trials and presented in the upper and lower rows, respectively. Each column corresponds to a unique type of artifacts:

(a) *ICA* vs. *AWICA* and *EEMD-ICA*

It can be observed that the approach based on the classical ICA performed the worst in term of both NMSE and SSIM when dealing with any type of artifacts.

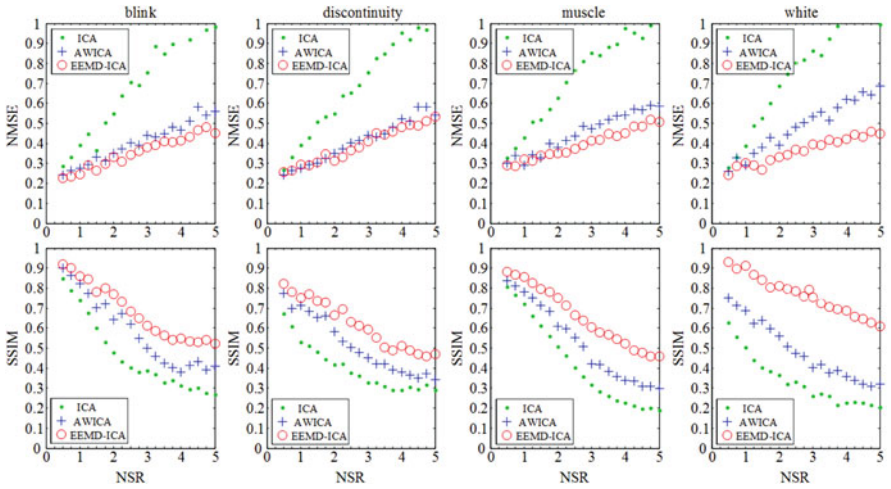

Fig. 5.3 Artifact rejection performance measure (y axis, NMSE in the *top row* and SSIM in the *bottom row*) by three methods (ICA, AWICA, and EEMD-ICA) for four types of simulated artifacts (columns) of increasing SNR (x axis, in the range of SNR from 0.1 to 1.5)

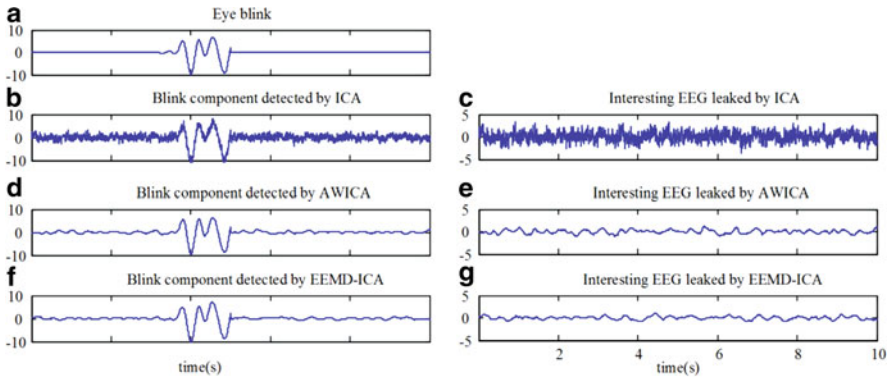

Fig. 5.4 The artifact component detected and rejected by the three approaches. (**a**) is the simulated eyeblink. (**b**),(**d**), and (**f**) are the artifact components detected by ICA, AWICA, and EEMD-ICA, respectively, and (**c**), (**e**), and (**g**) are the underlying useful EEG signals (cerebral activities) contained in the (**b**),(**d**), and (**f**)

That is because the number of data channels is eight, which was far less than the number of the latent sources. Hence, the ICA method cannot sufficiently separate the artifactual components. As illustrated in Fig. 5.4, although the blink component (Fig. 5.4b) detected by ICA obviously indicates the presence of strong artifact (the original artifact shown in Fig. 5.4a), it also contains a considerable amount of cerebral activities of interest (Fig. 5.4c). Directly rejecting such blink components would lead to loss of useful information, and this inevitably results in serious distortion when reconstructing the artifact-free EEG. With the assistance of decomposition methods such as EEMD and wavelet, a dataset with additional channels can be established to meet the demand of ICA. Thus, ICA works effectively in separating artifactual source even from the original data with a limited number of channels. Figure 5.4d and f clearly indicate that the blink components detected by AWICA and the EEMD-ICA contain much less useful EEG data (Fig. 5.4e and g) than that detected by ICA.

Moreover, EEMD method can be regarded as a dyadic filter for any data (Wu and Huang 2009), which is similar to a multilevel wavelet decomposition. When the artifactual data are concentrated in a single sub-band (via decomposition with wavelet or EEMD), only one sub-band will account for the artifact signal. ICA can focus on a specific frequency range rather than processing the entire dataset. In this manner, although the artifact components might still contain neural activities when the ICA does not work in the optimal case, these neural activities are only confined in the frequency range in connection with the artifacts. Thus, information loss in the other frequency ranges can be avoided.

(b) *AWICA* vs. *EEMD-ICA*

From the upper row of Fig. 5.3, it can be observed that the difference among NMSEs measured upon the AWICA and EEMD-ICA approaches is insignificant when the SNR is high (SNR>1). With the gradual decrease of SNR, the EEMD-

ICA approach performs better and better than the AWICA does. This is attributed to the merit of EEMD method, which is much more resistant to noises than its counterparts.

In contrast, as shown from the lower row of Fig. 5.3, the EEMD-ICA approach significantly outperforms AWICA in terms of SSIM in almost all cases. NMSE is formulated in a manner that all the samples are equally treated, and this causes that the content-dependent variations between the two signals in comparison cannot be accounted for. On the contrary, the SSIM measures the structural similarity between two signals, which may be more suited for structured neural data (such as EEG) than the NMSE does. From this fact, it can be concluded that the EEMD-ICA approach can retain more structural information of the data of interest than AWICA.

As illustrated in Fig. 5.5, an eyeblink was simulated and mixed with the original EEG (Fig. 5.5a), and the denoising outputs of AWICA and EEMD-ICA were showed in Fig. 5.5b. From both the segments with artifacts (Fig. 5.5c) and without artifacts (Fig. 5.5d), it can be observed that (1) the outputs of AWICA (the channels

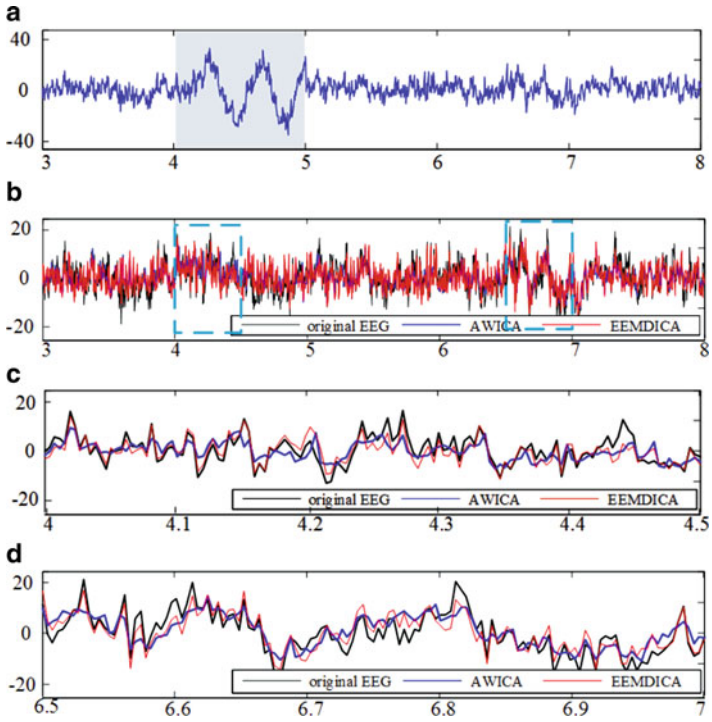

Fig. 5.5 Comparison between AWICA and EEMD-ICA for removing eyeblink artifact. (**a**) A semi-simulated data channel containing eyeblink artifact from 4 to 5 s; (**b**) the *top* channel is the original EEG before noise was added, and the middle and the *bottom* channels are the denoised outputs using AWICA and EEMD-ICA, respectively. The denoised segment contaminated by artifacts from 4 to 4.5 s is highlighted in (**c**), and the denoising segment from 6.5 to 7 s outside artifacts is highlighted in (**d**)

in the middle) only follow the trend of the original EEG (the channels at the top) and (2) the outputs from the EEMD-ICA (the channels at the bottom) not only keep the trend but also maintain the structural information (such as phases) of the original EEG.

The advantage of EEMD over wavelet is that EEMD can break the data into its oscillatory modes. Therefore it is inevitable that the EEMD-ICA approach would outperform AWICA in the case of handling oscillatory signals, such as EEG. Additionally, EEMD is a data-driven method rather than relying on a predefined linear basis as the wavelet does, which enables it to deal with very local variations of nonlinear and nonstationary neural data. EEMD-ICA can thus retain more structural information of the original data than the AWICA approach does.

(c) Performance for handling white noises

As shown in the fourth column of Fig. 5.3, the EEMD-ICA approach can achieve a performance of dealing with the white noises dramatically better than the rest. That is because the EEMD method is a noise-assisted method, which adds white noises to the data under processing to address the mixed mode problem with EMD. In the EEMD method, the EMD algorithm is applied to decompose an "ensemble" of white noise-added data rooted from the original data. The average of the IMFs in the ensemble is the final result of decomposition. With the help of white noises, the EEMD automatically eliminates mode mixing in all cases. At the same time, the EEMD method itself owns the intrinsic characteristic to resist white noises.

(d) Practicability

In sophisticated scientific and engineering applications, the efficiency is a premise when ensuring the effectiveness of artifact removal. The classical ICA approach is the fastest one. The AWICA approach is about four times slower, while the EEMD-ICA approach can be about tens of times slower. This is reasonable as EEMD demands repetitive processing of many trials of the noise-added signals, and it is highly compute intensive. Real-time application of EEMD based on conventional computing platform is therefore impractical.

Considering the applications of EEMD-ICA in real practice, the parallelized EEMD method, namely, G-EEMD, can be employed. It has been developed by successfully adopting the technology of general-purpose computing on graphics processing units (GPGPU) in our previous work (Chen et al. 2010). The G-EEMD exhibits an efficiency hundreds of times better and excessively high-performance/price ratio compared to the original serial implementation of EEMD, which paves the way of EEMD-ICA in practice.

5.4 The Effects of Artifact Rejection on Seizure Detection

Artifact rejection serves as a preprocessing method of neural data processing. Its effectiveness can be further examined against real-life problems, e.g., seizure detection. An absence EEG records sudden and abrupt seizures, which reflect

transient signs and/or symptoms of abnormal, excessive, or synchronous neural activities in the brain. It may have significant impact on the educational development of sufferers (Killory et al. 2011). Seizure detection plays a very important role in studying the mechanism of absence and in the process of recovery (Zeng et al. 2016). In real-world applications, intensive noises contained in raw EEG recordings will inevitably introduce significant bias to seizure detection. This study investigated the effectiveness of artifact rejection methods in EEG-based seizure detection.

5.4.1 EEG Recordings

Seven patients (four males and three females with absence epilepsy) aged from 8 to 21 years old were recruited after taking consent from the Ethics Committee of Peking University People's Hospital. The EEG data were recorded using the Neurofile NT digital video EEG system from scalp surface electrodes (International 10–20 System) at a sampling rate of 256 Hz using a 16-bit A/D converter and filtered within a frequency band of 0.5–35 Hz. Nineteen electrodes were used and the impedance levels were set at less than 50 kΩ.

The EEG segments (a duration of 2 s) were selected from seizure-free, pre-seizure, and seizure intervals, and each state has 60 EEG epochs. Many of these epochs were contaminated by eyeblinking, muscle artifacts, etc. Experimental results from these raw data were referred to as the baseline for further comparison.

ICA, AWICA, and EEMD-ICA approaches were used to first preprocess the raw EEG epochs, respectively, and three "artifact-free" datasets were constructed for classification again. In addition, another 60 EEG epochs free of artifact had also been produced by an experienced clinician by inspecting the EEG visually. This manually selected data will be used to develop a gold standard to benchmark three artifact rejection approaches.

5.4.2 Results and Discussion

In this study, multi-scale permutation entropy (MPE) proposed in our previous work is used as an indicator for identifying seizure-free, pre-seizure, and seizure states (Ouyang et al. 2013). The scale factor is set as 5. To classify three states, discriminant analysis (DA) is used as classifier and the type of DA is quadratic (Cai et al. 2008). In order to develop robust classifiers, we choose the tenfold cross validation data resampling technique for training and testing the classifiers. The classification accuracy is used as a metric for evaluating the effect of three artifact rejection methods, which is defined as the number of correct classifications/the total number of states.

The result shows that a classification accuracy of 70.6 % can be obtained from the raw EEG, which can be used as the baseline to calculate the performance gains after artifact rejection. And the manually selected data can achieve an accuracy of

89.7 %, which can be considered as the idea performance of "artifact-free" datasets preprocessed by some optimized artifact rejection method. After artifact rejection for the raw data by ICA, AWICA, and EEMD-ICA approaches, the classification accuracies are 78.7 %, 83.3 %, and 87.4 %.

Comparing the results of raw dataset with the manually selected dataset, it is easy to mistake the pre-seizure and seizure states as seizure-free states under the interference of noise. This is because the permutation entropy was proposed to measure the irregularity of nonstationary time series (Bandt and Pompe 2002; Li et al. 2008), and the noises would often strengthen the irregularity of the EEG (as illustrated in II.B.1)). Under the influences of noises, the EEG during the pre-seizure and seizure states would have increasing irregularity and may be misclassified as the seizure-free state, where EEG is the most irregular. However, to distinguish the pre-seizure state and seizure state from the seizure-free state is the major concern in research and clinical practice. Hence, appropriate artifact rejection is needed before the seizure detection.

Comparing the results of raw dataset with the "artifact-free" datasets, it suggests that all of the three artifact rejection approaches can obviously improve the performance of classification and achieve gains of 8.1 %, 12.7 %, and 16.8 %, respectively. In comparison with the ICA method, both AWICA and EEMD-ICA can further improve the performance of seizure detection. This indicates that both wavelet and the EEMD decomposition can enhance the performance of ICA in denoising. In addition, EEMD-ICA is even superior to AWICA with a 4.1 % higher accuracy, which is the closest to the ideal situation. This is because EEMD excels in dealing with oscillation data, which will benefit MPE to use the local order structure of the time series to extract informative features from epilepsy EEG data (Ouyang et al. 2013; Bandt and Pompe 2002; Li et al. 2008). Hence, it can be concluded that EEMD-ICA can preserve more structural information than its counterparts to achieve the best performance.

5.5 Conclusions

This study developed an approach for artifact removal in EEG recordings, a vital issue in EEG preprocessing. The approach combines EEMD and ICA for selection of artifactual components and concentration of artifacts, respectively. Entropy and kurtosis are defined to indicate the presence of artifacts of various types. The effectiveness of the proposed approach was examined using both semi-simulated data purposely contaminated with selected artifacts and absence EEG data in real life. Comparisons were made against the classical ICA and AWICA approaches, and EEMD-ICA always performed the best.

When using SSIM as the metric, EEMD-ICA significantly outperformed the other two approaches for all types of noise. EEMD-ICA can almost double that of AWICA and triple that of ICA when handling intensive noises. When the SNR was high, the difference between the three approaches was not significant in terms of

NMSE. When SNR became lower, the EEMD-ICA approach's superiority turned to be very significant. In particular, the EEMD-ICA approach handled the white noises very well due to the noise-assisted EEMD algorithm.

The effectiveness of the artifact rejection approaches had been evaluated via characterizing the dynamics of absence EEG. All of the three artifact rejection approaches can improve the accuracy of classifying the seizure-free, pre-seizure, and seizure states. EEMD-ICA still outperformed the other two approaches, whose performance was the most close to that of the gold standard. The performance of EEMD-ICA was encouraging because more structural information can be reserved than the other two approaches did. EEMD-ICA manifests a suitable tool for rejecting artifacts as many as possible while retaining sufficient structural information of noisy EEG data.

References

Bandt C, Pompe B. Permutation entropy: a natural complexity measure for time series. Phys Rev Lett. 2002;88(17).

Cai D, He XF, Han JW. SRDA: an efficient algorithm for large-scale discriminant analysis. IEEE Trans Knowl Data Eng. 2008;20(1):1–12.

Candy JV. Bayesian signal processing: classical, modern and particle filtering methods. New York: Wiley-Interscience; 2009.

Cassani R, Falk TH, Fraga FJ, Kanda PA, Anghinah Renato. The effects of automated artifact removal algorithms on electroencephalography – based Alzheimer's disease diagnosis. Front Aging Neurosci. 2014;6:55.

Castellanos NP, Makarov VA. Recovering EEG brain signals: artifact suppression with wavelet enhanced independent component analysis. J Neurosci Methods. 2006;158(2):300–12.

Chen D, Li D, Xiong MZ, Bao H, Li XL. GPGPU-aided ensemble empirical-mode decomposition for EEG analysis during anesthesia. IEEE Trans Inf Technol Biomed. 2010;14(6):1417–27.

Comon P, Jutten C. Handbook of blind source separation. London: Academic Press; 2010.

Daly I, Billinger M, Scherer R, Muller-Putz G. On the automated removal of artifacts related to head movement from the EEG. IEEE Transact Neural Syst Rehabil Eng. 2013;21(3):427–34.

Daubechies I, Lu JF, Wu HT. Synchrosqueezed wavelet transforms: an empirical mode decomposition-like tool. Appl Comput Harmon Anal. 2011;30(2):243–61.

De Clercq W, Vergult A, Vanrumste B, Van Paesschen W, Van Huffel S. Canonical correlation analysis applied to remove muscle artifacts from the electroencephalogram. IEEE Trans Biomed Eng. 2006;53(12 Pt 1):2583–7.

Delorme A, Sejnowski T, Makeig S. Enhanced detection of artifacts in EEG data using higher-order statistics and independent component analysis. Neuroimage. 2007;34(4):1443–9.

Diniz P. Adaptive filtering: algorithms and practical implementation. New York: Springer; 2008.

Eriksson J, Koivunen V. Identifiability, separability, and uniqueness of linear ICA models. IEEE Signal Process Lett. 2004;11(7):601–4.

Fatourechi M, Bashashati A, Ward RK, Birch GE. EMG and EOG artifacts in brain computer interface systems: a survey. Clin Neurophysiol. 2007;118(3):480–94.

Fox D, Hightower J, Liao L, Schulz D. Bayesian filtering for location estimation. IEEE Pervasive Comput. 2003;2(3):24–33.

Gratton G, Coles MG, Donchin E. A new method for off-line removal of ocular artifact. Electroencephalogr Clin Neurophysiol. 1983;55(4):468–84.

Hild KE, Erdogmus D, Principe JC. An analysis of entropy estimators for blind source separation. Signal Process. 2006;86(1):182–94.

Huang NE, Shen Z, Long SR, Wu MLC, Shih HH, Zheng QN, Yen NC, Tung CC, Liu HH. The empirical mode decomposition and the Hilbert spectrum for nonlinear and non-stationary time series analysis. Proc Roy Soc-Math Phys Eng Sci. 1998;454(1971):903–95.

Hyvärinen A. Fast and robust fixed-point algorithms for independent component analysis. IEEE Transact Neural Netw. 1999;10(3):626–34.

Hyvärinen A, Karhunen J, Oja E. Independent component analysis. New York: Wiley; 2001.

Ille N, Berg P, Scherg M. Artifact correction of the ongoing EEG using spatial filters based on artifact and brain signal topographies. J Clin Neurophysiol. 2002;19(2):113–24.

Izzetoglu M, Devaraj A, Bunce S, Onaral B. Motion artifact cancellation in NIR spectroscopy using Wiener filtering. IEEE Trans Biomed Eng. 2005;52(5):934–8.

James CJ, Gibson OJ. Temporally constrained ICA: an application to artifact rejection in electromagnetic brain signal analysis. IEEE Trans Biomed Eng. 2003;50:8.

Kelly JW, Siewiorek DP, Smailagic A, Collinger JL, Weber DJ, Wang W. Fully automated reduction of ocular artifacts in high-dimensional neural data. IEEE Trans Biomed Eng. 2011;58(3):598–606.

Killory BD, Bai X, Negishi M, Vega C, Spann MN, Vestal M, Guo J, Berman R, Danielson N, Trejo J, Shisler D, Novotny EJ, Constable RT, Blumenfeld H. Impaired attention and network connectivity in childhood absence epilepsy. Neuroimage. 2011;56(4):2209–17.

Kopsinis Y, McLaughlin S. Development of EMD-based denoising methods inspired by wavelet thresholding. IEEE Trans Signal Process. 2009;57(4):1351–62.

Krishnaveni V, Jayaraman S, Anitha L, Ramadoss K. Removal of ocular artifacts from EEG using adaptive thresholding of wavelet coefficients. J Neural Eng. 2006;3(4):338–46.

Li XL, Cui SY, Voss LJ. Using permutation entropy to measure the electroencephalographic effects of sevoflurane. Anesthesiology. 2008;109(3):448–56.

Mammone N, La Foresta F, Morabito FC. Automatic artifact rejection from multichannel scalp EEG by wavelet ICA. IEEE Sensors J. 2012;12(3):533–42.

Mijović B, Vos MD, Gligorijević I, Taelman J, Huffel SV. Source separation from single-channel recordings by combining empirical-mode decomposition and independent component analysis. IEEE Trans Biomed Eng. 2010;57(9):2188–96.

Morbidi F, Garulli A, Prattichizzo D, Rizzo C, Rossi S. Application of kalman filter to remove TMS-induced artifacts from EEG recordings. IEEE Trans Control Syst Technol. 2008;16(6):1360–6.

Ouyang GX, Li J, Liu XZ, Li XL. Dynamic characteristics of absence EEG recordings with multiscale permutation entropy analysis. Epilepsy Res. 2013;104(3):246–52.

Romero S, Mananas MA, Barbanoj MJ. A comparative study of automatic techniques for ocular artifact reduction in spontaneous EEG signals based on clinical target variables: a simulation case. Comput Biol Med. 2008;38(3):348–60.

Romero S, Mananas MA, Barbanoj MJ. Ocular reduction in EEG signals based on adaptive filtering, regression and blind source separation. Ann Biomed Eng. 2009;37(1):176–91.

Sweeney KT, McLoone SF, Ward TE. The use of ensemble empirical mode decomposition with canonical correlation analysis as a novel artifact removal technique. IEEE Trans Biomed Eng. 2013;60(1):97–105.

Wang Z, Bovik AC. Mean squared error: love It or leave It? a new look at signal fidelity measures. IEEE Signal Process Mag. 2009;26(1):98–117.

Wu ZH, Huang NE. Ensemble empirical mode decomposition: a noise-assisted data analysis method. Adv Adapt Data Anal. 2009;1(1):1–41.

Zeng K, Chen D, Ouyang G, Wang L, Liu X, Li X. An EEMD-ICA approach to enhancing artifact rejection for noisy multivariate neural data. IEEE Transact Neural Syst Rehabil Eng. 2014;24(6):630–8.

Zeng K, Yan J, Wang Y, Sik A, Ouyang G, Li X. Automatic detection of absence seizures with compressive sensing EEG. Neurocomputing. 2016;171:497–502.

Zhang ZL, Jung TP, Makeig S, Rao BD. Compressed sensing of EEG for wireless telemonitoring with Low energy consumption and inexpensive hardware. IEEE Trans Biomed Eng. 2013;60(1):221–4.

Chapter 6
Order Time Series Analysis of Neural Signals

Gaoxiang Ouyang and Xiaoli Li

6.1 Introduction

The electroencephalogram (EEG) signal is a measure of the summed activity of approximately 1–100 million neurons lying in the vicinity of the recording electrode and may provide insight into the functional structure and dynamics of the brain (Sleigh et al. 2004). Therefore, the exploration of hidden dynamical structures within neural signals is of both basic and clinical interests (Stacey and Litt 2008). Recently, an order time series analysis method was proposed by Bandt and Pompe (Bandt and Pompe 2002). This method measures the irregularity of non-stationary time series. The basic premise of this method is consideration of the order relations between the values of a time series and not the values themselves. The advantages of this method are its simplicity, robustness, and low complexity in computation [3–4] without further model assumptions. Also, the Bandt-Pompe method is robust in the presence of observational and dynamical noise (Bandt and Pompe 2002; Rosso et al. 2007). This method does show a fundamental distinction between deterministic chaos and noisy systems (Amigo et al. 2007). These advantages facilitate the use of methods based on the Bandt-Pompe algorithm for investigating the intrinsic ordinal structures in complex time series from physical systems (Bahraminasab et al. 2008) and physiological systems (Zanin et al. 2012). In this chapter, the order time series analysis is used to track transient dynamics of EEG recordings.

G. Ouyang (✉) • X. Li
State Key Laboratory of Cognitive Neuroscience and Learning & IDG/McGovern Institute for Brain Research, Beijing Normal University, Beijing 100875, China

Center for Collaboration and Innovation in Brain and Learning Sciences, Beijing Normal University, Beijing 100875, China
e-mail: ouyang@bnu.edu.cn; xiaoli@bnu.edu.cn

X. Li (eds.), *Signal Processing in Neuroscience*, DOI 10.1007/978-981-10-1822-0_6

6.2 Order Time Series Analysis

Order time series analysis is a new technique in evaluating the dynamic characteristics of a given time series (Bandt and Pompe 2002; Bandt 2005). Given a time series of length L, $\{x_1, x_2, \ldots, x_L\}$, a vector can be generated using an embedding procedure: $S_t = \left[x_t, x_{t+\tau}, \ldots, x_{t+(m-1)\tau}\right]$ where m and τ are the embedding dimension and the lag, respectively. This vector S_t can be rearranged in an ascending order, $\left[x_{t+(j_1-1)\tau} \leq x_{t+(j_2-1)\tau} \cdots \leq x_{t+(j_m-1)\tau}\right]$. To obtain a unique result, we set $j_{r-1} < j_r$ in the case of $x_{t+(j_{r-1}-1)\tau} = x_{t+(j_r-1)\tau}$. For m different numbers, there will be $m! = (1 \times 2 \times \cdots \times m)$ possible order patterns π_i, $i = m!$, also called permutations. For example, for $m = 3$, there are six order patterns between $x_t, x_{t+\tau}$ and $x_{t+2\tau}$, as shown in Fig. 6.1a, and the relation $x_{t+2\tau} < x_t < x_{t+\tau}$ corresponds to the order pattern $\pi_4 = 231$. Figure 6.1b illustrates the order patterns of a white noise time series (left) and the logistic map (right) [$x_{n+1} = 4x_n(1 - x_n)$ and $0 < x_0 < 1$], with $m = 3$ and $\tau = 1$. Then we can count the occurrences of the order pattern π_i, which is denoted as $C(\pi_i)$, and the relative frequency is calculated by $p(\pi_i) = C(\pi_i) / (L - (m-1)\tau)$, $i = 1, 2, \cdots m!$, as seen in Fig. 6.1c.

6.2.1 Permutation Entropy

The complexity of time series also can be quantified by using order time series analysis. A new permutation method was proposed by Bandt and Pompe (Bandt and Pompe 2002) to map a continuous time series onto an order pattern; the statistics of the order patterns is called permutation entropy. Based on Shannon's information theory, the permutation entropy is defined as

$$PE(m) = -\sum_{i=1}^{m!} p(\pi_i) \ln p(\pi_i) \tag{6.1}$$

The corresponding normalized permutation entropy is

$$NPE = PE(m) / \ln(m!) \tag{6.2}$$

The largest value of *NPE* is 1, meaning that the time series is completely random; the smallest value of *NPE* is 0, meaning that the time series is very regular. In short, the permutation entropy refers to the local order structure of the time series. More details can be found in (Bandt and Pompe 2002; Bandt 2005).

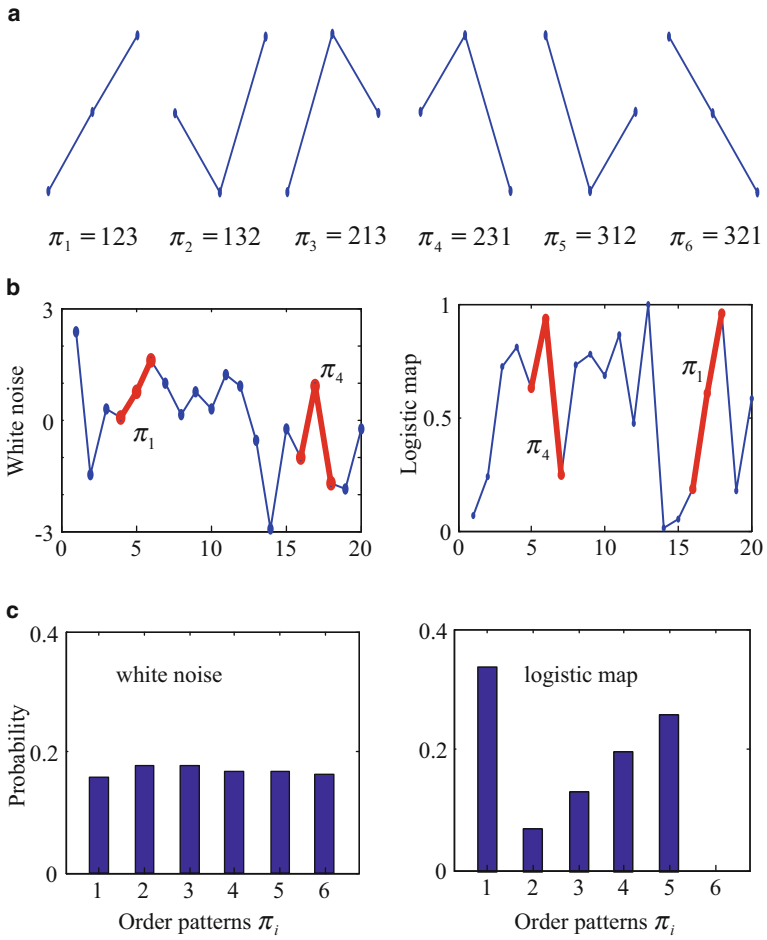

Fig. 6.1 Order patterns in simple time series. (**a**) The six order patterns of the dimension $m = 3$. (**b**) Illustration of the order procedure for $m = 3$ and $\tau = 1$ for white noise and logistic map time series. (**c**) Probability distribution of order pattern π_i

6.2.2 Forbidden Order Patterns

As shown in Fig. 6.1c, the distributions of order patterns of the white noise and logistic map time series are quite different. With regard to the white noise time series, all order patterns appear (i.e., no patterns are forbidden) because of the characteristics of random behavior, and the probability distribution of the order patterns is even (Ouyang et al. 2009). In contrast, with the logistic map time series, the pattern of $\pi_6 = 321$ disappears because of the characteristics of deterministic behavior, called the *forbidden order pattern* (Amigo et al. 2007). Furthermore, if

an order pattern of dimension m is "forbidden," its absence pervades all longer dimensions of m in the form of more missing order patterns (Amigo et al. 2008).

Most chaotic systems exhibit FOP, and in many cases, the measure of the number of these patterns is related to other classic metric entropy rates (e.g., Lyapunov exponent) (Amigo et al. 2007). In other words, the existence of FOP should be a hallmark of deterministic orbit generation, and it can be used to distinguish deterministic from random systems (Amigo et al. 2008). However, when FOP analysis is applied to real-time series, the finiteness of sequences will produce *false FOP* (i.e., order patterns missing in a random sequence without constraints). Thus, the application of this method requires some attention since real-time series are *finite* (making it possible that random sequences have "false" FOP with finite probability) and *noisy* (blurring the difference between determinism and randomness) (Amigo and Kennel 2008). To this end, a sufficiently long series is required to avoid producing false forbidden patterns. Given the embedding dimension m and the lag τ and a time series of length L, the number of possible order patterns is $m!$, while the number of groups of data is $L-(m-1)\tau$. To ensure that all possible order patterns of dimension m occur in a time series of length L, the condition $L-(m-1)\tau \geq m!$ must be satisfied (Amigo et al. 2007). For this reason, given a dimension of length m, we need to choose $L \geq (m+1)!$.

6.2.3 Dissimilarity Index

As shown in Fig. 6.1c, the distributions of the ordinal patterns of the white noise and logistic map time series are quite different. With the white noise time series, the characteristics of random processes, the probability distribution should be even since any ordinal pattern has the same probability of occurrence when the time series is long enough to exclude statistical fluctuations. However, when the series corresponds to a deterministic process, as in the example of the logistic map, there are some patterns that will be encountered frequently in the time series due to the underlying deterministic structure. Therefore, we can quantify the distance between the frequency distributions to measure dissimilarity between two time series. In this study, we evaluate the distance using the Wootters statistical distance. We defined the normalized Wootters distance between two time series X and Y by

$$D_m(x,y) = \frac{2}{\pi}\cos^{(-1)}\left[\sum_{i=1}^{m!}\left(p_x(\pi_i)\cdot p_y(\pi_i)\right)^{(1/2)}\right] \tag{6.3}$$

where $p_x(\pi_i)$ and $p_y(\pi_i)$ represent the frequency distributions of the time series x and y, respectively. This measure ranges from 0 to 1 ($0 \leq D_m \leq 1$) (Ouyang and Li 2010). When $D_m = 0$, it indicates that the order pattern distribution in the two series is identical. In contrast, $D_m = 1$ indicates that one of the two series is totally different.

6.3 Applications

Absence seizures are a form of generalized seizure accompanied by spike-and-wave complexes in the electroencephalogram (EEG). People with absence epilepsy have repeated seizures that cause momentary lapses of consciousness. These sudden and abrupt seizures most commonly occur in childhood or adolescence and may have a significant impact on the educational development of patients. The prediction of absence seizures using detectable dynamic changes in the EEG is still debated (Suffczynski et al. 2006). In this chapter, the order time series analysis is used to track transient dynamics of EEG recordings. The aim of this study is to confirm whether or not the pre-seizure state in absence epilepsy can be detected.

To investigate the predictability of absence seizures, 110 30-s EEG signals of GAERS were selected from 18 GAERS, each with a concluding 10-s absence seizure EEG segment. Seizure onset was determined manually by an experienced experimental scientist by observing abrupt increases in EEG amplitude coupled with simultaneous behavioral immobility, twitching of the vibrissae and facial muscles, and diminished muscle tone in the neck (Danober et al. 1998). Experiments were performed in 18 male Genetic Absence Epilepsy Rats from Strasbourg (GAERS) of at least 13 weeks of age. At this stage of development, all GAERS display the characteristic repeated spike-wave discharges (SWD) on the EEG during absence seizures. All procedures were performed under a British Home Office project license [UK Animals (Scientific Procedures) Act, 1986] at the University of Birmingham by Dr. Douglas Richards. GAERS were anesthetized with medetomidine/ketamine (0.5 and 75 mg/kg i.p., respectively) for the duration of the surgery, with immediate postoperative reversal of the effects of medetomidine with atipamezole (1 mg/kg s.c.). In all animals, a bipolar twisted-wire EEG electrode (MS303/1; Semat Technical, St. Albans, UK) was implanted in the frontal cortex (mm, relative to bregma; AP, 2.2: L, 2.4: V, 2.6 from the dura mater). The headmounts were secured to 2 skull screws with dental cement (Duralay II), and the animals were allowed to recover overnight with free access to water and rat diet. The following day, after connection of a cable to the EEG electrode, the animal was transferred to an EEG recording cage and left to acclimatize to this environment for at least 45 min. The signal from the EEG electrode was visualized directly on an oscilloscope and was further amplified (BioAmp ML 136), filtered, digitized (100 Hz), and stored using a PowerLab 2/20 running Chart v4.2 software (AD Instruments, Hastings, UK). Once the regular SWD were being observed, 30 min of EEG was recorded from each animal. The EEG data sets were preprocessed by a band-pass filter at 0.5–22 Hz.

6.3.1 Results of EEG Data

To investigate the dynamical order patterns in EEG series during different stages of an absence seizure, a moving window technique (window length of 1.4 s) is applied

to investigate the order patterns in EEG segments. The criterion for overlapped windows is that the time distance between two consecutive windows is 0.1 s (10 samples). For the analysis of absence seizures, only the lower dimension $m = 4$ is selected during the order pattern analysis. This is because the dimension m must satisfy the condition of $(m + 1)! < L$. Figure 6.2a shows an EEG series including one absence seizure. At time $t = 20$ s, an absence seizure occurred. The relative frequency $p(\pi_i)$ of order patterns in each EEG segment for dimension $m = 4$ is shown in Fig. 6.2b. Different relative frequency distributions of EEG segments during different seizure states can be seen. In particular, during the seizure state, the repeated SWD is characteristic of absence epilepsy, so some order patterns of EEG segments obviously are increasing from the seizure-free state to the seizure state. Therefore, the number of FOPs in the EEG segments increases markedly from the seizure-free state to the seizure state, as shown in Fig. 6.2c. Then, to investigate the number of FOPs in EEG series during different seizure states, EEG series are dissected from the seizure-free state (from 10 to 20 s prior to seizure onset), the pre-seizure state (from 0 to 10 s prior to seizure onset), and the seizure state (the first 10 s of the absence seizure itself). Thus, 3×10 s EEG epochs are obtained for each of the 110 seizures. Previous studies have shown that the duration of the pre-seizure state is only around a few seconds as determined by using synchronization measures (Aarabi et al. 2008).

To compare the number of FOPs in EEG epochs during different states, we calculated the average number of FOPs $< n(m, L) >$ for $(m + 1)! \leq L \leq 1000$ in the seizure-free, pre-seizure, and seizure EEG epochs, respectively, as shown in Fig. 6.3. The results show that the number of FOPs within seizure EEG epochs is much higher than that in seizure-free EEG epochs. The average number of FOPs with different moving window lengths, L, gradually increases from the seizure-free to seizure states for dimensions $m = 4$. It can be seen that a high number of FOPs in the EEG series during the seizure state are found, indicating that the determinism of the EEG recordings is significant during absence seizures. The results also show that EEG epochs during pre-seizure intervals exhibit a higher degree of determinism than those during seizure-free EEG epochs but a lower degree than those during seizure EEG epochs in absence epilepsy. These findings support the notion that the underlying dynamics of EEG series in absence epilepsy is related to their increased determinism (regularity) arising from the synchronous discharge of large numbers of neurons (Meeren et al. 2002; Polack et al. 2007).

6.3.2 Detection of Pre-Seizure EEG Changes

Next, to investigate the predictability of absence seizures with order time series analysis, the order time series analysis is applied to detect the pre-seizure state. Figure 6.4 shows the predictability analysis of an absence seizure using the dissimilarity index and permutation entropy. The EEG recording of 30 s is first divided into epochs of 1.4 s with an overlap of 1.3 s; the first 10-s EEG epoch

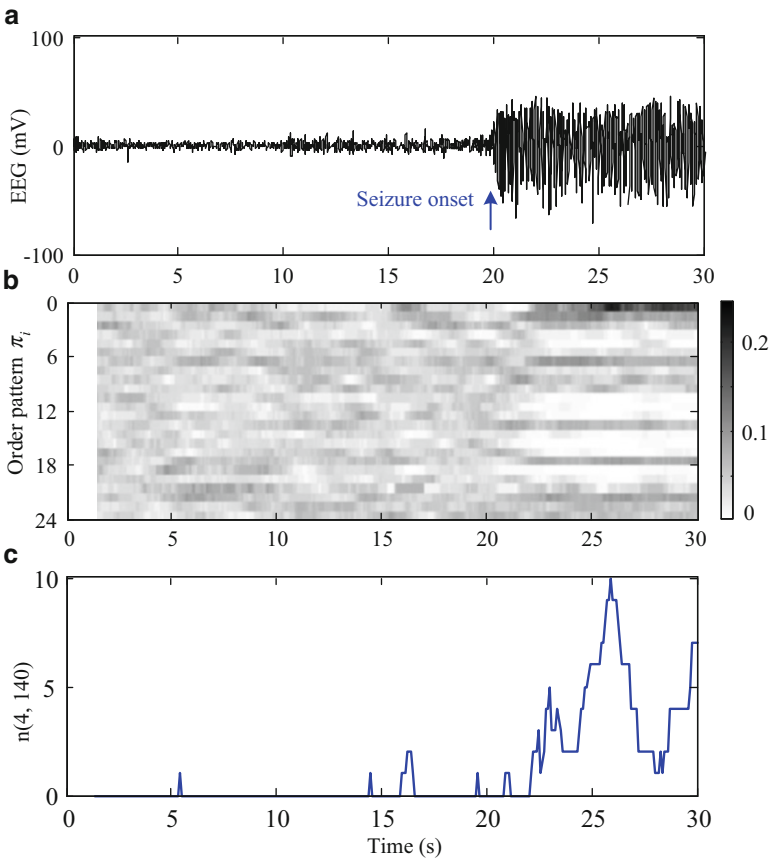

Fig. 6.2 The prediction analysis of absence seizures from EEG series. (**a**) The continuous EEG series with two seizures. (**b**) The relative frequency $p(\pi_i)$ of order patterns have been obtained using a moving window technique and are shown in a color scale, indicating the actual value from the smallest in white to the largest in black. (**c**) The time profile of the number of FOPs in each EEG segment

is selected as the reference window; and the original EEG recording is shown in Fig. 6.4a. At the end of the EEG recording, an absence seizure occurs. The dissimilarity D_m ($m = 4$ and $\tau = 2$) between the EEG windows and the reference window is then calculated, as shown in Fig. 6.4b, and threshold and anticipation time are plotted as well. It can be seen that the dissimilarity D_m gradually increases until the seizure occurs, which may indicate the underlying dynamics of the EEG series in absence epilepsy changing from random to deterministic prior to the occurrence of the absence seizure.

Then, the permutation entropy ($m = 4$ and $\tau = 2$) of each EEG epoch also is calculated, as shown in Fig. 6.4b, and a threshold and anticipation time are plotted as well. The results show that the values of permutation entropy are at a higher

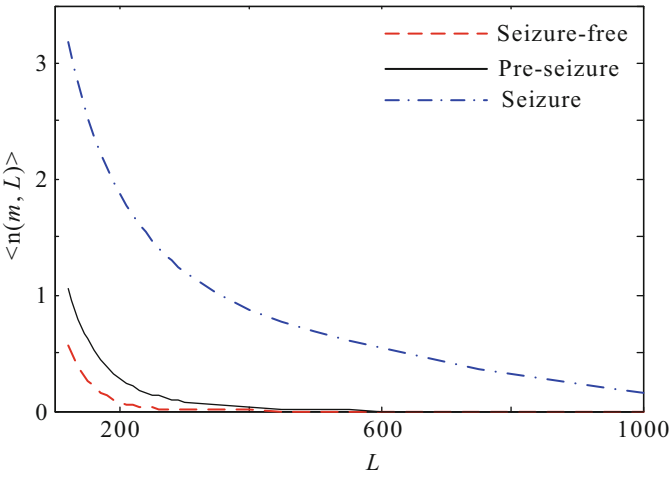

Fig. 6.3 Average number of FOPs of dimension m found in EEG epochs of length L, $< n\,(m, L) >$, for seizure-free data (*dashed line*), pre-seizure data (*solid line*), and seizure data (*dot-dashed line*), which gradually increases from the seizure-free to the seizure state for dimensions $m = 4$

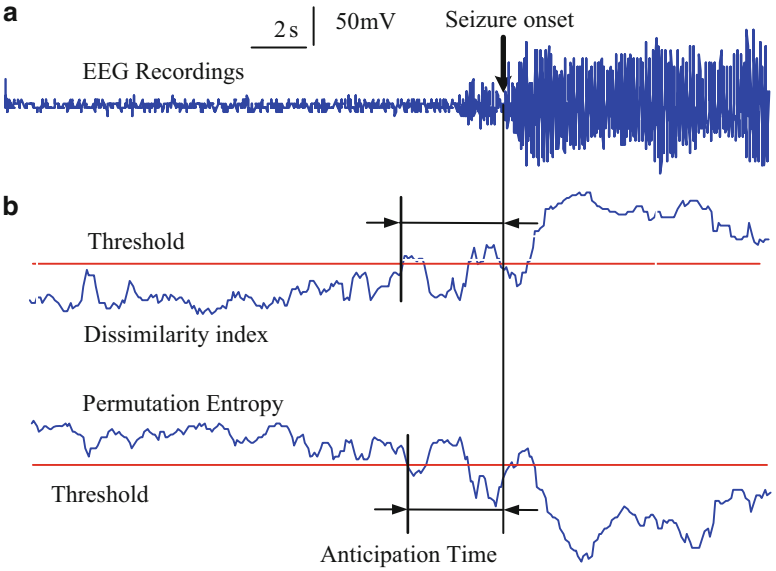

Fig. 6.4 The prediction analysis of absence seizure by using EEG recordings. (**a**) Original EEG recordings with a seizure. (**b**) The dissimilarity index and permutation entropy profiles. The threshold value $(\mu \pm k\sigma)k = 4$ of the dissimilarity index and permutation entropy are 0.2358 and 0.9222, respectively. The anticipation time of the dissimilarity index and permutation entropy is 4.1 s and 3.9 s, respectively

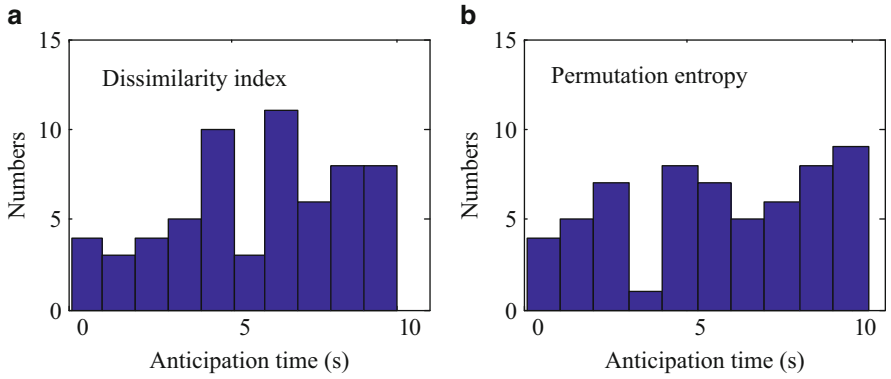

Fig. 6.5 The histogram of anticipation time for dissimilarity index (**a**) and permutation entropy (**b**), respectively. The max and min anticipation time is 10.0 s and 0.1 s for the dissimilarity index and 10.5 s and 0.1 s for permutation entropy, respectively

level during the normal state in comparison with the seizure state; permutation entropy begins to gradually decrease prior to the seizure, which may indicate the dynamical complexity of neural activity of the network changing from complex to simple (synchronization) prior to the occurrence of the epileptic seizure. It also can be seen that the dissimilarity index and permutation entropy are essentially flat during the reference window. In brief, order time series analysis, the dissimilarity index, and permutation entropy can successfully track the dynamical changes from normal to absence seizure.

The method described above is applied to analyze all of the seizures (110). The anticipation time is used to indicate the pre-seizure state. Once a positive anticipation time is obtained, this means that the absence seizure can be predicted. The distribution of anticipation time is shown in Fig. 6.5. An analysis of the entire EEG dataset found that the dissimilarity index successfully detected the pre-seizure state prior to the seizure in 62 of 110 seizures (56.4 %) and permutation entropy successfully detected the pre-seizure state prior to the seizure in 60 of 110 seizures (54.5 %). The mean anticipation times for the dissimilarity index and permutation entropy are 5.8 s and 5.9 s, respectively. These results show that the dissimilarity index is very similar to the permutation entropy for detecting pre-seizure EEG changes and the order time series analysis methods. Furthermore, the case study described above shows that the dissimilarity index and permutation entropy of a single-channel EEG of 1.4 s can be calculated in less than 2 ms using MATLAB (Math Works Inc.) on a 1.6 GHz personal computer. Therefore, the order pattern analysis calculation has a high computational efficacy and could be applied to clinical, real-time, online monitoring of absence seizures.

6.4 Conclusions

In this chapter, order time series analysis methods are used to track the transient dynamics of EEG recordings during the different absence seizure states in genetic absence epileptic rats. The results show that the number of FOPs in pre-seizure EEG epochs is higher than that in seizure-free EEG epochs but lower than that in seizure EEG epochs. A possible reason for this is that the epileptic process induces or enhances nonlinear, deterministic structures in an otherwise linear stochastic appearance of the EEG. Furthermore, we investigate order time series analysis as a tool to detect the pre-seizure state by using EEG recordings. The results show that order time series analysis can track the dynamical changes of EEG data so as to describe transient dynamics prior to the absence seizures. Experiments demonstrated that the dissimilarity index and permutation entropy successfully detected the pre-seizure state in 62 and 60 of 110 seizures, respectively. Another important advantage of the order time series analysis in detecting pre-seizures is the very simple algorithm and resulting faster computation. An important next goal will be to confirm the results presented here in a large clinical cohort of absence epilepsy patients.

References

Aarabi A, Walloisb F, Grebe R. Does spatiotemporal synchronization of EEG change prior to absence seizures? Brain Res. 2008;1188:207–21.

Amigo J, Kennel M. Forbidden ordinal patterns in higher dimensional dynamics. Phys D. 2008;237:2893–9.

Amigo J, Zambrano S, Sanjuan M. True and false forbidden patterns in deterministic and random dynamics. Europhys Lett. 2007;79:50001.

Amigo J, Elizalde S, Kennel M. Forbidden patterns and shift systems. J Comb Theory Ser A. 2008;115:485–504.

Bahraminasab A, Ghasemi F, Stefanovska A, McClintock P, Kantz H. Direction of coupling from phases of interacting oscillators: a permutation information approach. Phys Rev Lett. 2008;100:084101.

Bandt C. Ordinal time series analysis. Ecol Model. 2005;182:229–38.

Bandt C, Pompe B. Permutation entropy: a natural complexity measure for time series. Phys Rev Lett. 2002;88:174102.

Danober L, Deransart C, Depaulis A, et al. Pathophysiological mechanisms of genetic absence epilepsy in the rat. Prog Neurobiol. 1998;55:27–57.

Meeren H, Pijn J, Van Luijtelaar E, Coenen A, Lopes da Silva F. Cortical focus drives widespread corticothalamic networks during spontaneous absence seizures in rats. J Neurosci. 2002;22:1480–95.

Ouyang G, Li X. Ordinal pattern based similarity analysis for EEG recordings. Clin Neurophysiol. 2010;121:694–703.

Ouyang G, Li X, Dang C. Deterministic dynamics of neural activity during absence seizures in rats. Phys Rev E. 2009;79:041146.

Polack P, Guillemain I, Hu E, Deransart C, Depaulis A, Charpier S. Deep layer somatosensory cortical neurons initiate spike-and-wave discharges in a genetic model of absence seizures. J Neurosci. 2007;27:6590–9.

Rosso OA, Larrondo HA, Martin MT, Plastino A, Fuentes MA. Distinguishing noise from chaos. Phys Rev Lett. 2007;99:154102.

Sleigh JW, Steyn-Ross DA, Steyn-Ross ML, Grant C, Ludbrook G. Cortical entropy changes with general anaesthesia: theory and experiment. Physiol Meas. 2004;25:921–34.

Stacey W, Litt B. Technology insight: neuroengineering and epilepsy-designing devices for seizure control. Nat Clin Pract Neurol. 2008;4:190–201.

Suffczynski P, Lopes da Silva F, Parra J, Velis D, Bouwman B, van Rijn C, van Hese P, Boon P, Khosravani H, Derchansky M, Carlen P, Kalitzin S. Dynamics of epileptic phenomena determined from statistics of ictal transitions. IEEE Trans Biomed Eng. 2006;53(3):524–32.

Zanin M, Zunino L, Rosso OA, Papo D. Permutation entropy and its main biomedical and econophysics applications: a review. Entropy. 2012;14:1553–77.

Chapter 7
Dynamical Similarity Analysis of EEG Recordings

Gaoxiang Ouyang and Xiaoli Li

7.1 Introduction

EEG monitoring systems have become important clinical tools for the evaluation and treatment of epilepsy. The EEG is a measure of the summed activity of approximately 1–100 million neurons lying in the vicinity of the recording electrode (Buzsaki 2006) and may provide insight into the functional structure and dynamics of the brain (Stam 2005). Therefore, the exploration of hidden dynamical structures within EEG signals is of both basic and clinical interest (Stacey and Litt 2008). Recently, various methods have been used to analyse the temporal evolution of brain activity from EEG recordings (Stam 2005). They range from traditional linear methods such as Fourier transforms and spectral analysis (Rogowski et al. 1981) to nonlinear methods derived from the theory of nonlinear dynamical systems (also called chaos theory) such as Lyapunov exponents (Wolf et al. 1985) and correlation dimension (Rapp et al. 1985). To some extent, these chaos-based approaches are capable of extracting informative features from epilepsy EEG data (Lehnertz and Elger 1998), sleep EEG data (Ferri et al. 2003), and anaesthesia EEG data (Widman et al. 2000), and moreover, these chaos-based approaches are superior to the traditional linear methods (Rabinovich et al. 2006). However, chaos-based approaches assume that the signal is stationary and originates from a low-dimensional nonlinear system. In reality, a real EEG is a nonstationary signal and stems from a highly nonlinear system (Gribkov and Gribkova 2000). Therefore,

G. Ouyang (✉) • X. Li
State Key Laboratory of Cognitive Neuroscience and Learning & IDG/McGovern Institute for Brain Research, Beijing Normal University, Beijing 100875, China

Center for Collaboration and Innovation in Brain and Learning Sciences, Beijing Normal University, Beijing 100875, China
e-mail: ouyang@bnu.edu.cn; xiaoli@bnu.edu.cn

X. Li (eds.), *Signal Processing in Neuroscience*, DOI 10.1007/978-981-10-1822-0_7

chaos-based approaches must be used with care and caution in analysing EEG data (Eckmann and Ruelle 1992). It is thus important to develop new methods to characterize EEG changes in different physiological and pathological states (Eckmann and Ruelle 1992).

Recently, a dynamical similarity index (DSI) method was proposed by Baulac et al. (Le Van Quyen et al. 1999; Navarro et al. 2002). This method is composed of the phase space reconstruction of EEG dynamics and the measurement of dynamical similarity between a reference window and a test window (a segment of EEG recordings). The key issues of this method, aside from the reconstruction of phase space, are to determine a radius value, which is applied for the normalized cross-correlation integral to calculate the dynamical similarity index (Schreiber and Schmitz 1997), and the length of the windowed EEG recordings. It has been found that the dynamical similarity index rises or falls dramatically when the radius of hypersphere or the length of the EEG window is changed slightly. This is due to the fact that the data just outside the hypersphere (greater than the radius value) are not accounted and data in the hypersphere (less than the radius values) are treated equally because of the hard or binary boundary of the Heaviside function. To overcome these problems, a new dynamical similarity index is proposed in this chapter (Li et al. 2004). A Gaussian function is employed to replace the Heaviside function in the dynamical similarity; as a result, the hard boundary of Heaviside function becomes soft, so the closer the data points are, the more similar they are. This similarity measure is then used to investigate the dynamic characteristics of epileptic EEG data.

7.2 Dynamical Similarity Analysis

7.2.1 Phase Space Reconstruction

The first step in the analysis of a signal using nonlinear dynamics theory is the reconstruction of the phase space trajectory of the signal. The idea of using time-delay coordinates to reconstruct the trajectory in the phase space was proposed in Packard et al. (1980). Later, Takens proved a theorem that is the firm basis of the methods of delay (Takens 1981). The methods of delay usually are used to embed a scalar time series $u_1, u_2, \ldots, u_L$ into an m-dimensional space (Packard et al. 1980; Takens 1981):

$$\vec{x}_k = \left(u_k, u_{k+\tau}, \ldots, u_{k+(m-1)\tau}\right), \tag{7.1}$$

where $k = 1, 2, \ldots, L - (m-1)\tau$, τ is the delay time, and m is the embedding dimension, $m \geq 2$. The difficulty of this method is the choices of the delay time, τ, and the minimum embedding dimension, m.

Takens' theorem assumes that the data is infinite and noise-free, in which case the delay time, τ, can be chosen almost arbitrarily. However, real data sets are always

finite and noisy; the choice of the delay time must therefore be considered carefully. If τ is too small, the reconstructed attractor is compressed along the identity line and this is called *redundancy*; if τ is too large, the attractor dynamics may become disconnected causally, and this is called *irrelevance* (Kim et al. 1999). The most common method for choosing a proper time delay is based on detection of the first local minimum of the mutual information (*MI*) function (Fraser and Swinney 1986), since the first minimum of the $MI(\tau)$ portrays the time delay where the signal $u_{t+\tau}$ adds maximal information to the knowledge we have from u_t (Fraser and Swinney 1986).

As for the choice of the embedding dimension, if m is too small, the geometry is not unfolded entirely; if m is too large, it leads to excessive computations and enhances the problem of contamination by rounding or instrumental error. As shown in Grassberger et al. (1991), the dimensionality of various parts of nonstationary signals may be different from each other. On the other hand, as indicated in Ding et al. (1993), noise will tend to increase the required dimension. Hence, it is important to choose a sufficiently large embedding dimension that contains the relevant dynamics in the presence of noise. In this study, the mutual information method (Fraser and Swinney 1986) and Cao's method (Cao 1997) are employed to estimate the delay time and the embedding dimension.

7.2.2 Correlation Sum

In nonlinear dynamical analysis, the correlation sum is the estimator of the correlation integral (Grassberger and Procaccia 1983), which reflects the local probability density in state space. It counts the number of pairs of vectors in state space that are closer than a given hypersphere radius r:

$$C(r) = \frac{1}{N^2} \sum_{i=1}^{N} \sum_{j=1}^{N} \Theta\left(r - \left\|\vec{x}_i - \vec{x}_j\right\|\right) \tag{7.2}$$

where N is the number of considered states $\vec{x}_i$, r is a predefined cutoff distance, $\|\cdot\|$ is the norm (e.g. the Euclidean norm), and $\Theta(\cdot)$ is a Heaviside function ($\Theta(x) = 1$ for $x > 0$ and $\Theta(x) = 0$ for $x \leq 0$).

7.2.3 Nonlinear Similarity Index

The dynamical similarity index, proposed by Le Van Quyen et al. (1999), was designed to measure the dynamical similarity between the two attractors X and Y. The computation procedure for the dynamical similarity index is as follows:

1. Given two time series $x_1, x_2, \ldots, x_n$ and $y_1, y_2, \ldots, y_l$, the time-delay vectors $\vec{x}$ and $\vec{y}$ first are reconstructed with embedding dimension m and the delay time τ.
2. The correlation sum of state space x and y, respectively, is calculated:

$$\begin{aligned} C(x,x) &= \frac{1}{N_x{}^2}\sum_{i=1}^{N_x}\sum_{j=1}^{N_x}\Theta\left(r - \left\|\vec{x}_i - \vec{x}_j\right\|\right) \\ C(y,y) &= \frac{1}{N_y{}^2}\sum_{i=1}^{N_y}\sum_{j=1}^{N_y}\Theta\left(r - \left\|\vec{y}_i - \vec{y}_j\right\|\right) \end{aligned} \tag{7.3}$$

   where $\|\cdot\|$ denotes the Euclidian norm, Θ the Heaviside step function, and N_x and N_y the number of vectors in the state space of the time series x and y, respectively.
3. Then, the cross-correlation sum between x and y is calculated (Schreiber and Schmitz 1997):

$$C(x,y) = \frac{1}{N_x N_y}\sum_{i=1}^{N_x}\sum_{j=1}^{N_y}\Theta\left(r - \left\|\vec{x}_i - \vec{y}_j\right\|\right) \tag{7.4}$$

   where $\|\cdot\|$ denotes the Euclidian norm, Θ the Heaviside step function, and N_x and N_y the number of vectors in the state space of the time series x and y, respectively.
4. To further improve the discriminatory power between two dynamics, the autocorrelation sum $C(x, x)$ and $C(y, y)$ are used; the dynamical similarity index (*DSI*) is written as:

$$DSI = C(x,y) \,/\, \sqrt{C(x,x)\, C(y,y)} \tag{7.5}$$

   where *DSI* ranges from 0 to 1 and provides a sensitive measure of the closeness between two dynamics.

If the time series x and y have the same underlying dynamics, the value of *DSI* is around one; otherwise, it goes down to zero. The details of the dynamical similarity index computation can be found in Le Van Quyen et al. (1999). In calculating the dynamical similarity index, a Heaviside function is used to calculate the correlation integral in Eq. (7.2). This function leads to the following two problems (Sarkara and Leong 2003):

1. The rigid boundary of the Heaviside function results in the absence of some information. For instance, when the data point is just outside the boundary, i.e. the Euclidian distance $\|\cdot\|$ is just greater than the radius value r, this data point is considered to be outside the box.

2. The contributions of all of the data points inside the hypersphere, i.e. the Euclidian distances less than the radius value r, are treated equally.

These two problems make the calculation of the dynamical similarity index brittle and the choice of the radius value difficult. The similarity index varies dramatically with a slight change of the data point position and the length of time series or with a slight change of the radius value. These problems can be avoided if the Heaviside function in Eq. (7.2) is replaced by a Gaussian function; this is because the Gaussian function is a *soft* boundary in calculating the correlation sum; all of the data points are members of the Gaussian function. Any members can be distinguished based on the distance between the points and the centre of the Gaussian function. If the radius of the Gaussian function is changed, the contribution of each point changes gracefully rather than abruptly as in the case of the crisp boundary of the Heaviside function.

The new dynamical similarity index calculation is composed of two main steps. The first step is to construct reference dynamics from the time series. The second step is to compute the similarity index between the time series based on a Gaussian function with a radius r. Instead of the Heaviside function in Eq. (7.4), it can be written as:

$$C_G(x, y) = \frac{1}{N_x N_y} \sum_{i=1}^{N_x} \sum_{j=1}^{N_y} \exp\left(-\left\|\vec{x}_i - \vec{y}_j\right\|^2 / r^2\right). \tag{7.6}$$

The function $C_G(x, y)$ measures the average similarity between any data points of the test window and all of its neighbours. The new similarity index (NSI) also is defined as:

$$NSI = C_G(x, y) / \sqrt{C_G(x, x)\, C_G(y, y)} \tag{7.7}$$

where *NSI* ranges from 0 to 1 and provides a sensitive measure of the closeness between the two windows. The new similarity *NSI* possesses the characteristics of *DSI* in Eq. (7.5) as well.

7.3 Simulation Analysis and Results

7.3.1 Neural Mass Model

A neural mass model known as the nonlinear lumped-parameter cerebral cortex (LPCC) model (Lopes da Silva et al. 1974; Jansen and Rit 1995; Wendling et al. 2000) is used to test the performance of this new method in this study. The following set of six differential equations governs the model:

Table 7.1 Physiological interpretation and standard values of model parameters (Adapted from Jansen and Rit 1995)

Parameter	Interpretation	Standard value
A	Average excitatory synaptic gain	3.25 mV
B	Average slow inhibitory synaptic gain	22 mV
a	Dendritic average time constant in the feedback excitatory loop	$a = 100\ s^{-1}$
b	Dendritic average time constant in the slow feedback inhibitory loop	$b = 50\ s^{-1}$
C1, C2	Average number of synaptic contacts in the excitatory feedback loop	C1 = C, C2 = 0.8 C (with C = 135)
C3, C4	Average number of synaptic contacts in the slow feedback inhibitory loop	C3 = C4 = 0.25 C

$$\begin{cases} \dot{y}_0(t) = \dot{y}_3(t), \\ \dot{y}_3(t) = AaS\,(y_1 - y_2) - 2ay_3(t) - a^2 y_0(t), \\ \dot{y}_1(t) = \dot{y}_4(t), \\ \dot{y}_4(t) = Aa\,\{p(t) + C_2 S\,[C_1 y_0(t)]\} - 2ay_4(t) - a^2 y_1(t), \\ \dot{y}_2(t) = \dot{y}_5(t), \\ \dot{y}_5(t) = Bb\,\{C_4 S\,[C_3 y_0(t)]\} - 2by_5(t) - b^2 y_2(t). \end{cases} \tag{7.8}$$

All of the values of the parameters in the model are set based on a physiological basis, as listed in Table 7.1, more details of which can be found in Jansen and Rit (1995) and Wendling et al. (2000). In the model, the intrapopulation behaviour is influenced primarily by the excitatory neuron parameter, A, and the inhibitory neuron parameter, B. The parameters A and B modulate the balance of excitation and inhibition ($h_e(t) = u(t)Aate^{-at}$ and $h_i(t) = u(t)Bbte^{-bt}$). By altering the excitatory and inhibitory parameters, the model can produce signals that strongly resemble intracranial EEG recordings (Wendling et al. 2000).

In this study, the extrinsic input $p(t)$ represents Gaussian white noise with assigned mean value and variance (mean $(p) = 90$, std$(p) = 30$), which describes the overall density of action potentials coming from other regions. For each simulation described below, the differential equations are solved numerically using a fourth- and fifth-order Runge–Kutta algorithm. Initial conditions are set to zero in all simulations, and an integration step size of 5 ms is used.

7.3.2 Similarity Analysis of Simulated EEG Data

The determination of radius r is a difficult issue within this new method as well as the dynamical similarity index. There is no well-founded criterion to choose the radius (Thiel et al. 2002). Generally speaking, too small a value of r results in a low similarity index in spite of the same underlying dynamics of the time series. On the

contrary, too large a value results in a high similarity index when the time series share the same or different underlying dynamics. The effect of the radius value, r, on the similarity method is discussed here. In the example shown in Fig. 7.1a, the excitatory and inhibitory parameters in the model are set as $A = 3.25$ and $B = 22$, for which the model produces a signal similar to normal background activity when other parameters are set to standard values (Wendling et al. 2000). We discarded the first 2000 iterated times as transient and obtained the next 4000 data points (20 s) for experiments. The similarity index ($m = 5$, $\tau = 2$) is calculated between the first 2000 points and last 2000 points from simulated EEG data over a series of r, as shown in Fig. 7.1b (log–log plot). The values of r are set to the order of magnitude of the standard deviation (σ) of the time series, which ranged from 0.2σ to 2σ. Given the r values, the similarity indexes *DSI* and *NSI* have a progressive increase from 0.45 to 1 and from 0.61 to 1. Their mean and deviation is 0.88 ± 0.16 and 0.92 ± 0.10, respectively. As shown in Fig. 7.1b, compared with the dynamical similarity index *DSI*, the new similarity index *NSI* is not more sensitive to the selected values r. In

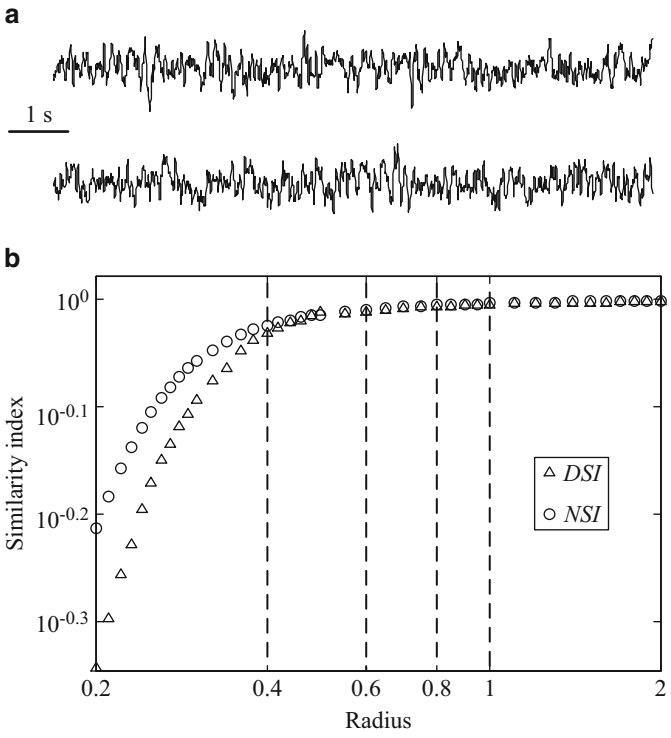

Fig. 7.1 Log–log plot of similarity *DSI* and *NSI* vs. radius. When the radius r increased from 0.2σ to 2σ, the similarity indexes *DSI* and *NSI* have a progressive increase from 0.45 to 1 and from 0.61 to 1, respectively

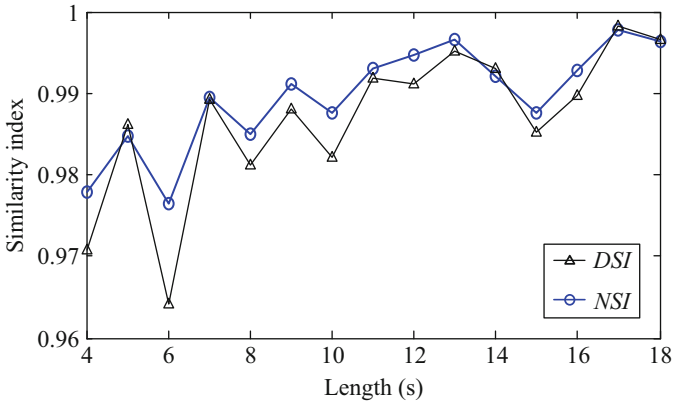

Fig. 7.2 The effect of length of EEG segment on the similarity index

this study, the radius r is determined by the 1σ of the time series, giving a stable similarity index with simulated EEG segments of several seconds' duration.

The similarity index also varies with the length of the EEG segment. We investigated the sensitivity of the similarity indexes *DSI* and *NSI* on the length of the EEG segment. For each simulation, we discarded the first 2000 iterated times as transient and obtained the next $2N$ data points for experiments. The similarity index ($m = 5$, $\tau = 2$, $r = 1$) is calculated between the first N points and last N points from simulated EEG data over a series of N, as shown in Fig. 7.2. It has been found that the fluctuation of *DSI* is more significant than that of the *NSI*; their mean and deviation is 0.987 ± 0.009 and 0.990 ± 0.006, respectively. The deviation of *DSI* is higher than that of *NSI*. Thus, the new similarity index *NSI* is less sensitive to the length of the EEG segment.

In the next experiment, the excitatory parameter, A, in the model is gradually increased from 3.25 to 3.8 (Fig. 7.3a), as a result of which the model produces signals that are similar to epileptic activity when parameter A approaches 3.8 (Fig. 7.3b). The simulated EEG signals are sampled at 200 Hz and then the dissimilarity measure is applied to the long-term EEG signals using a moving-window technique. The criterion of windows overlapped such that the time distance between two consecutive windows is 1 s (200 data points). In this test, the first recording of 10 s is selected as the reference. The similarity index between EEG windows and the reference segment is determined for the moving window of a length of 2000 points with an overlap of 1800 points on dimension $m = 4$, delay $\tau = 2$, and radius $r = 1$. Prior to 50 s, with the excitatory parameter $A = 3.25$, both EEG windows and the reference segment are similar to the background activity with the same underlying dynamics. Therefore, as shown in Fig. 7.3c, the value of the similarity index, both *DSI* and *NSI*, is close to 1. However, the similarity index started to increase with the gradual increase of the excitatory parameter, A. After 250 s, the brain activity is interrupted by regular 3-s spikes; the neural mass model

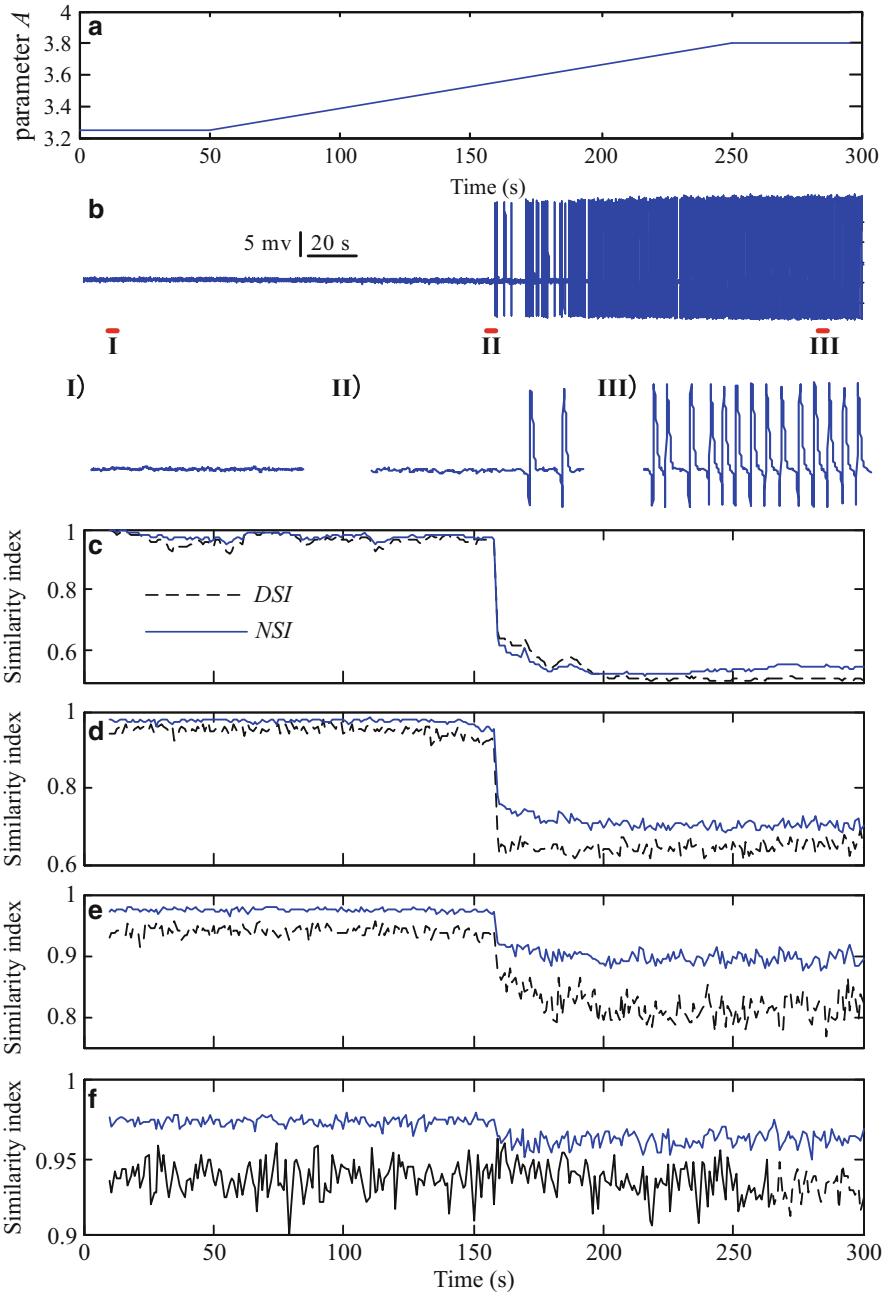

Fig. 7.3 Simulation analysis using a neural mass model. (**a**) The excitatory parameter A of the model. (**b**) The long-term EEG signals (*top*) and examples of zoomed EEG signals. (**c**), (**d**), (**e**), and (**f**) The time course of the similarity index between EEG window and reference segment and with additive Gaussian noise of signal-to-noise ratio (SNR) 6, 0, and −6

produces signals that are similar to epileptic activity. The similarity index between the EEG window and the reference segment is smaller than 0.6 after 250 s. It is also evident that the values of *DSI* fluctuated more than those of NSI during the seizure-free state.

To further test the performance of the similarity measure, independent realizations of white noise are added to the reference segment and each EEG window. The signal-to-noise ratio (SNR) is set at 6, 0, and −6, respectively, in order to test the performance of the similarity measure at different noise intensities. As shown in Fig. 7.3d, e, and f, the observational noise caused an increase in the similarity index during the seizure state. When the noise level is high (SNR = −6), the similarity measures between the reference segment and EEG window during the epileptic state are greater than those when the noise level SNR = 6. On the other hand, when the noise is too strong (SNR = −6), as shown in Fig. 7.3f, the values of similarity index *DSI* are not changed from the normal state to the seizure state. However, the similarity index *NSI* still consistently decreases with respect to the excitatory parameter, *A*. Therefore, the similarity index is sensitive to the changes of excitatory parameter *A*, demonstrating that the proposed similarity measure successfully can reveal the dynamic characteristics of simulated EEG in the different states.

7.3.3 Application to Epileptic EEG Data

Three data sets (denoted I, II, and III), each containing 110 single-channel EEG epochs of 10 s duration, are analysed in this study. These EEG epochs were obtained from 18 male genetic absence epilepsy rats from Strasbourg (GAERS) of at least 13 weeks of age. At this stage of development, all GAERS display the characteristic repeated spike-wave discharges (SWD) on the EEG during absence seizures (Danober et al. 1998). All procedures were performed under a British Home Office project licence [UK Animals (Scientific Procedures) Act, 1986] at the University of Birmingham by Dr. Douglas Richards. Many of the details of the experiments can be found in Chap. 6. The EEG data sets were preprocessed using a band-pass filter at 0.5–22 Hz.

To investigate the dynamic characteristics of EEG data during different seizure phases, EEG signals of GAERS were selected and dissected from seizure-free (group I), pre-seizure (group II), and seizure (group III) intervals. One hundred and ten EEG epochs were selected for each data set. Seizure onset is determined manually by an experienced experimental scientist by observation of abrupt increases in EEG amplitude coupled with simultaneous behavioural immobility, twitching of the vibrissae and facial muscles, and diminished muscle tone in the neck (Danober et al. 1998). As an example, three EEG recordings for the seizure-free, pre-seizure, and seizure states are magnified and displayed in Fig. 7.4. It is shown that similar amplitudes of EEG recordings in groups I and II range around some 4 mv, and EEG recordings demonstrate a high-amplitude firing pattern during the seizure state.

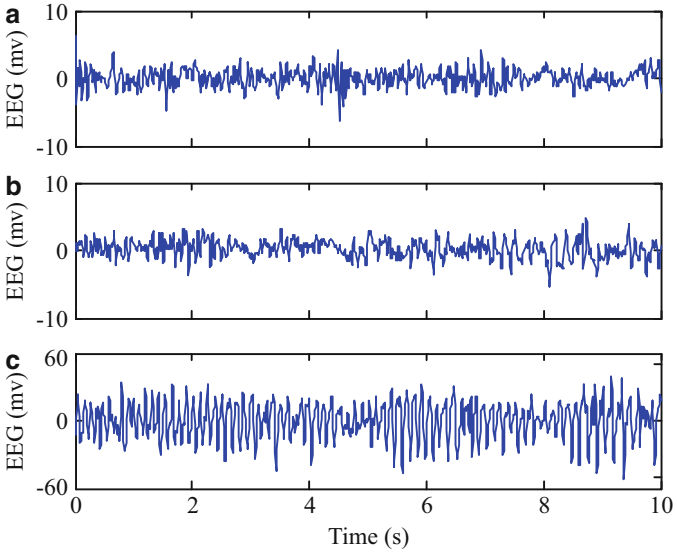

Fig. 7.4 Sample EEGs for (from *top to bottom*) groups I, II, and III

To calculate a similarity index from EEG data, we have to reconstruct a phase space from the EEG data. The embedding dimension and delay time of the EEG signals are determined using the mutual information measure and Cao's method. Given τ and m, a standard method to reconstruct the underlying dynamics may be carried out. Then, the delay time τ and the embedding dimension m of entire EEG epochs are determined by using the methods described above. The optimum values of τ range from 4 to 15 samples (mean and standard deviation is 8.84 ± 2.09) for different EEG segments. Thus, the optimum delay time, $\tau = 9$, is selected for the phase space reconstruction of the three EEG data sets. The optimum embedding dimension m ranges from 6 to 13 (mean and standard deviation is 9.85 ± 1.09) for different EEG segments. Therefore, $m = 10$ is suitable for the topologically proper reconstruction of the EEG data.

Then, to investigate the sensitivity of the similarity index on the length of the radius value r, two EEG segments I1 and I2 [as shown in Fig. 7.5a] during the seizure-free state are selected to compute the similarity index. The similarity index between $S1$ and $S2$ should be close to 1 because they are all from the seizure-free stage, showing a great degree of similarity in the dynamic properties of the brain's electrical activity. We calculate the similarity indexes *DSI* and *NSI* ($m = 10$, $\tau = 9$), respectively, between the two segments over a series of r, as shown in Fig. 7.5b (log–log plot).

The values of r are set to the order of magnitude of the standard deviation (σ) of the time series, which ranges from 1σ to 4σ. Given the r values, the similarity indexes *DSI* and *NSI* show a progressive increase from 0.03 to 1 and from 0.42 to 1. Their mean and standard deviation are 0.67 ± 0.35 and 0.90 ± 0.15, respectively.

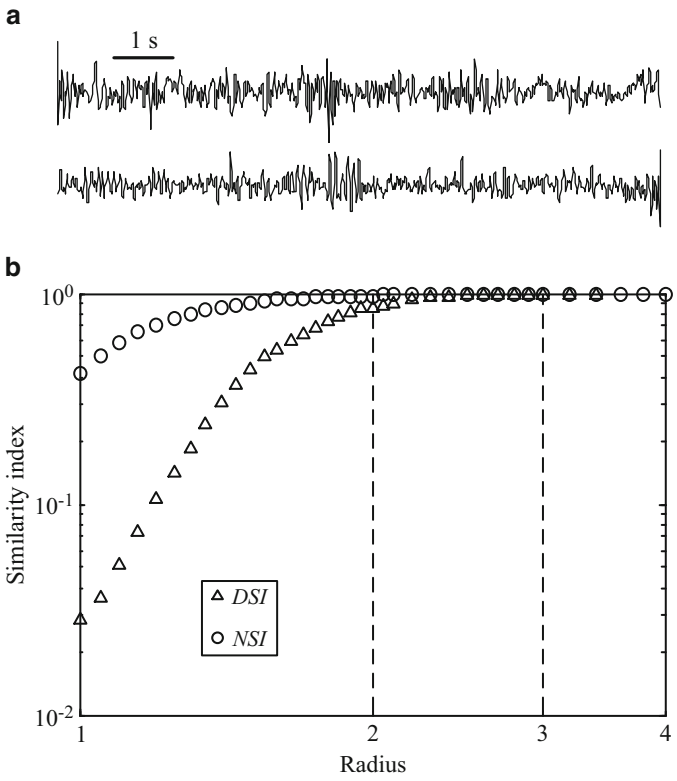

Fig. 7.5 Log–log plot of similarity *DSI* and *NSI* vs. radius for EEG data

As shown in Fig.7.5b, compared with the dynamical similarity index *DSI*, the new similarity index *NSI* is not more sensitive to the selected values *r*. In this study, the radius *r* is determined by the 2σ of the EEG signals.

Next, to investigate the dynamic characteristics of EEG series during different stages of an absence seizure, EEG series are dissected from the seizure-free state (from 10 to 20 s prior to seizure onset), the pre-seizure state (from 0 to 10 s prior to seizure onset), and the seizure state (the first 10 s of the absence seizure itself). Thus, 3×10 s EEG epochs are obtained for each of the 110 seizures.

To reveal the similarity measure of the EEG recordings during the different phases of the seizure, the average similarity measure of a pair of EEG signals in the same seizure states and across different seizure states is calculated. As listed in Table 7.2, it can be seen that the average similarity measures between EEG segments within the seizure-free state are close to 1. These results suggest that the EEG segments within the seizure-free state share the same dynamic characteristics. However, the similarity measures between EEG segments across different seizure states are typically smaller than those within the seizure-free state. These results support the view that there are changes in the dynamic characteristics for different

Table 7.2 The similarity measure *NSI* of EEG data at the seizure-free, pre-seizure, and seizure states (mean ± std)

Similarity	Seizure-free	Pre-seizure	Seizure
Seizure-free	0.950 ± 0.018	0.929 ± 0.035	0.836 ± 0.087
Pre-seizure	–	0.955 ± 0.030	0.806 ± 0.100
Seizure	–	–	0.812 ± 0.092

Table 7.3 The similarity measure *DSI* of EEG data at the seizure-free, pre-seizure, and seizure states (mean ± std)

Similarity	Seizure-free	Pre-seizure	Seizure
Seizure-free	0.707 ± 0.072	0.700 ± 0.107	0.458 ± 0.181
Pre-seizure	–	0.841 ± 0.118	0.447 ± 0.227
Seizure	–	–	0.439 ± 0.192

absence seizure states (Stacey and Litt 2008). The results of similarity measure *DSI* are listed in Table 7.3, which is similar to similarity measure *NSI* for change detection in dynamic characteristics during different seizure states.

7.4 Conclusions

In this chapter, the improved dynamical similarity method, i.e. new similarity index *NSI*, is proposed to analyse epileptic EEG recordings. Compared with the dynamical similarity index proposed by Le Van Quyen et al. (1999), the new similarity index has more advantages than the dynamical similarity index. The summary is as follows: (i) the new similarity index *NSI* is insensitive to the selection of the radius value r and the EEG signal length, and (ii) the new similarity index method is more robust to noise. Furthermore, similarity measures between EEG segments during the seizure-free state are higher than those during different states, indicating that the changes in dynamic characteristics can be found during different absence seizure states. An important next goal is to implement the new similarity index *NSI* to test a large number of epileptic patients in order to analyse the efficacy of the change detection in dynamic characteristics during different seizure states.

References

Buzsaki G. Rhythms of the brain. Oxford: Oxford University Press; 2006.

Cao L. Practical method for determining the minimum embedding dimension of a scalar time series. Phys D. 1997;110:43–50.

Danober L, Deransart C, Depaulis A, et al. Pathophysiological mechanisms of genetic absence epilepsy in the rat. Prog Neurobiol. 1998;55:27–57.

Ding M, Grebogi C, Ott E, Sauer T, Yorke J. Estimating correlation dimension from a chaotic time series: when does plateau onset occur? Phys D. 1993;69:404–24.
Eckmann J, Ruelle D. Fundamental limitation for estimating dimension and Lyapunov exponents in dynamical systems. Phys D. 1992;56:185–7.
Ferri R, Chiaramonti R, Elia M, Musumeci S, Ragazzoni A, Stam C. Nonlinear EEG analysis during sleep in premature and full-term infants. Clin Neurophysiol. 2003;114:1176–80.
Fraser AM, Swinney HL. Independent coordinates for strange attractors from mutual information. Phys Rev A. 1986;33:1134–40.
Grassberger P, Procaccia I. Characterization of strange attractors. Phys Rev Lett. 1983;50:346–9.
Grassberger P, Schreiber T, Schaffrath C. Nonlinear time sequence analysis. Int J Bifurcation Chaos. 1991;1:521–47.
Gribkov D, Gribkova V. Learning dynamics from non-stationary time series: analysis of electroencephalograms. Phys Rev E. 2000;61:6538–45.
Jansen B, Rit V. Electroencephalogram and visual evoked potential generation in mathematical model of coupled cortical columns. Biol Cybern. 1995;73:357–66.
Kim HS, Eykholt R, Salas JD. Nonlinear dynamics, delay times, and embedding windows. Phys D. 1999;127:48–60.
Lehnertz K, Elger C. Can epileptic seizures be predicted? Evidence from nonlinear time series analysis of brain electrical activity. Phys Rev Lett. 1998;80:5019–22.
Le Van Quyen M, Martinerie J, Baulac M, Varela F. Anticipating epileptic seizures in real time by a non-linear analysis of similarity between EEG recordings. NeuroReport. 1999;10:2149–55.
Li X, Ouyang G, Yao X. Dynamical characteristics of pre-epileptic seizures in rats with recurrence quantification analysis. Phys Lett A. 2004;333:164–71.
Lopes da Silva FH, Hoek A, Smith H, Zetterberg LH. Model of brain rhythmic activity. Kybernetik. 1974;15:27–37.
Navarro V, Martinerie J, Le Van Quyen M, Clemenceau S, Baulac M, Adam C, Varela F. Seizures anticipation in human neocortical partial epilepsy. Brain. 2002;125:640–55.
Packard N, Crutchfield J, Farmer J, Shaw R. Geometry from a time series. Phys Rev Lett. 1980;45(9):712–6.
Rabinovich M, Varona P, Selverston A, Abarbanel H. Dynamical principles in neuroscience. Rev Mod Phys. 2006;78:1213–65.
Rapp P, Zimmerman I, Alano A, Deguzman G, Greenbaum N. Experimental studies of chaotic neural behaviour cellular activity and electroencephalographic signal. In: Othmer H, editor. Nonlinear oscillations in biology and chemistry, Lecture notes in biomathematics. Berlin: Springer; 1985. p. 175–205.
Rogowski Z, Gath I, Bental E. On the prediction of epileptic seizures. Biol Cybern. 1981;42:9–15.
Sarkara M, Leong T. Characterization of medical time series using fuzzy similarity-based fractal dimensions. Artif Intell Med. 2003;27:201–22.
Schreiber T, Schmitz A. Classification of time series data with nonlinear similarity measures. Phys Rev Lett. 1997;78:1475–8.
Stacey W, Litt B. Technology insight: neuroengineering and epilepsy-designing devices for seizure control. Nat Clin Pract Neurol. 2008;4:190–201.
Stam C. Nonlinear dynamical analysis of EEG and MEG: review of an emerging field. Clin Neurophysiol. 2005;116(10):2266–301.
Takens F. In: Rand DA, Young LS, editors. Dynamical systems and turbulence, Lecture notes in mathematics. Berlin: Springer; 1981. p. 336.
Thiel M, Romano M, Kurths J. Influence of observational noise on the recurrence quantification analysis. Phys D. 2002;171:138–52.
Wendling F, Bellanger JJ, Bartolomei F, Chauvel P. Relevance of nonlinear lumped-parameter models in the analysis of depth-EEG epileptic signals. Biol Cybern. 2000;83:367–78.
Widman G, Schreiber T, Rehberg B, Hoeft A, Elger C. Quantification of depth of anesthesia by nonlinear time series analysis of brain electrical activity. Phys Rev E. 2000;62:4898–903.
Wolf A, Swift JB, Swinney HL, et al. Determining Lyapunov exponents from a time series. Phys D. 1985;16:285–317.

Chapter 8
Entropy Measures in Neural Signals

Zhenhu Liang, Xuejing Duan, and Xiaoli Li

8.1 Introduction

The concept of entropy was first proposed as a thermodynamic principle by Clausius in 1865. It described the distribution probability of molecules of gaseous or fluid systems. In 1949, Claude E. Shannon introduced entropy to information theory to describe the distribution of the signal component (Shannon and Weaver 1949). Since then, entropy had been investigated to analyze neural signals.

So far, various entropy measures have been proposed and used to quantify neural signals ranging from spike trains (Zhaohui and Xiaoli 2013), local field potentials (LFP) (Hu and Liang 2013) to electroencephalogram (EEG) (Zandi et al. 2013). Especially, for the noninvasive and high temporal resolution, EEG is widely used in clinical neurological disease diagnosis and brain-state monitoring, such as epilepsy (Zandi et al. 2009), Alzheimer's disease (Cao et al. 2015), depth of anesthesia (DoA) measures (Liang et al. 2015), cognition analysis (Song and Zhang 2016), and brain–computer interface (Zhang et al. 2015). In this chapter, we focus on the entropy measures in DoA monitoring.

Z. Liang • X. Duan
Institute of Electric Engineering, Yanshan University, Qinhuangdao 066004, China

Key Laboratory of Industrial Computer Control Engineering of Hebei Province, Yanshan University, Qinhuangdao 066004, China
e-mail: zhl@ysu.edu.cn

X. Li (✉)
State Key Laboratory of Cognitive Neuroscience and Learning & IDG/McGovern Institute for Brain Research, Beijing Normal University, Beijing 100875, China

Center for Collaboration and Innovation in Brain and Learning Sciences, Beijing Normal University, Beijing 100875, China
e-mail: xiaoli@bnu.edu.cn

X. Li (eds.), *Signal Processing in Neuroscience*, DOI 10.1007/978-981-10-1822-0_8

In the operating room, it is important to guarantee successful surgery and ensure patient safety and comfort. How to intelligently monitor the anesthetic drug effect on the brain is an important clinical concern for the anesthesiologists (Monk et al. 2005). The central nervous system (CNS) is the target of anesthetic drugs and the EEG. EEG has been widely used as a surrogate parameter to quantify the anesthetic drug effect (Rampil 1998; Jameson and Sloan 2006; Bruhn et al. 2006). However, only limited information can be gleaned from the EEG signal purely by waveform observation. With the development of signal processing methods, our understanding of EEG has greatly improved. Various EEG signal processing methods have been applied to analyze, identify or detect mental disorder, and investigate consciousness mechanisms (Rampil 1998; Okogbaa et al. 1994; Burton and zilberg 2002; Natarajan et al. 2004; Abásolo et al. 2006).

As yet, numerous entropy algorithms have been proposed and used to quantify depth of anesthesia. The number of entropy-related articles retrieved from PubMed comes to 244, covering the Shannon entropy (ShEn) (Yoon et al. 2011; Bruhn et al. 2001), spectral entropy (SpEn) (which includes response entropy (RE) and state entropy (SE)) (Klockars et al. 2012; Viertiö-Oja et al. 2004), approximate entropy (ApEn) (Bruhn et al. 2000), permutation entropy (PE) (Li et al. 2008a, 2012), wavelet entropy (WE) (Särkelä et al. 2007), and Hilbert–Huang spectral entropy (HHSE) (Li et al. 2008b). In addition to these mentioned entropies, sample entropy (SampEn) and fuzzy entropy (FuzzyEn) were also considered here.

Firstly, the entropy methods based on the frequency domain are useful for estimating anesthetic drug effect. SpEn was the first frequency–domain method successfully applied and commercialized into the M-entropy module (Viertiö-Oja et al. 2004). In this system, two parameters are calculated: response entropy (RE) and state entropy (SE). SE primarily includes the spectrum of EEG signals from 0.8 Hz to 32 Hz, whereas RE includes electromyography (EMG) activity, ie, from 0.8 Hz to 47 Hz (Viertiö-Oja et al. 2004). It can be seen that the window of spectral entropy is variable, but not self-adaptive. Conversely, the window in the wavelet transform (WT) is adaptively variable through an artificially given basis function. This has been suggested as a useful tool for presenting EEG signals in different time and frequency scales (Zoughi et al. 2012). In particular, the entropy of a signal in the wavelet domain (ie, WE) indicates signal variation at each frequency scale (Rosso et al. 2001). However, in practice, the wavelet transform can only deal with linear, nonstationary signals. To overcome this shortcoming, Huang et al. in 1998 proposed empirical mode decomposition (EMD), in conjunction with Hilbert transform (Hilbert–Huang transform), as a method to process nonlinear and nonstationary signals (Huang et al. 1998). This method can adaptively generate the basic function and isn't restrained by the Heisenberg uncertainty principle, making it suitable for analysis of abruptly changing signals. This method has been widely used to extract features of EEG recordings (Liang et al. 2000; Rilling et al. 2003; Li 2006; Shalbaf et al. 2012). In particular, Li et al. developed Hilbert–Huang spectral entropy (HHSE) and successfully applied it to anesthetic EEG signals (Li et al. 2008b).

Then, as we know, the dynamics of the EEG show some nonlinear and chaotic characteristics in the time domain. So, many entropy methods based on time domain and phase space have also been applied to analyze EEG signals. ShEn, as a basic entropy method, has been used for signal analysis (Shannon and Weaver 1949). It measured the predictability of later amplitude values of the signal based on the probability distribution of prior amplitude values and was proved to be a simple and robust electroencephalographic measure of anesthetic drug effect (Bruhn et al. 2001). But the ShEn value is variable for each individual, so it is not reliable for clinical application. In 1991, the ApEn algorithm, derived from Kolmogorov–Sinai entropy, was published (Pincus 1991). It was also based on the information of amplitude values and quantified the predictability of subsequent amplitude values of the signal. It has been widely used in biomedical signals, including the EEG signals during anesthesia. The existing study showed that it correlated well with the concentration of desflurane (Bruhn et al. 2000). However, ApEn lacked relative consistency and was highly dependent on data length. To overcome this limitation, Richman and Moorman proposed another statistics named SampEn in 2000, which removed self-matching and relieved the data length bias (Richman and Moorman 2000). In recent years, it has been used for analyzing EEG signals (Montirosso et al. 2010; Yoo et al. 2012). FuzzyEn was proposed by Chen et al. (Chen et al. 2007). It is based on the fuzzy membership functions to define the vectors' similarity, using the soft and continuous boundaries of fuzzy functions to ensure the continuity and validity of FuzzyEn's definition (Chen et al. 2009). ApEn, SampEn, and FuzzyEn are all based on phase space reconstruction, making them computationally complex. In 2002, Bandt and Pompe introduced the interesting concept of PE which was based on symbolic dynamics and was a complex measure for time series analysis (Bandt and Pompe 2002). Because of its simple concept and fast computation, it has been widely used in EEG signal analysis (Li et al. 2008a; Cao et al. 2004; Li et al. 2007). Furthermore, its derivatives, multi-scale permutation entropy (MPE) (Li et al. 2010) and composite PE index (CPEI), (Olofsen et al. 2008) have been successfully applied to analyze EEG signals during anesthesia.

We noticed that the definitions of all the above entropies are based on the Shannon information theory, which belonged to a short-range or extensive concept. However, the physical systems especially the biomedical systems are often characterized by either long-range interactions, long-term memories, or multifractality (Zunino et al. 2008). To describe these characters, two generalized forms of entropy were proposed: Renyi entropy (Renyi 1970) and Tsallis entropy ($q$entropy) (Tsallis et al. 1998). The Tsallis entropy has a parameter q for non-extensity. If $q > 1$, the entropy is more sensitive to events that occur often; if $0 < q < 1$, it is more sensitive to the events that occur seldom (Maszczyk et al. 2008). In the limit of $q \to 1$, it coincides with the Shannon entropy. These generalized entropies can provide additional information about the importance of specific events, such as outliers or rare events. The two classes of entropies and their combinations with current signal processing methods have been applied to EEG analysis (Bezerianos et al. 2003; Tong et al. 2003; Inuso et al. 2007) and proved to be advantageous than

the Shannon versions (Zunino et al. 2008; Arefian et al. 2009). To make the research more instructive, we believe it is useful to investigate these non-extensive entropy measures along with those extensive Shannon entropies in DoA monitoring.

In this study, we involved the Tsallis wavelet entropy (TWE) and Renyi wavelet entropy (RWE) proposed by Rosso et al. (Rosso et al. 2003, 2006), the Tsallis permutation entropy (TPE) proposed by Zunion et al. (Zunino et al. 2008), and a new Renyi permutation entropy (RPE).

For illustrative purposes, we divided the entropies into two families:

1. Entropies based on the time–frequency domain: RE, SE, WE, and HHSE
2. Entropies based on the time domain: ApEn, SampEn, FuzzyEn, and PE

Additionally, many attempts have been made to develop multi-scale entropy (MSE) algorithms for describing the multi-scale properties of neural populations in recent years (Costa et al. 2002, 2005; Chen and Yang 2012; Aziz et al. 2005), in both normal (He and et al. 2010; Bell et al. 2012; Nunez et al. 2001) and diseased states (Escudero et al. 2006; Ouyang et al. 2009; Labate et al. 2013). For the decomposition methods, Costa et al. proposed MSE based on the consecutive coarse-graining (CG) procedure combined with Zhang's and Pincus's approaches (approximate entropy) to assess the complexity of time series (Costa et al. 2002; Pincus 1991). This method has been widely used in analyzing complex physiologic time series (Costa et al. 2002, 2005; Thuraisingham and Gottwald 2006). Based on this method, Li et al. proposed multi-scale permutation entropy to track the effects of sevoflurane anesthesia on the central nervous system. The results showed that single-scale permutation entropy was blind to subtle transitions between light and deep anesthesia, while the MPE index tracked these changes accurately (Li et al. 2010). However, this coarse-graining process reduced the length of a time series as the scale increased. When applied to a short-term time series, it may yield an imprecise estimation of entropy (Wu et al. 2013). To overcome this shortcoming, Wu proposed the moving-average (MA) procedure to achieve the same length at each scale (Wu et al. 2013) and evaluated the effectiveness of CG and MA by the synthetic noise signal analysis.

For multi-scale entropy measures, the Shannon entropy (ShEn) (Shannon 2001), sample entropy (SampEn) (Richman and Moorman 2000), and permutation entropy (PE) (Bandt and Pompe 2002) are usually used for multi-scale analysis. ShEn is a typical measure which quantifies the distribution probability of time or frequency domain. Compared with approximate entropy, SampEn removes self-matching and is less dependent on data length (Richman and Moorman 2000). Many MSE measures are based on it. In our previous work, multi-scale sample entropy (MSSE) measures based on the CG procedure were proposed for DoA measures (Wang et al. 2014). Further, multi-scale permutation entropy (MSPE) based on the coarse-graining procedure has been proposed and used to analyze the dynamics of physiological time series in many studies (Li et al. 2010; Aziz et al. 2005; Morabito et al. 2012; Takahashi et al. 2010). In this chapter, we only considered the MSE based on SampEn and PE.

This chapter is organized as follows. Section 2 describes all single-scale entropy measures, and Sect. 3 gives the multi-scale entropy measures of PE and SampEn based on CG and MA methods. In Sect. 4, the details of EEG data set, the pharmacokinetic/pharmacodynamic modeling, and the results of the application of all entropy measures to the real EEG are presented. Finally, the conclusion is given in Sect. 5. The parameter selection of some entropy measures was discussed in Appendix.

8.2 Entropy Measures

8.2.1 Response Entropy and State Entropy

The probability density function (PDF) of the signal power spectrum in the frequency domain is quantified. The details of the SpEn algorithm can be found in (Rezek and Roberts 1998; Inouye et al. 1991), which is as the same as applying in the M-entropy module (Viertiö-Oja et al. 2004). SpEn contains RE and the SE, which is computed as follows:

$$RE = \frac{H_{sp0.8-47}}{\log\left(N_{0.8-47}\right)} \tag{8.1}$$

$$SE = \frac{H_{sp0.8-32}}{\log\left(N_{0.8-47}\right)} \tag{8.2}$$

We described the degree of skewness in the frequency distribution by SpEn. For example, in the normalized case, the SpEn of a pure sine wave with a single spectral peak is 0, while that of white noise is 1.

8.2.2 Wavelet Entropy (SWE, TWE, and RWE)

WE can differentiate specific brain states under spontaneous or stimulus-related conditions and recognize the time localizations of a dynamic process. To calculate wavelet entropy, wavelet energy E_j of a signal is determined at each scale j as follows:

$$E_j = \sum\nolimits_{k=1}^{L_j} d(k)^2 \tag{8.3}$$

where k and L_j are the summation index and the number of coefficients at each scale j within a given epoch, respectively. The total energy over all scales is obtained by

$$E_{\text{total}} = \sum\nolimits_j E_j = \sum\nolimits_j \sum\nolimits_{k=1}^{L_j} d_j(k)^2 \tag{8.4}$$

Then the wavelet energy is divided by total energy to obtain the relative wavelet energy at each scale$j$:

$$p_j = \frac{E_j}{E_{\text{total}}} = \frac{E_j}{\sum_j E_j} = \frac{\sum_{k=1}^{L_j} d(k)^2}{\sum_j \sum_{k=1}^{L_j} d_j(k)^2} \tag{8.5}$$

SWE is calculated from the Shannon entropy of p_j distribution between scales as follows:

$$S^{(s)} = -\sum_j p_j \log p_j \tag{8.6}$$

The details of the algorithm used in this study can be seen in (Särkelä et al. 2007).

And TWE is defined as

$$S_q^{(T)} = \frac{1}{q-1} \sum_j \left[p_j - (p_j)^q \right] \tag{8.7}$$

where q is a non-extensity parameter.

Based on the definition of the Renyi entropy (Renyi 1970), RWE is defined as (Rosso et al. 2006)

$$S_a^{(R)} = \frac{1}{1-a} \log \left[\sum_j (p_j)^a \right] \tag{8.8}$$

For $S_q^{(S)}$, the normalized SWE is

$$\text{SWE} = S^{(s)} / \log N_J \tag{8.9}$$

where N_J is the number of wavelet resolution levels.

And $S_q^{(T)}$is normalized by dividing $\left[1 - N_J^{1-q}\right] / (q-1)$, defined by (Rosso et al. 2003)

$$\text{TWE} = \frac{s_q^{(T)}}{\left[1 - N_J^{1-q}\right] / (q-1)} \tag{8.10}$$

Further, the normalized $S_a^{(R)}$ is defined as (Maszczyk et al. 2008)

$$\text{RWE} = \frac{s_a^{(R)}}{\log N_J} \tag{8.11}$$

The values of the three WE measures depended on the wavelet basis function, the number of decomposed layers (n), and the data length (N). Furthermore, TWE and

RWE are related to the parameters q and a, respectively. Among these parameters, the wavelet basis function is the most important. Because of the lack of a fixed criterion, it is very difficult to select an appropriate wavelet basis function in practical applications, and many studies select it based on experiments. The details of the selection process in this study can be found in Appendix A.

8.2.3 Hilbert–Huang Spectral Entropy

HHSE is dependent on Hilbert–Huang transform, which applies the Shannon entropy concept to the Hilbert–Huang spectrum. The detailed algorithm is shown in (Li et al. 2008b). For a given nonstationary signal $x(t)$, the EMD method decomposes the signal into a series of intrinsic mode functions (IMFs) $C_n(1, 2, \ldots, N)$, where N is the number of IMFs. The signal $x(t)$ can be written by

$$x(t) = \sum_{i=1}^{n-1} imf(t)_i + r_n(t) \tag{8.12}$$

Applying the Hilbert transform to the IMF components

$$Z(t) = imf(t) + iH\left[imf(t)\right] = a(t)e^{i\int \omega(t)dt} \tag{8.13}$$

in which $a(t) = \sqrt{imf^2(t) + H^2\left[imf(t)\right]}$, $\omega(t) = \frac{d}{dt}\left[\arctan\left(H\left[imf(t)\right]/imf(t)\right)\right]$, and

$$h(\omega) = \int H(\omega, t)\, dt \tag{8.14}$$

where $\omega(t)$ and $a(t)$ are the amplitude of IMF and the instantaneous frequency, respectively.

In order to simplify the representation, the Hilbert–Huang spectrum is indicated as a function of frequency (f) instead of angular frequency (ω). The marginal spectrum is normalized by

$$\widehat{h}(f) = h(f)/\sum h(f) \tag{8.15}$$

Next, the Shannon entropy concept is applied to the Hilbert–Huang spectrum, and Hilbert–Huang spectral entropy is obtained by

$$\text{HHSE} = -\sum_{f} \widehat{h}(f) \log\left(\widehat{h}(f)\right) \tag{8.16}$$

where HHSE represents Hilbert–Huang spectral entropy. The frequency resolution and data length (N) can affect the HHSE values. For precise computation of the frequency resolution, we choose the frequency resolution as 0.1 Hz. N directly influences the EMD. Generally, the boundary effect may be induced if N is too large or too small, which can contaminate the data and distort the power spectrum. The selection of N used in this study is given in Appendix B.

8.2.4 Approximate Entropy

ApEn is derived from Kolmogorov entropy which was introduced by Pincus in 1991 (Pincus 1991). ApEn can be used to analyze a finite length signal and belongs to nonlinear dynamics describing the unpredictability or randomness of a signal. Its computation involves embedding the signal into phase space and estimating the rate of increment in the number of phase space patterns within a predefined value r—when the embedding dimension of phase space is increasing from m to $m + 1$.

For a time series $x(i)$ $(1 \le i \le N)$ of finite length N, reconstitution of the $N-m+1$ vectors $X_m(i)$ follows the form:

$$X_m(i) = \{x(i), x(i+1), \ldots x(i+m-1)\}, i = 1, 2, \ldots N - m + 1 \tag{8.17}$$

where m is embedding dimension.

Let $C_{\mathrm{i}}^m(r)$ be the probability that any vector $X_m(j)$ is within r of $X_m(i)$, defined as

$$C_i^m(r) = \frac{1}{N-m+1} \sum_{j=1}^{N-m+1} \Theta\left(d_{ij}^m - r\right); i, \mathrm{j} = 1, 2, \ldots N - m + 1 \tag{8.18}$$

where d is the distance between the vectors $X_m(i)$ and $X_m(j)$, defined as

$$d_{ij}^m = d\left[X_i^m, X_j^m\right] = \max\left(|x(i+k) - x(j+k)|\right), k = 0, 1, \ldots, m \tag{8.19}$$

and Θ is the Heaviside function.

After that, define a parameter $\Phi^m(r)$:

$$\Phi^m(r) = (N-m+1)^{-1} \sum_{i=1}^{N-m+1} \ln C_i^m(r) \tag{8.20}$$

Next, when the dimension increases to $m + 1$, repeat the above process.

$$\Phi^{m+1}(r) = (N-m)^{-1} \sum_{i=1}^{N-m} \ln C_i^{m+1}(r) \tag{8.21}$$

Finally, approximate entropy is defined by

$$\mathrm{ApEn}\,(m, r, N) = \Phi^m(r) - \Phi^{m+1}(r) \tag{8.22}$$

We showed the detailed algorithm in (Bruhn et al. 2000). The data length (N), tolerance (r), and embedding dimension (m) will influence the ApEn index. According to (Pincus 1991) and (Bruhn et al. 2000), N is recommended to be 1000, r = 0.1–0.25 of the standard deviation of the signal and $m = 2-3$. We described the selection process of these parameters in Appendix C.

8.2.5 *Sample Entropy*

The SampEn that Richman and Moorman proposed (Richman and Moorman 2000) is based on ApEn but differs from it in three ways:

1. SampEn removes self-matches.
2. In order to avoid $\ln 0$ caused by eliminating self-matches, SampEn computes additional operation of the total number of template well-matches prior to computing the logarithmic operation.
3. For an equal number of patterns for the embedding dimensions m and $m + 1$, the time series reconstitution in SampEn has $N - m$ rows instead of $N - m + 1$ in ApEn with an embedding dimension of m.

The first step is the same as ApEn. When the embedding dimension is m, the total number of template matches is

$$B^m(r) = (N-m)^{-1}\sum_{i=1}^{N-m} C_i^m(r) \tag{8.23}$$

Similarly, when the embedding dimension is $m + 1$, the total number of template matches is

$$A^m(r) = (N-m)^{-1}\sum_{i=1}^{N-m} C_i^{m+1}(r) \tag{8.24}$$

Finally, the SampEn of the time series is estimated by:

$$\mathrm{SampEn}\,(r, m, N) = -\ln\frac{A^m(r)}{B^m(r)} \tag{8.25}$$

SampEn is based on ApEn, so its parameters and selection procedures are the same as ApEn (see Appendix D).

8.2.6 Fuzzy Entropy

Zadeh introduced the concept of "fuzzy set" (Zadeh 1965) in 1965. It provided a mechanism for measuring the degree to which a pattern belonged to a given class, by introducing the concept of "membership degree" with a fuzzy function $u_C(x)$. The nearer the value of $u_C(x)$ to unity, the higher the membership grade of x in the set C. Inspired by this, Chen et al. (Chen et al. 2007). developed FuzzyEn based on SampEn. FuzzyEn uses the fuzzy membership function $u(d_{ij}^m, r)$ to obtain the similarity between X_i^m and X_j^m instead of the Heaviside function.

FuzzyEn is based on SampEn, so the parameters and selection procedures n of the two kinds of entropies are the same (see Appendix E).

8.2.7 Permutation Entropy

There are three types of PE measures involved in this study. PE is an ordinal analysis method, in which a given time series is divided into a series of ordinal patterns for describing the order relations between the present and a fixed number of equidistant past values (Bandt 2005). The advantages of this method are its simplicity, robustness, and low computational complexity (Li et al. 2007). For an N-point-normalized time series $\{x(i) : 1 \leq i \leq N\}$, firstly the time series is reconstructed:

$$X_i = \{x(i), x(i+\tau), \ldots x(i+(m-1)\tau)\}, i = 1, 2, \ldots, N-(m-1)\tau \quad (8.26)$$

where τ is time delay and m is embedding dimension.

Then, rearrange X_i in an increasing order:

$$\{x(i+(j_1-1)\tau) \leq x(i+(j_2-1)\tau) \leq \cdots \leq x(i+(j_m-1)\tau)\} \quad (8.27)$$

There are $m!$ permutations for m dimensions. Each vector X_i can be mapped to one of the $m!$ permutations.

Next, the probability of the j th permutation occurring p_j can be defined as

$$p_j = \frac{n_j}{\sum_{j=1}^{m!} n_j} \quad (8.28)$$

where n_j is the number of times the j th permutation occurs.

Based on the probability of the j th permutation p_j, we define SPE, TPE, and RPE as follows.

SPE can be viewed as the Shannon entropy associated with the probability distribution p_j:

$$S_1^{(s)} = -\sum_{j=1}^{m!} p_j \log p_j \tag{8.29}$$

And the normalized SPE is

$$\mathrm{SPE}_n = \frac{S_1^{(s)}}{S_{1\,\max}^{(s)}} = \frac{\sum_{j=1}^{m!} p_j \log p_j}{\log(m!)} \tag{8.30}$$

Based on the definition of the Tsallis entropy, Zunino et al. proposed the normalized TPE and defined it as (Zunino et al. 2008)

$$\mathrm{TPE} = \frac{\sum_{j=1}^{m!} \left(p_j - p_j^q\right)}{1 - (m!)^{1-q}} \tag{8.31}$$

Furthermore, the normalized RPE measure based on the Renyi entropy and permutation probability distribution p_j is

$$\mathrm{RPE}_n = \frac{\log \sum_{j=1}^{m!} p_j^a}{(1-a)\ln m!} \tag{8.32}$$

In (Li et al. 2008a, 2010, 2012), SPE was used to evaluate the effect of sevoflurane and isoflurane anesthesia on the brain. In this study, the $m = 6$ and $\tau = 1$ are selected for sevoflurane anesthesia as proposed in (Li et al. 2008a). The SPE's parameters for isoflurane anesthesia are the same as those used by Li et al. (Li et al. 2012). TPE and RPE are first used in DoA measure; therefore, selection of the appropriate parameters of TPE and RPE is based on the experiments. The details of the selection process were shown in Appendix F.

8.3 Multi-Scale Entropy Measures

8.3.1 Multi-Scale Decomposition Procedures

8.3.1.1 Coarse Graining

Given a one-dimensional discrete time series $\{x_1, x_2, \ldots x_i, \ldots, x_N\}$, construct a set of consecutive coarse-grained time series $\{y^{(s)}\}$, where s is the scale factor. As shown in Fig. 8.1a, each coarse-grained time series is derived according to the following equation:

$$y_j^{(s)} = \frac{1}{s} \sum_{i=(j-1)s+1}^{js} x_i, \quad 1 \le j \le N/s \tag{8.33}$$

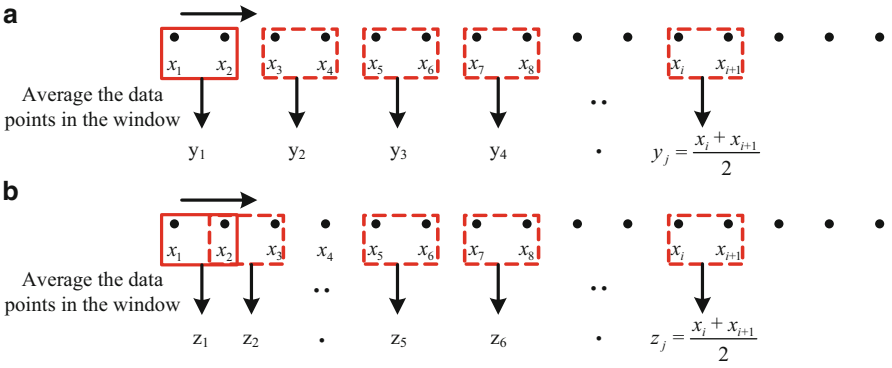

Fig. 8.1 Illustrations of multi-scale decomposition procedures: (**a**) Coarse graining for scale = 2. The window size is the scale level s. (**b**) Moving average for scale = 2. The window size is the scale level s, and overlap size is $s - 1$

The length of each coarse-grained time series equals to the length of the original time series N divided by s.

8.3.1.2 Moving Average

Similar to the coarse-graining procedure, each element of a moving average is defined as follows (Wu et al. 2013):

$$z_j^{(s)} = \frac{1}{s} \sum_{i=j}^{j+s-1} x_i, \quad 1 \le j \le N - s + 1 \tag{8.34}$$

The details of the moving-average procedure are shown in Fig. 8.1b. Compared to the CG procedure, the moving average does not largely reduce the length of a time series. The length of a moving-average time series is $N - s + 1$. And this makes the moving-average procedure more reliable than CG for short-term time series analysis (Wu et al. 2013).

8.3.2 Multi-Scale Permutation Entropy Based on CG and MA

Six multi-scale permutation entropy (MSPE) measures, namely: SPE, RPE, and TPE based on CG procedure (CG-SPE, CG-RPE, CG-TPE, respectively) and SPE, RPE, and TPE based on MA procedure (MA-SPE, MA-RPE, MA-TPE, respectively), are formed by means of combining the three PE measures with two multi-scale decomposition methods.

In terms of the multi-scale decomposition method, we choose five scales (from 1 to 5). In regard to the entropy measurements, the calculation depends on the length of epoch N and the embedding dimension m, and there is a necessary condition $m! < N$. According to our previous study (Liang et al. 2015; Li et al. 2008a), we choose $m = 6$, so the length of the chosen epoch needs to be bigger than 720 for scale $= 5$. The length of moving-average time series just has a small change and makes no difference to the epoch length selection. While the length of each coarse-grained time series is $N/5$, to fulfill the requirement, we can either extend N or decrease m to the second-best option $m = 3$ (Li et al. 2010).

In this study, the parameter selection criteria are based on the performance in distinguishing awake and anesthetized states. At the sampling rate of 100 Hz, we designed two parameter groups $N = 1000$, $m = 3$ and $N = 4000$, $m = 6$ for comparison, and other parameters are set as $\tau = 1$, $a = 2$, and $q = 0.9$ for RPE and TPE (Liang et al. 2015).

Figure 8.2 shows the changes of CG-SPE, CG-RPE, and CG-TPE over the five scales based on two sets of parameters in different states. All the indices monotonously decreased in anesthesia phase. It is obvious that in the $N = 4000$, $m = 6$ part, the difference between two states is more significant, and this indicates

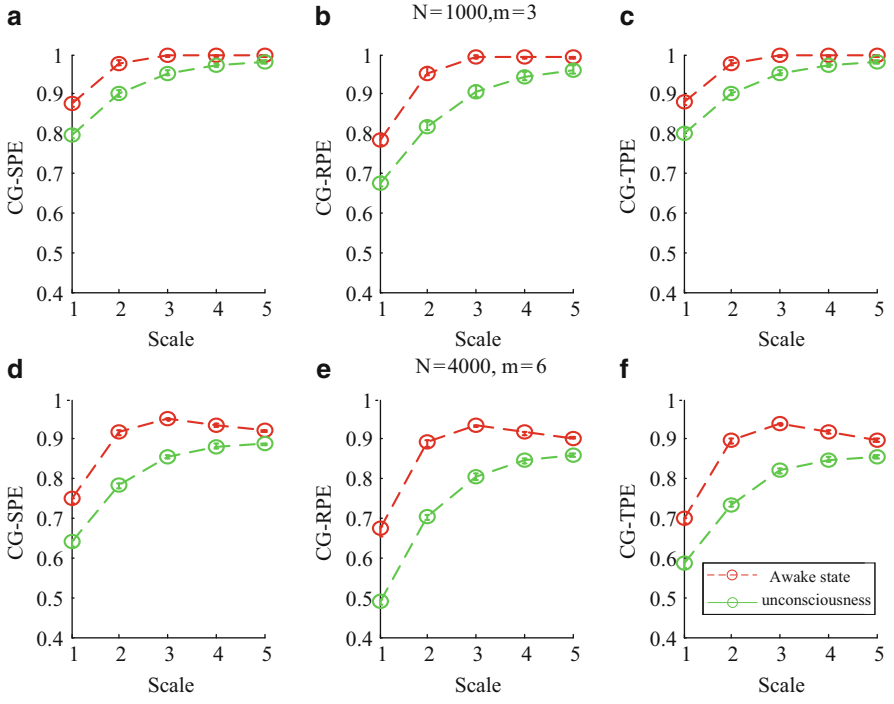

Fig. 8.2 The changes of CG-based MSPE measures with different parameters in different anesthesia states. (**a**–**c**): $N = 1,000$, $m = 3$, $\tau = 1$, $a = 2$, and $q = 0.9$ (**d**–**f**): $N = 4,000$, $m = 6$, $\tau = 1$, $a = 2$, and $q = 0.9$

that the second serials of parameters have better ability in distinguishing awake and anesthetized states. Therefore, $N = 4000$, $m = 6$; $\tau = 1$; $a = 2$; and $q = 0.9$ were selected for MSPE based on CG and $N = 1000$, $m = 6$; $\tau = 1$; $a = 2$; and $q = 0.9$ for MSPE based on MA.

Similar to the study in (Li et al. 2010), MSPE is calculated as follows:

$$\mathrm{MSPE} = \frac{1}{s}\sum_{i=1}^{s} PE\,|_{\mathrm{scale}\ \ i} \tag{8.35}$$

where PE $PE|_{\mathrm{scale}\,i}$ should be SPE, TPE, or RPE at scale i. We only considered $s = 1,\ 2$ and 3.

8.3.3 Multi-Scale Sample Entropy Based on CG (CG-SampEn) and MA (MA-SampEn)

Similar to MSPE, the composed multi-scale sample entropy (MSSE) is described as

$$\mathrm{MSSE} = \frac{1}{s}\sum_{i=1}^{s} \mathrm{SampEn}\,|_{\mathrm{scale}\ \ i} \tag{8.36}$$

where scales 1, 2, and 3 are considered in this work. Base on the above descriptions, we set the parameters $m = 2$, and $r = 0.2$*SD for CG-SampEn and MA-SampEn. The condition of scale 1 is similar as the single SampEn mentioned above.

8.4 Characterization and Comparison of Different Methods

8.4.1 EEG Data Set

In this study, the data set we used was from a previous study (McKay et al. 2006), in which 19 patients aged 18–63 years were recruited from Waikato Hospital, Hamilton, New Zealand. The subjects were scheduled for elective gynecologic, general, or orthopedic surgery. All patients were rested for at least 6 h before anesthesia and received no premedication. Patients were American Society of Anesthesiologists physical status I or II and signed written informed consent following approval by the Waikato Hospital ethics committee.

Before application of Ag/AgCl electrodes, the skin was carefully cleaned with an alcohol swab to ensure electrode-skin impedance to be less than 7.5 kΩ. Three electrodes were used to record the EEG signals between the forehead and temple. RE and SE were measured every 5 s with a plug-in M-entropy S/5 module (Datex–

Ohmeda). The sevoflurane concentration was measured at the mouth at 100/s. All data were recorded and stored by a laptop computer. Off-line analysis was performed using the MATLAB (version 8, MathWorks, Inc.) software.

8.4.2 Pharmacokinetic/Pharmacodynamic Modeling

To derive the relationship between the effect-site anesthetic drug concentration and the measured EEG index, PK/PD modeling was used. These methods have been successfully used to evaluate the proposed EEG indices (Li et al. 2008a; Olofsen et al. 2008). It describes the relationship between drug dose and its effect through two successive physiological processes (McKay et al. 2006). The pharmacokinetic (PK) side of the model describes the drug concentration changes in the blood over time, while the pharmacodynamic (PD) part shows the relation between the concentration of the drug at effect site and its measured effect. The simplest effect-site model is a first-order model, defined as

$$dC_{eff}/dt = k_{eo}\left(C_{et} - C_{eff}\right) \tag{8.37}$$

where C_{eff} denotes the effect-site concentration, k_{eo} is the first-order rate constant for efflux from the effect compartment, and C_{et} is the end-tidal concentration.

In addition, a nonlinear inhibitory sigmoid $E_{\max}$ model was used to describe the relationship between the estimated C_{eff} and the measured EEG indices:

$$\text{Effect} = E_{\max} - (E_{\max} - E_{\min}) \times \frac{{C_{eff}}^{\gamma}}{EC_{50}^{\gamma} + {C_{eff}}^{\gamma}} \tag{8.38}$$

where Effect is the processed EEG measure, $E_{\max}$ and $E_{\min}$, respectively, are the maximum and minimum Effect for each individual, EC_{50} is the drug concentration that causes 50 % of the maximum Effect, and γ is the slope of the concentration–response relationship.

The coefficient of determination R^2 is calculated by

$$R^2 = 1 - \frac{\sum_{i=1}^{n}(y_i - \widehat{y}_i)^2}{\sum_{i=1}^{n}(y_i - \overline{y})^2} \tag{8.39}$$

where y_i is the measured Effect for a given time and $\hat{y}_i$ is the corresponding modeled Effect.

The C_{eff} is estimated by iteratively running the above model with a series of k_{eo} values, with the optimal k_{eo} yielding the greatest R^2 for each patient.

8.4.3 Statistical Analysis

To further evaluate the correlation between the measured EEG index and the underlying anesthetic drug effect, prediction probability (P_k) statistics were applied, as described in (Smith et al. 1996). Given two random data points with different C_{eff}, P_k described the probability of the measured EEG index correctly predicted the C_{eff} of the two points. Its definition is

$$P_k = \frac{P_c + P_{tx}/2}{P_c + P_d + P_{tx}} \tag{8.40}$$

where P_c, P_d, and P_{tx} separated the probability of two data points drawn at random, independently and with replacement from the population are a concordance, a discordance, or an x-only tie. $P_k = 1$ meant that the EEG index was perfectly concordant with C_{eff}; whereas $P_k = 0.5$ meant the EEG index was obtained by chance. When the monotonic relation between the drug concentration and the EEG index was negative, the resultant P_k value was replaced by 1- P_k.

In addition, the Kolmogorov–Smirnov test was used to determine whether the data sets were normally distributed. To assess the index stability during the awake state and the sensitivity to the induction process, the relative coefficient of variation (CV) (Li et al. 2008a) was used.

8.4.4 All the Entropy Measure Comparison Without Multi-Scale Procedures

First we applied these entropy measures to the EEG data recorded from sevoflurane anesthesia. Figure 8.3a showed a preprocessed EEG recording and the derivative from the EEG signal during the whole sevoflurane induction process: from awake to induction, then to deep anesthesia, and finally recovery. With the deepening of anesthesia, the mean amplitude of the EEG gradually increased, then decreased during recovery. The concurrent end-tidal sevoflurane concentration is represented by the black line in Fig. 8.3b. It can be regarded as the drug concentration in the blood, derived from the recorded sevoflurane concentration at the mouth (represented by gray line). The detailed spectrogram is shown in Fig. 8.3c. The changes in RE, SE, SWE, TWE, RWE, HHSE, ApEn, SampEn, FuzzyEn, SPE, TPE, and RPE of the EEG recording were successively given in Fig. 8.3d–k. As can be seen, all the entropy indices generally followed the changes in EEG pattern as the drug concentration changed.

Loss of consciousness (LoC) is the most important clinical time point during anesthesia. We investigated the ability of these entropies in tracking LoC. Figure 8.4 showed the changes in each index around LoC (from LoC-30s to LoC + 30s) for all subjects during sevoflurane anesthesia. For these plots, the index values were

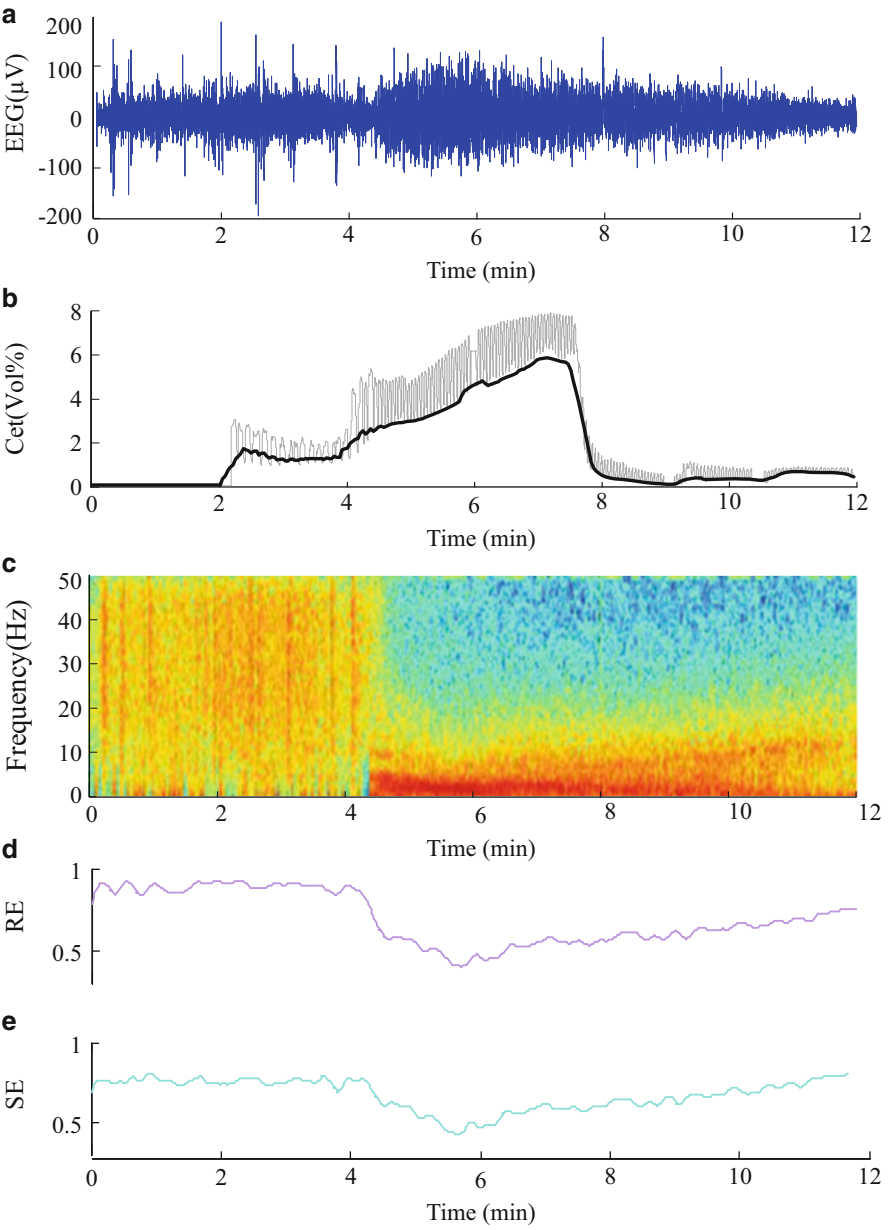

Fig. 8.3 An EEG recording from a patient undergoing sevoflurane anesthesia and corresponding entropy indices versus time. (**a**) Preprocessed EEG recording. (**b**) Sevoflurane concentration recorded at the mouth (*gray line*) and the derived end-tidal sevoflurane concentration (*black line*). (**c**) The spectrogram computed by short-time Fourier transform using a Hamming window with a length of 1 s and 50 % overlapping. (**d**)–(**k**) The time course of the studied EEG derivative. The indices are calculated over a window of 10 s with an overlap of 75 %

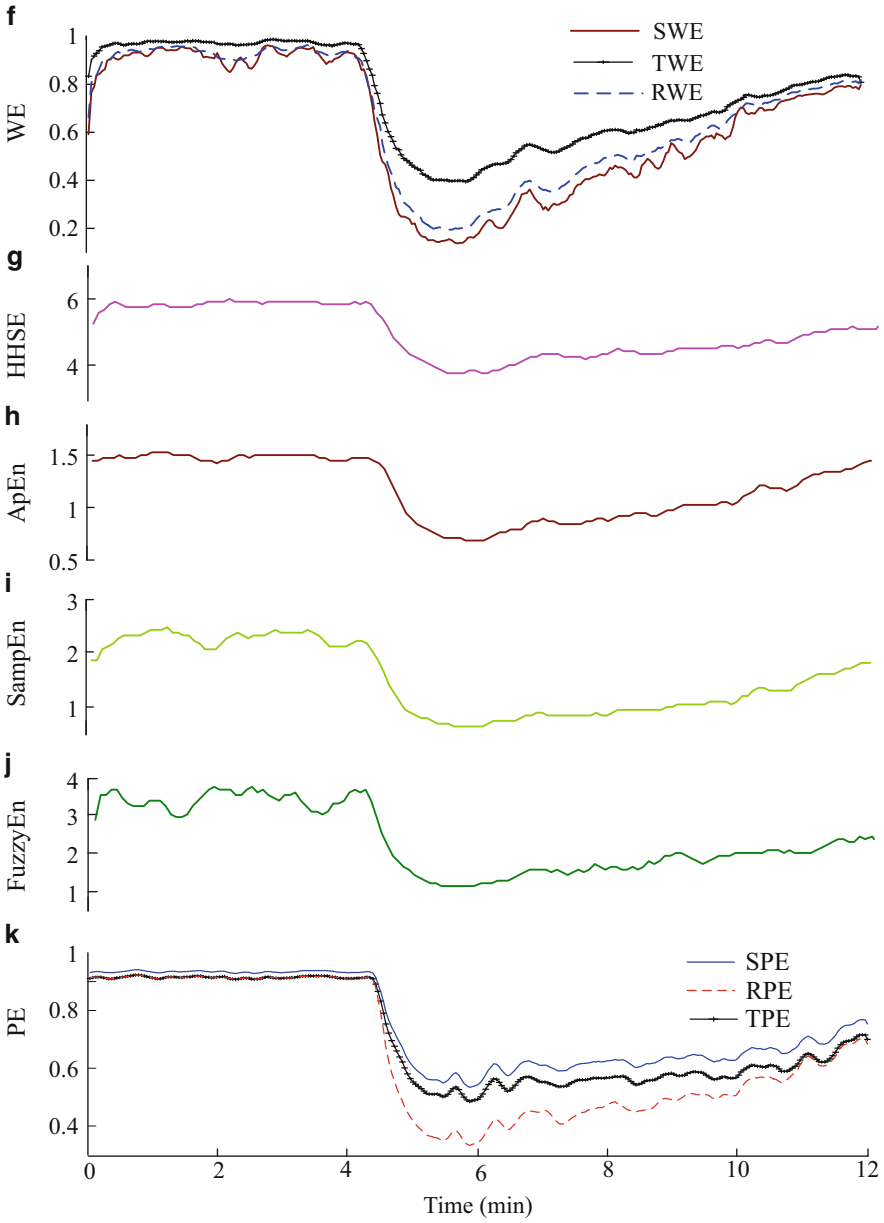

Fig. 8.3 (continued)

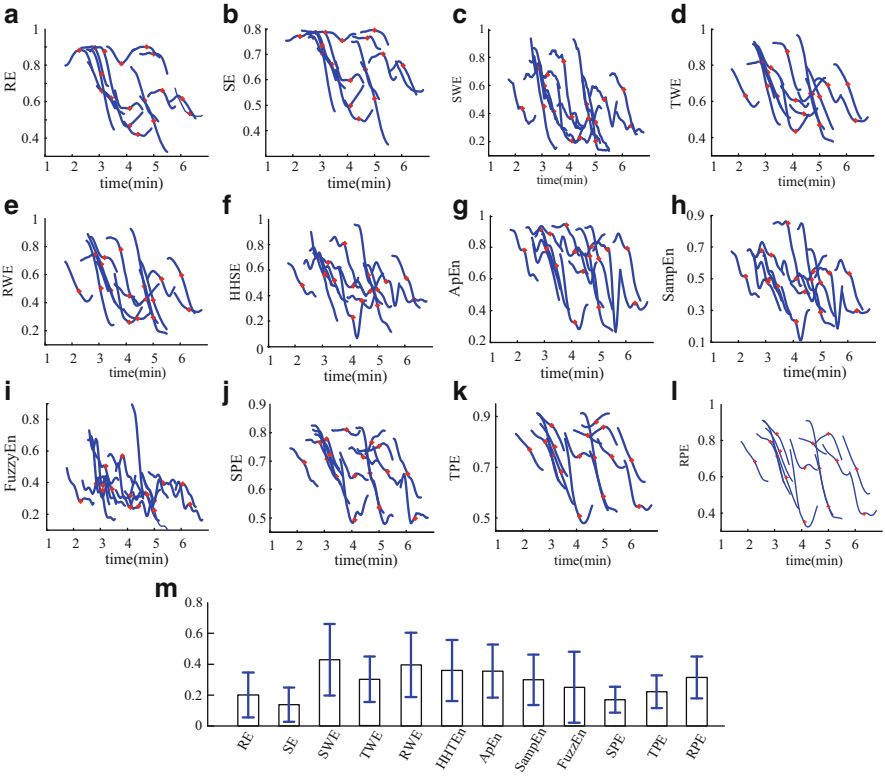

Fig. 8.4 Entropy analysis around the time of LoC for subject undergoing sevoflurane anesthesia (n = 19). (**a**–**l**) The normalized indices around LoC (from LoC − 30 s to LoC + 30 s) for all subjects. The *red* plus sign denotes the point of LoC. (**m**) Statistical analysis of the absolute slope of the linear-fitted polynomials versus time for studied indices. *Bar* height indicates the mean value, and the *lower* and *upper* lines are the 95 % confidence interval of each index

normalized to range from 0 to 1. It can be seen from Fig. 8.4a–l that SWE decreased most rapidly, followed by RWE. Thus, SWE appeared to be the most sensitive to LoC. To verify this, we calculated the absolute slope values (mean ± SD) of the linear-fitted polynomials versus time for these indices, as shown in Fig. 8.4m. As can be seen, the absolute slope value for SWE (0.43 ± 0.23) is the largest.

To further compare the ability of the indices to distinguish different anesthesia states, the sevoflurane anesthesia procedure was divided to describe four states, ie, awake, induction, deep anesthesia, and recovery. For each index, a box plot is given in Fig. 8.5. The data was not normally distributed, so the statistics of the 19 patients undergoing sevoflurane anesthesia were expressed as median (min–max), as shown in Table 8.1. All the entropy indices monotonically decreased as anesthesia deepened, then increased during recovery. These changes were consistent with the results in Fig. 8.3. The overlap of the three types of PE (SPE, TPE, and RPE) values

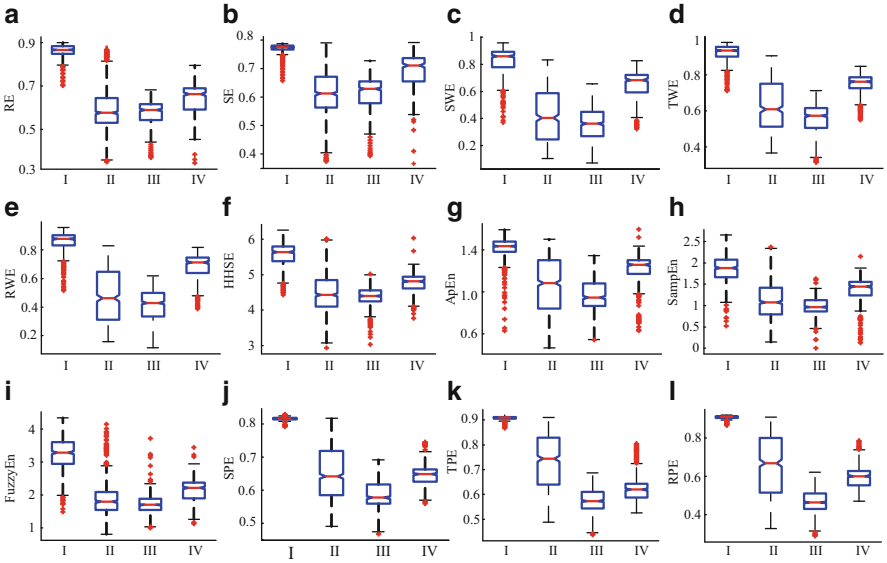

Fig. 8.5 *Box plots* of RE, SE, SWE, TWE, RWE, HHSE, ApEn, SampEn, FuzzyEn, SPE, TPE, and RPE at awake (I), induction (II), deep anesthesia (III), and recovery (IV) states

Table 8.1 The statistics of the studied indices at different anestehsia states (median (min–max))

	Awake	Induction	Deep anesthesia	RoC
RE	0.87 (0.65–0.90)	0.58 (0.35–0.89)	0.59 (0.37–0.68)	0.66 (0.34–0.79)
SE	0.77 (0.65–0.79)	0.61 (0.37–0.79)	0.63 (0.39–0.73)	0.71 (0.37–0.79)
SWE	0.86 (0.37–0.96)	0.40 (0.10–0.83)	0.36 (0.07–0.66)	0.68 (0.32–0.83)
TWE	0.93 (0.71–0.98)	0.61 (0.37–0.91)	0.57 (0.32–0.71)	0.76 (0.55–0.85)
RWE	0.88 (0.52–0.96)	0.46 (0.16–0.83)	0.43 (0.12–0.62)	0.71 (0.39–0.82)
HHSE	5.63 (4.43–6.26)	4.43 (2.93–6.01)	4.40 (3.02–5.02)	4.81 (3.76–6.03)
ApEn	1.44 (0.63–1.59)	0.95 (0.54–1.35)	1.08 (0.47–1.50)	1.26 (0.63–1.60)
SampEn	1.88 (0.52–2.65)	1.08 (0.15–2.37)	0.97 (0.01–1.63)	1.44 (0.13–2.16)
FuzzyEn	3.28 (1.49–4.33)	1.80 (0.81–4.14)	1.70 (1.01–3.72)	2.22 (1.13–3.44)
SPE	0.81 (0.79–0.83)	0.64 (0.49–0.82)	0.58 (0.46–0.82)	0.65 (0.56–0.75)
TPE	0.91 (0.87–0.92)	0.74 (0.49–0.91)	0.57 (0.44–0.69)	0.62 (0.53–0.80)
RPE	0.91 (0.87–0.92)	0.67 (0.33–0.91)	0.46 (0.29–0.62)	0.60 (0.47–0.79)

RE response entropy in the M-entropy module, *SE* state entropy, *SWE* Shannon wavelet entropy, *TWE* Tsallis wavelet entropy, *RWE* Renyi wavelet entropy, *HHSE* Hilbert–Huang spectral entropy, *ApEn* approximate entropy, *SampEn* sample entropy, *FuzzyEn* fuzzy entropy, *SPE* Shannon permutation entropy, *TPE* Tsallis permutation entropy, *RPE* Renyi permutation entropy

Table 8.2 The CV of the studied indices at different anestehsia states

	Awake	Induction	Deep anesthesia	RoC
RE	0.025	0.149	0.047	0.052
SE	0.016	0.122	0.047	0.050
SWE	0.080	0.338	0.177	0.077
TWE	0.024	0.161	0.063	0.038
RWE	0.043	0.276	0.127	0.057
HHSE	0.029	0.089	0.027	0.024
ApEn	0.040	0.193	0.064	0.043
SampEn	0.095	0.259	0.087	0.094
FuzzyEn	0.089	0.193	0.088	0.073
SPE	0.006	0.115	0.028	0.025
TPE	0.003	0.138	0.030	0.028
RPE	0.004	0.219	0.043	0.041

between the awake and deep anesthesia states was smaller than the other indices. This means PE has a better ability to separate these states and a greater robustness to individual differences.

To estimate the baseline variability and the sensitivity to the induction process of each index, the CV values of all the indices for the sevoflurane data set are computed, and the results are given in Table 8.2. During the awake state, the CV value of SampEn was 0.095 which was the highest. The CV value of TPE was 0.003, significantly lower than the other indices. The CV values of SPE and RPE were also very low. This illustrated that PE measures were less sensitive to noise, while SampEn methods were the least robust against noise. During induction, the CV of SWE (0.338) was the highest. This demonstrated that SWE had a faster response speed compared to the other indices.

To further compare the performance of the studied indices, PK/PD modeling was performed to describe the relationship between the index values and the estimated sevoflurane effect-site concentration. Table 8.3 gave these parameters for sevoflurane anesthesia, in which the maximum coefficient of determination (R^2) gave the correlation between the index values and the anesthetic effect-site concentration. Figure 8.6 showed the R^2 values of the indices for the data sets. It can be seen that the R^2 for TPE (0.95, 95 % confidence interval 0.92–0.98) was significantly higher than the other entropy indices.

To assess how the indices could correctly predict the drug effect-site concentrations, we evaluated the prediction probability P_k of all the indices from the PK/PD modeling for all the subjects, as shown in Fig. 8.7, and the statistical results are shown in Table 8.4. For sevoflurane, the P_k of RPE is equal (0.87, 95 % confidence interval is 0.83–0.90), slightly higher than RWE (0.85) and TWE 0.81 (95 % confidence interval 0.79–0.84). Also, the P_k of RPE was higher than that of TPE and SPE. Similarly, the P_k of RWE was the highest in the three WE methods. It meant that the Renyi entropy had a better performance in predicting drug effect-site concentrations compared with the Shannon entropy and Tsallis entropy. The

Table 8.3 The PK/PD modeling parameters for sevoflurane

	$t_{1/2}k_{eo}$ (min)	γ	E_{max}	E_{min}	EC_{50}	R^2
RE	0.04 ± 0.03	8.25 ± 7.62	0.46 ± 0.09	0.13 ± 0.06	1.19 ± 0.60	0.80 ± 0.14
SE	0.06 ± 0.06	5.22 ± 2.32	0.35 ± 0.09	0.14 ± 0.05	1.71 ± 0.93	0.72 ± 0.16
SWE	0.07 ± 0.02	4.01 ± 3.12	1.01 ± 0.16	0.15 ± 0.07	1.42 ± 0.51	0.79 ± 0.12
TWE	0.03 ± 0.01	3.81 ± 1.86	0.50 ± 0.10	0.05 ± 0.16	1.54 ± 0.63	0.86 ± 0.06
RWE	0.04 ± 0.02	5.95 ± 3.98	0.58 ± 0.10	0.12 ± 0.07	1.68 ± 0.60	0.85 ± 0.06
HHSE	0.05 ± 0.02	4.15 ± 3.43	1.99 ± 0.41	0.62 ± 0.34	1.56 ± 1.15	0.80 ± 0.06
ApEn	0.05 ± 0.02	8.22 ± 6.62	0.82 ± 0.17	0.22 ± 0.11	1.84 ± 0.52	0.78 ± 0.11
SampEn	0.05 ± 0.02	5.68 ± 4.45	1.46 ± 0.38	0.40 ± 0.22	1.64 ± 0.62	0.75 ± 0.12
FuzzyEn	0.06 ± 0.04	2.75 ± 1.54	2.14 ± 0.40	0.58 ± 0.32	1.05 ± 0.38	0.69 ± 0.17
SPE	0.70 ± 0.32	4.65 ± 1.57	0.32 ± 0.05	0.08 ± 0.03	1.30 ± 0.33	0.94 ± 0.04
TPE	0.18 ± 0.01	6.98 ± 3.19	0.39 ± 0.04	0.02 ± 0.12	1.33 ± 0.37	0.96 ± 0.02
RPE	0.02 ± 0.01	4.67 ± 3.25	0.50 ± 0.14	0.10 ± 0.16	1.40 ± 0.48	0.95 ± 0.03

$t_{1/2}k_{eo}$ = blood effect-site equilibration constant
γ = slope parameter of the concentration–response relation
E_{max} = EEG parameter value corresponding to the maximum drug effect
E_{min} = EEG parameter value corresponding to the minimum drug effect
EC_{50} = concentration that causes 50 % of the maximum effect
R^2 = maximum coefficients of determination

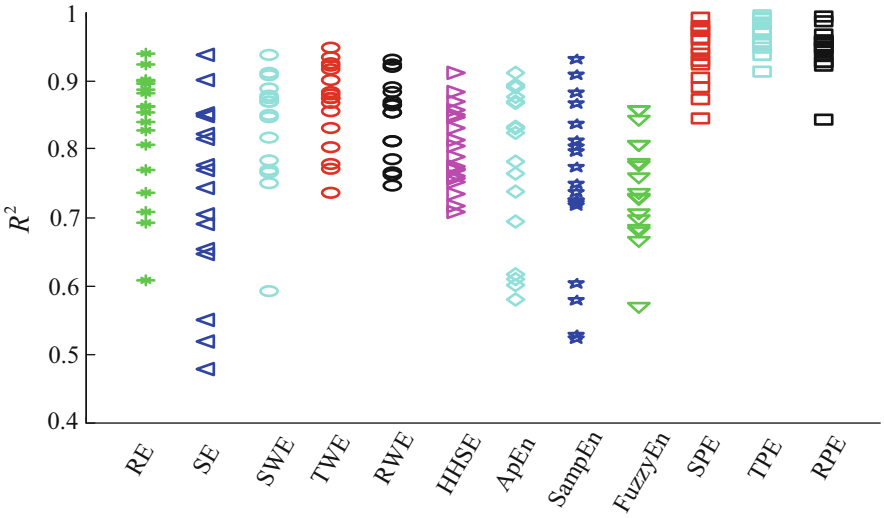

Fig. 8.6 Maximum coefficient of determination values for sevoflurane anesthesia (n = 19). For comparison, the R^2 values for each index are expressed by a different sign and color

differences between RPE and the other indices were statistically significant (all $p < 0.005$, paired t-test). And the difference between RPE, TPE, and SPE were statistically significant ($p = 0.03$ and 0.01, respectively; paired t-test), which meant that RPE had a stronger ability to track the sevoflurane effect-site concentration

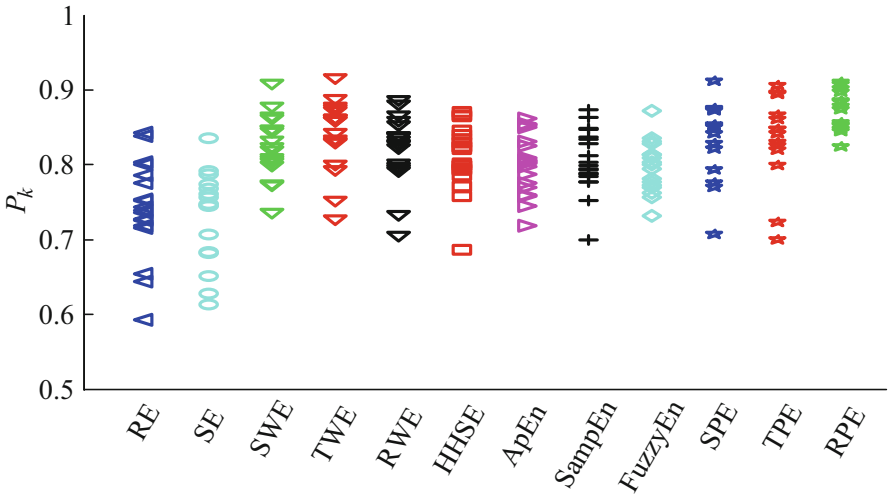

Fig. 8.7 Statistical analysis of prediction probability (P_k) values for sevoflurane (n = 19)

Table 8.4 The P_k statistics for each entropy index

Entropy index	P_k Sevoflurane
RE	0.74 ± 0.06
SE	0.73 ± 0.06
SWE	0.83 ± 0.04
TWE	0.84 ± 0.05
RWE	0.85 ± 0.05
HHSE	0.81 ± 0.04
ApEn	0.80 ± 0.04
SampEn	0.81 ± 0.03
FuzzyEn	0.80 ± 0.03
SPE	0.83 ± 0.05
TPE	0.83 ± 0.06
RPE	0.87 ± 0.03

during anesthesia. In order to get a more intuitive comparison, the best curve fits of all indices against the effect-site concentration are demonstrated (Fig. 8.8).

To compare the timeliness performance of each index in tracking DoA, we recorded the computing time of each index for the same subject. Twenty EEG recordings from the two data sets were selected. The calculated epoch length (N) of each algorithm was 10 s, and the overlap was 5.0 s. The computing time for 1 min EEG data for each index was given in Table 8.5. The fastest index was WE (0.025 ± 0.001 s). The RE/SE and PE computation times were 0.096 ± 0.008 s and 0.545 ± 0.016 s, respectively. HHSE (14.718 ± 1.563 s) was the slowest. The desktop computer used for this test had the following configuration: Intel Core i3 CPU, four cores at 2.93 GHz, with 2GB of RAM, and running Windows XP professional operating system.

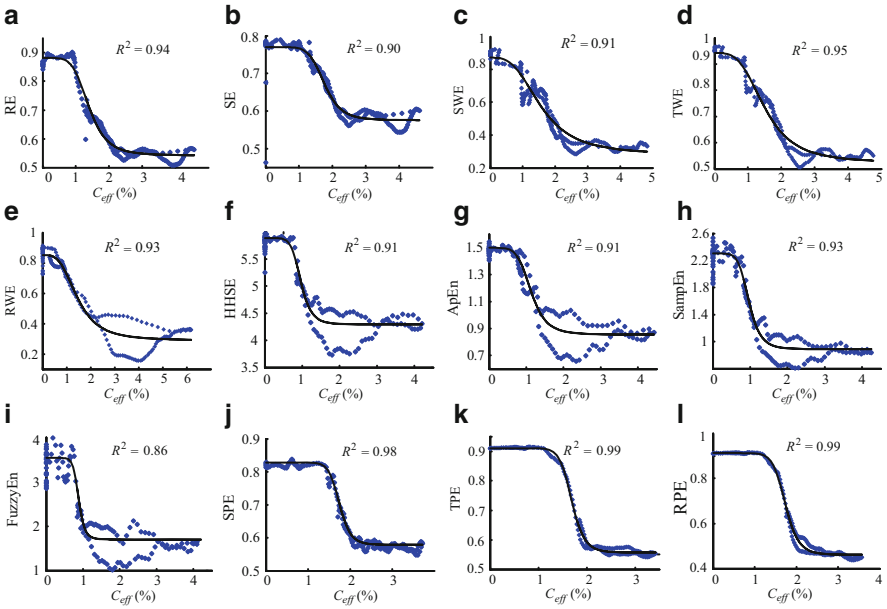

Fig. 8.8 Dose-response curves between the RE(**a**), SE(**b**), SWE(**c**), TWE(**d**), RWE(**e**), HHSE(**f**), ApEn(**g**), SampEn(**h**), FuzzyEn(**i**), SPE(**j**), TPE(**k**), RPE (**l**), and the sevoflurane C_{eff} for the best fit, with the greatest value of R^2 shown above the figures. The *dots* denote the measured EEG index values. The *solid lines* denote the PK/PD-modeled EEG index values

Table 8.5 The computing time for different entropy indices for 1 min data length

Entropy index	Calculation time(s)
RE/SE	0.096 ± 0.008
SWE/RWE/TWE	0.025 ± 0.001
HHSE	14.718 ± 1.563
ApEn	2.490 ± 0.098
SampEn	2.541 ± 0.073
FuzzyEn	4.785 ± 0.119
SPE/RPE/TPE	0.545 ± 0.016

8.4.5 MSE Comparison with CG- and MA-Decomposed Procedures

Although there are various MSE measures, we only considered multi-scale sample entropy and multi-scale permutation entropy. And the decomposed procedures of CG and MA were also considered. The traditional MSEs were based on the CG decomposed procedure. So, MA-SampEn, MA-SPE, MA-TPE, and MA-RPE were first proposed in this study.

Figure 8.9 showed the six multi-scale permutation entropy measures applying to the same data set used above. The scale of s = 1, 2, 3, and composed scale index

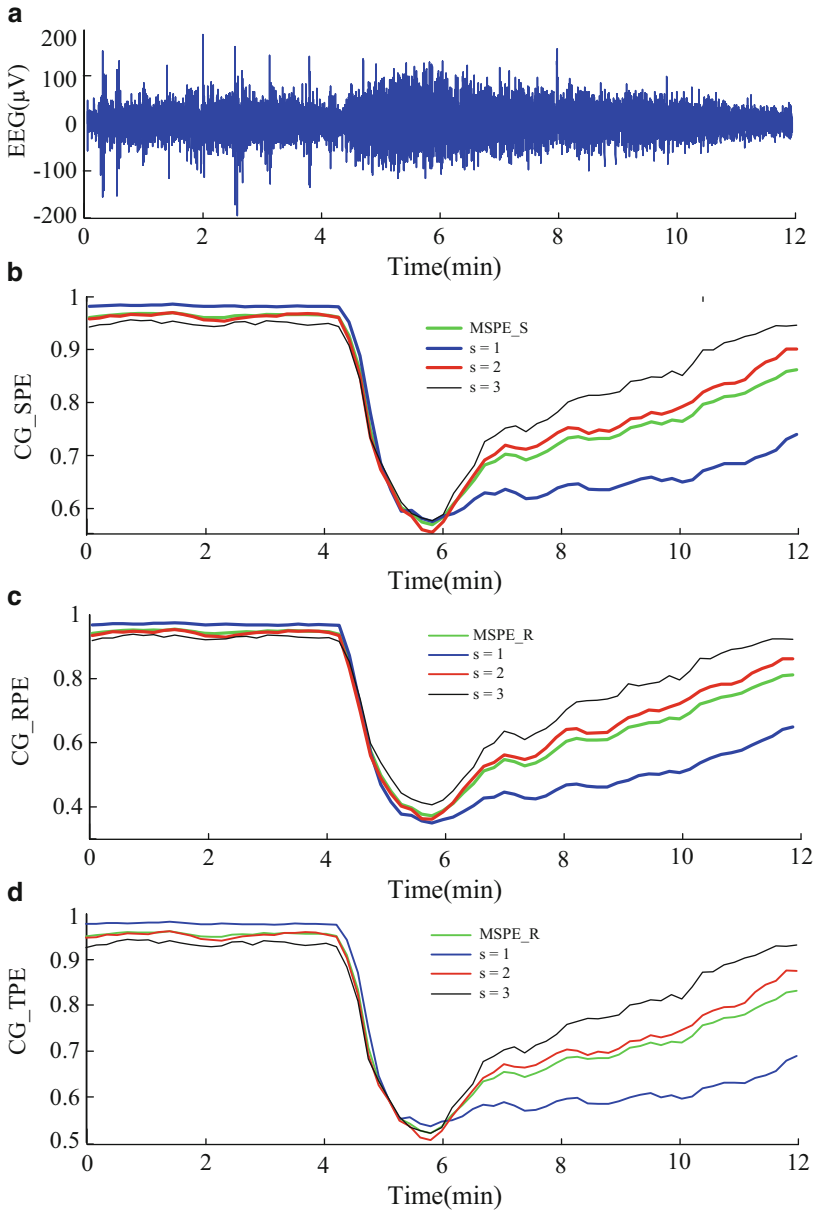

Fig. 8.9 The EEG signal (**a**) and MSPE of SPE (**b**), RPE (**c**), and TPE (**d**) at scales 1, 2, 3, and composed MSPE indices

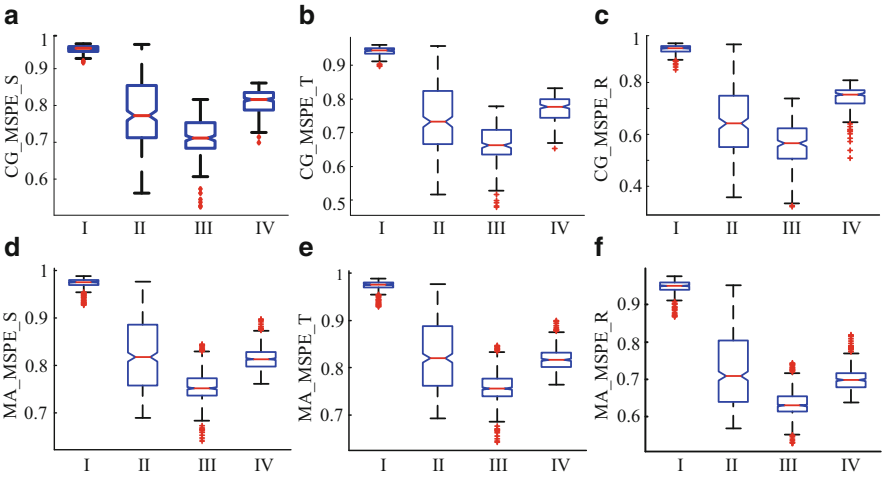

Fig. 8.10 The box plots of MSPE based on CG- and MA-decomposed procedure. (**a**)–(**c**) The MSPE with CG of the Shannon permutation entropy (**a**), Tsallis permutation entropy (**b**), and Renyi permutation entropy (**c**). (**d**)–(**f**) The MSPE with MA of the Shannon permutation entropy (**d**), Tsallis permutation entropy (**e**), and Renyi permutation entropy (**f**)

(the mean of s = 1, 2, and 3) with each entropy were plotted in Figure b–d. It can be seen that all the curves could track the changes of anesthesia. Considering the decomposed procedure, the parameters of MSPE were different from the single-scale PE. The selection details were discussed in Sect. 8.3.2. It can be seen from the figures that there was no big difference between MSPE for s = 1, 2, 3, and composed measures. Only the composed scale measures of MSPE were calculated for all the subjects for statistics.

The box plots of composed scale MSPE with six multi-scale permutation entropies were shown in Fig. 8.10. The results showed that all the MSPE with composed measures could distinguish different anesthesia states like the single-scale PE (such as SPE, TPE, and RPE) did.

The multi-scale sample entropy measures based on CG and MA analysis were shown in Fig. 8.11. It was obvious that the MSSE showed bigger fluctuations in the awake state compared with the MSPE indices. The box plots of CG-SampEn and MA-SampEn for s = 1, 2, 3, and the composed scale measures were shown in Figs. 8.12 and 8.13, respectively. The statistics of all MSPE and MSSE indices were shown in Table 8.6 and 8.7. The CVs of the CG-SPE, MA-SPE, and MA-TPE were 0.005 (mean) at the awake state, which were the smallest in all the MSE measures. Compared with MSSE, MSPE had smaller CVs during the awake state. It meant that MSPE has better antinoise performance than MSSE. Moreover, CG-RPE in induction processes had the highest CV (0.197) in all MSPE measures, which meant that CG-RPE was more sensitive to the anesthesia-state changes.

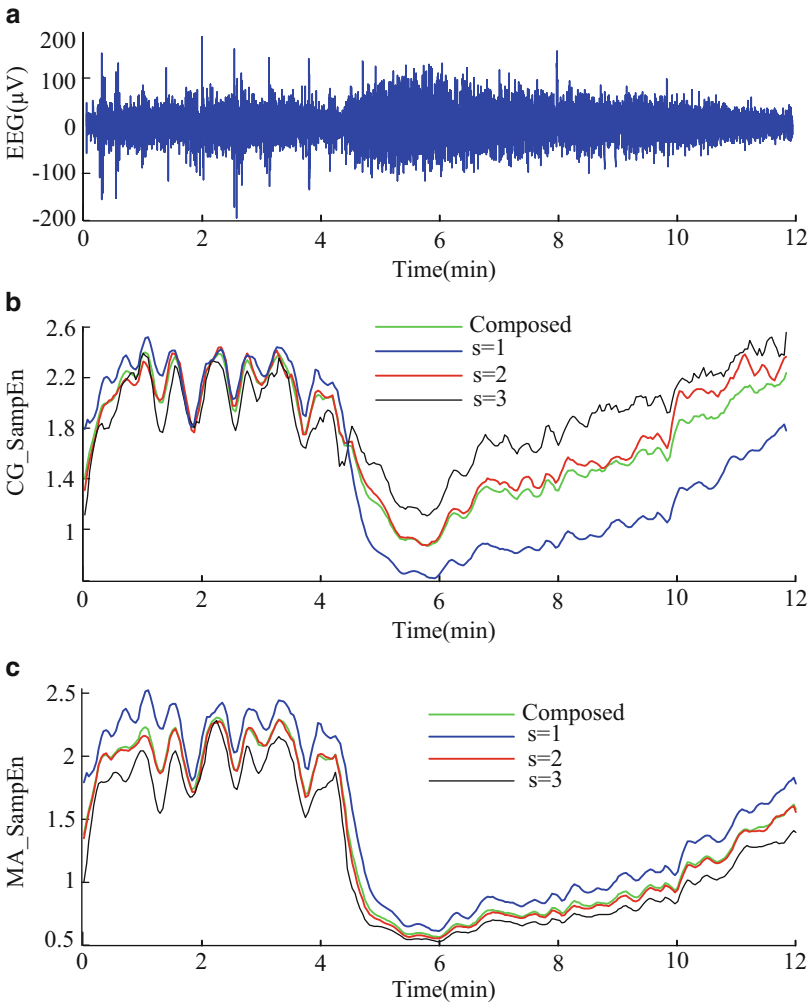

Fig. 8.11 The raw EEG and the corresponding multi-scale sample entropy measures

8.5 Conclusions

In this study, we investigated the performance of twelve entropy algorithms and two kinds of MSE (MSPE and MSSE) measures to assess the effect of GABAergic anesthetic agents on EEG activity. The EEG data under sevoflurane anesthesia were employed as the test samples for evaluating the different entropy algorithms. We compared their performance in estimating DoA. PK/PD modeling and prediction probability statistics were applied to assess their effectiveness. In order to make the

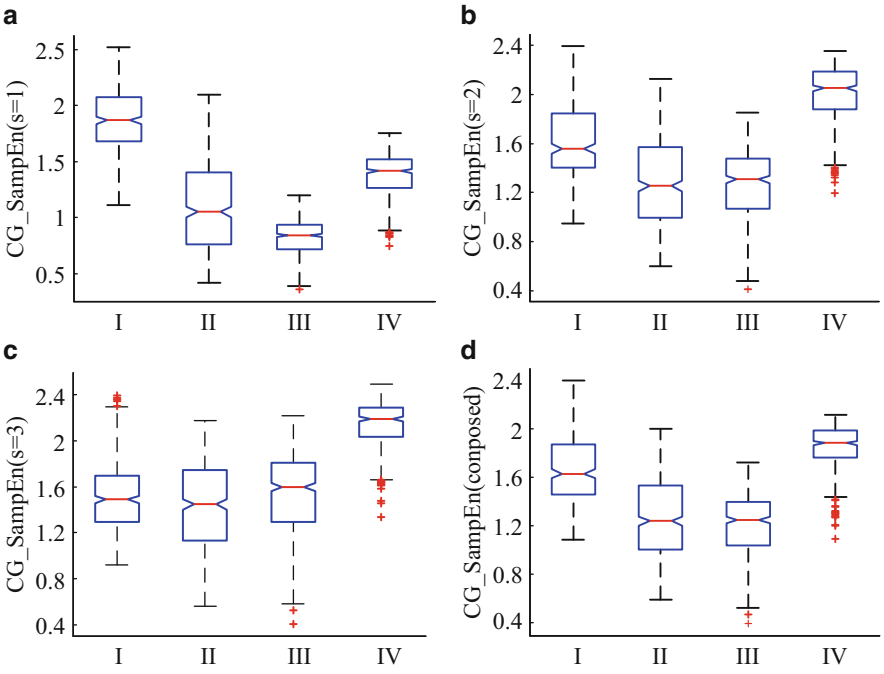

Fig. 8.12 The MSSE based on CG-decomposed procedure at s = 1(**a**), s = 2(**b**), s = 3(**c**), and the composed measures

comparisons more clear, the single-scale entropy (12 entropy measures) and multi-scale entropy measures were assessed separately.

Firstly, the twelve entropy measures were divided into two classes: time–domain-based and time–frequency–domain-based analyses. ApEn, SampEn, FuzzyEn, and PE are time–domain analysis methods. All these entropy algorithms are based on nonlinear theories, and the first three are phase space analytical methods (Chen et al. 2009). PE is based on ordinal pattern analysis of the time series (Bandt 2005). Considering that EEG has nonlinear characteristics, these four methods have their respective advantages. For example, FuzzyEn and PE are less sensitive to the signal quality and calculation length (Li et al. 2008a; Pincus 1991). Compared with ApEn and SampEn, FuzzyEn can resolve more details in the time series and has more accurate definition in theory (Chen et al. 2009). RE, SE, WE, and HHSE indices are based on the time–frequency domain. The start point of RE and SE is the spectral entropy, which has the particular advantage that the contributions to entropy from any particular frequency range are explicitly separated. In order to achieve optimal response time, RE and SE adopt variable time windows for each particular frequency called time–frequency-balanced spectral entropy (Viertiö-Oja et al. 2004). Compared with the variable time windows of RE and SE, the window function of WE is variable in both time and frequency domains. The

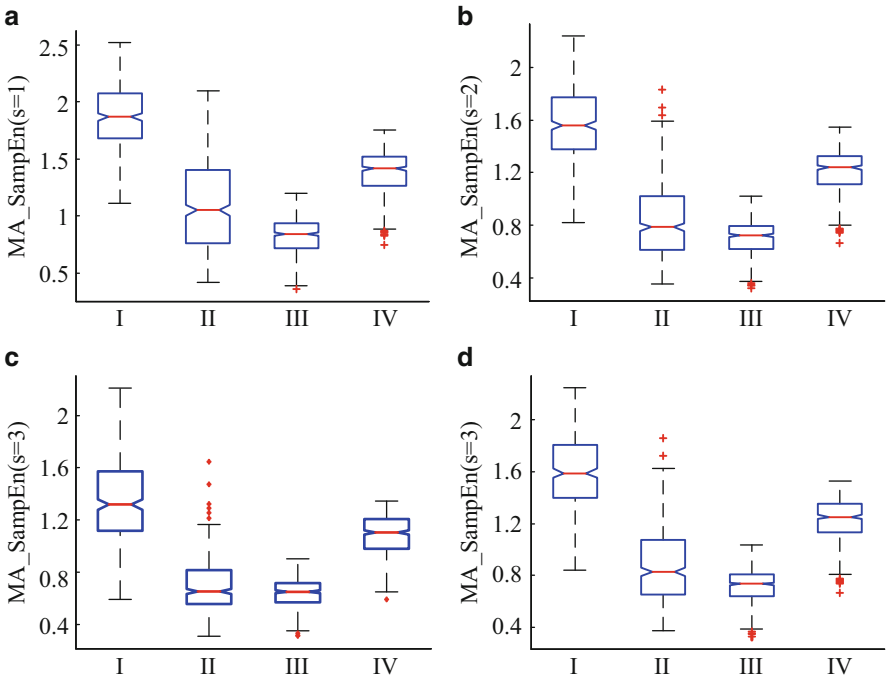

Fig. 8.13 The MSSE based on MA-decomposed procedure at s = 1(**a**), s = 2(**b**), s =3 (**c**), and the composed (**d**) scale

HHSE algorithm is based on the EMD and Hilbert transform (Li et al. 2008b). The advantage of this method is that it can estimate the instantaneous amplitude and phase/frequency. Also it can break down a complicated signal without a basis function (such as sine or wavelet functions) into several oscillatory modes that are embedded in this complicated signal. The marginal spectrum gives a more accurate and nearly continuous distribution of EEG energy, which is completely different from the Fourier spectrum (Li et al. 2008b).

Although all the entropy algorithms have theoretical advantages with respect to the characterization of EEG recordings during GABAergic anesthesia, we still need to assess their practical performance from several perspectives. In qualitative terms, all the indices are effective at tracking the changes of drug concentration through the EEG analysis. As demonstrated in the presented figures and tables, all the entropies decreased with the deepening of anesthesia. However, there are quantitative differences between these indices for assessing different anesthesia states. This is because the principles underlying each algorithm are entirely different. Entropies based on the time domain measure the predictability of future amplitude values of the electroencephalogram based on the knowledge of one or two previous amplitude values. With increasing GABAergic anesthetic drug concentration, the EEG signals become more regular, which leads to a reduction in the ApEn value. Entropies based

Table 8.6 The statistics of the MSE indices at different anestehsia states (median (min-max))

	Awake	Induction	Deep anesthesia	RoC
CG-SPE	0.96 (0.92–0.97)	0.77 (0.56–0.97)	0.71 (0.52–0.82)	0.82 (0.70–0.86)
CG-TPE	0.94 (0.90–0.96)	0.73 (0.52–0.96)	0.66 (0.48–0.78)	0.78 (0.65–0.83)
CG-RPE	0.93 (0.85–0.95)	0.64 (0.36–0.95)	0.57 (0.32–0.74)	0.76 (0.51–0.81)
MA-SPE	0.97 (0.93–0.99)	0.82 (0.69–0.98)	0.75 (0.64–0.84)	0.81 (0.76–0.90)
MA-TPE	0.98 (0.93–0.99)	0.82 (0.69–0.98)	0.76 (0.64–0.85)	0.82 (0.76–0.90)
MA-RPE	0.95 (0.87–0.97)	0.71 (0.57–0.95)	0.63 (0.53–0.74)	0.70 (0.64–0.82)
CG-SampEn (composed)	1.63 (1.09–2.40)	1.24 (0.59–2.00)	1.25 (0.40–1.73)	1.88 (1.09–2.12)
MA-SampEn (composed)	1.59 (0.88–2.24)	0.83 (0.38–1.86)	0.74 (0.33–1.04)	1.25 (0.67–1.53)

CG-SPE coarse-graining Shannon permutation entropy, *CG-TPE* coarse-graining Tsallis permutation entropy, *CG-RPE* coarse-graining Renyi permutation entropy, *MA-SPE* moving-average Shannon permutation entropy, *MA-TPE* moving-average Tsallis permutation entropy, *MA-RPE* moving-average Renyi permutation entropy, *CG-SampEn* coarse-graining sample entropy, *MA-SampEn* moving-average sample entropy

Table 8.7 The CV of the studied indices at different anestehsia states

	Awake	Induction	Deep anesthesia	RoC
CG-SPE	0.005	0.112	0.03	0.03
CG-TPE	0.006	0.126	0.037	0.031
CG-RPE	0.008	0.197	0.073	0.046
MA-SPE	0.005	9.075	0.017	0.019
MA-TPE	0.005	0.074	0.017	0.018
MA-RPE	0.009	0.111	0.022	0.027
CG-SampEn (composed)	0.035	0.069	0.068	0.051
MA-SampEn (composed)	0.034	0.085	0.058	0.063

on the time–frequency domain, such as RE and SE, also decrease with increasing DoA because the EEG shifts to a simpler frequency pattern as the anesthetic dose increases (Rampil 1998).

In all of the 12 entropy measures, TWE, RWE, TPE, and RPE are based on the Tsallis entropy and Renyi entropy theories, respectively. The Tsallis entropy and Renyi entropy theories are considered as generalized entropy compared to the Shannon entropy. Similar to the Renyi entropy, the Tsallis entropy used the non-extensive parameter q to measure the information of specific events. The results showed that TPE and RPE were better than SPE in assessing the effects of anesthesia. Similar results also can be seen in TWE, RWE, and SWE. The excellent performance indicates their potential usefulness in anesthesia analysis.

Furthermore, four measures were considered for the evaluation of each index. Firstly, the coefficient of determination and prediction probability statistics were used to assess the correlation of each index with the anesthetic drug effect-site concentration. Three PE measures had a higher P_k and R^2 compared to the

other indices. Secondly, CV was used to evaluate the sensitivity of each index to artifacts during the awake state (Li et al. 2008b, 2010). The results showed that PE outperformed the other indices at this level. In all entropy measures, SWE had the highest CV during anesthesia induction, indicating that this index was superior at discriminating awake and anesthetized states. Thirdly, the performance for estimating the point of LoC was considered. Although all the entropy measures could distinguish between awake and anesthetized states (see Fig. 8.4), the speed of transition (slope) between the two states was fastest for SWE, while SE had the slowest transition. Finally, the computing time was used to assess algorithm complexity. The results showed that the WE index is the fastest algorithm of all the entropy indices tested. HHSE was the slowest: its computing time for the same data length was about 580 times longer than that of WE. In order to improve the computational efficiency, the parallelized method based on the graphics processing unit has been proposed (Chen et al. 2010).

The multi-scale entropy provides a new perspective in neural population analysis. Although there are various multi-scale decomposition procedures and entropy measures (Li et al. 2010; Costa et al. 2002; Ahmed and Mandic 2011; Park et al. 2007), few of current MSE studies offer systematic analysis of the performance of MSE measures. In this chapter, two kinds of entropy measures (PE and SampEn) based on two multi-scale decomposition procedures (CG and MA) were analyzed.

As we know, there were other multi-scale decomposition methods, such as wavelet transform (WT) and empirical mode decomposition (EMD) (Unser and Aldroubi 1996; Hsu et al. 2007; Stamoulis et al. 2011), and they provided excellent performance in time–frequency–domain analysis. Other entropies, such as ApEn (Costa et al. 2002; Pincus 1991) and FuzzyEn (Zou and Lei 2012), were also used to form MSE measures, while PE and SampEn has been proved to be better than the others. Further, as a symbolic dynamic method, PE was not suitable to join with time–frequency–domain analysis, ie, WT and EMD. Therefore, only CG and MA were considered to form multi-scale decomposition methods.

In terms of the two decomposition procedures CG and MA, from the aspect of algorithm mechanism, each procedure has its advantages and disadvantages. Both of them are typical morphology methods. The CG procedure reduces the length of a time series with the increase of scale. It is superior in long-term time series analysis but may yield an imprecise estimation of entropy in short-term time series (Wu et al. 2013). For this reason, CG-based MSPEs have poor performance in tracking EEG signals. MA procedure solves this problem but brings computing redundancy.

Through the real data analysis, the antinoise ability, the ability to track the strength change of neural oscillations, and the sensitivity of distinguishing the different mental states of the six MSPE and two MSSE measures were evaluated and concluded as follows:

(i) The MSPE measures have a better antinoise ability than MSSE measures. For MSPE, with the increase of scales, the differences of distinguishing different anesthesia states are negligible, but the ability of antinoise increases. And MA-TPE at scale 3 performs the best.

(ii) All the MSEs at scale = 1, 2, 3, and composed scale measures have the same trend in tracking the strength change of neural oscillations. MA-RPE is more sensitive in tracking the changes of different anesthesia states.
(iii) Considering the data length and the characteristics of real-time computing, the CG-SPE, CG-RPE, CG-TPE, and CG-SampEn indices may be not suitable for analyzing anesthesia EEG recordings.

In conclusion, we gave an in-depth comparison of the twelve single-scale entropy measures and eight MSE measures. The results may provide valuable references to neural signal analysis, especially for the evaluation of anesthetic effects. In particularly, the PE indices, especially RPE measure, performed better than the other entropy indices in several aspects. However, some other issues should be addressed and need to be further explored. Firstly, we only assessed the performance of different measures on anesthesia EEG data sets. In consideration of the complexity of neural populations, the conclusions may not be suitable for all neurophysiological signals. Secondly, for the MSE measures, how to combine the different scales to better reflect the inner characteristics of the nonlinear signals should be further studied. In addition, to develop a useful tool as a dependable clinical measure, each entropy measure still needs additional optimization of parameters.

Appendices

Each entropy index contains several parameters, which can severely impact the output of its index. Therefore, it is very important to select the appropriate parameters. In anesthesia researches, there are many methods to select parameters including the interindividual variations, eg, the relationship with drug effect-site concentration obtained from PK/PD and prediction probability (Li et al. 2012, [88]). In this study, the method of selecting the parameters is based on indices' performance in distinguishing different anesthesia states and interindividual variations. Fifty data sets in awake, deep anesthesia, and recovery states from 19 patients are selected, respectively. The RE and SE algorithms applied in the study adopts the Datex–Ohmeda S/5™ entropy module (Viertiö-Oja et al. 2004). The PE's parameter selection is based on our previous work (Li et al. 2012, 2010). The details of other entropy algorithm's parameters are discussed as follows. All the results are given by mean ± standard deviation. The blue, red, and green colors represent the awake state, deep anesthesia state, and recovery state, respectively.

Appendix A: WE

There are three types of WE measures (SWE, TWE, RWE) considered in this study. The parameters include basis functions, the data length N, the Tsallis entropy parameter q, and the Renyi entropy parameter a. The basis functions and data

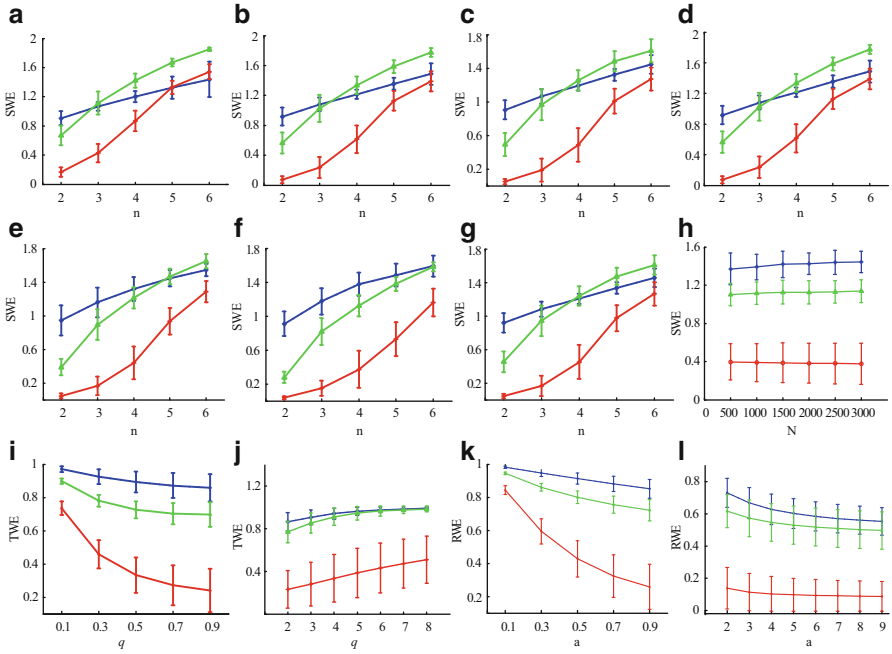

Fig. 8.14 The changes of WE in different anesthesia with different parameters. (**a**–**g**) The change of SWE with different wavelet basis functions: (**a**) haar, (**b**) db2, (**c**) coif2, (**d**) sym2, (**e**) bior2.2, (**f**) bior3.3, and (**g**) bior4.4. The horizontal axis shows the number of layers (n) decomposed by corresponding wavelet function. The vertical axis shows SWE values. (**h**) The changes of SWE with different N. (**i**–**j**) The changes of TWE with $0 < q < 1$ (*i*) and $q > 1$ (*j*). (**k**–**l**) The changes of RWE with $0 < a < 1$ (**k**) and $a > 1$ (**l**)

length selection are based on the SWE. First, several common basis functions including Haar, Daubechies, Coiflets, Symlets, and Biorthogonal wavelet families were selected. The result is shown in Fig. 8.14a–e. N is assumed to be 1000. As can be seen, only the SWE based on the biorthgonal basis function can completely separate anesthesia state (red color) from awake (blue color), and recovery states (green color), without overlap. However, there are some basic functions in the biorthgonal family. Figure 8.14e–g show the results obtained by bior2.2, bior3.3, and bior4.4. It can be seen that the SWE achieved by bior3.3 not only distinguishes anesthesia states from non-anesthesia but also differentiates between awake and recovery states, especially when the number of layers is 2 and 3. So in this study, the bior3.3 was chosen as the wavelet basis function, and the number of layers was 3. Then, based on them, the selection of N is given in Fig. 8.14h. N ranges from 500 to 3000 points with the step of 500 points under the sample of 100 Hz. The figure shows that when $N \geq 1000$, there is no significant difference in WE for each state. So $N = 1000$ (10 s) was selected to calculate the WE. Furthermore, based on the parameters of basis function and N, the selections of q in TWE and a in RWE are given in Fig. 8.14i–l.

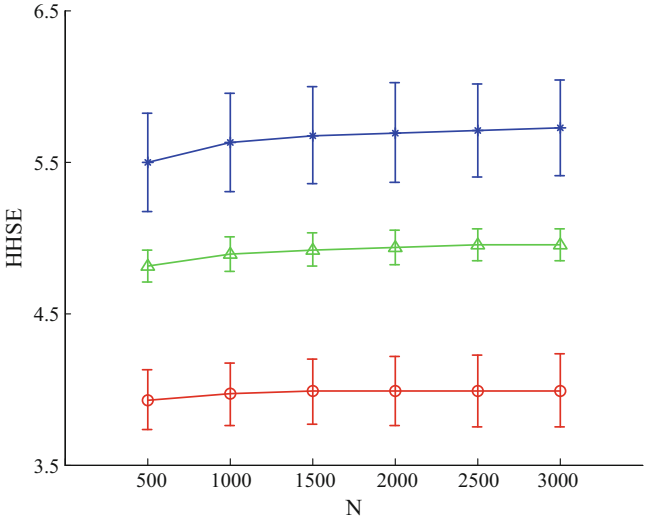

Fig. 8.15 The change of HHSE with different N at different anesthesia states. N is from 500 to 3000 stepped by 500 points

Appendix B: HHSE

In order to choose an appropriate data length N in HHSE algorithm at the sample rate of 100 Hz, a series of N were used to calculate the HHSE in different anesthesia states. The result is shown in Fig. 8.15. All values of N could distinguish different anesthesia states. And when the data length was equal to or greater than 1000, the HHSE value would be nearly invariable with the changes of N. So $N = 1000$ (10 s) was selected in this study.

Appendix C: ApEn

Figure 8.16a–b, respectively, give the result of ApEn over different r in different anesthesia states with $N = 1000$, $m = 2$, and $m = 3$. With increasing r, the ApEn values in awake state and recovery state increased and then decreased, while it monotonously changes with r in deep anesthesia state. Both figures show that when r is 0.2 or 0.25 of SD, the difference between deep anesthesia and other states is larger. Considering that the r in ApEn is also used to suppress the noise, its value is chosen as small as possible. The r was chosen as 0.2 of SD. Figure 8.16c shows the selection of m with $N = 1000$ and $r = 0.2$*SD. It can be seen that ApEn nearly doesn't change with m. Meanwhile when m is 2, the interindividual variations of ShEn is smaller. With $r = 0.2$*SD and $m = 2$, the selection of N is shown in

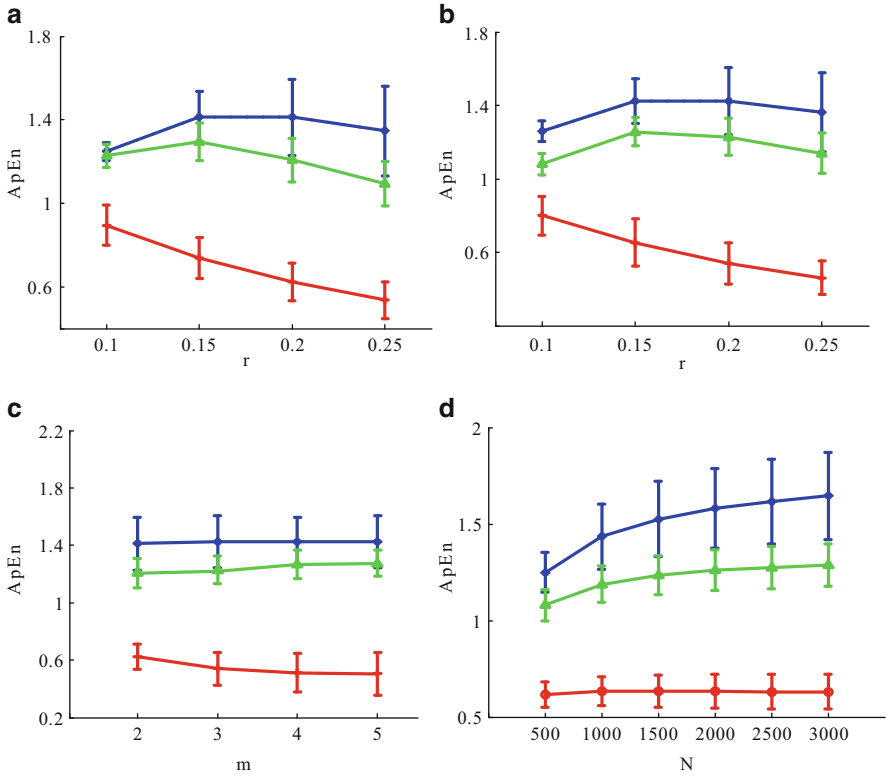

Fig. 8.16 The changes of ApEn with different parameters at different anesthesia states. (**a**) $m = 2$, $N = 1000$; (**b**) $m = 3$, $N = 1000$;(**c**) $r = 0.2$*SD, $N = 1000$; (**c**) $r = 0.2$*SD, $m = 2$

Fig. 8.16d. The ApEn was very dependent on N, and it increased with enlarging N, as well as its interindividual variations, especially in awake and recovery states. The difference between awake and anesthesia state also became larger, but when N was greater than 1000, the difference was not obvious. Therefore, $r = 0.2$*SD, $m = 2$, and $N = 1000$ were selected in this study, which is consistent with the study (Bruhn et al. 2000) through different methods to choose parameter was used.

Appendix D: SampEn

Figure 8.17a–b, respectively, show the changes of SampEn over different r in different anesthesia states, with $N = 1000$, $m = 2$ and 3. The SampEn values monotonously decrease with increasing r in all states. The difference between awake state and deep anesthesia was obvious, but not between awake and recovery state. There is much overlap between them. Considering the interindividual variations,

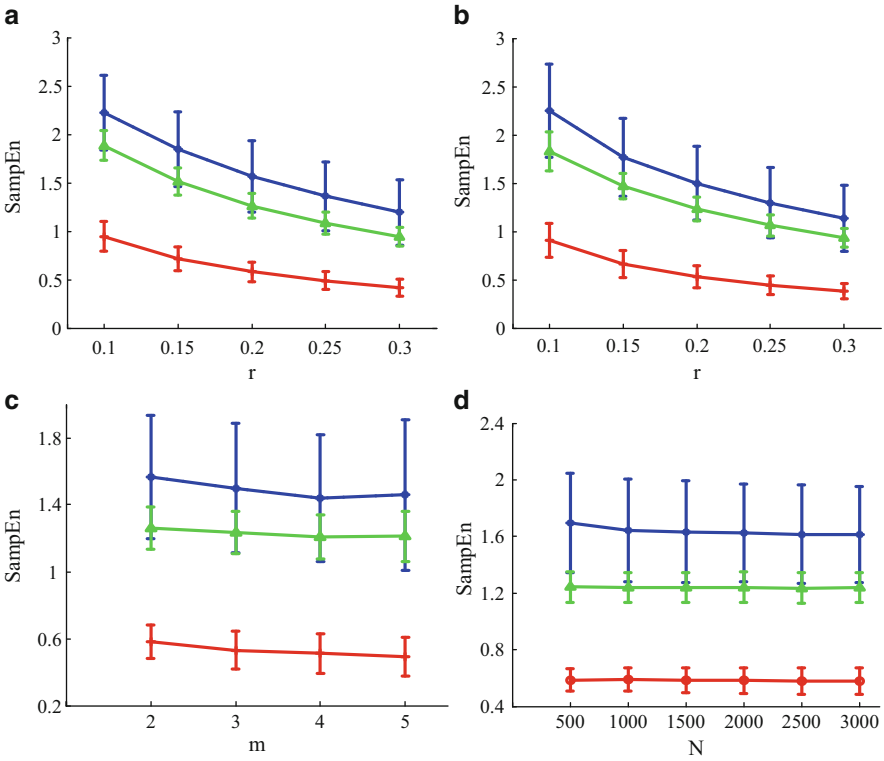

Fig. 8.17 The changes of SampEn with different parameters at different anesthesia states. (**a**) m=2, N=1000; (**b**) m=3, N=1000; (**c**) r=0.2*SD, N=1000; (**c**) r=0.2*SD, m=2

$r = 0.2$ is better. Figure 8.17c shows the changes of SampEn over different m with $r = 0.2$, $N = 1000$. There is no significant difference in different m values. For simplicity, $m = 2$ was selected. The selection of N is given in Fig. 8.17d. The SampEn values with $r = 0.2$, $m = 2$ were almost invariable as N increased. This implies that SampEn values are not dependent on N. Finally, $N = 1000$ (10 s at the sample rate of 100 Hz), $m = 2$, and $r = 0.2$*SD were selected in this study.

Appendix E: FuzzyEn

Figure 8.18 gives the changes of FuzzyEn with different parameters in different anesthesia states. Accordingly, we selected $r = 0.2$, $m = 2$, and $N = 1000$ for the computation of FuzzyEn in this study.

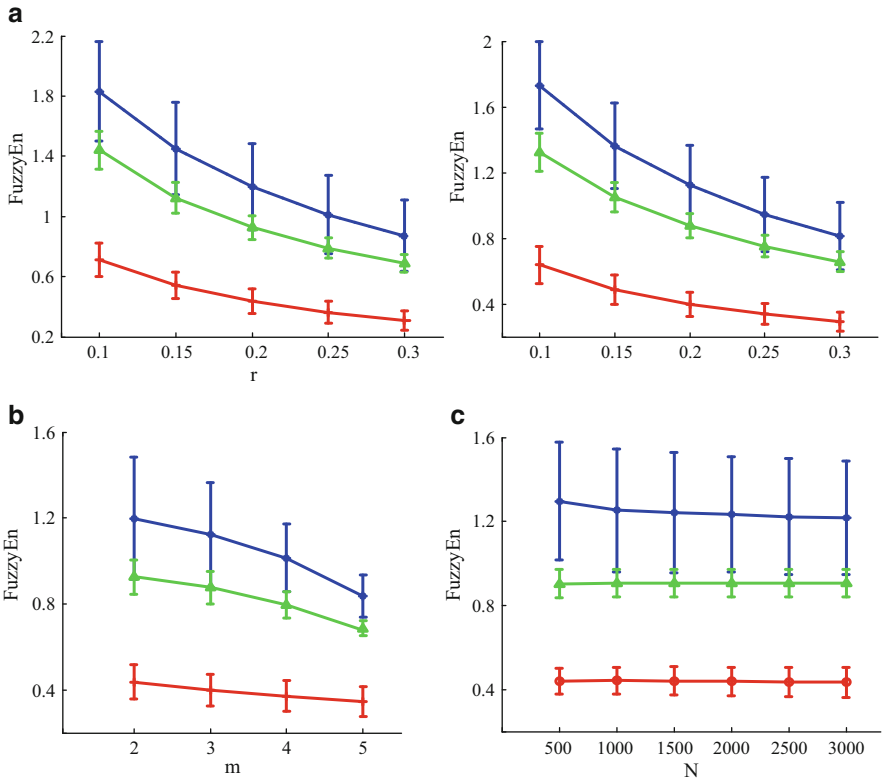

Fig. 8.18 The changes of FuzzyEn with different parameters at different anesthesia states. (**a**) $m = 2$, $N = 1000$; (**b**) $m = 3$, $N = 1000$;(**c**) $r = 0.2$*SD, $N = 1000$; (*c*) $r = 0.2$*SD, $m = 2$

Appendix F: TPE and RPE

The embedded dimension m, lag τ, and data length N had been discussed in our previous study (Li et al. 2008a, 2010, 2012). It is suggested that $m = 6$ and $\tau = 1$ are suitable for the sevoflurane DoA monitoring, and $m = 3$ $\tau = 2$ is better for isoflurane analysis. So, for the parameters of TPE and RPE, we only considered the embedded dimension of 3 and 6. For the sevoflurane, using $\tau = 1$ and isoflurane is $\tau = 2$. Figure 8.19a–b are the TPE of three anesthesia states at the $0 < q < 1$ and $q > 1$, respectively, the $m = 3$. Figure 8.19c–d show the TPE of $m = 6$ at $0 < q < 1$ and $q > 1$, respectively. It can be seen that in $m = 6$, $q = 0.9$ has a better performance in TPE. Figure 8.19e–h are the RPE measure of three anesthesia states similar as Fig. 8.19a–d. We select the $m = 6$ and $a = 2$ for RPE calculation.

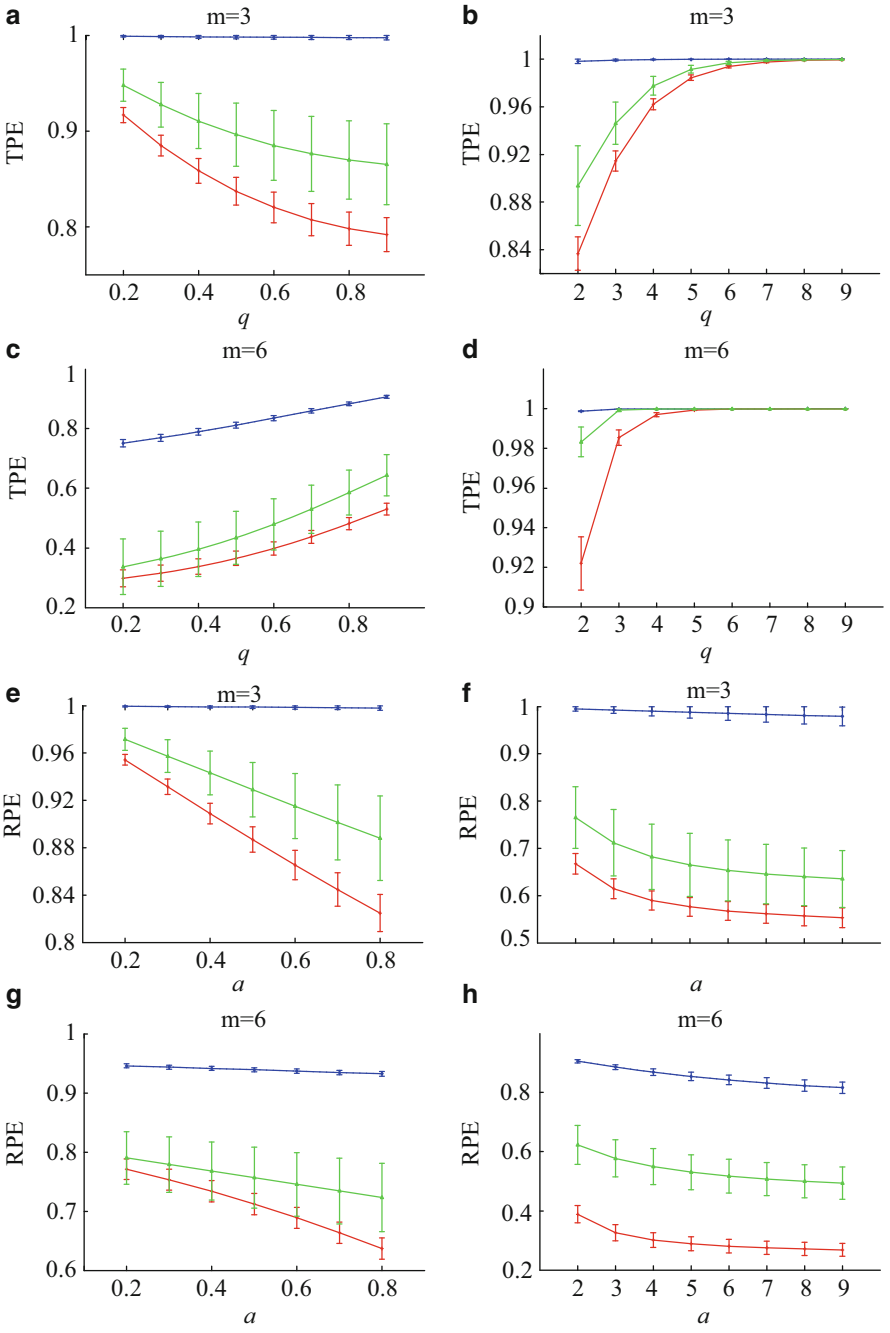

Fig. 8.19 The changes of TPE and RPE with different parameters at different anesthesia states. (**a**–**d**) The TPE measures with different parameters: (**a**) $m = 3$, $0 < q < 1$; (**b**) $m = 3$, $q > 1$; (**c**) $m = 6$, $0 < q < 1$; and (**d**) $m = 6$, $q > 1$. (**e**–**h**) The RPE measures with different parameters: (**e**) $m = 3$, $0 < a < 1$; (**f**) $m = 3$, $a > 1$; (**g**) $m = 6$, $0 < a < 1$; and (**h**) $m = 6$, $a > 1$

References

Abásolo D, et al. Entropy analysis of the EEG background activity in Alzheimer's disease patients. Physiol Meas. 2006;27(3):241.

Ahmed MU, Mandic DP. Multivariate multiscale entropy: a tool for complexity analysis of multichannel data. Phys Rev E. 2011;84(6):061918.

Arefian NM, et al. Clinical analysis of eeg parameters in prediction of the depth of anesthesia in different stages: a comparative study. Tanaffos. 2009;8(2):46–53.

Aziz W, Arif M. Multiscale permutation entropy of physiological time series. In: 9th International multitopic conference, IEEE INMIC 2005; 2005, IEEE.

Bandt C. Ordinal time series analysis. Ecol Model. 2005;182(3):229–38.

Bandt C, Pompe B. Permutation entropy: a natural complexity measure for time series. Phys Rev Lett. 2002;88(17):174102.

Bell IR, et al. Nonlinear dynamical systems effects of homeopathic remedies on multiscale entropy and correlation dimension of slow wave sleep EEG in young adults with histories of coffee-induced insomnia. Homeopathy. 2012;101(3):182–92.

Bezerianos A, Tong S, Thakor N. Time-dependent entropy estimation of EEG rhythm changes following brain ischemia. Ann Biomed Eng. 2003;31(2):221–32.

Bruhn J, Röpcke H, Hoeft A. Approximate entropy as an electroencephalographic measure of anesthetic drug effect during desflurane anesthesia. Anesthesiology. 2000;92(3):715–26.

Bruhn J, et al. Shannon entropy applied to the measurement of the electroencephalographic effects of desflurane. Anesthesiology. 2001;95(1):30–5.

Bruhn J, et al. Depth of anaesthesia monitoring: what's available, what's validated and what's next? Br J Anaesth. 2006;97(1):85–94.

Burton D, Zilberg E. Methods and apparatus for monitoring consciousness. 2002. wo patent wo/2002/100,267.

Cao Y, et al. Detecting dynamical changes in time series using the permutation entropy. Phys Rev-Ser E. 2004;70(4; PART 2):46217–46217.

Cao Y, et al. Characterization of complexity in the electroencephalograph activity of Alzheimer's disease based on fuzzy entropy. Chaos. 2015;25(8):083116.

Chen Y, Yang H. Multiscale recurrence analysis of long-term nonlinear and nonstationary time series. Chaos, Solitons Fractals. 2012;45(7):978–87.

Chen W, et al. Characterization of surface EMG signal based on fuzzy entropy. Neural Syst Rehabil Eng, IEEE Trans. 2007;15(2):266–72.

Chen W, et al. Measuring complexity using FuzzyEn, ApEn, and SampEn. Med Eng Phys. 2009;31(1):61–8.

Chen D, et al. GPGPU-aided ensemble empirical-mode decomposition for EEG analysis during anesthesia. Inf Technol Biomed IEEE Trans. 2010;14(6):1417–27.

Costa M, Goldberger AL, Peng C-K. Multiscale entropy analysis of complex physiologic time series. Phys Rev Lett. 2002;89(6):068102.

Costa M, Goldberger AL, Peng C-K. Multiscale entropy analysis of biological signals. Phys Rev E. 2005;71(2):021906.

Escudero J, et al. Analysis of electroencephalograms in Alzheimer's disease patients with multiscale entropy. Physiol Meas. 2006;27(11):1091.

He L, et al. Feature extraction with multiscale autoregression of multichannel time series for P300 speller BCI. In: Acoustics speech and signal processing (ICASSP), 2010 IEEE International Conference on. 2010, IEEE.

Hsu W-Y, et al. Wavelet-based fractal features with active segment selection: application to single-trial EEG data. J Neurosci Methods. 2007;163(1):145–60.

Hu M, Liang H. Perceptual suppression revealed by adaptive multi-scale entropy analysis of local field potential in monkey visual cortex. Int J Neural Syst. 2013;23(2):1350005.

Huang NE, et al. The empirical mode decomposition and the Hilbert spectrum for nonlinear and non-stationary time series analysis. Proc R Soc London, Ser A. 1998;454(1971):903–95.

Inouye T, et al. Quantification of EEG irregularity by use of the entropy of the power spectrum. Electroencephalogr Clin Neurophysiol. 1991;79(3):204–10.
Inuso G, et al. Brain activity investigation by EEG processing: wavelet analysis, kurtosis and Renyi's entropy for artifact detection. In: Information acquisition. 2007. ICIA'07. International Conference on; 2007, IEEE.
Jameson LC, Sloan TB. Using EEG to monitor anesthesia drug effects during surgery. J Clin Monit Comput. 2006;20(6):445–72.
Klockars JG, et al. Spectral entropy as a measure of hypnosis and hypnotic drug effect of total intravenous anesthesia in children during slow induction and maintenance. Anesthesiology. 2012;116(2):340–51.
Labate D, et al. Entropic measures of EEG complexity in Alzheimer's disease through a multivariate multiscale approach. Sensors J, IEEE. 2013;13(9):3284–92.
Li X. Temporal structure of neuronal population oscillations with empirical model decomposition. Phys Lett A. 2006;356(3):237–41.
Li X, Ouyang G, Richards DA. Predictability analysis of absence seizures with permutation entropy. Epilepsy Res. 2007;77(1):70.
Li X, Cui S, Voss LJ. Using permutation entropy to measure the electroencephalographic effects of sevoflurane. Anesthesiology. 2008a;109(3):448.
Li X, et al. Analysis of depth of anesthesia with Hilbert–Huang spectral entropy. Clin Neurophysiol. 2008b;119(11):2465–75.
Li D, et al. Multiscale permutation entropy analysis of EEG recordings during sevoflurane anesthesia. J Neural Eng. 2010;7(4):046010.
Li D, et al. Parameter selection in permutation entropy for an electroencephalographic measure of isoflurane anesthetic drug effect. J Clin Monit Comput. 2012;27(2):113–23.
Liang H, Lin Z, McCallum R. Artifact reduction in electrogastrogram based on empirical mode decomposition method. Med Biol Eng Comput. 2000;38(1):35–41.
Liang Z, et al. EEG entropy measures in anesthesia. Front Comput Neurosci. 2015;9:16.
Maszczyk T, Duch W. Comparison of Shannon, Renyi and Tsallis entropy used in decision trees. In: Artificial Intelligence and Soft Computing–ICAISC 2008. Springer; 2008. p. 643–51.
McKay IDH, et al. Pharmacokinetic-pharmacodynamic modeling the hypnotic effect of sevoflurane using the spectral entropy of the electroencephalogram. Anesth Analg. 2006;102(1):91.
Monk TG, et al. Anesthetic management and one-year mortality after noncardiac surgery. Anesth Analg. 2005;100(1):4.
Montirosso R, et al. Infant's emotional variability associated to interactive stressful situation: a novel analysis approach with Sample Entropy and Lempel–Ziv complexity. Infant Behav Dev. 2010;33(3):346–56.
Morabito FC, et al. Multivariate multi-scale permutation entropy for complexity analysis of Alzheimer's disease EEG. Entropy. 2012;14(7):1186–202.
Natarajan K, et al. Nonlinear analysis of EEG signals at different mental states. Biomed Eng Online. 2004;3(1):7.
Nunez PL, Wingeier BM, Silberstein RB. Spatial-temporal structures of human alpha rhythms: theory, microcurrent sources, multiscale measurements, and global binding of local networks. Hum Brain Mapp. 2001;13(3):125–64.
Okogbaa OG, Shell RL, Filipusic D. On the investigation of the neurophysiological correlates of knowledge worker mental fatigue using the EEG signal. Appl Ergon. 1994;25(6):355–65.
Olofsen E, Sleigh J, Dahan A. Permutation entropy of the electroencephalogram: a measure of anaesthetic drug effect. Br J Anaesth. 2008;101(6):810–21.
Ouyang G, Dang C, Li X. Multiscale entropy analysis of EEG recordings in epileptic rats. Biomed Eng Appl Basis Commun. 2009;21(03):169–76.
Park J-H, et al. Multiscale entropy analysis of EEG from patients under different pathological conditions. Fractals. 2007;15(04):399–404.
Pincus SM. Approximate entropy as a measure of system complexity. Proc Natl Acad Sci. 1991;88(6):2297.

Rampil IJ. A primer for EEG signal processing in anesthesia. Anesthesiology. 1998;89(4):980–1002.
Renyi A. Probability theory. Amsterdam: North-Holland; 1970.
Rezek I, Roberts SJ. Stochastic complexity measures for physiological signal analysis. Biomed Eng, IEEE Trans. 1998;45(9):1186–91.
Richman JS, Moorman JR. Physiological time-series analysis using approximate entropy and sample entropy. Am J Phys Heart Circ Phys. 2000;278(6):H2039–49.
Rilling G, Flandrin P, Gonçalvés P. On empirical mode decomposition and its algorithms. In: IEEE-EURASIP workshop on nonlinear signal and image processing, NSIP-03, Grado (I). 2003.
Rosso OA, et al. Wavelet entropy: a new tool for analysis of short duration brain electrical signals. J Neurosci Methods. 2001;105(1):65–76.
Rosso O, Martin M, Plastino A. Brain electrical activity analysis using wavelet-based informational tools (II): Tsallis non-extensivity and complexity measures. Physica A. 2003;320:497–511.
Rosso O, et al. EEG analysis using wavelet-based information tools. J Neurosci Methods. 2006;153(2):163–82.
Särkelä MOK, et al. Quantification of epileptiform electroencephalographic activity during sevoflurane mask induction. Anesthesiology. 2007;107(6):928–38.
Shalbaf R, et al. Using the Hilbert–Huang transform to measure the electroencephalographic effect of propofol. Physiol Meas. 2012;33(2):271–85.
Shannon CE. A mathematical theory of communication. ACM SIGMOBILE Mob Comput Commun Rev. 2001;5(1):3–55.
Shannon CE, Weaver W. The mathematical theory of communication. Urbana: University of Illinois Press; 1949, v (ie vii), 125 p.
Smith WD, Dutton RC, Smith TN. Measuring the performance of anesthetic depth indicators. Anesthesiology. 1996;84(1):38–51.
Song Y, Zhang J. Discriminating preictal and interictal brain states in intracranial EEG by sample entropy and extreme learning machine. J Neurosci Methods. 2016;257:45–54.
Stamoulis C, Chang BS. Multiscale information for network characterization in epilepsy. In: Engineering in Medicine and Biology Society, EMBC, 2011 Annual international conference of the IEEE. 2011, IEEE.
Takahashi T, et al. Antipsychotics reverse abnormal EEG complexity in drug-naive schizophrenia: a multiscale entropy analysis. Neuroimage. 2010;51(1):173–82.
Thuraisingham RA, Gottwald GA. On multiscale entropy analysis for physiological data. Physica A. 2006;366:323–32.
Tong S, et al. Parameterized entropy analysis of EEG following hypoxic–ischemic brain injury. Phys Lett A. 2003;314(5):354–61.
Tsallis C, Mendes R, Plastino AR. The role of constraints within generalized nonextensive statistics. Physica A. 1998;261(3):534–54.
Unser M, Aldroubi A. A review of wavelets in biomedical applications. Proc IEEE. 1996;84(4):626–38.
Viertiö-Oja H, et al. Description of the Entropy™ algorithm as applied in the Datex-Ohmeda S/5™ Entropy module. Acta Anaesthesiol Scand. 2004;48(2):154–61.
Wang Y, et al. Multi-scale sample entropy of electroencephalography during sevoflurane anesthesia. J Clin Monit Comput. 2014;28(4):409–17.
Wu S-D, et al. Modified multiscale entropy for short-term time series analysis. Physica A. 2013;392(23):5865–73.
Yoo CS, et al. Automatic detection of seizure termination during electroconvulsive therapy using sample entropy of the electroencephalogram. Psychiatry Res. 2012;195(1):76–82.
Yoon YG, et al. Monitoring the depth of anesthesia from rat EEG using modified Shannon entropy analysis. Conf Proc IEEE Eng Med Biol Soc. 2011;2011:4386–9.
Zadeh LA. Fuzzy sets. Inf Control. 1965;8(3):338–53.
Zandi AS, et al. An entropy-based approach to predict seizures in temporal lobe epilepsy using scalp EEG. Conf Proc IEEE Eng Med Biol Soc. 2009;2009:228–31.

Zandi AS, et al. Circadian variation of scalp EEG: a novel measure based on wavelet packet transform and differential entropy. Conf Proc IEEE Eng Med Biol Soc. 2013;2013:6297–300.
Zhang R, et al. Predicting inter-session performance of SMR-based brain-computer interface using the spectral entropy of resting-state EEG. Brain Topogr. 2015;28(5):680–90.
Zhaohui L, Xiaoli L. Estimating temporal causal interaction between spike trains with permutation and transfer entropy. Plos One. 2013;8(8):e70894.
Zou X, Lei M. Pattern recognition of surface electromyography signal based on multi-scale fuzzy entropy. Sheng Wu Yi Xue Gong Cheng Xue Za Zhi. 2012;29(6):1184–8.
Zoughi T, Boostani R, Deypir M. A wavelet-based estimating depth of anesthesia. Eng Appl Artif Intell. 2012;25(8):1710–22.
Zunino L, et al. Fractional Brownian motion, fractional Gaussian noise, and Tsallis permutation entropy. Physica A. 2008;387(24):6057–68.

Chapter 9
Synchronization Measures in EEG Signals

Zhenhu Liang, Yang Bai, Ye Ren, and Xiaoli Li

9.1 Introduction

Synchronization measures have been wildly used in many scientific and technical disciplines. Particularly, synchronization phenomena have become an important feature in understanding mechanism of normal (Roelfsema et al. 1997; Steriade et al. 1993; Mizuhara and Yamaguchi 2007) or abnormal (Uhlhaas and Singer 2006) brain functions. And it is found that synchronization between neuronal populations plays a key role in information processing in the brain (Engel et al. 2001a; Li et al. 2007a; Schnitzler and Gross 2005; Aviyente et al. 2011a).

So far, there exist many synchronization detection methods, such as cross correlation, coherence, mutual information, phase synchronization, and event synchronization, and they have been proposed to quantify the degree of synchronization in different neural systems. These synchronization measures have been proved effective in epileptic seizure prediction and detection (Zheng et al. 2014; Mirowski et al. 2009; Slooter et al. 2006) and Alzheimer (Koenig et al. 2005; Stam et al. 2005) and autism (Mehran et al. 2012) detection and assessment. Also, synchronization

Z. Liang • Y. Bai • Y. Ren
Institute of Electric Engineering, Yanshan University, Qinhuangdao 066004, China

Key Laboratory of Industrial Computer Control Engineering of Hebei Province, Yanshan University, Qinhuangdao 066004, China
e-mail: zhl@ysu.edu.cn

X. Li (✉)
State Key Laboratory of Cognitive Neuroscience and Learning & IDG/McGovern Institute for Brain Research, Beijing Normal University, Beijing, China

Center for Collaboration and Innovation in Brain and Learning Sciences, Beijing Normal University, Beijing, China
e-mail: xiaoli@bnu.edu.cn

X. Li (eds.), *Signal Processing in Neuroscience*, DOI 10.1007/978-981-10-1822-0_9

measures were used to explore consciousness state-related mechanisms, such as sleep (Birchler-Pedross et al. 2011; Moroni et al. 2012) and anesthesia (Koskinen et al. 2001; Shalbaf et al. 2015).

The theoretical foundations are various for different synchronization methods. It was difficult to give unified criteria for selecting effective synchronization methods, when investigating different brain functions or understanding mechanisms of different brain diseases. In this chapter, we gave an example of using different synchronization measures to understand mechanism of anesthesia effect on the brain and evaluated performance of these synchronization measures in distinguishing the states of anesthesia.

How general anesthetic agents induce unconsciousness in the central nervous system may provide a direction for future rational anesthetic drug design and improved intraoperative monitoring (Lewis et al. 2012). Over the last decade, many theories have been proposed to explain the mechanism of consciousness, such as the cognitive binding. A number of recent studies gave evidence that breakdown of long-distance cortical connectivity across multiple brain regions in particular frontal-parietal cortices may play a critical role in loss of consciousness (LoC) (Voss and Sleigh 2007; Nallasamy and Tsao 2011; Lee et al. 2009a, b). At the same time, many different signal processing methods based on different information theories have been proposed to quantify neuro-synchrony (Pereda et al. 2005; Breakspear 2004; Kaminski and Liang 2005; Stam 2005).

In this chapter, we systematically investigate changes in electroencephalogram (EEG) synchrony during anesthesia induced by propofol, using a range of different synchronization measures. The aim is to evaluate various information coupling measures in separating different anesthesia states. Some novel synchronization measures, and methods proposed in our previous work, are used. Among these, cross correlation (COR) is probably the most commonly applied method. Coherence and phase synchronization (PS) are based on the frequency domain, while wavelet coherence (WTC) is based on time-frequency domain. Mutual information (MI) is based on information theory. Nonlinear interdependence (NI) and cross recurrence analysis are based on state space theory.

Any future practical monitor of anesthesia must be quick, robust, and operable. Therefore, unlike most studies which incorporate many channels (Dauwels et al. 2010), we only considered synchronization and information coupling between two channels of EEG. In this chapter, we concentrated on the coupling between prefrontal and primary motor cortices. In order to compare their properties within the same context, we applied the synchronization methods to the same EEG data set with a range of depth of anesthesia states: awake, unconscious state, and recovery of consciousness (RoC). To validate the relative effectiveness of these synchronization algorithms, we evaluated performance of each algorithm on modeling pharmacokinetic/pharmacodynamic (PK/PD) drug effects. We quantified the correlation coefficients (R_{ij}) between each synchrony measure and the bispectral index (BIS), the prediction probability (P_k) of each measure with the BIS and with effect-site propofol concentration (ESPC). Our goal is to select the most

effective measure in clinical anesthetic depth evaluation and to further understand the underlying neurophysiological mechanisms of anesthesia.

Different approaches for measuring synchronization rely on certain characteristic features of the dynamical system under investigation. However, the underlying dynamic properties of the experimental data are usually not completely known. It is important to validate the measures against model systems where the synchrony of the underlying dynamics are known and can be artificially manipulated (Kreuz et al. 2007). Therefore, we adopted three coupled model systems with different properties to evaluate the performance of each method for tracking coupling strength.

This chapter is organized as follows: Sect. 9.2 describes each synchronization measure and its parameter selection. Section 9.3 gives three nonlinear dynamical coupled models, the EEG recordings, and preprocessing. Section 9.4 illustrates the criteria for measure evaluation in models, as well as the statistical methods. The results of the applications of the synchronization measures to the model and real EEG show in Sect. 9.5. Finally, the conclusions are given in Sect. 9.6.

9.2 Synchronization Measures

9.2.1 Cross Correlation

The cross correlation is a classical and simple measure of the interdependence between two time series. It can be used to evaluate the linear relationship between two variables X and Y based on a delay time τ, which may reflect a causal relationship between the signals. The calculation of the COR is described in the following:

Given two time series, $x(t)$ and $y(t)$, and normalized to have zero mean and unit variance, their cross correlation function is

$$C_{xy}(\tau) = \frac{1}{N-\tau} \sum_{t=1}^{N-\tau} x(t+\tau)\, y(t) \tag{9.1}$$

where N is the total number of samples and τ is the time lag between the signals.

The details of this method can be found in Zhou et al. (2009). There are two parameters that affect the value: data length N and delay time τ. The parameter selections are introduced in Appendix A.

9.2.2 Cross Coherence

Coherence is a popular method for detecting neuronal sources that are working together in a spatially distributed network and to determine how strongly they

collaborate (Thatcher et al. 2008). It is a frequency domain-based method which measures the linear correlations of two time series (Nunez 2006). We considered two coherence calculation methods: coherence based on Fourier transformation (FTC) and wavelet transformation (WTC).

Given two time series x and y, subdivide into M segments of equal length L. The basic coherence function is computed by averaging over these segments. The coherence function with magnitude square $C_{xy}(f)$ is described by

$$C_{xy}(f) = \frac{|\langle X(f)Y^*(f)\rangle|^2}{|\langle X(f)\rangle|\,|\langle Y(f)\rangle|} \tag{9.2}$$

where $X(f)$ and $Y(f)$ are the Fourier transforms of time series x and y, respectively. Y^* denotes the complex conjugate of Y, and $\langle X(f)\rangle$ is the average of $X(f)$ computed over the M segments, similar to $\langle Y(f)\rangle$ and $\langle X(f)Y^*(f)\rangle$. $|Y|$ stands for the magnitude of Y.

Similar to FTC, the wavelet coherence function calculates the ratio of the cross spectrum to the product of the auto-spectrum of the two series, x and y, which is defined as

$$(c^w(s,\tau))^2 = \frac{\left|S^w_{xy}(s,\tau)\right|^2}{S^w_{xx}(s,\tau)\,S^w_{yy}(s,\tau)} \tag{9.3}$$

where $S^w_{xy}(s,\tau)$ is the localized power spectrum, it is

$$S^w_{xy}(s,\tau) = \frac{1}{s\int_T W_x(s,\tau)\,W^*_y(s,\tau)\,d\tau}, \quad T = [\tau - \Delta\tau, \tau + \Delta\tau] \tag{9.4}$$

Here T is selected based on the time resolution desired in the coherence map. And the auto-spectrum $S^w_{xx}(s,\tau)$ and $S^w_{yy}(s,\tau)$ are defined similar to $S^w_{xy}(s,\tau)$.

The power spectrum is calculated based on the Morlet wavelet transform (MWT). The details are described in Li et al. (2007b). The normalized average synchronization based on the coherence of signals x and y at a frequency band $[f_L, f_H]$ is defined by

$$d_{xy} = \frac{1}{N_w}\sum_{w=f_L}^{f_H} H_{xy}(f) \tag{9.5}$$

where $H_{xy}(f)$ could be replaced by the $C_{xy}(f)$ or $C^w(s,\tau)$. N_w is the number of summands in the summation, so the synchronization value of d_{xy} is between 0 and 1 (Li et al. 2013).

The WTC index across five frequency bands, $\delta\,(1-4\text{Hz})$, $\theta\,(4-8\text{Hz})$, $\alpha\,(8-13\text{Hz})$, $\beta\,(13-30\text{Hz})$, and $\gamma 1\,(30-40\text{Hz})$, was calculated and denoted as WTC_δ, WTC_θ, WTC_α, WTC_β, and $\text{WTC}_{\gamma 1}$, respectively, in this chapter.

9.2.3 Phase Synchronization

PS analysis has been independently proposed by Lachaux et al. (Lachaux et al. 1999) and Mormann et al. (Mormann et al. 2000) and applied later by Allefeld and Kurths (Allefeld and Kurths 2003, 2004). This approach is based on the concept of synchronization of chaotic oscillators studied by Rosenblum et al. (Rosenblum et al. 1996). Phase synchronization is sensitive to nonlinear coupling (David et al. 2004) and is a promising tool for quantifying coupling in multichannel electroencephalogram or magnetoencephalogram (MEG) recordings (David et al. 2004; Engel et al. 2001b; David and Friston 2003) and may be helpful for understanding communication mechanisms in the brain (Li et al. 2007b; Le Van Quyen and Bragin 2007; Aviyente et al. 2011b).

There are various PS estimation methods; however, two steps are fundamental: instantaneous phase estimation and phase-locking quantification. Li et al. employed the windowed harmonic wavelet transform (WHWT) to extract the instantaneous phase of brain signals and show that WHWT performs better than traditional methods, such as the Hilbert transform (HT) (Li et al. 2011). So we chose WHWT to calculate the instantaneous phase in this study. The algorithm is described as follows.

Consider two time series $x(t)$ and $y(t)$; the Fourier transform is used to achieve the corresponding expressions in the frequency domain, $X(f)$ and $Y(f)$. Then, multiply $X(f)$ by the conjugate of the windowed harmonic wavelet $W_w(f)$ denoted as $A(f) = X(f)W_w^*(f)$. Take the inverse Fourier transform of $A(f)$ to obtain the signal with WHWT denoted by $a(t)$, as presented by (Park and Kim 2001)

$$a(t) = u(t) + jH\left[u(t)\right] = u(t) + \frac{j}{\pi}\int_{-\infty}^{\infty}\frac{u\left(\tau\right)}{t-\tau}d\tau = S(t)e^{j\varphi(t)} \tag{9.6}$$

where $H\left[\cdot\right]$ stands for the operation of Hilbert transform. The magnitude is represented as $S(t) = \sqrt{\left(u(t)\right)^2 + \left(H\left[u(t)\right]\right)^2}$, and the instantaneous phase of $a(t)$ is

$$\varphi(t) = \tan^{-1}\left(\frac{H\left[\left(u(t)\right)\right]}{u(t)}\right) = \tan^{-1}\left(\frac{\text{imag}\left[a(t)\right]}{\text{real}\left[a(t)\right]}\right) \tag{9.7}$$

The phase difference can be defined with the instantaneous phase $\phi_x(t)$ and $\phi_y(t)$ (achieved through the WHWT of the scalar observations $x(t)$ and $y(t)$):

$$\Delta\phi_{xy}(t) = \phi_x(t) - \phi_y(t) \tag{9.8}$$

There are mainly three PS calculation methods used. Among them, phase-locking value (PLV) (Lachaux et al. 2000) is based on time windows with a specified length N. Here, we denote it as PS_{PLV}:

$$\text{PS}_{\text{PLV}} = \frac{1}{N}\left|\sum\nolimits_{t=1}^{N} e^{j\Delta\phi_{xy}}\right| \tag{9.9}$$

where the PS_{PLV} is bound between 0 and 1.

Another method is based on Shannon entropy (PS_{SE}) (Tass et al. 1998). It can be defined as:

$$PS_{SE} = \frac{S_{max} - S}{S_{max}} \tag{9.10}$$

where $S = -\sum_{k=0}^{N} p_k \ln p_k$ is the entropy of the distribution of the cyclic relative phase $\Psi = \Delta\phi_{xy} \mod 2\pi$. And $S_{max} = \ln N$, where N is the number of bins used for the distribution. The optimum of bins (N) is set as $e^{0.626+0.4\ln(L-1)}$, where L is the number of data points. The range of PS_{SE} is between 0 and 1.

The third PS measure is based on conditional probability (PS_{CP}) and is described as follows:

Divide the interval $[0, 2\pi]$ into n bins and denote the values of $\phi_x \mod 2\pi$ falling into the l-th bin as θ_l and the number of points within this bin as M_l. Then, compute the M_l corresponding values $\eta_{ij} = \phi_y \mod 2\pi\big|_{\phi_x \mod 2\pi=\theta}$, where $i = 1 \cdots M_l$. Last, we average over all n bins $\Lambda_l = 1/M_l \sum_{i=1}^{M_l} e^{i\eta_{i,l}}$ and get the synchronization index

$$PS_{CP} = 1/n \sum_{i=1}^{n} |\Lambda_l| \tag{9.11}$$

In this study, we divide the EEG data into five frequency bands, δ, θ, α, β, and $\gamma 1$, as similar as WTC. The PS indexes were calculated in each frequency bands with time epochs (T_e). The Appendix B gives the discussion of the effect of epoch lengths on each PS indexes.

9.2.4 *Mutual Information Based on Kernel Estimation (KerMI)*

The mutual information is a widely used nonlinear measure with calculating the interdependence between variables.

The mutual information between two discrete random variables $x(t)$ and $y(t)$ ($t = 1, 2, \ldots, N$) calculated with marginal probabilities $p_x(x)$ and $p_y(y)$ and joint probability $p_{xy}(x, y)$, which is defined as

$$I(x, y) = \sum_{x,y} p_{xy}(x, y) \log \frac{p_{xy}(x, y)}{p_x(x) p_y(y)} \tag{9.12}$$

The most straightforward approach for estimating probability is partitioning $x(t)$ and $y(t)$ into K ($k = 1, 2, \ldots, K$) bins of finite size and counting the numbers of points falling into each bins. The number of points within the bin is denoted as $Q_x(k)$,

$Q_y(k)$, and $Q_{xy}(k)$. Then, the probabilities can be denoted as $p_x = \frac{Q_x(k)}{N}$, $p_y = \frac{Q_y(k)}{N}$, and $p_{xy} = \frac{Q_{xy}(k)}{N}$.

Kernel techniques are attractive alternative to binning a distribution which is discussed thoroughly in Silverman (1986). Rather than simply counting the points of time series, we can determine the distance-dependent weight of each point that employs the kernel function. In this study, we considered the Gaussian kernel (Beirlant et al. 1997). Then, the marginal probability density and joint probability density estimated by the Gaussian kernel estimator can be denoted as (Steuer et al. 2002),

$$p_x(x) = \frac{1}{N}\frac{1}{\sqrt{2\pi h^2}}\sum_{t=1}^{N} e^{-\frac{1}{2h^2}(x-x_t)^2}, \quad p_y(y) = \frac{1}{N}\frac{1}{\sqrt{2\pi h^2}}\sum_{t=1}^{N} e^{-\frac{1}{2h^2}(y-y_t)^2} \tag{9.13}$$

$$p_{xy}(x,y) = \frac{1}{N}\frac{1}{2\pi h^2}\sum_{t=1}^{N} e^{-\frac{1}{2h^2}\left((x-x_t)^2+(y-y_t)^2\right)} \tag{9.14}$$

where parameter h is the window width of the kernels.

Finally, we can obtain the mutual information based on kernel estimation,

$$\mathrm{KerMI} = \frac{1}{N}\sum_{t=1}^{N}\log\left[\frac{p_{xy}(x,y)}{p_x(x)p_y(y)}\right] \tag{9.15}$$

The approximately optimal window width h is given by $h_{\mathrm{opt}} \approx \sigma\left(\frac{4}{d+2}\right)^{1/(d+4)} N^{-1/(d+4)}$ with $d = 2$ being the dimension of Gaussian kernel estimation and σ the average marginal standard deviation (SD) (Silverman 1986).

9.2.5 *Permutation Cross Mutual Information (PCMI)*

Recently, permutation analysis and conditional mutual information were integrated to estimate the coupling direction between two cardiorespiratory series (Bandt and Pompe 2002). Then PCMI was proposed with integration of permutation analysis and cross mutual information.

Given a time series x_t ($t = 1, 2, \ldots$), form the embedding vector X_t [$x_t, x_{t+\tau}, \ldots, x_{t+m\tau}$] with the embedding dimension m and lag τ. Then, arrange the vector X_t in an increasing order as a symbol of vectors: $\left[x_{t+(j_1-1)\tau} \le x_{t+(j_2-1)\tau} \le \cdots \le x_{t+(j_m-1)\tau}\right]$. For m dimensions, there will be $m!$ permutations, and each vector X_t in m-dimensional space can be mapped to one of the $m!$ permutations. Next, the probability distribution of permutations in the symbol sequences can be calculated, denoted $p_1, p_2, \ldots, p_k$, where $m = 6$.

Based on the permutation probability distribution of X and Y, the permutation entropy $H(X)$ and $H(Y)$ can be calculated. And the joint entropy of $H(X, Y)$ from the cross-probability distribution is described as

$$H(X, Y) = -\sum_{xeX} \sum_{yeY} p(x, y) \log p(x, y) \tag{9.16}$$

where $p(x, y)$ is the joint probability distribution of X and Y.

The PCMI requires three parameters to be defined before application: the embedded dimension m, the lag τ, and the epoch length. Previous studies found that at a sample rate of 100 Hz, $m = 6$, $\tau = 1$ and epoch length of 1000 resulted in the best PCMI performance (Liang et al. 2013). Therefore we use $m = 6$, $\tau = 1$, epoch = 1000 for calculation of PCMI in this study.

9.2.6 Nonlinear Interdependence

Nonlinear interdependence provides a measure of generalized synchronization in nonlinear systems, namely, the interdependence according to the distance of delay vectors in bivariate data. It was demonstrated that nonlinear interdependence can not only compute the coupling strength but also indicate the coupling direction (Quiroga et al. 2000; Breakspear and Terry 2002a, 2002b).

In the study of Quiroga et al. (2002), nonlinear interdependence was used to disclose the coupling information of two EEG recordings in rats. The details of the algorithm are described as follows:

Two time series are treated as two systems X and Y, with embedding dimension m and time lag τ. Then reconstruct the delay vectors $X_n = \left(x_n, \ldots, x_{n-(m-1)\tau}\right)$ and $Y_n = \left(y_n, \ldots, y_{n-(m-1)\tau}\right)$. Defining $r_{n,j}$ and $s_{n,j}, j = 1, \ldots, k$ as the time indexes of the k nearest neighbors of X_n and Y_n, respectively.

The mean squared Euclidean distance to its k neighbors for each X_n is defined as

$$R_n^{(k)}(X) = \frac{1}{k} \sum_{j=1}^{k} \left(X_n - X_{r_{n,j}}\right)^2 \tag{9.17}$$

The y-conditioned mean squared Euclidean distance is defined using the time partners of the closest neighbors of Y_n replacing the nearest neighbors' indexes

$$R_n^{(k)}(X \,|\, Y) = \frac{1}{k} \sum_{j=1}^{k} \left(X_n - X_{s_{n,j}}\right)^2 \tag{9.18}$$

There are three interdependence measures defined in the Refs (Quiroga et al. 2000, 2002). The first is $S^{(k)}(X|Y)$, described as

$$S^{(k)}(X|Y) = \frac{1}{N} \sum_{n=1}^{N} \frac{R_n^{(k)}(X)}{R_n^{(k)}(X|Y)} \tag{9.19}$$

When the elements in X_n have an average squared radius, then $R(X) = 1/N\sum_{n=1}^{N} R_n^{(N-1)}(X)$. If the systems are highly correlated, we get $R_n^{(k)}(X|Y) \approx R_n^{(k)}(X) \leq R(X)$. While $R_n^{(k)}(X|Y) \approx R(X) \geq R_n^{(k)}(X)$, if they are independent. Since $R_n^{(k)}(X|Y) \geq R_n^{(k)}(X)$ by construction, we have $0 < S^{(k)}(X|Y) \leq 1$.

A low value of $S^{(k)}(X|Y)$ indicates the two series are independent, while high value indicates the two series are synchronous.

The second interdependence measure $H^{(k)}(X|Y)$ is defined as

$$H^{(k)}(X|Y) = \frac{1}{N}\sum \log \frac{R_n(X)}{R_n^{(k)}(X|Y)} \tag{9.20}$$

The third interdependence measure is the normalized method, defined as

$$N^{(k)}(X|Y) = \frac{1}{N}\sum_{n=1}^{N} \frac{R_n(X) - R_n^{(k)}(X|Y)}{R_n(X)} \tag{9.21}$$

In this study, the $S^{(k)}(X|Y)$, $H^{(k)}(X|Y)$, and $N^{(k)}(X|Y)$ indexes were calculated, and the parameter selection is discussed in Appendix C.

9.2.7 Cross Recurrence Analysis

Cross recurrence analysis was introduced to examine the intricate recurrent structuring between paired signals which were also time delayed and embedded in higher dimensional space (Eckmann et al. 1987).

Considering two time series $x(t)$ and $y(t)$, the cross recurrence plot (CRP), which is a bivariate extension of the recurrence plot (RP), is introduced to analyze the dependencies between two different systems (Zbilut et al. 1998; Marwan and Kurths 2002). Similar to the RP, the cross recurrence matrix is defined by

$$CR_{i,j}^{\vec{x},\vec{y}}(\varepsilon) = \Theta\left(\varepsilon - \left\|\vec{x}_i - \vec{y}_j\right\|\right), i = 1,\ldots,N, j = 1,\ldots,N \tag{9.22}$$

where N is the number of measured points $\vec{x}_i$ or $\vec{y}_j$ and ε is a threshold distance. $\Theta(\cdot)$ is the Heaviside function (i.e., $\Theta(x) = 0$, if $x < 0$, and $\Theta(x) = 1$ otherwise) and $\|\cdot\|$ is a norm function.

There are various ways of quantifying the RP, such as recurrence rate, determinism (DET), laminarity, and entropy of diagonal length (ENTR). In this study, the DET index was used to evaluate the synchronization of the two systems.

Stochastic behavior causes none or short diagonals, whereas deterministic behavior causes longer diagonals and fewer single, isolated recurrence points. The

DET calculates the ratio of recurrence points that form diagonal structures (of at least length $l_{\min}$) to all recurrence points, which can characterize the behavior of the nonlinear system, and is defined by

$$\mathrm{DET} = \frac{\sum_{l=l_{\min}}^{l} lP(l)}{\sum_{l=1}^{l} lP(l)} \tag{9.23}$$

where $P(l)$ is the frequency distribution of the lengths of the diagonal structures in the CRP. $l_{\min}$ is the threshold, which excludes the diagonal lines which are formed by the tangential motion of the phase space trajectory. For $l_{\min} = 1$, the determinism is one.

The selection of the parameters for DET is detailed in Appendix D.

9.3 Simulation Models and EEG Recordings

9.3.1 Three Nonlinear Dynamical Coupled Model Systems

In our analysis, we used the time series x_1 and y_1 (length of 4096) generated from three coupled model systems to compare the synchronization measures.

The first model system consisted of two coupled Hénon maps, as proposed in Schiff et al. (1996). The equations of motion for the driver and the responder are:

$$\begin{aligned} x_{1,n+1} &= 1.4 - x_{1,n}^2 + b_x x_{2,n} \\ x_{2,n+1} &= x_{1,n} \\ y_{1,n+1} &= 1.4 - \left(C x_{1,n} y_{1,n} + (1-C)\, y_{1,n}^2\right) + b_y y_{2,n} \\ y_{2,n+1} &= y_{1,n} \end{aligned} \tag{9.24}$$

The parameters were set to $b_x = b_y = 0.3$ to yield identical systems with a sampling interval of 1. The coupling strength C was varied from 0 to 0.8 in steps of 0.01.

The second system employed two coupled Rössler systems (Palus and Stefanovska 2003). The equations of motion of this coupling model are:

$$\begin{aligned} \dot{x}_1 &= -w_x x_2 - x_3 \\ \dot{x}_2 &= w_x x_1 + 0.15 x_2 \\ \dot{x}_3 &= 0.2 + x_3 (x_1 - 10) \\ \dot{y}_1 &= -w_y y_2 - y_3 + C (x_1 - y_1) \\ \dot{y}_2 &= w_y y_1 + 0.15 y_2 \\ \dot{y}_3 &= 0.2 + y_3 (y_1 - 10) \end{aligned} \tag{9.25}$$

The equations were integrated using Runge-Kutta 4th order with a sampling interval of 0.3. A parameter mismatch between the two systems was introduced by setting $w_x = 0.95$ and $w_y = 1.05$. The coupling strength C was varied from 0 to 2 in steps of 0.025.

The third system adopted two Lorenz systems (Kreuz et al. 2007). The equations of motion of this coupling model are:

$$\begin{aligned}
\dot{x}_1 &= 10\,(x_2 - x_1) \\
\dot{x}_2 &= x_1\,(28 - x_3) - x_2 \\
\dot{x}_3 &= x_1 x_2 - \tfrac{8}{3} x_3 \\
\dot{y}_1 &= 10\,(y_2 - y_1) \\
\dot{y}_2 &= y_1\,(28.001 - y_3) - y_2 \\
\dot{y}_3 &= y_1 y_2 - \tfrac{8}{3} y_3 + C\,(x_3 - y_3)
\end{aligned} \tag{9.26}$$

The equations were integrated using Runge-Kutta 4th order with a sampling interval of 0.01. The coupling strength C was varied from 0 to 2 in steps of 0.025.

9.3.2 Real EEG Recordings and Preprocessing

Following the previously published work (Williams and Sleigh 1999), we studied the EEG data recording from ten human volunteers with the permission of the Waikato Hospital Ethical Committee. During the recording, the volunteers (American Society of Anesthesiologists physical status I or II) were recruited to undergo a brief propofol anesthetic and recovered in accordance with normal procedures of the Australian and New Zealand College of Anaesthetists (ANZCA) guidelines. Before the experiment, all subjects gave written informed consent after obtaining the permission of the hospital ethical committee. In order to record credible EEG recordings, the silver-silver chloride scalp electrodes were placed at the position of Fp1-F7 and C3-T3 with the ground electrode placed at FpZ according to the 10–20 international system to produce bipolar signals (Fig. 9.1a). The raw EEG and the BIS values were recorded with the Aspect A-1000 EEG monitor (Aspect Medical Systems, Natick, MA, USA) with the sampling frequencies of 256 Hz and 0.2 Hz, respectively.

Fig. 9.1b illustrates the whole experimental sequence diagram. The propofol intravenous infusion was 150 ml/h (1500 mg/h) in an antecubital vein via a syringe driver pump initially, and the BIS and raw EEG data were recorded when the infusion started. Then, a verbal list of dissimilar objects was read to the subject at 30-s intervals who held a syringe filled with water between the forefinger and thumb. When the syringe dropped (LoC time), the infusion and the read of the list of dissimilar stopped, and the time was recorded as “syringe-drop time.” The subject was then allowed to awake and given the play of a prerecorded tape of random numbers and some verbal commands such as “move your right foot.” The

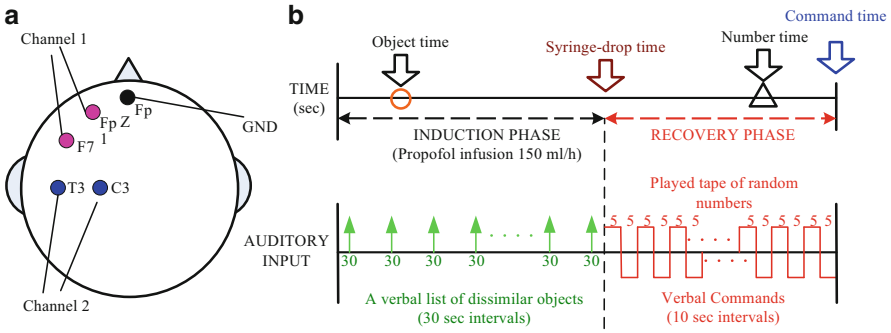

Fig. 9.1 (**a**) Positions of scalp electrodes at Fp1-F7 and C3-T3. (**b**) The diagram of experimental sequence. The "object time" (*circle*), "syringe-drop time", "number time" (*triangle*), and "command time" were marked in the diagram. A verbal list of dissimilar objects was executed in 30-s intervals in the induction phase. The tape of random numbers was played, and verbal commands were given in 10-s intervals in the recovery phase

Table 9.1 The event times for each subject (in seconds)

Subject	"Object time"	"Syringe-drop time"	"Number time"	"Command time"
#1	180	283	435	475
#2	150	379	732	757
#3	90	357	639	649
#4	90	421	792	802
#5	30	454	[a]	650
#6	120	289	360	380
#7	180	433	[a]	588
#8	90	202	[a]	545
#9	30	401	822	832
#10	90	355	560	570

"Object time" = the time point of the last object remembered for the subject during the induction phase
"Syringe-drop time" = the time point that the subject dropped the syringe, denoting the end the induction and time point of loss of consciousness
"Number time" = the time point of the first number remembered during emergence process
"Command time" = the time point corresponding to the subject's correct response to verbal command
[a]Subjects who did not remember any number until responding to verbal command

verbal commands lasted 5 s and they were at 10-s intervals. We recorded the time as "command time" as soon as the subject responded the verbal command correctly (recovery of consciousness (RoC) time). The subjects were questioned as to the first number that they could recall and the last object that they could remember during propofol induction, and these two time points were recorded as "object time" and "number time," respectively. The study was terminated about 60 s after LoC time. Table 9.1 shows the four recorded times of all subjects.

In the EEG preprocessing, we mainly focused on three types of artifacts: baseline drift, head movement noise, and physiological noise (such as electrooculogram (EOG) and electromyogram (EMG)). And different kinds of artifact were processed with different artifact-rejection approach. Firstly, baseline drift and head movement noise are usually in the low-frequency band (<0.5 Hz), and the function eegfilt.m in EEGLAB was used to reduce this noise (Delorme and Makeig 2004). Using statistical mean and standard deviation methods (Seo 2006), amplitude values beyond the range mean $\pm$ 2SD or the raw data with amplitude larger than 200 μV were rejected as considered as outliers. EOG artifacts were reduced through a stationary wavelet transform based on an appropriate threshold (Li et al. 2008a). Finally, inverse filtering was used to identify transient events in the EEG and was employed to detect and remove EMG and other high-amplitude transient artifacts (Fatourechi et al. 2007; Schlögl 2000).

In practice, the EEG data were divided into a series of 10-s epochs, with an overlap of 75 % (in particular, the data were divided into different lengths of time epoch for the calculation of PS indexes.) Synchronization indexes were calculated based on these epochs. In order to evaluate the synchronization performance in consciousness detecting, we chose three states from the whole period: awake state (AS) (the period before "object time"), unconscious state (US) (the period between LoC time and "number time"), and recovery state (RS) (the period after "command time"). Then the efficacy of the indexes was evaluated by the capability for distinguishing different anesthetic states.

9.4 Evaluation Criteria and Statistics

9.4.1 Criteria for Measures Evaluation in Model

We assume that an increase of coupling strength necessarily leads to an enhance of synchronization. To compare the different synchronization measures in terms of their capability to reflect different degrees of coupling, we used the degree of monotonicity (Kreuz et al. 2007) to evaluate the dependence on the coupling strength C of the synchronization measures.

Each synchronization index is computed at $r = 81$ monotonously increasing coupling strengths for each model system, resulting in values S_i, $i = 1, 2, \ldots, r$. If s depends monotonically on the coupling strength C, the $S_i \leq S_j$, $i \leq j$. The degree of monotonicity is defined as

$$\mathrm{DoM} = \frac{2}{r(r-1)} \sum_{i=1}^{r-1} \sum_{j=i+1}^{r} \mathrm{sign}\left(s_j - s_i\right) \tag{9.27}$$

The $\mathrm{DoM} = 1$ if the sequence $s_1, s_2, \ldots, s_r$ has a strictly monotonous increasing trend, while $\mathrm{DoM} = -1$ if it has a monotonically decreasing trend.

9.4.2 Statistical Analysis

We did statistical analysis of comparing the strength of association of each synchrony measure with the BIS index and propofol effect-site concentration (derived from pharmacokinetic/pharmacodynamic (PK/PD) modeling) (Williams and Sleigh 1999) and also the ability of each measure to separate the wakeful from unresponsive behavioral states in the subjects. For each subject, the strength of association between the various synchrony measures and the bispectral index (BIS) or effect-site propofol concentration (ESPC) C_{eff} was assessed using prediction probability (P_k). A P_k value of 1 means that the synchrony measure index is perfectly concordant with the BIS or C_{eff}. A value of 0.5 means that the synchrony measure is not superior to that expected by chance. We also used box plots to visualize and evaluate the performance of each index for distinguishing different anesthesia states. The relative coefficient of variation (CV) (the ratio of standard deviation (SD) to mean) was used to evaluate the index stability during awake and its sensitivity to the induction process (Li et al. 2008b). Further, the R_{ij} was used to assess the correlation of different synchrony measures and BIS with each other. For all tests, $P < 0.05$ was considered significantly.

9.5 Results

9.5.1 Model Simulation Results

Figure 9.2a–d showed the attractors of the responder ($y_1(t)$ and $y_2(t)$) of Hénon maps at four coupling strengths $C = 0$, $C = 0.6$, $C = 0.7$, and $C = 0.8$, while Fig. 9.2e–h showed the plot of the first component of the driver ($x_1(t)$) versus the first component of the responder ($y_1(t)$) at corresponding coupling strengths C. The attractor of the responder looked the same for $C = 0$ (Fig. 9.2a) and $C = 0.8$ (Fig. 9.2d). By contrast, the driver and responder were completely independent when $C = 0$ (Fig. 9.2e) and identical synchronization between driver and responder could be observed when $C = 0.8$ (Fig. 9.2h). Between $C = 0$ and $C = 0.8$, a rather sharp transition to a synchronized state took place around $C = 0.7$ (Fig. 9.2g). The coupled Rössler systems at four coupling strengths $C = 0$, $C = 0.5$, $C = 1$, and $C = 2$ were shown in Fig. 9.3. Figure 9.3a–d showed the attractors of the responder ($y_1(t)$ and $y_2(t)$), and a clear tendency toward the identity of driver ($x_1(t)$) and responder ($y_1(t)$) could be observed in Fig. 9.3e–h. Figure 9.4a–d showed the attractors of the responder ($y_1(t)$ and $y_3(t)$) of coupled Lorenz systems at four coupling strengths $C = 0$, $C = 0.4$, $C = 1.15$, and $C = 2$, whereas Fig. 9.4e–h showed the plot of the driver ($x_1(t)$) and the responder ($y_1(t)$) at corresponding coupling strengths C. The transition toward the synchronized state took place around $C = 1.15$ (Fig. 9.4g).

We used the simulated data x_1 and y_1 of three coupled model systems to calculate the synchronization indexes mentioned in Sect. 9.2 at different coupling strength.

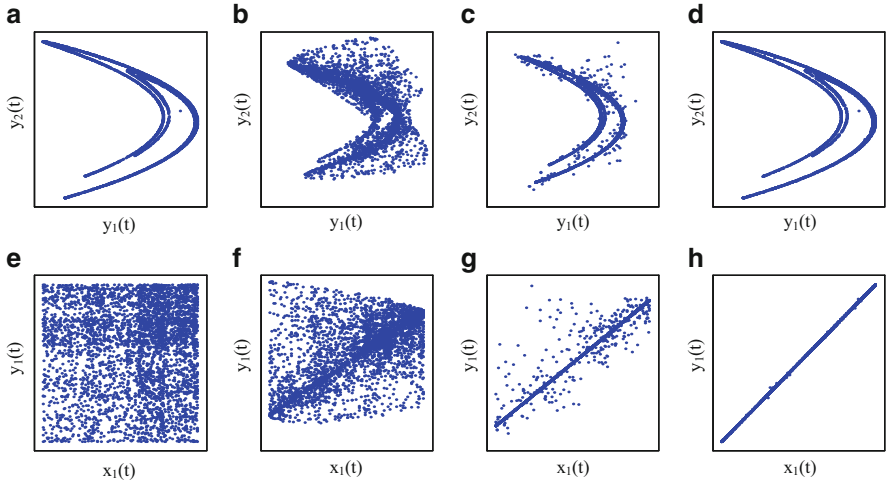

Fig. 9.2 Coupled Hénon maps for different coupling strengths C. (**a**) and (**e**) $C = 0$, (**b**) and (**f**) $C = 0.6$, (**c**) and (**g**) $C = 0.7$, and (**d**) and (**h**) $C = 0.8$

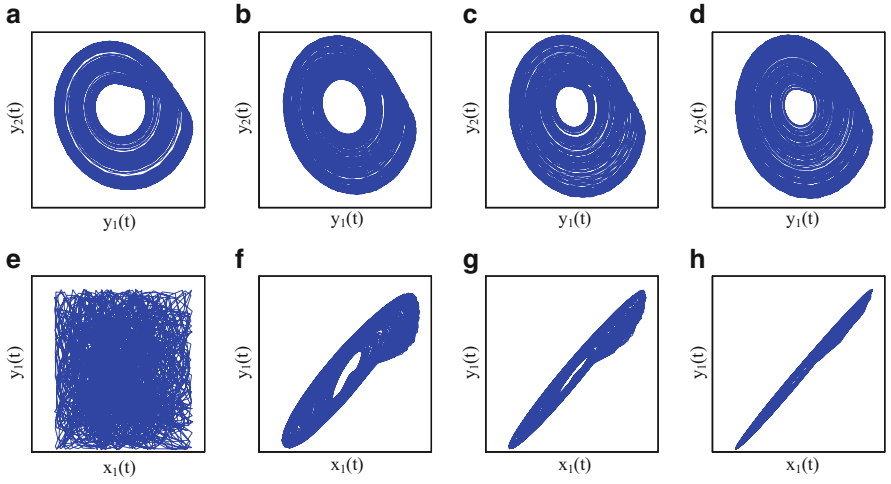

Fig. 9.3 Coupled Rössler systems for different coupling strengths C. (**a**) and (**e**) $C = 0$, (**b**) and (**f**) $C = 0.5$, (**c**) and (**g**) $C = 1$, and (**d**) and (**h**) $C = 2$

The index value at increasing coupling strength C for the Hénon, Rössler, and Lorenz systems was shown in Figs. 9.5, 9.6, and 9.7.

Different model systems exhibited different behaviors with increasing coupling strength. In Fig. 9.5, the value of synchronization indexes, with the exception of DET and WTC, showed a rising trend with increasing coupling strength C, and they had a steep rise at a coupling strength $C = 0.7$. It can be seen from Fig. 9.5a that the COR, KerMI, PCMI, NI, and FTC values started at zero when $C = 0$ and showed

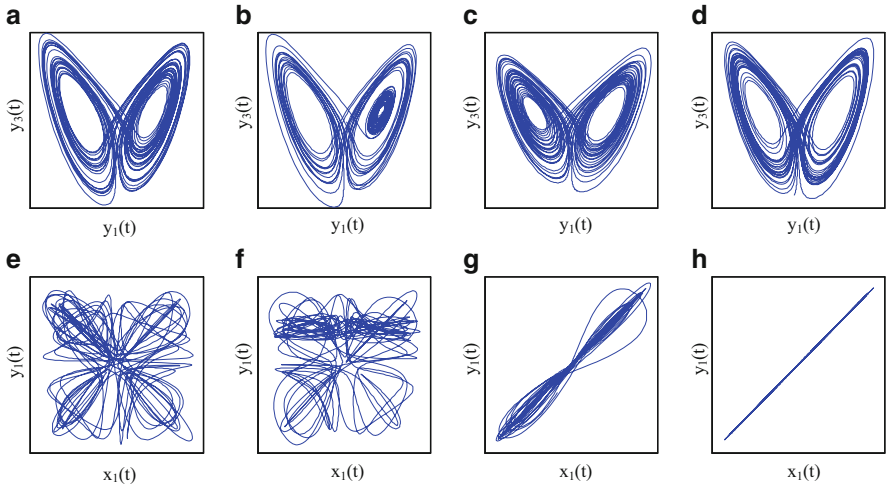

Fig. 9.4 Coupled Lorenz systems for different coupling strengths C. (**a**) and (**e**) $C = 0$, (**b**) and (**f**) $C = 0.4$, (**c**) and (**g**) $C = 1.15$, and (**d**) and (**h**) $C = 2$

less fluctuations. The PCMI rose more gradually, while the NI exhibited a sharp increase at higher C. In terms of PS_{PLV}, PS_{SE}, and PS_{CP}, high values were obtained for uncoupled or weakly coupled Hénon systems and more fluctuations could be observed (Fig. 9.5b). DET and WTC decreased slightly when the coupling strength was weak and increased after $C = 0.45$. They stayed in the range of about 0.3 to 0.4 during the whole coupling strength. As can be seen from the Fig. 9.6, most values of synchronization indexes saw an increase at about $C = 0.2$, while PS_{SE} and DET saw a sharp decrease. Particularly, DET had a high value (DET = 0.9095) when $C = 0$ and it remained at high value during the whole range of coupling strength. By contrast, WTC had a low value (WTC = 0.0511) when $C = 0$ and it stayed at low values, reaching 0.049 when $C = 2$. In Fig. 9.7, a sharp rise appeared when $C = 1.15$ for most indexes. The KerMI and three PS indexes had a nonzero value when $C = 0$, and three PS indexes showed more fluctuations. In terms of DET and WTC, fluctuating during the whole range of coupling strength, DET gained high values and WTC had low values as they were presented in the coupled Rössler systems (Fig. 9.6c).

The values of DoM of the synchronization measures for the Hénon, Rössler, and Lorenz systems were shown in Fig. 9.8. In terms of different model systems, almost all the highest value of DoM of each synchronization measure was obtained in Hénon and Rössler systems. The DoM values of the Lorenz system were smaller than that of the Hénon and Rössler systems, which was due to the fluctuations in Lorenz system. Regarding the different synchronization measures, PCMI had the highest DoM value in both Hénon system (DoM = 0.985) and Lorenz system (DoM = 0.770), and KerMI gained the highest DoM value in Rössler system (DoM = 0.998). Also, we found that the higher DoM values were obtained for

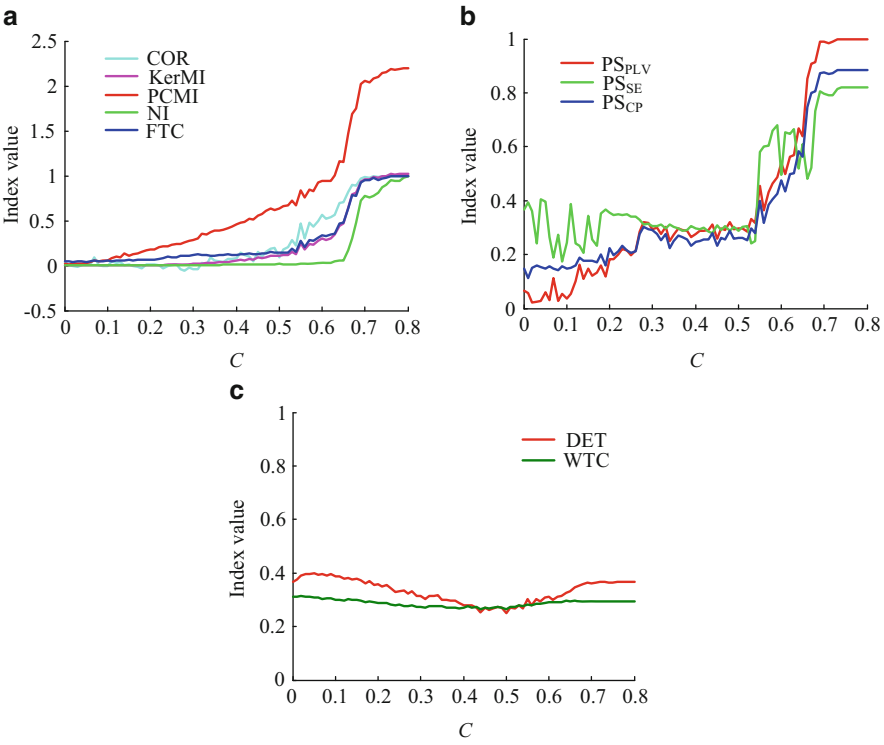

Fig. 9.5 Synchronization measures applied to coupled Hénon systems. (**a**) COR, KerMI, PCMI, NI, and FTC. (**b**) PS indexes of PS_{PLV}, PS_{SE}, and PS_{CP}. (**c**) DET and WTC

NI in Hénon (DoM = 0.984) and Rössler (DoM = 0.988) systems. These results illustrated that PCMI, KerMI, and NI had a better ability to track the increasing coupling strength. By contrast, DET and WTC gained the negative DoM values which meant that they even had the monotonically decreasing trend with increasing coupling strength.

9.5.2 Application to Real EEG Recordings

FTC and WTC were calculated with pairwise channels for each subject in order to find a better coherence method to quantify the synchronization in frequency domain.

The EEG recordings of two channels from one subject were shown in Fig. 9.9a, b, c, and d and showed the FTC and WTC spectrums during the whole period. In terms of FTC spectrum, EEG signals were divided into a series of 10-s epochs with overlap of 75 %. The epochs were windowed using a Hamming window and FFT length was set to be 128. As can be seen from the figure, FTC spectrum could not

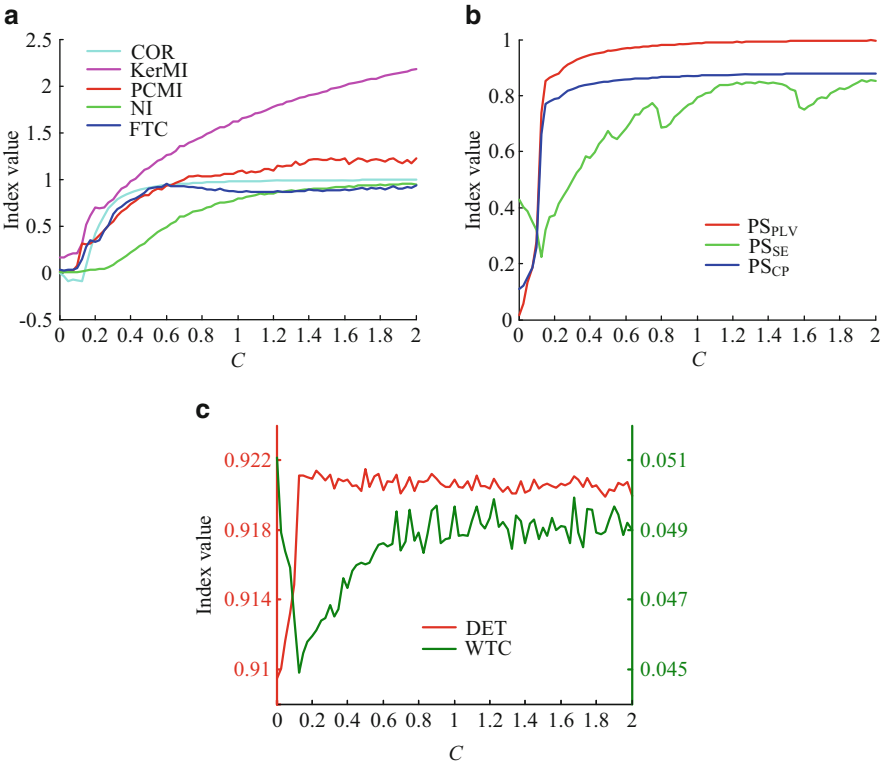

Fig. 9.6 Synchronization measures applied to coupled Rössler systems. (**a**) COR, KerMI, PCMI, NI, and FTC. (**b**) PS indexes of PS_{PLV}, PS_{SE}, and PS_{CP}. (**c**) DET and WTC

reflect the changes of coherence during the whole period (Fig. 9.9c). With similar results as the spectrogram shows, the WTC spectrum in the δ, α, and β frequency bands increased obviously during unconscious state (Fig. 9.9d). Therefore, WTC index was extracted from WTC spectrum to quantify the synchronization during propofol-induced anesthesia period.

Then the synchronization indexes were computed during the whole anesthetic period for all subjects. Figure 9.10a gives an example of one subject from the left prefrontal and left primary motor cortex, respectively.

Figure 9.10b–c was the corresponding C_{eff} and BIS index. Figure 9.10d–k showed the values of all synchronization indexes for the same subject. In each frequency band (δ, θ, α, β, and $\gamma 1$), three PS indexes were calculated, and results showed that the PS_{PLV} and PS_{CP} had similar results, which was consistent with previously reported results in Quiroga et al. (2002), and the PS_{CP} will not be further reported. It also can be seen that the PCMI, NI, PS_{PLV} (δ, θ, α, and $\gamma 1$), and PSSE (δ, β) saw a decreasing trend with the increasing C_{eff} value, whereas KerMI, DET, and WTC (δ, θ, and α frequency bands) showed an increasing trend which was consistent with the C_{eff}.

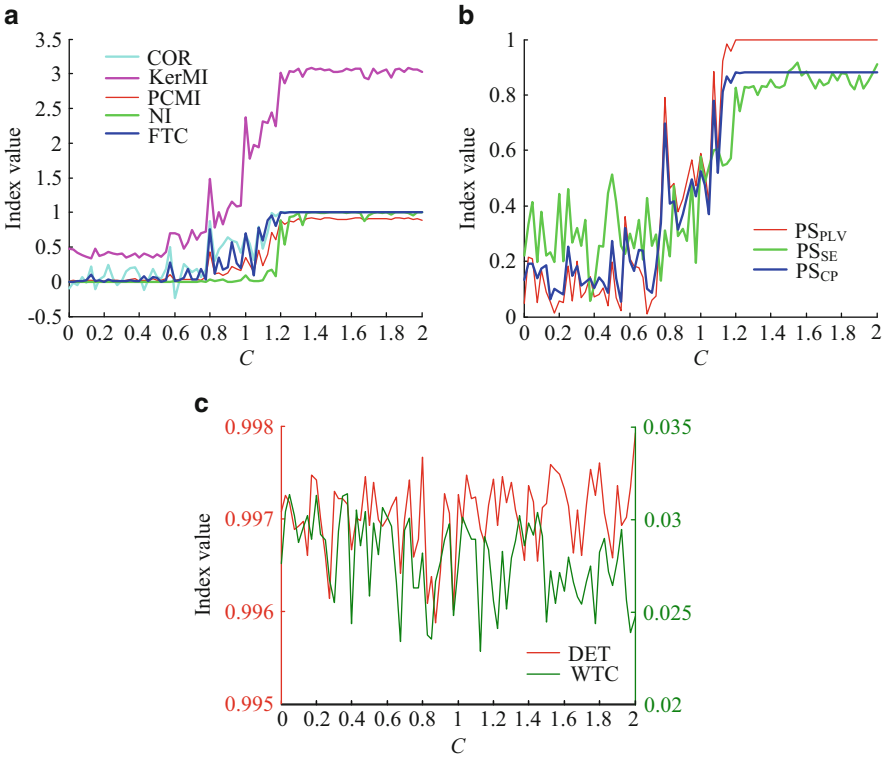

Fig. 9.7 Synchronization measures applied to coupled Lorenz systems. (**a**) COR, KerMI, PCMI, NI, and FTC. (**b**) PS indexes of PS_{PLV}, PS_{SE}, and PS_{CP}. (**c**) DET and WTC

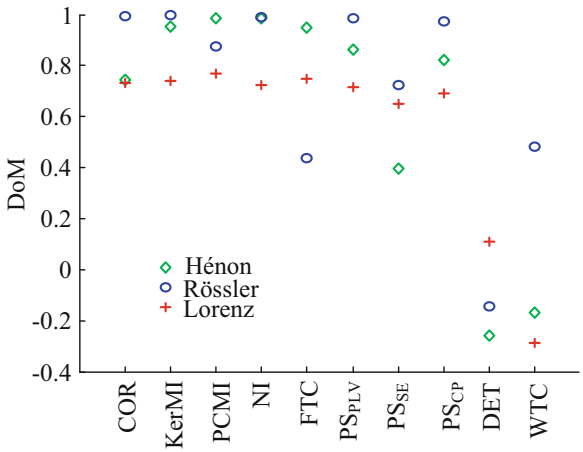

Fig. 9.8 Degree of monotonicity of synchronization indexes for the Hénon, Rössler, and Lorenz systems

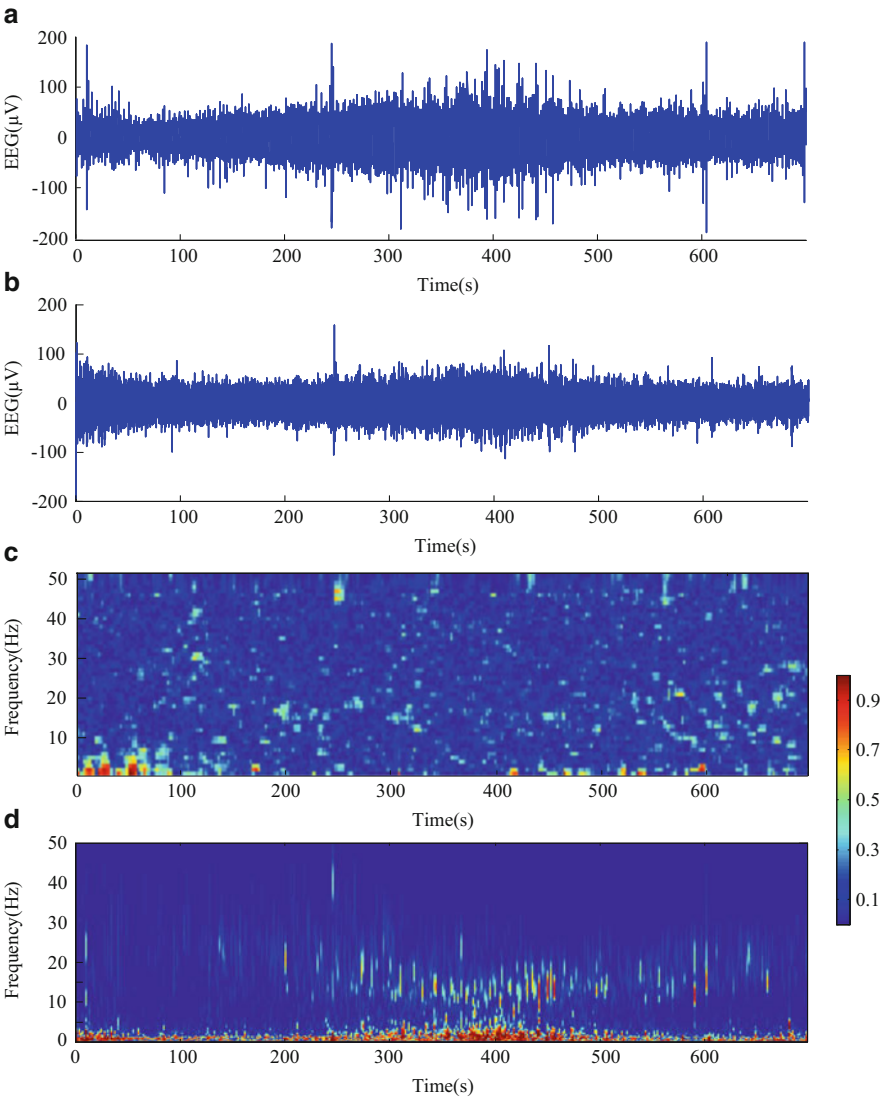

Fig. 9.9 (**a**)–(**b**) Two-channel preprocessed EEG recordings of one subject over the whole experiment period. (**c**) The FTC spectrum of the two EEG recordings. (**d**) The WTC spectrum of the two EEG recordings

The statistical parameter P_k were used to quantify the ability of predicting BIS (P_{K_BIS}) and the C_{eff} ($P_{KC_{eff}}$) of the synchronization measures. The box plots of P_k values of each synchronization indexes with BIS and C_{eff} were shown in Fig. 9.11. The median of P_k values of all measures were displayed in Table 9.2. It can be seen from Fig. 9.11 and Table 9.2 that PCMI had the highest P_k value with BIS

($P_{K\_BIS} = 0.855$) and ESPC ($P_{KC_{eff}} = 0.794$). DET ranked second with the value $P_{K\_BIS} = 0.823$ and $P_{KC_{eff}} = 0.781$. These figures demonstrated that PCMI and DET could best predict the BIS and follow the ESPC. The P_k values of NI, KerMI, and COR were smaller than PCMI and DET.

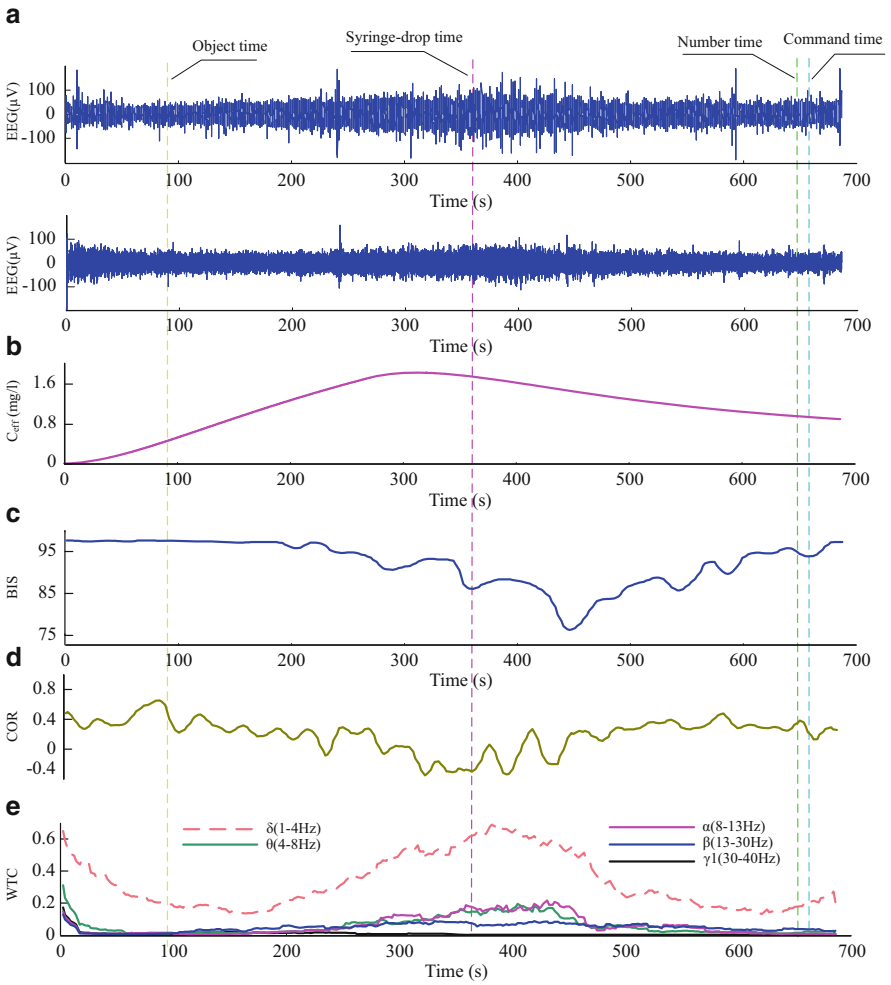

Fig. 9.10 Two EEG recordings from one subject and corresponding synchronization measures versus time. (**a**) Two preprocessed EEG recordings from *left* prefrontal and *left* primary motor cortex recorded simultaneously at 256 Hz. The data were resampled to 100Hz for analysis. The recordings include the transitions from the conscious state to unconscious state and from unconsciousness to RoC. The four *dashed gray lines* are the time marks of the experiments. (**b**) Effect-site propofol concentration for the same subject. (**c**) The BIS value of the same subject derived from one EEG monitor. (**d**)–(**k**) Time course of synchronization measures, plotted with a time intervals of 10 s with 75 % overlap

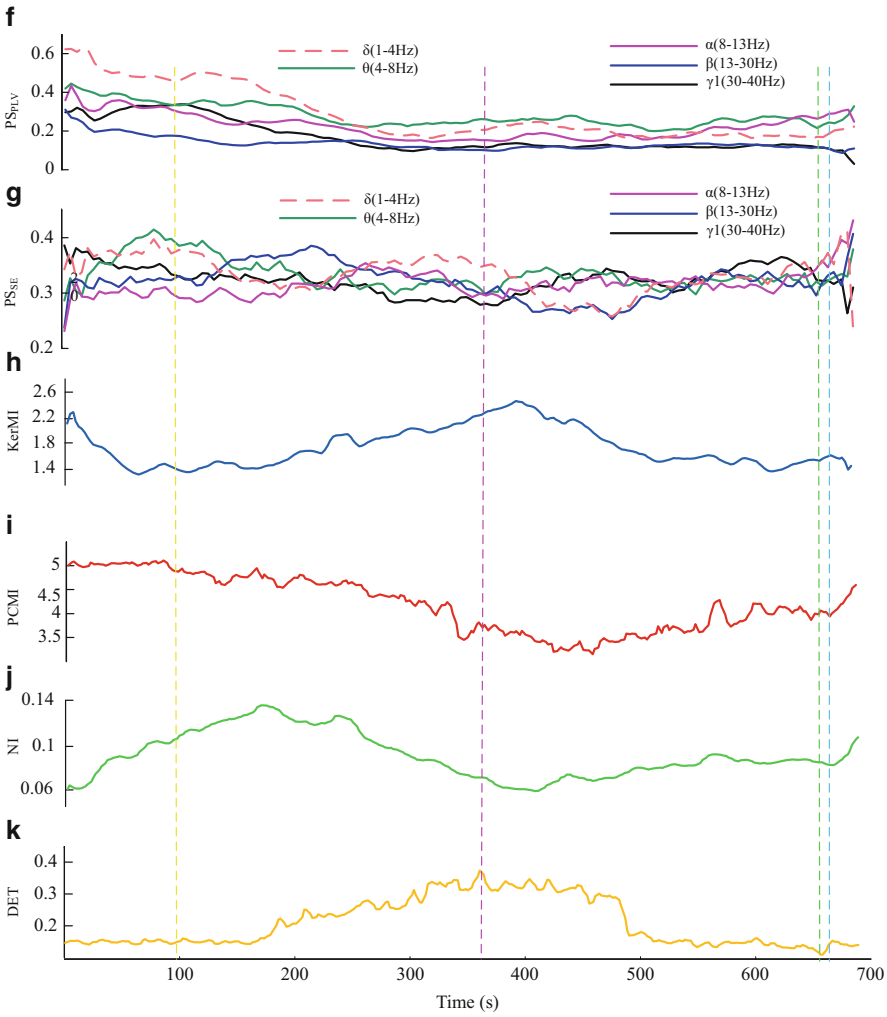

Fig. 9.10 (continued)

Furthermore, in order to evaluate the ability of the synchronization measures in distinguishing different anesthetic states which is essential for depth of anesthesia monitoring, we give the synchronization indexes and the box plots of the index values at three anesthetic states (awake, unconscious, and recovery) in Fig. 9.12. It can be seen from Fig. 9.12 that KerMI, PCMI, NI, and DET could significantly distinguish awake and unconscious states as well as unconscious and recovery states ($p < 0.001$), whereas COR could only distinguish awake and unconscious states ($p < 0.001$). As for WTC, there was a significant rise in unconscious state and a significant drop in recovery state for all frequency bands (Fig. 9.12b–f). In terms

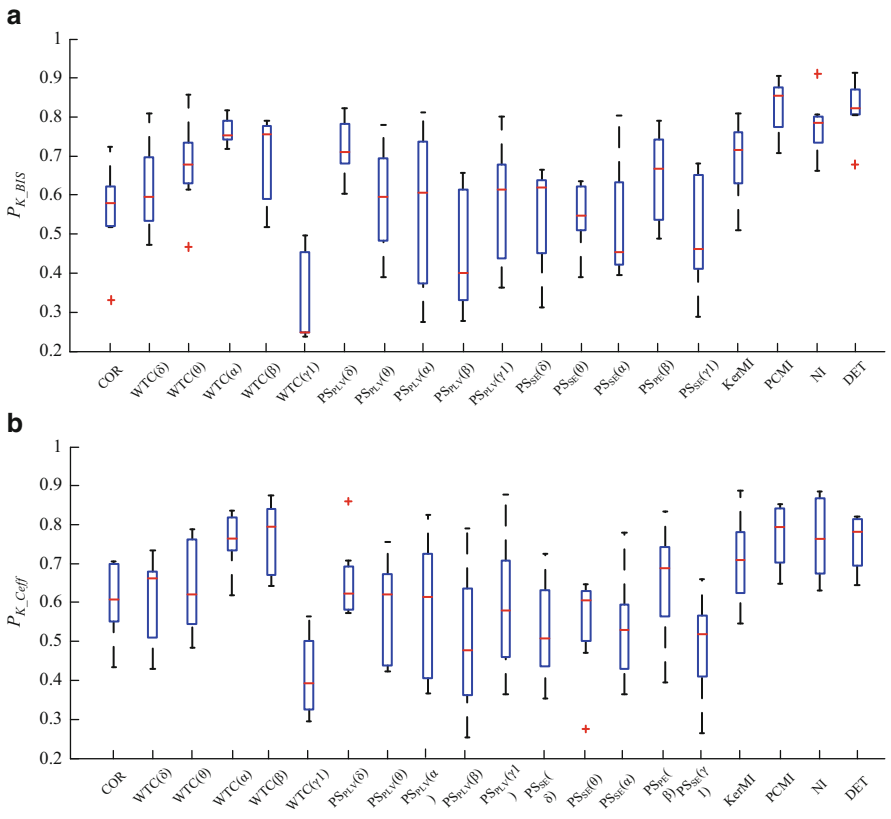

Fig. 9.11 Statistical analysis of all subjects for each of the synchronization measures. (**a**) The prediction probability value of the indexes with the BIS as an independent variable. (**b**) The prediction probability value of the synchronization indexes with the ESPC index (C_{eff}) of all subjects

of PS_{PLV}, the phase synchronization dropped significantly in unconscious state for PS_{PLV} (δ, θ, α, and $\gamma 1$) and had no significant changes in recovery state, while PS_{PLV} (β) could not distinguish the three anesthetic states (Fig. 9.12g–k). PS_{SE} could only distinguish three states at θ and β frequency bands (Fig. 9.12l–p). There was an increase in unconscious state and a decrease in recovery state for KerMI and DET, while the trends were opposite for PCMI and NI.

It is crucial for the DoA monitoring that the index value should stay stable during each anesthetic state. Table 9.3 represents the CV values of synchronization indexes that calculated with all subjects at awake, unconscious, and recovery states.

As can be seen from Table 9.3, PCMI had the low CV in awake state (CV = 0.085), unconscious state (CV = 0.146), and recovery state (CV = 0.105). The CV of NI, PS_{PLV}, PS_{SE}, and DET was lower than COR and KerMI, which were

Table 9.2 Median of P_K of different synchronization indexes with BIS and C_{eff}

	COR	WTC (δ)	WTC (θ)	WTC (α)	WTC (β)	WTC ($\gamma 1$)	PS_{PLV} (δ)	PS_{PLV} (θ)	PS_{PLV} (α)	PS_{PLV} (β)
BIS	0.579	0.594	0.677	0.753	0.755	0.248	0.711	0.595	0.605	0.399
C_{eff}	0.607	0.662	0.621	0.763	0.794	0.393	0.624	0.621	0.615	0.479
	PS_{PLV} ($\gamma 1$)	PS_{SE} (δ)	PS_{SE} (θ)	PS_{SE} (α)	PS_{SE} (β)	PS_{SE} ($\gamma 1$)	KerMI	PCMI	NI	DET
BIS	0.613	0.619	0.545	0.453	0.667	0.460	0.714	0.855	0.783	0.823
C_{eff}	0.580	0.509	0.605	0.530	0.688	0.520	0.709	0.794	0.764	0.781

COR cross correlation
WTC coherence based on wavelet transformation
PS_{PLV} phase synchronization based on phase-locking value
PS_{SE} phase synchronization based on Shannon entropy
KerMI mutual information based on kernel estimation
PCMI permutation cross mutual information
NI nonlinear interdependence
DET determinism

all smaller than WTC in awake and unconscious states. These results illustrated that PCMI, NI, PS, and DET are more robust to noise during the propofol-induced anesthesia.

Although with various results for the synchronization measures, they also have somewhat relevance with the BIS and C_{eff}. Thus, the correlation coefficient R was calculated.

BIS and ESPC of all subjects and the averaged R over all subjects were shown in Fig. 9.13. It can be seen that the PCMI had the highest correlation coefficient with BIS ($R = 0.846$) and C_{eff} ($R = 0.739$). DET ranked second with BIS ($R = 0.843$) and C_{eff} ($R = 0.703$). As for PS and WTC, PS_{PLV} (δ) and WTC (α) correlated with BIS and C_{eff} higher than that of other frequency bands. In terms of the relation among different synchronization measures, PCMI correlated closely with DET ($R = 0.949$) and NI ($R = 0.838$).

9.6 Conclusions

We considered seven types of synchronization measures, including cross correlation, cross coherence based on Fourier transforms and wavelet transform, three phase synchronization measures at different frequency bands, three different mutual information measure-based methods, nonlinear interdependence, and cross recurrence analysis. These seven types of method quantify synchronization based on different foundations. The cross correlation demonstrates the relationship of EEG magnitude between different channels. If EEG magnitude increases in one channel and at the same time (or within a preset time lag) it also occurs in the other channel, the COR value will be high. The cross coherence is a time-frequency domain method

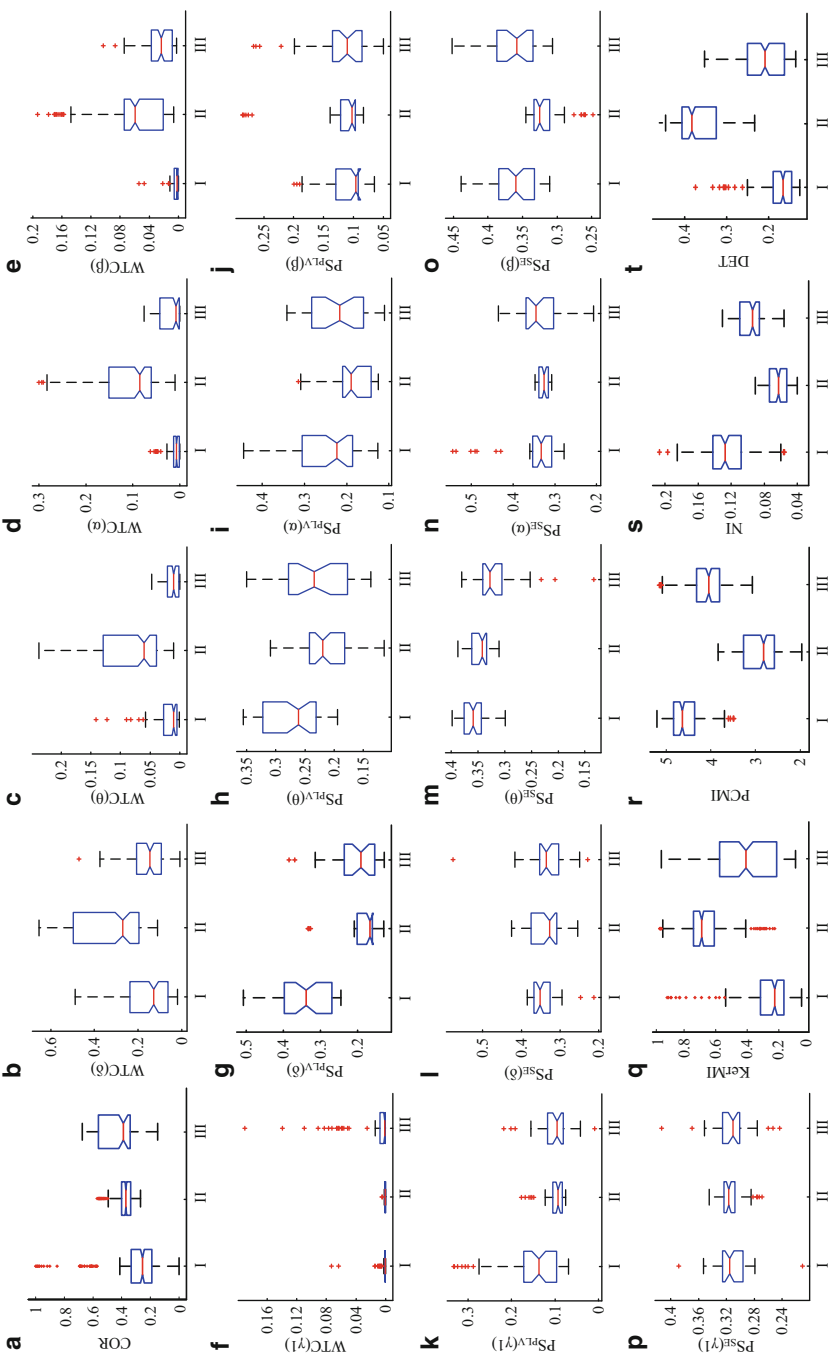

Fig. 9.12 Box plots of synchronization indexes in different anesthesia states (I, awake state; II, unconscious state; III, recovery state)

Table 9.3 CV of the studied indexes at different anesthetic states

	Awake state	Unconscious state	Recovery state
COR	0.633	0.186	0.299
WTC(δ)	0.684	0.479	0.636
WTC(θ)	1.206	0.743	0.981
WTC(α)	1.334	0.705	1.118
WTC(β)	1.595	0.733	0.822
WTC($\gamma 1$)	2.89	1.356	2.077
$PS_{PLV}(\delta)$	0.243	0.280	0.323
$PS_{PLV}(\theta)$	0.183	0.263	0.262
$PS_{PLV}(\alpha)$	0.350	0.290	0.309
$PS_{PLV}(\beta)$	0.326	0.490	0.480
$PS_{PLV}(\gamma 1)$	0.491	0.255	0.427
$PS_{SE}(\delta)$	0.095	0.141	0.185
$PS_{SE}(\theta)$	0.064	0.059	0.177
$PS_{SE}(\alpha)$	0.180	0.038	0.155
$PS_{SE}(\beta)$	0.089	0.079	0.096
$PS_{SE}(\gamma 1)$	0.082	0.0578	0.103
KerMI	0.627	0.227	0.548
PCMI	0.085	0.146	0.105
NI	0.220	0.165	0.209
DET	0.226	0.138	0.269

The meaning of the indexes refers to the legend of Table 9.2

and can separate the cross-channel associations within different frequency bands. In this study, we used two cross coherence evaluation methods (Fourier transform and wavelet transform) to quantify the coherence. It is generally thought that the wavelet decomposition has better time resolution than the Fourier-based method. Phase synchronization analysis is a classic neuronal oscillation analysis method that is somewhat independent of the raw amplitude of the signal. The instantaneous phase extraction is based on the WHWT, which was proposed in our previous study (Li et al. 2011). Mutual information has been widely applied in EEG analysis as a way of estimating information integration between different EEG channels or brain regions for mechanism analysis and neurological disease diagnosis, such as epilepsy seizure, Alzheimer's disease and autism, etc. (Abásolo et al. 2008; Hall and Sarkar 2011; Langen et al. 2009). It is based on the hypothesis that state information of one channel can be used to reduce the uncertainty for understanding the other channel if they are associated in some way. In practical terms, the probability density can be estimated in a number of different ways. We applied two different methods, kernel density estimation and permutation entropy, to calculate the MI value. Nonlinear interdependence and cross recurrence analysis are nonlinear time series analysis methods based on reconstruction of the phase space of the signals. The nonlinear interdependence measure of $S^{(k)}(X|Y)$ and the determinism measure can be used as indexes to quantify synchrony. Although we considered a large variety of synchrony

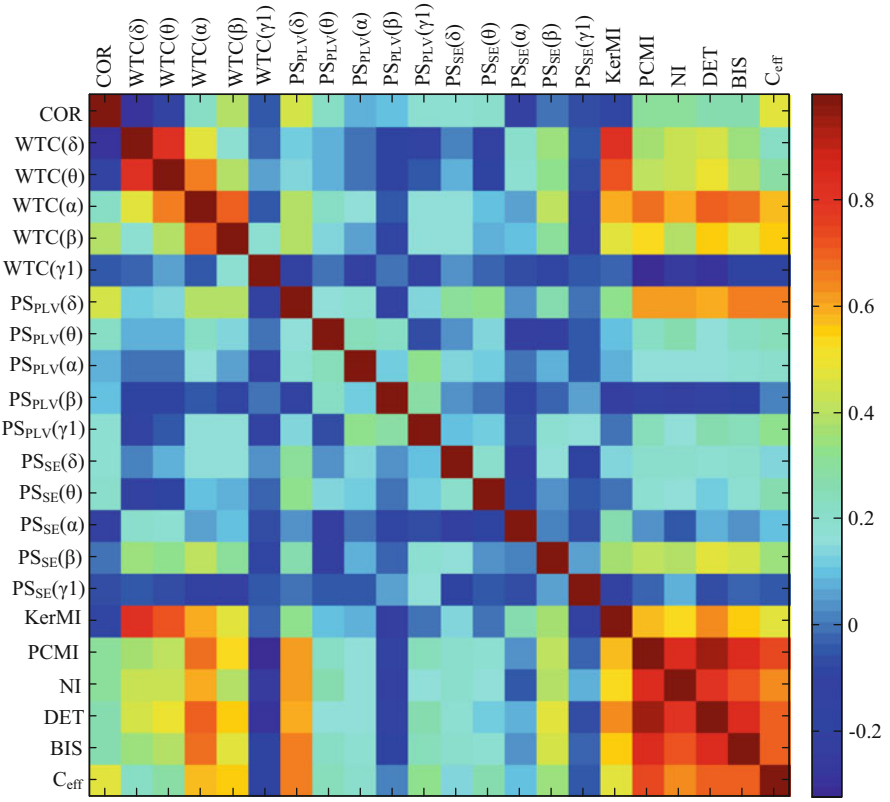

Fig. 9.13 Correlation coefficients R among different synchronization measures, BIS, and C_{eff} averaged over all subjects

measure, it is impossible to include all existing measures in this study. Of the seven types of methods tested, each has their own representative features. The measures we have studied probe different aspects of the system or time series, such as phase, symbolic dynamics, time-frequency relationships, etc.

Neurophysiological signals are complex, nonlinear, and nonstationary. The features of the coupling dynamics underlying these signals, however, are not well understood (Andrzejak et al. 2003), making the choice of evaluative measure somewhat arbitrary. At the very least, the measures to be used must be validated against a test standard. To evaluate the performance of the synchrony measures we utilized, three nonlinear coupling models were used, upon which each method was tested. The results show that the synchronization measures could track the changes of coupling strength in the models, but with differing, somewhat nonlinear characteristics. All methods show an abrupt change at a certain coupling strength threshold.

The synchronization measures were able to distinguish the different anesthesia states (see Fig. 9.12) with the exception of COR. Of all the measures, PCMI appears to be superior to the other methods, for the following reasons. Firstly, it is less sensitive to noise in the EEG signal during the awake state (seen in Fig. 9.9). Furthermore, PCMI correlated closely with propofol effect-site concentration and BIS index (a higher P_k and R_{ij} (see Table. 9.2)) and is less affected by the amplitude of the EEG (the distribution probability calculation based on the permutation (Li et al. 2008c; Olofsen et al. 2008)).

Interestingly, the WTC, KerMI, and DET methods exhibit an opposite trend of changes in anesthetic levels compared with the other measures. This phenomenon is difficult to explain in the context of understanding anesthetic mechanisms. To some extent it can be explained on the basis of the simulation model analysis, which shows that WTC and DET change out of phase with the other methods. However, the KerMI index increases with increasing coupling strength in the simulations and appears to contradict the reductions seen with the other measures when applied to the EEG. Clearly, the EEG signal is more complex than simulated by simple nonlinear models, and further insight is required into the underlying principles underpinning the different synchrony measures.

Although all synchrony measures could track this fundamental shift in EEG pattern, each algorithm responded in characteristic fashion. The WTC is a time-frequency measurement method, which characterizes the phase synchrony at each frequency point. It can be seen that the spectrum of the WTC is similar to the EEG spectrogram of the recordings computed using a short-time Fourier transform. WTC is based on the summation of the coherence of the frequency band at each time point. Because it takes signal amplitude into account, the value of WTC at δ frequency band increases most obviously with the deepening of anesthesia. Among the three phase synchronization methods, which measure the phase difference of two EEG signals, only PS_{PLV} and PS_{CP} at the δ frequency band clearly distinguished the awake state from unconscious state. PCMI and KerMI are both mutual information measures, but their calculation principles are different. PCMI is related to the permutation pattern probability distribution. With deepening anesthesia the permutation pattern decreases because the EEG signals become more regular. On the other hand, the KerMI quantifies the difference in amplitude between time-domain neighboring signals. The high value of KerMI during anesthesia is on account of the small difference in signal magnitude between adjacent signals. The slower fluctuation of signal, the smaller the difference between adjacent points. So, when anesthesia deepens and the signals become regular, the KerMI will increase. The nonlinear method DET, which is based on the recurrence plot, describes the complexity of the nonlinear system. When anesthesia deepens, the EEG signal becomes more regular and the DET measure will increase with this trend. In our case we are looking at the cross recurrence, i.e., the recurrence occurs when the trajectory in one channel becomes close to that of the other channel, thus reflecting the inner coupling changes during anesthesia.

It is not meaningful to attempt to quantify on the basis of one or other measure the extent to which synchronization either strengthens or weakens during anesthesia.

Because each measure is derived from a different perspective, their outputs can be seen as complementary, not conflicting. Such as, we could say that coherence between two brain areas during anesthesia is increased based on the WTC. At the same time, mutual information based on the permutation measure decreases with deepening anesthesia. Further, PCMI, PS_{PLV} at δ frequency band (δ $(1-4Hz)$), and NI show a declining trend with increasing propofol concentration, reflecting a reduction in long-range coupling. From the perspective of information theory, PCMI is based on the permutation pattern probability distribution, which decreases with the deepening of anesthesia. This decreasing pattern to some extent reflects the marked decrease in the mean firing rate in the cortex (Olofsen et al. 2008; Hentschke et al. 2005). Moreover, Lewis et al. found that propofol-induced unconsciousness is associated with an increase in the low-frequency EEG (<1 Hz) band. Consistent with these observations, we found that PS_{PLV} and PS_{CP} values at the delta frequency band exhibit an abrupt change at the loss of consciousness point. This suggests that the appearance of low-frequency activity might be a good proxy for loss of long-distance coupling (Lewis et al. 2012). The NI index significantly drops in unconsciousness state in our study, suggesting that disparate brain regions have weaker interdependence with increasing drug effect. This is consistent with the findings of previous studies (Lee et al. 2009b; Jameson and Sloan 2006; Schrouff et al. 2011). The increase in wavelet coherence of the slow oscillation (<1Hz), δ rhythm (1–4Hz), and α rhythm (8–13Hz) during deep anesthesia suggests that propofol enhances corresponding band activity. We found that the high WTC values during deep anesthesia state are also consistent with the results of our previous study (Li et al. 2013).

In conclusion, we found that most of the synchronization measures that we investigated can track the anesthetic effect on the EEG. However, each measure responded in distinctive fashion, on account of their corresponding characteristic principles. Each method may be seen to capture specific synchrony criteria. It is important to underscore that these issues need to be carefully taken into account when formulating and verifying theories explaining anesthesia mechanisms. The different measures responded in characteristic fashion, suggesting that each may tell us something different about the mechanism by which anesthetic drugs disrupt cortical information processing and coupling. These in-depth analyses have important implications for understanding of other neural mechanisms.

Appendices

In order to evaluate the synchronization measures in different anesthetic states efficiently, we discussed the parameter selections of COR, PS, NI, and DET. The indexes corresponding to the states of awake, unconscious, and recovery were selected for comparison. The values of synchronization indexes under different parameters were shown in Fig. 9.14, 9.15, 9.16, 9.17, and 9.18.

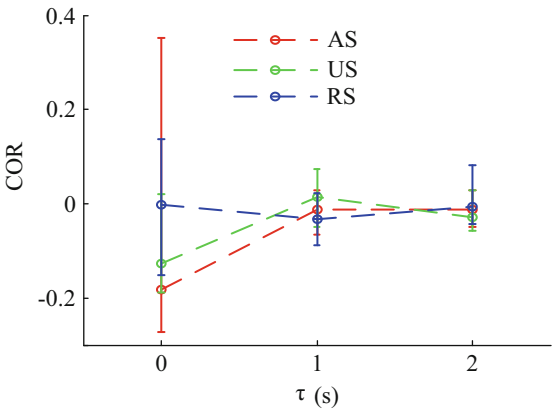

Fig. 9.14 COR values at different time lag τ in awake state (AS) (*red*), unconscious state (US) (*green*), and recovery state (RS) (*blue*)

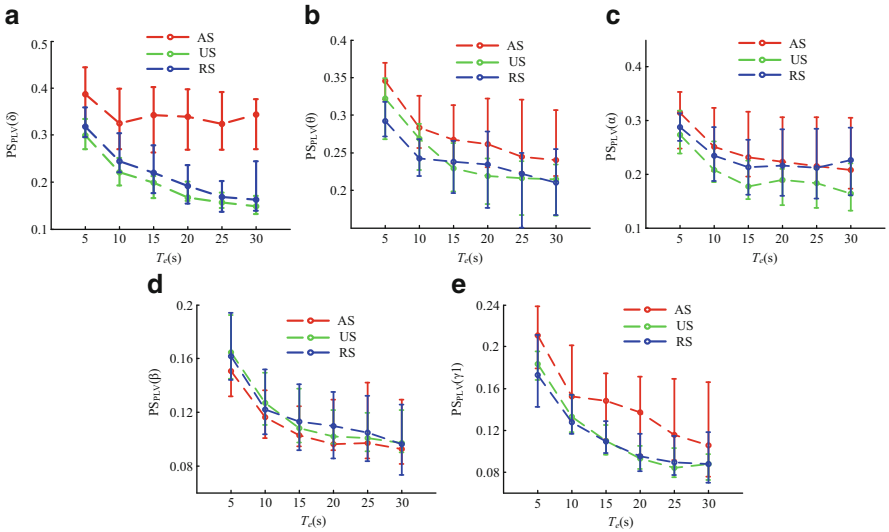

Fig. 9.15 PS_{PLV} values of five frequency bands (δ, θ, α, β, and $\gamma 1$) with different epoch length T_e in AS (red), US (green), and RS (blue)

Appendix A. COR

Figure 9.14 shows the cross correlation indexes of different delay times τ at different study states (red, awake state (AS); green, unconsciousness state (US); and blue, recovery state (RS)) for all ten subjects under propofol anesthesia. We chose two positive delay times, two negative delay times, and the zero delay time. The cross correlation values are positive and higher when $\tau = 0$ at both the awake state and recovery state. Besides, the COR value reveals quite large negative correlation at the deep anesthesia state when $\tau = 0$. For this reason, we choose the zero delay time.

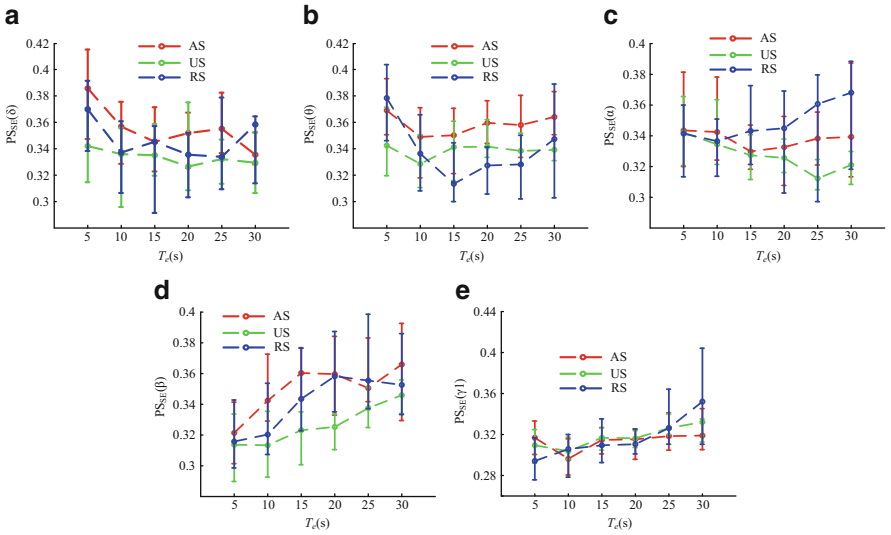

Fig. 9.16 PS_{SE} values range of five frequency bands (δ, θ, α, β, and $\gamma 1$) with different epoch length T_e in AS (*red*), US (*green*), and RS (*blue*)

Appendix B. PS

Figures 9.15 and 9.16 show the PS_{PLV} (δ, θ, α, β, and $\gamma 1$) and PS_{SE} (δ, θ, α, β, and $\gamma 1$) indexes at different T_e in awake state (red), unconscious state (green), and recovery state (blue). It can be seen from Fig. 9.15 that the PS_{PLV} values of each frequency band decreased with T_e increasing. The difference between awake and unconscious states of PS_{PLV} (δ) was larger than PS_{PLV} in other frequency bands. By contrast, PS_{SE} had some fluctuation at different epoch lengths T_e (Fig. 9.16). And $T_e = 20$ was selected in our study.

Appendix C. NI

Firstly, Fig. 9.17a shows the NI values with the parameter of time lag $\tau = 1$, nearest neighbors $k = 20$ in different embedding dimension m in AS (red), US (green), and RS (blue) of all subjects. The NI values with $\tau = 2$ and $k = 20$ in different m were shown in Fig. 9.17b. It can be seen from Fig. 9.17a and b that NI increased monotonically with increasing m. And the difference of NI indexes between these states became wider with the increase of m. Considered the calculation complexity, $m = 5$ was selected for the NI indexes. Then, Fig. 9.17c shows NI indexes with $m = 5$ and $k = 20$ in different τ. The difference of NI indexes between awake and

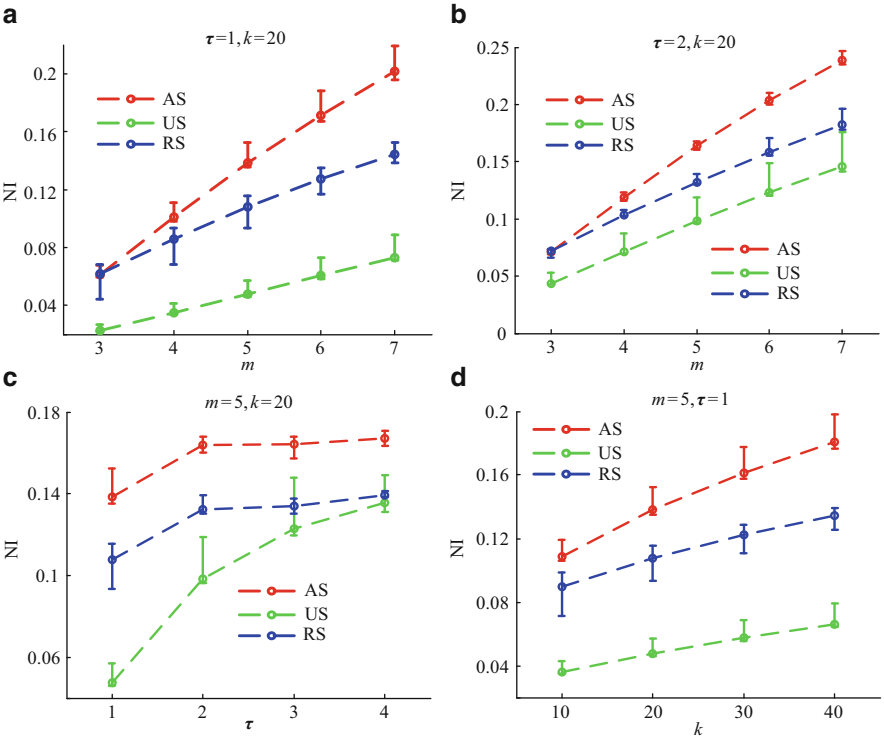

Fig. 9.17 NI values range at different parameters of embedding dimension m, time lag τ, and the number of nearest neighbors k in AS (*red*), US (*green*), and RS (*blue*)

unconscious states became smaller with increasing τ, so we chose $\tau = 1$. Finally, the NI values with $m = 5$ and $\tau = 1$ in different nearest neighbors k were shown in Fig. 9.17d and we selected $k = 20$ in this study.

Appendix D. DET

Figure 9.18a, b, and c shows the DET value range with embedding dimension $m = 3$, $m = 4$, and $m = 5$, respectively, in threshold of diagonal length $l_{\min} = 2$ in different time lag τ in awake state (red), unconscious state (green), and recovery state (blue) of all subjects. $m = 3$ and $\tau = 2$ were selected for the great DET difference between awake and unconscious states. DET indexes with $m = 3$ and $\tau = 2$ in different $l_{\min}$ were shown in Fig. 9.18d and $l_{\min} = 2$ was selected.

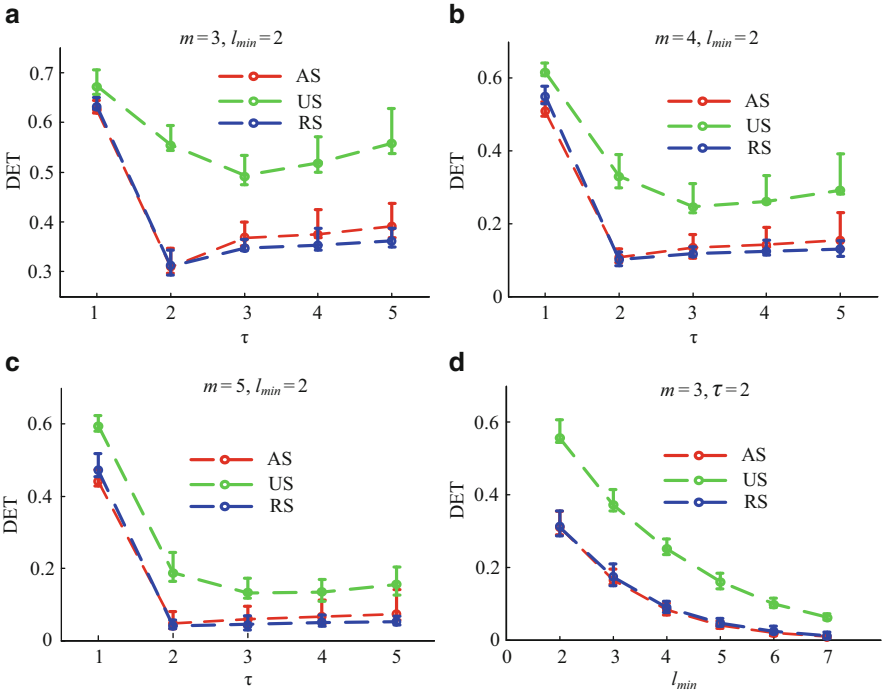

Fig. 9.18 DET indexes range with different parameters of embedding dimension m, time lag τ, and threshold of diagonal length $l_{\min}$ in AS (*red*), US (*green*), and RS (*blue*)

References

Abásolo D et al. Approximate entropy and auto mutual information analysis of the electroencephalogram in Alzheimer's disease patients. Med Biol Eng Comput. 2008;46(10):1019–28.

Allefeld C, Kurths J. Multivariate phase synchronization analysis of EEG data. IEICE Trans Fundam Electron Commun Comput Sci. 2003;86(9):2218–21.

Allefeld C, Kurths J. An approach to multivariate phase synchronization analysis and its application to event-related potentials. Int J Bifurcation Chaos. 2004;14(02):417–26.

Andrzejak RG et al. Bivariate surrogate techniques: necessity, strengths, and caveats. Phys Rev E. 2003;68(6):066202.

Aviyente S et al. A phase synchrony measure for quantifying dynamic functional integration in the brain. Hum Brain Mapp. 2011a;32(1):80–93.

Aviyente S et al. A phase synchrony measure for quantifying dynamic functional integration in the brain. Hum Brain Mapp. 2011b;32(1):80–93.

Bandt C, Pompe B. Permutation entropy: a natural complexity measure for time series. Phys Rev Lett. 2002;88(17):174102.

Beirlant J et al. Nonparametric entropy estimation: an overview. Int JMath Stat Sci. 1997;6:17–40.

Birchler-Pedross A et al. Higher frontal EEG synchronization in young women with major depression: a marker for increased homeostatic sleep pressure? Sleep. 2011;34(12):1699–706.

Breakspear M. "Dynamic" connectivity in neural systems. Neuroinformatics. 2004;2(2):205–24.

Breakspear M, Terry J. Topographic organization of nonlinear interdependence in multichannel human EEG. Neuroimage. 2002a;16(3):822–35.
Breakspear M, Terry J. Nonlinear interdependence in neural systems: motivation, theory, and relevance. Int J Neurosci. 2002b;112(10):1263–84.
Dauwels J et al. A comparative study of synchrony measures for the early diagnosis of Alzheimer's disease based on EEG. Neuroimage. 2010;49(1):668–93.
David O, Friston KJ. A neural mass model for meg/eeg: coupling and neuronal dynamics. Neuroimage. 2003;20(3):1743–55.
David O, Cosmelli D, Friston KJ. Evaluation of different measures of functional connectivity using a neural mass model. Neuroimage. 2004;21(2):659–73.
Delorme A, Makeig S. EEGLAB: an open source toolbox for analysis of single-trial EEG dynamics including independent component analysis. J Neurosci Methods. 2004;134(1):9–21.
Eckmann J-P, Kamphorst SO, Ruelle D. Recurrence plots of dynamical systems. Europhys Lett. 1987;4(9):973–7.
Engel AK, Fries P, Singer W. Dynamic predictions: oscillations and synchrony in top–down processing. Nat Rev Neurosci. 2001a;2(10):704–16.
Engel AK, Fries P, Singer W. Dynamic predictions: oscillations and synchrony in top–down processing. Nat Rev Neurosci. 2001b;2(10):704–16.
Fatourechi M et al. EMG and EOG artifacts in brain computer interface systems: a survey. Clin Neurophysiol. 2007;118(3):480–94.
Hall Jr CW, Sarkar A. Mutual information in natural position order of electroencephalogram is significantly increased at seizure onset. Med Biol Eng Comput. 2011;49(2):133–41.
Hentschke H, Schwarz C, Antkowiak B. Neocortex is the major target of sedative concentrations of volatile anaesthetics: strong depression of firing rates and increase of GABAA receptor-mediated inhibition. Eur J Neurosci. 2005;21(1):93–102.
Jameson LC, Sloan TB. Using EEG to monitor anesthesia drug effects during surgery. J Clin Monit Comput. 2006;20(6):445–72.
Kaminski M, Liang H. Causal influence: advances in neurosignal analysis. Critic Rev ™ Biomed Eng. 2005;33(4):347–430.
Koenig T et al. Decreased EEG synchronization in Alzheimer's disease and mild cognitive impairment. Neurobiol Aging. 2005;26(7b):165–71.
Koskinen M et al. Propofol anesthesia induces phase synchronization changes in EEG. Clin Neurophysiol. 2001;112(2):386–92.
Kreuz T et al. Measuring synchronization in coupled model systems: a comparison of different approaches. Physica D Nonlinear Phenomena. 2007;225(1):29–42.
Lachaux JP et al. Measuring phase synchrony in brain signals. Hum Brain Mapp. 1999;8(4):194–208.
Lachaux J-P et al. Studying single-trials of phase synchronous activity in the brain. Int J Bifurcation Chaos. 2000;10(10):2429–39.
Langen M et al. Changes in the developmental trajectories of striatum in autism. Biol Psychiatry. 2009;66(4):327–33.
Le Van Quyen M, Bragin A. Analysis of dynamic brain oscillations: methodological advances. Trends Neurosci. 2007;30(7):365–73.
Lee U et al. Propofol induction reduces the capacity for neural information integration: implications for the mechanism of consciousness and general anesthesia. Conscious Cogn. 2009a;18(1):56–64.
Lee U et al. The directionality and functional organization of frontoparietal connectivity during consciousness and anesthesia in humans. Conscious Cogn. 2009b;18(4):1069–78.
Lewis LD et al. Rapid fragmentation of neuronal networks at the onset of propofol-induced unconsciousness. Proc Natl Acad Sci. 2012;109(49):E3377–86.
Li X et al. Interaction dynamics of neuronal oscillations analysed using wavelet transforms. J Neurosci Methods. 2007a;160(1):178–85.
Li X et al. Interaction dynamics of neuronal oscillations analysed using wavelet transforms. J Neurosci Methods. 2007b;160(1):178–85.

Li X, Cui S, Voss LJ. Using permutation entropy to measure the electroencephalographic effects of sevoflurane. Anesthesiology. 2008a;109(3):448.
Li X et al. Analysis of depth of anesthesia with Hilbert-Huang spectral entropy. Clin Neurophysiol. 2008b;119(11):2465–75.
Li X, Cui S, Voss L. Using permutation entropy to measure the electroencephalographic effects of sevoflurane. Anesthesiology. 2008c;109(3):448.
Li D et al. Phase synchronization with harmonic wavelet transform with application to neuronal populations. Neurocomputing. 2011;74(17):3389–403.
Li D et al. Effects of volatile anesthetic agents on cerebral cortical synchronization in sheep. Anesthesiology. 2013;119(1):81–8.
Liang Z et al. Permutation auto-mutual information of electroencephalogram in anesthesia. J Neural Eng. 2013;10(2):026004.
Marwan N, Kurths J. Nonlinear analysis of bivariate data with cross recurrence plots. Phys Lett A. 2002;302(5):299–307.
Mehran A, Hojjat A, Amir A. Fuzzy synchronization likelihood-wavelet methodology for diagnosis of autism spectrum disorder. J Neurosci Methods. 2012;211(2):203–9.
Mirowski P et al. Classification of patterns of EEG synchronization for seizure prediction. Clin Neurophysiol. 2009;120(11):1927–40.
Mizuhara H, Yamaguchi Y. Human cortical circuits for central executive function emerge by theta phase synchronization. Neuroimage. 2007;36(1):232–44.
Mormann F et al. Mean phase coherence as a measure for phase synchronization and its application to the EEG of epilepsy patients. Physica D Nonlinear Phenomena. 2000;144(3):358–69.
Moroni F et al. Slow EEG rhythms and inter-hemispheric synchronization across sleep and wakefulness in the human hippocampus. Neuroimage. 2012;60(1):497–504.
Nallasamy N, Tsao DY. Functional connectivity in the brain: effects of anesthesia. Neuroscientist. 2011;17(1):94–106.
Nunez PL. Electric fields of the brain: the neurophysics of EEG. Oxford: Oxford University Press; 2006.
Olofsen E, Sleigh J, Dahan A. Permutation entropy of the electroencephalogram: a measure of anaesthetic drug effect. Br J Anaesth. 2008;101(6):810.
Palus M, Stefanovska A. Direction of coupling from phases of interacting oscillators: an information-theoretic approach. Phys Rev E Stat Nonlin Soft Matter Phys. 2003; 67(5 Pt 2):055201–055201.
Park H, Kim D-S. Evaluation of the dispersive phase and group velocities using harmonic wavelet transform. NDT E Int. 2001;34(7):457–67.
Pereda E, Quiroga RQ, Bhattacharya J. Nonlinear multivariate analysis of neurophysiological signals. Prog Neurobiol. 2005;77(1):1–37.
Quiroga RQ, Arnhold J, Grassberger P. Learning driver-response relationships from synchronization patterns. Phys Rev E. 2000;61(5):5142.
Quiroga RQ et al. Performance of different synchronization measures in real data: a case study on electroencephalographic signals. Phys Rev E. 2002;65(4):041903.
Roelfsema PR et al. Visuomotor integration is associated with zero time-lag synchronization among cortical areas. Nature. 1997;385(6612):157–61.
Rosenblum MG, Pikovsky AS, Kurths J. Phase synchronization of chaotic oscillators. Phys Rev Lett. 1996;76(11):1804.
Schiff SJ et al. Detecting dynamical interdependence and generalized synchrony through mutual prediction in a neural ensemble. Phys Rev E. 1996;54(6):6708.
Schlögl A. The electroencephalogram and the adaptive autoregressive model: theory and applications. Aachen: Shaker; 2000.
Schnitzler A, Gross J. Normal and pathological oscillatory communication in the brain. Nat Rev Neurosci. 2005;6(4):285–96.
Schrouff J et al. Brain functional integration decreases during propofol-induced loss of consciousness. Neuroimage. 2011;57(1):198–205.

Seo, S. A review and comparison of methods for detecting outliers in univariate data sets. University of Pittsburgh; 2006.
Shalbaf R et al. Frontal-temporal synchronization of EEG signals quantified by order patterns cross recurrence analysis during propofol anesthesia. IEEE Trans Neural Syst Rehabil Eng. 2015;23(3):468–74.
Silverman BW. Density estimation for statistics and data analysis, vol. 26. Boca Raton: CRC press; 1986.
Slooter AJ et al. Seizure detection in adult ICU patients based on changes in EEG synchronization likelihood. Neurocrit Care. 2006;5(3):186–92.
Stam CJ. Nonlinear dynamical analysis of EEG and MEG: review of an emerging field. Clin Neurophysiol. 2005;116(10):2266–301.
Stam CJ et al. Disturbed fluctuations of resting state EEG synchronization in Alzheimer's disease. Clin Neurophysiol Off J Int Fed Clin Neurophysiol. 2005;116(3):708–15.
Steriade M, McCormick DA, Sejnowski TJ. Thalamocortical oscillations in the sleeping and aroused brain. Science. 1993;262(5134):679–85.
Steuer R et al. The mutual information: detecting and evaluating dependencies between variables. Bioinformatics. 2002;18 Suppl 2:S231–40.
Tass P et al. Detection of n: m phase locking from noisy data: application to magnetoencephalography. Phys Rev Lett. 1998;81(15):3291–4.
Thatcher RW, North DM, Biver CJ. Development of cortical connections as measured by EEG coherence and phase delays. Hum Brain Mapp. 2008;29(12):1400–15.
Uhlhaas PJ, Singer W. Neural synchrony in brain disorders: relevance for cognitive dysfunctions and pathophysiology. Neuron. 2006;52(1):155–68.
Voss L, Sleigh J. Monitoring consciousness: the current status of EEG-based depth of anaesthesia monitors. Best Pract Res Clin Anaesthesiol. 2007;21(3):313–25.
Williams M, Sleigh J. Auditory recall and response to command during recovery from propofol anaesthesia. Anaesth Intensive Care. 1999;27(3):265.
Zbilut JP, Giuliani A, Webber CL. Detecting deterministic signals in exceptionally noisy environments using cross-recurrence quantification. Phys Lett A. 1998;246(1):122–8.
Zheng Y et al. Epileptic seizure prediction using phase synchronization based on bivariate empirical mode decomposition. Clin Neurophysiol. 2014;125(6):1104–11.
Zhou D, Thompson WK, Siegle G. MATLAB toolbox for functional connectivity. Neuroimage. 2009;47(4):1590–607.

Chapter 10
Estimating Coupling Direction Between Neuronal Populations

Gaoxiang Ouyang and Xiaoli Li

10.1 Introduction

Synchronization phenomena have been found in biological systems; examples include cardiorespiratory interaction (Rosenblum 2002) and neuronal oscillations (Rosenblum and Pikovsky 2001; Roelfsema et al. 1997). Synchronization analysis has been a focus of attention with respect to biological systems (Rosenblum and Pikovsky 2001). Synchronization between brain areas has been the subject of a number of studies in both the normal (Roelfsema et al. 1997; Rodriguez et al. 1999) and diseased brain (Uhlhass and Singer 2006). To further understand synchronization in the brain, we need to identify the coupling direction between neuronal signals recorded from different brain areas. In this chapter, we present a novel methodology based on permutation analysis and conditional mutual information for estimation of a directionality index between two neuronal populations (Li and Ouyang 2010).

G. Ouyang • X. Li (✉)
State Key Laboratory of Cognitive Neuroscience and Learning & IDG/McGovern Institute for Brain Research, Beijing Normal University, Beijing 100875, China

Center for Collaboration and Innovation in Brain and Learning Sciences, Beijing Normal University, Beijing 100875, China
e-mail: ouyang@bnu.edu.cn; xiaoli@bnu.edu.cn

X. Li (eds.), *Signal Processing in Neuroscience*, DOI 10.1007/978-981-10-1822-0_10

10.2 Coupling Direction

Generally, synchronization analysis contains the coupling strength and direction between neural series. Several methods have been proposed to estimate the coupling direction in bivariate neural series. First of all, a Granger causality-based method has been proposed to investigate the coupling directions of neuronal signals (Brovelli et al. 2004; Lungarella and Sporns 2006; Wang et al. 2008). The results have shown that the Granger causality-based method can be applied successfully to linear models, but it has been demonstrated that the change in cross-prediction error cannot be applied directly to indicate the coupling direction in nonlinear systems (Palus and Vejmelka 2007). Information theory-based methods also have been proposed to estimate the coupling direction between neural series; typical methods include transfer entropy (Schreiber 2000) and conditional mutual information (Palus et al. 2001; Vejmelka and Palus 2008). The advantages and disadvantages of the coupling direction based on information theory can be found in (Hlavackova-Schindler et al. 2007). The detection of relationships between the instantaneous phases of interacting oscillators also can be used to identify the coupling direction, including the evolution map approach (EMA) and the instantaneous period approach (IPA) (Rosenblum 2002; Rosenblum and Pikovsky 2001). Unfortunately, the EMA and IPA are sensitive to noise in the time series, so they are not very suitable for analyzing noisy and non-stationary EEG recordings. In order to detect the weak coupling direction of oscillators, state-space and phase-dynamics approaches have been proposed (Smirnov and Bezruchko 2003; Smirnov and Andrzejak 2005). The state-space approach requires optimal embedding parameters, and the phase-dynamics approach requires a strong oscillatory behavior, so the application of these two methods is also limited. Furthermore, these two approaches are sensitive to noise in the time series, like EPA and IPA.

Recently, order pattern analysis and conditional mutual information have been integrated to estimate the coupling direction between two time series in interacting oscillators and apply it to cardiorespiratory data (Bahraminasab et al. 2008). In this chapter, we apply this new method to estimate the coupling direction between neuronal populations based on the probability distribution of order patterns and conditional mutual information. The so-called permutation conditional mutual information (PCMI) is compared with the traditional conditional mutual information method. The performance of the PCMI method is assessed by utilizing a coupling neural mass model.

10.2.1 Mutual Information

Consider two neuronal populations $X = \{x_t\}$ and $Y = \{y_t\}$, which are recorded from two different brain areas, respectively. The probability distribution functions of neuronal populations are denoted as $p(x)$ and $p(y)$, and their joint probability

function is defined as $p(x,y)$. In the mutual information computation, the probability distribution functions can be estimated by a histogram method. A key parameter in this method is to determine the number of bins (denoted as NBin in the study), and then the entropy of X and Y are defined as

$$H(X) = -\sum_{x \in X} p(x) \log p(x) \tag{10.1}$$

and

$$H(Y) = -\sum_{y \in Y} p(y) \log p(y) \tag{10.2}$$

The joint entropy of $H(X,Y)$ is defined as

$$H(X, Y) = -\sum_{x \in X} \sum_{y \in Y} p(x, y) \log p(x, y) \tag{10.3}$$

The common information contained in X and Y can be estimated by the following mutual information (MI) calculation:

$$I(X; Y) = H(X) + H(Y) - H(X, Y) \tag{10.4}$$

MI is a measure derived from Shannon's information theory to estimate the information gained from observations of the effect of one random event on another (Hlavackova-Schindler et al. 2007). Intuitively, the mutual information $I(X;Y)$ measures the information about X that is shared by Y. The relation between MI and entropy is illustrated in Fig. 10.1. If X and Y are independent, then X contains no information about Y and vice versa, so their mutual information is zero. If X and Y are identical, then all information conveyed by X is shared with Y. Knowing X reveals nothing new about Y and vice versa; therefore, the mutual information is the same as the information conveyed by X (or Y) alone, namely, the entropy of X. For more details of MI, see (Hlavackova-Schindler et al. 2007).

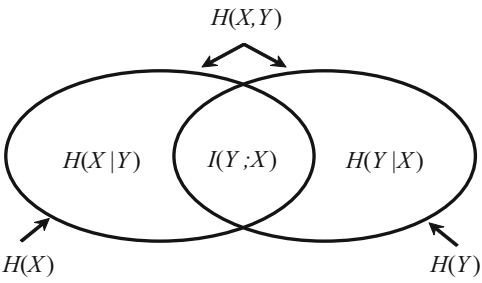

Fig. 10.1 Diagram indicating the mutual information common to variables X and Y. The mutual information $I(X;Y)$ is defined by the intersection of the two sets, whereas the joint entropy $H(X,Y)$ is defined by the union of the two sets

10.2.2 Conditional Mutual Information and Directionality

If the random variables X and Y are statistically independent, the joint entropy $H(X,Y)$ becomes $H(X,Y) = H(X) + H(Y)$. In general, the joint entropy may be expressed in terms of conditional entropy $H(X|Y)$ as follows:

$$H(X,Y) = H(X|Y) + H(Y) \tag{10.5}$$

The conditional entropy $H(X|Y)$ of X given Y is denoted as

$$H(X|Y) = -\sum_{x\in X}\sum_{y\in Y} p(x,y)\log p(x|y) \tag{10.6}$$

Then the conditional mutual information (CMI) between two series X and Y is defined as (Palus et al. 2001; Vejmelka and Palus 2008)

$$I^{\delta}{}_{X\to Y} = I(X;\Delta_{\delta}Y|Y) = H(X|Y) + H(\Delta_{\delta}Y|Y) - H(X,\Delta_{\delta}Y|Y) \tag{10.7}$$

and

$$I^{\delta}{}_{Y\to X} = I(Y;\Delta_{\delta}X|X) = H(Y|X) + H(\Delta_{\delta}X|X) - H(Y,\Delta_{\delta}X|X) \tag{10.8}$$

where $\Delta_{\delta}X$ is an observable process derived from the process X in its future δ steps, i.e., $\Delta_{\delta}X : x_{t+\delta} = x_t$. The information that is transferred from the process X (or Y) to the process Y (or X) at some later point in time can be defined as

$$I_{X\to Y} = \frac{1}{N}\sum_{\delta=1}^{N} I^{\delta}{}_{X\to Y} \tag{10.9}$$

and

$$I_{Y\to X} = \frac{1}{N}\sum_{\delta=1}^{N} I^{\delta}{}_{Y\to X} \tag{10.10}$$

Based on the conditional mutual information, the directionality index between X and Y can be defined by

$$D_{XY} = \left(\frac{I_{X\to Y} - I_{Y\to X}}{I_{X\to Y} + I_{Y\to X}}\right) \tag{10.11}$$

The value of D_{XY} ranges from 1 to 1. $D_{XY} > 0$, meaning that the process X drives Y; $D_{XY} < 0$ means that the process Y drives X, and $D_{XY} = 0$ means that the interactions

between X and Y are symmetrical. In the method described above, two parameters must be determined, i.e., the number of bins (NBin) and the future step δ.

10.2.3 Permutation Conditional Mutual Information

The EEG is a continuously variable signal, the amplitude and frequency of which change over time. Actually, the signals are composed of ascending and descending patterns. The statistical analysis of these two simple patterns may help us to indicate the change in a dynamical system. To obtain more information from a dynamical signal, we may set up more complicated patterns (see Fig. 10.2b, Π_1–Π_6). In this study, these different patterns are referred to as the order pattern. The EEG signals consist of a sequence of order patterns. Based on the probability distribution of these order patterns, a new complexity measure called permutation entropy is proposed (Bandt and Pompe 2002) and has been successfully used to analyze neural signals (Li et al. 2008, 2014).

The algorithm for the calculation of the probability distribution of order patterns is very simple. Figure 10.2a shows the original series (upper) and the discrete points (bottom) for the short interval, marked by a black bar. For example, the first three points belong to the Π_2 pattern. The main procedure of the algorithm is as follows:

1. Given a sequence of order patterns [order: $m = 3$, so $3! = 6$ different patterns; see Fig. 10.2b].
2. An epoch of the neural signal is extracted, and the number of different patterns in the signal is estimated [see Fig. 10.2a].
3. The probability of occurrence of each pattern in the signal is calculated [see Fig. 10.2c]. Let $f(\pi_i), i \in (1 : m!)$ denote the frequency of the order pattern in the time series; its relative frequency is defined as

$$p(\pi) = f(\pi) / (L - (m-1)\tau) \tag{10.12}$$

where L is the length of the time series. In the following section, $p(\pi)$ is simplified as $p(x)$ for the x signal.

If we analyze two signals [one is shown in Fig. 10.2a; another signal is not plotted here], the joint probability of the occurrence of each order pattern in the signals, $p(x, y)$, can be calculated as shown in Fig. 10.2d.

Once we obtain the probability distribution functions of two series X and Y, new conditional mutual information is obtained through the replacement of the probability distribution functions (Bahraminasab et al. 2008), called permutation conditional mutual information (PCMI). It is noted that the probability distribution function in PCMI is based on the order pattern of signals, but in CMI, it is based on the amplitude of signals. The advantages of the PCMI will be discussed in the following sections through comparison with the CMI method.

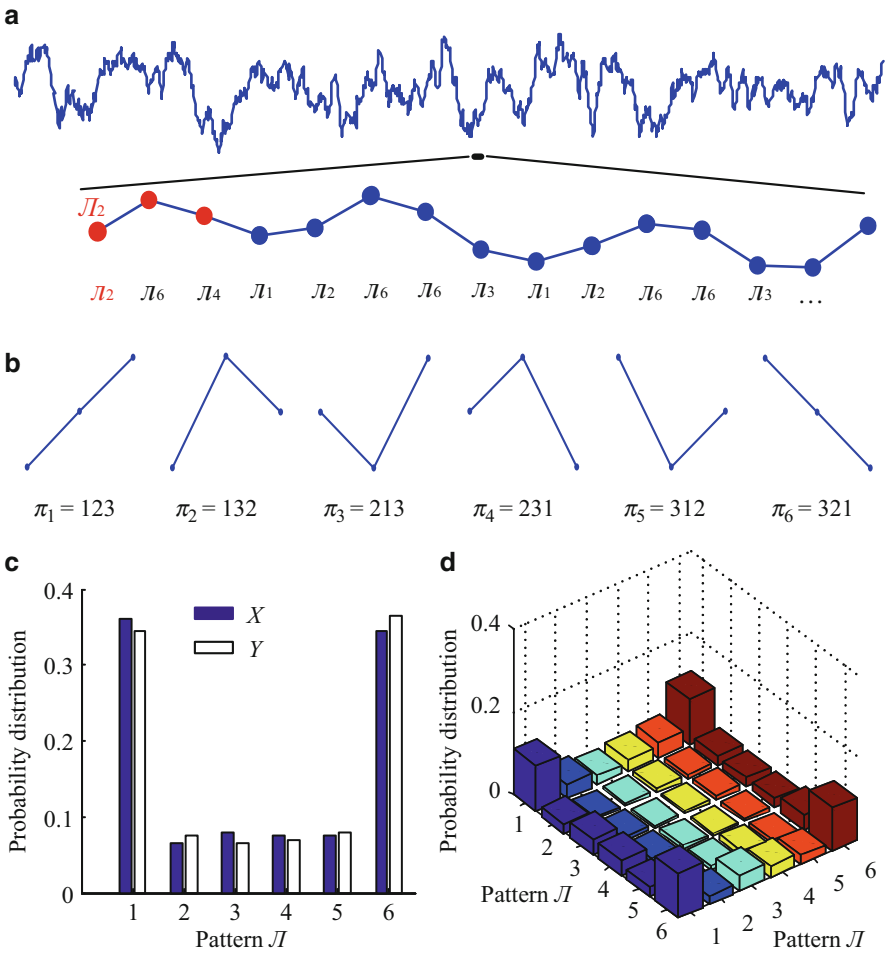

Fig. 10.2 The probability distribution of order patterns in simulated EEG. (**a**) A segment of simulated EEG (*upper*) and some order patterns (order = 3 and delay = 1) (*bottom*). (**b**) All order patterns of the order of 3 (3!). (**c**) The probability distribution of order patterns of EEG *X* and *Y*. (**d**) The cross-probability distribution of order patterns for EEG *X* and *Y*

10.3 Simulation Analysis and Results

10.3.1 Coupled Neural Mass Model

The neural mass model is based on physiologically relevant parameters (Wendling et al. 2000). The advantage of this model is that it can be used to validate the performance of the signal processing through comparison with the model parameters; in

contrast, the signal processing method validated by the neural mass model can give a direct physiological interpretation of real data from animals or human beings.

In this study, a neural mass model (Wendling et al. 2000; Jansen and Rit 1995; Lopes da Silva et al. 1974) is applied to generate two coupling or non-coupling populations in order to test the performance of the proposed method. The following set of seven differential equations governing the model ($n = 1,2$) is below (Wendling et al. 2000):

$$\begin{cases} \dot{y}_0^n(t) = \dot{y}_3^n(t), \\ \dot{y}_3^n(t) = AaS\left(y_1^n(t) - y_2^n(t)\right) - 2a\dot{y}_3^n(t) - a^2 y_0^n(t), \\ \dot{y}_1^n(t) = \dot{y}_4^n(t), \\ \dot{y}_4^n(t) = Aa\left\{p(t) + C_2 S\left[C_1 y_0^n(t)\right] + \sum_{i=1,N} K^i y_6^i(t)\right\} - 2a\dot{y}_4^n(t) - a^2 y_1^n(t), \\ \dot{y}_2^n(t) = \dot{y}_5^n(t), \\ \dot{y}_5^n(t) = Bb\left\{C_4 S\left[C_3 y_0^n(t)\right]\right\} - 2b\dot{y}_5^n(t) - b^2 y_2^n(t). \\ \dot{y}_6^n(t) = \dot{y}_7^n(t), \\ \dot{y}_7^n(t) = Aa_d S\left(y_1^n(t) - y_2^n(t)\right) - 2a_d\dot{y}_7^n(t) - a_d^2 y_6^n(t). \end{cases} \tag{10.13}$$

All values for the parameters of the model are set based on a physiological basis, as listed in Table 10.1, the details of which can be found in (Wendling et al. 2000; Jansen and Rit 1995). In the model, intrapopulation behavior is influenced primarily by the excitatory neuron parameter, A, and the inhibitory neuron parameter, B. The parameters A and B modulate the balance of excitation and inhibition ($h_e(t) = u(t)Aate^{-at}$ and $h_i(t) = u(t)Bbte^{-bt}$). By altering the excitatory and inhibitory

Table 10.1 Physiological interpretation and standard values of model parameters (adapted from (Wendling et al. 2000; Jansen and Rit 1995))

Parameter	Interpretation	Standard value
A	Average excitatory synaptic gain	3.25 mV
B	Average slow inhibitory synaptic gain	22 mV
a	Dendritic average time constant in the feedback excitatory loop	$a = 100\ \mathrm{s}^{-1}$
b	Dendritic average time constant in the slow feedback inhibitory loop	$b = 50\ \mathrm{s}^{-1}$
Cl, C2	Average number of synaptic contacts in the excitatory feedback loop	$C1 = C$, $C2 = 0.8\ C$ (with $C = 135$)
C3, C4	Average number of synaptic contacts in the slow feedback inhibitory loop	$C3 = C4 = 0.25\ C$
a_d	Average time delay on efferent connection from a population	$a_d = 33\ \mathrm{s}^{-1}$
K^{ij}	Connectivity constant associated with the connection between two populations i to j	No standard value

parameters, the model can produce signals that strongly resemble intracranial EEG recordings (Wendling et al. 2000). Another important parameter is the connective strength, K; this parameter manages the degree and coupling direction between neuronal populations. In this study, two coupled neuronal populations are generated to test its directionality index by altering the above three parameters, in particular the connective strength, K.

In the model described above, the extrinsic input $p(t)$ represents Gaussian white noise with an assigned mean value and variance [mean(p) =90, STD(p) = 30] that describes the overall density of action potentials coming from other regions. For each simulation described below, the differential equa tions are solved numerically using a fourth-fifth order Runge-Kutta algorithm (Matlab code: ode45.m). Initial conditions are set to zero in all simulations, and an integration step size of 5 ms (sampling frequency: 200 Hz) is used. The first 1000 points of the simulated signals are discarded in order to avoid transient behavior.

10.3.2 Directionality Index with Different Coupling Strength

Given $A_1 = A_2 = 3.25$ and $B_1 = B_2 = 22$ for two unidirectional coupling populations, and the coupling parameter $K^{21} = 0$, K^{12} changes from 0 to 20 with a step of 2. Two neuronal populations of 10 s are generated. In this case, population 1 drives population 2 with the different coupling coefficients. Figure 10.3a plots the directionality index estimated by PCMI and CMI; the directionality index increases with the increase in the coupling coefficients. With the connective strengths $K^{12} = 0$ and $K^{21} = 0$, the directionality index of PCMI and CMI is close to 0, indicating that

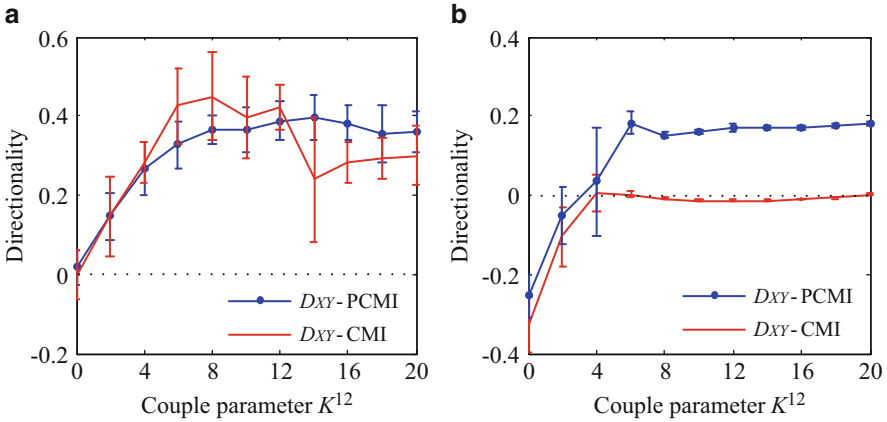

Fig. 10.3 Influence of coupling coefficients on the directionality index for unidirectional coupled neuronal populations (**a**) and bidirectional coupled neuronal populations (**b**). Symbols represent the mean values of entropy for each group, and bars represent the standard deviation

there are no coupling relations between populations 1 and 2. However, the variation of the CMI directionality index is more intense. As the connective strength K^{12} increases from 0 to 20, the directionality index of both PCMI and CMI increases with the increase of the connective strength K^{12}. Both PCMI and CMI can indicate correctly the coupling direction between two populations, namely, that population 1 drives population 2.

Then, we investigate the performance of PCMI and CMI for bidirectional neural mass populations. Given $A_1 = A_2 = 3.25$ and $B_1 = B_2 = 22$ for two unidirectional coupling populations and the coupling parameter $K^{21} = 4$, K^{12} changes from 0 to 20 with a step of 2. When K^{12} is less than K^{21}, population 2 drives population 1, and vice versa. Two neuronal populations of 10 s are generated. Figure 10.3b plots the directionality index estimated by PCMI and CMI with respect to the coupling strength; the directionality index increases with the increase of the coupling strength of K^{12}. When $K^{12} = K^{21} = 4$, the directionality index is around zero; when $K^{12} < K^{21}$, the directionality index is less than 0, and when $K^{12} > K^{21}$, the directionality index is greater than 0. In the comparison between PCMI and CMI, PCMI is superior to CMI in identifying the directionality index.

10.3.3 Robustness of Directionality Index Against Noise

The robustness of the directionality index is evaluated further by adding noise into the neuronal populations. Only the measurement noise is considered here, which does not perturb the inherent dynamics of systems. Independent sources of white noise are added to the neuronal populations generated by neural mass model. Given $A_1 = A_2 = 3.25$ and $B_1 = B_2 = 22$ for two unidirectional coupling populations and the coupling parameters $K^{12} = 10$ and $K^{21} = 0$, two neuronal populations of 10 s are generated. Population 1 drives population 2. The signal-to-noise ratio (SNR) ranges from -10 dB to 20 dB with a step of 2 dB. The directionality index at the different noise intensities is tested. As seen in Fig. 10.4a, the directionality index estimated by PCMI and CMI decreases with the amplitude of added white noise. It is obvious that the PCMI method can identify the directionality index when the SNR > 6. With further increases in SNR, PCMI is superior to CMI in identifying the coupling direction between the two neuronal populations.

Then, we investigate the performance of PCMI and CMI for bidirectional neural mass populations. Given $A_1 = A_2 = 3.25$ and $B_1 = B_2 = 22$ for two oscillators and the coupling parameters $K^{12} = 2$ and $K^{21} = 10$, population 1 drives population 2. Two neuronal populations of 10 s are generated. The signal-to-noise (SNR) ratio ranges from -10 dB to 20 dB with a step of 2 dB. The directionality index at the different noise intensities is tested. Figure 10.4b plots the directionality index estimated by PCMI and CMI with respect to the levels of white noise. It can be seen that the directionality index of PCMI increases with the increase of SNR. When SNR is greater than 2, the PCMI method can identify the directionality index. However, the CMI method cannot indicate the coupling direction between

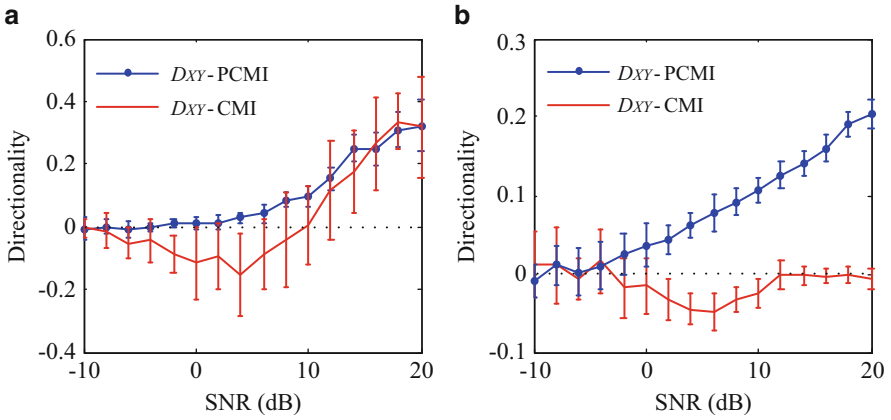

Fig. 10.4 Influence of noise level on the directionality index for unidirectional coupled neuronal populations (**a**) and bidirectional coupled neuronal populations (**b**). Symbols represent the mean values of entropy for each group, and bars represent the standard deviation

populations 1 and 2. PCMI is superior to CMI in identifying the coupling direction between the two neuronal populations.

10.3.4 Application to Epileptic Seizures

Figure 10.5a shows 60 s pre-ictal to ictal segments of neuronal population activity from the CA1 and CA3 of rat hippocampus. The seizure starts at approximately 6.5 s in the recording. The seizure activity recorded from the RCA1 (right CA1) begins suddenly, while that recorded from RCA3 (right CA3) develops more gradually. First, we investigate the coupling direction of CA1 and CA3 in the right hippocampus. The filtered directionality index between the RCA1 and RCA3 over time is plotted in Fig. 10.5b. It is obvious that most of the coupling direction between RCA1 and RCA3 is significant and the RCA3 drives RCA1 for the whole duration of the seizure.

10.4 Conclusions

In this chapter, a novel method is proposed to analyze the coupling direction of bivariate neuronal populations. A simulation study on the efficacy of the new method as a tool to identify causal connectivity between neuronal populations has been presented. Simulations suggest that the PCMI method is adequate to estimate the coupling direction under a large range of SNRs and coupling efficiency and

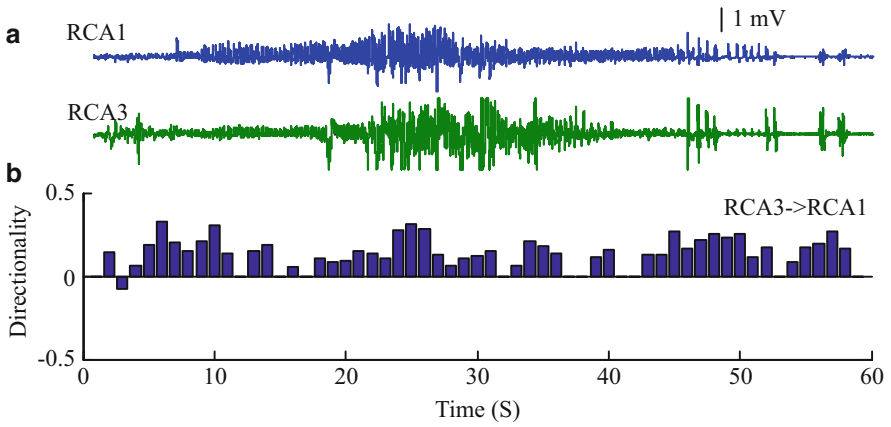

Fig. 10.5 The coupling dynamics between the right CA1-CA3 in the hippocampus from the pre-ictal to ictal states. (**a**) The recordings at the CA1 and CA3 in the hippocampus (*right*: R). (**b**) The filtered directionality index between the right CA1 and CA3

that it is better than the traditional CMI method. The PCMI was applied to analyze the coupling dynamics in the hippocampus (CA1 and CA3) during pre-ictal to ictal states. The relationship between the information flow and the propagation of seizure in the CA1 and CA3 can be described by the PCMI method. A further interesting question is whether the method proposed herein is suited to analyze the interaction in real EEG recordings. This issue needs to be investigated in future studies.

References

Bahraminasab A, Ghasemi F, Stefanovska A, McClintock P, Kantz H. Direction of coupling from phases of interacting oscillators: a permutation information approach. Phys Rev Lett. 2008;100:084101.

Bandt C, Pompe B. Permutation entropy: a natural complexity measure for time series. Phys Rev Lett. 2002;88:174102.

Brovelli A, Ding MZ, Ledberg A, Chen YH, Nakamura R, Bressler SL. Beta oscillations in a large-scale sensorimotor cortical network: directional influences revealed by granger causality. Proc Natl Acad Sci U S A. 2004;101:9849–54.

Hlavackova-Schindler K, Palus M, Vejmelka M, Bhattacharya J. Causality detection based on information-theoretic approaches in time series analysis. Phys Rep. 2007;441:1–46.

Jansen B, Rit V. Electroencephalogram and visual evoked potential generation in mathematical model of coupled cortical columns. Biol Cybern. 1995;73:357–66.

Li X, Ouyang G. Estimating coupling direction between neuronal populations with permutation conditional mutual information. Neuroimage. 2010;52:497–507.

Li X, Cui S, Voss LJ. Using permutation entropy to measure the electroencephalographic effects of sevoflurane. Anesthesiology. 2008;109(3):448–56.

Li J, Yan J, Liu X, Ouyang G. Using permutation entropy to measure the changes in EEG signals during absence seizures. Entropy. 2014;16:3049–61.

Lopes da Silva FH, Hoek A, Smith H, Zetterberg LH. Model of brain rythmic activity. Kybernetic. 1974;15:27–37.
Lungarella M, Sporns O. Mapping information flow in sensorimotor networks. PLoS Comput Biol. 2006;2:1301–12.
Palus M, Vejmelka M. Directionality of coupling from bivariate time series: how to avoid false causalities and missed connections. Phys Rev E. 2007;75:056211.
Palus M, Komarek V, Hrncir Z, Sterbova K. Synchronization as adjustment of information rates: detection from bivariate time series. Phys Rev E. 2001;63:046211.
Rodriguez E, George N, Lachaux J, Martinerie J, Renault B, Varela F. Perception's shadow: long-distance synchronization of human brain activity. Nature. 1999;397:430–3.
Roelfsema P, Engel A, Konig P, Singer W. Visuomotor integration is associated with zero time-lag synchronization among cortical areas. Nature. 1997;385:157–61.
Rosenblum G. Identification of coupling direction: application to cardio respiratory interaction. Phys Rev E. 2002;65:041909.
Rosenblum G, Pikovsky A. Detecting direction of coupling in interacting oscillators. Phys Rev E. 2001;64:045202.
Schreiber T. Measuring information transfer. Phys Rev Lett. 2000;85:461–4.
Smirnov D, Andrzejak R. Detection of weak directional coupling: phase-dynamics approach versus state-space approach. Phys Rev E. 2005;71:036207.
Smirnov D, Bezruchko B. Estimation of interaction strength and direction from short and noisy time series. Phys Rev E. 2003;68:046209.
Uhlhass P, Singer W. Neural synchrony in brain disorders: relevance for cognitive dysfunctions and pathophysiology. Neuron. 2006;52:155–68.
Vejmelka M, Palus M. Inferring the directionality of coupling with conditional mutual information. Phys Rev E. 2008;77:026214.
Wang X, Chen Y, Ding MZ. Estimating granger causality after stimulus onset: a cautionary note. Neuroimage. 2008;41:767–76.
Wendling F, Bellanger JJ, Bartolomei F, Chauvel P. Relevance of nonlinear lumped-parameter models in the analysis of depth-EEG epileptic signals. Biol Cybern. 2000;83:367–78.

Chapter 11
The Comodulation Measure of Neuronal Oscillations

Duan Li and Xiaoli Li

11.1 Introduction

Recent observations suggest that these neuronal oscillations at different frequency bands interact (e.g. Steriade 2001; Jensen and Colgin 2007; Isler et al. 2008). These comodulations are believed to be associated with 'self-organising' and 'emergent properties' of neural networks; thus the measurement of the comodulation relationship is a requirement for the exploration and validation of the functional roles of neuronal populations. The traditional method is the bispectral (bicoherence) analysis (Nikias and Raghuveer 1987), which has been developed to inspect the comodulation within the output from neural populations (Schanze and Eckhorn 1997; Schack et al. 2002). The bispectral analysis includes amplitude and phase information and is a very good tool to quantify quadratic phase coupling (QPC) amongst the components of a signal, so it can be used to characterise the nonlinearity of the dynamical system (Koronovskii and Hramov 2002). In this chapter, we concentrate on the bicoherence method, which is derived from the bispectral analysis but with the amplitude normalised to one; in this way, the bicoherence can be used to isolate phase relationship between oscillations with different frequency bands.

D. Li
School of Information Science and Engineering, Yanshan University, Qinhuangdao, China
e-mail: liduan@ysu.edu.cn

X. Li (✉)
State Key Laboratory of Cognitive Neuroscience and Learning,
Beijing Normal University, Beijing 100875, China
e-mail: xiaoli@bnu.edu.cn

X. Li (eds.), *Signal Processing in Neuroscience*, DOI 10.1007/978-981-10-1822-0_11

Bicoherence analysis has been applied successfully to evaluate QPC types of non-linear effects in neural series (e.g. Shils et al. 1996; Schanze and Eckhorn 1997; Schack et al. 2002; von Stein et al. 2000), in particular, to investigate the effect of anaesthetic drugs on the electroencephalogram (EEG) (Johansen and Sebel 2000; Hagihira et al. 2002, 2004; Hayashi et al. 2007, 2008; Morimoto et al. 2006). This method has become a core technology of the Bispectral Index System (BIS) monitor (Aspect Medical System, Natick, MA). In order to successfully apply Fourier bicoherence to practical EEG signals, at least 3 min of data (at sampling rate 128 Hz, epoch length 2 s and 75 % overlap) are required to calculate reliable bicoherence values (Hagihira et al. 2002). However neuronal interactions change quickly, so we are forced to analyse the phase coupling of neuronal oscillations over relatively short periods of time. For this reason, Fourier analysis is not well suited for the comodulation measure of neuronal oscillations.

Recently, wavelet bicoherence was proposed to detect the phase coupling with reasonable temporal resolution (van Milligen et al. 1995; Chung and Powers 1998; Larsen et al. 2001). In computing wavelet bicoherence, a Morlet function is often applied. The estimation of Morlet wavelet-based bicoherence needs a relatively complex algorithm and some parameter choices. To overcome the drawback of the traditional continuous wavelet transform (CWT), a general harmonic wavelet transform (GHWT) was introduced (Newland 1993, 1994a, b), which is similar to the ordinary discrete wavelet transform for multiresolution analyses using the fast Fourier transform algorithm. GHWT can provide a great deal of freedom for signal representation with a higher computational efficiency. A distinct advantage of the GHWT is that it combines advantages of the short-time Fourier transform and the CWT. The comparison between the GHWT and Morlet wavelet transform can be found in (Simonovski and Boltezar 2003).

In this chapter, we utilised GHWT to design a wavelet-based bicoherence statistic which uses a phase randomisation method to estimate the cross-frequency interactions of neuronal population, the performance of which was evaluated using a simple simulation study. In the following, this improved wavelet bicoherence was applied to measure the phase coupling mechanism in neuronal oscillations during waking and sleep states of rats and in scalp EEG signals recorded from human during general anaesthesia.

11.2 Bicoherence Measures

11.2.1 Fourier Bicoherence

The bicoherence, as the normalised form of bispectrum, is a measure of the amount of QPC that occurs in a signal. If a signal contains three components with frequencies of f_p, f_q and $f_p + f_q$, and the corresponding phases satisfy the relationship $\varphi(f_p) + \varphi(f_q) = \varphi(f_p + f_q) + const$, the three waves are quadratic phase coupled, and

the bicoherence value should be equal to 1, which will produce a peak in the bicoherence matrix at the intersection between f_p and f_q; if no such relation is satisfied, the bicoherence value is 0.

To estimate the bicoherence based on the Fourier transform, the data $x(t)$ are segmented into overlapping epochs. For the kth epoch $x_k(t)$, the mean is removed, a Blackman window is applied, the Fourier transform is computed, and its bispectrum is estimated as

$$B_k^F\left(f_p,f_q\right) = X_k\left(f_p\right) X_k\left(f_q\right) X_k^*\left(f_p+f_q\right) \tag{11.1}$$

where $X_k(\cdot)$ is the Fourier transform of $x_k(t)$ and * denotes the conjugate operation. The spectrum is computed as $P_k(\cdot) = |X_k(\cdot)|^2$. The bispectral and spectral estimates are smoothed across multiple epochs, and the bicoherence is then estimated as

$$b^F\left(f_p,f_q\right) = \frac{\left|B^F\left(f_p,f_q\right)\right|^2}{P\left(f_p\right) P\left(f_q\right) P\left(f_p+f_q\right)} \tag{11.2}$$

where $B^F(f_p,f_q)$ is the average estimate of the bispectrum over multiple epochs and $P(\cdot)$ is the average estimate of the power spectrum.

11.2.2 Wavelet Bicoherence

The wavelet bicoherence can be seen as a generalisation of the Fourier bicoherence. It can detect a temporally intermittent correlation due to its improved time resolution (van Milligen et al. 1995).

The CWT provides a method for the time-scale analysis of a nonstationary signal. By adjusting a wavelet function $\psi(t)$, we generate a set of wavelets with different time-scale properties. The wavelet coefficients describe the similarities between the signal and the wavelet at different scales and time translations (Mallat 1999). In CWT, several wavelet functions, such as Gabor, Morlet (Torrence and Compo 1998) and general harmonic wavelet functions (Newland 1994a), may be selected. In this chapter, the general harmonic wavelet function was adopted, which is defined as

$$\psi\left(t,\eta,A,B\right) = w_H\left(t,A,B\right) e^{i\eta t} \tag{11.3}$$

and

$$w_H\left(t,A,B\right) = \begin{cases} A + B\cos\left(\pi t\right), & |t| < 1 \\ 0, & \text{otherwise} \end{cases} \tag{11.4}$$

In this study, the $w_H(t,A,B)$ is a Hanning window function and $A = B = 1/\sqrt{3}$ (Simonovski and Boltezar 2003). Given a series of centre frequencies

f_p ($p = 1,2,\ldots,L$) and its frequency bandwidth f_b, the GHWT of a signal $x(\tau)$ is denoted as $a_x(f_p, \tau)$. The wavelet power spectrum in the frequency domain is defined by

$$P_{xx}\left(f_p\right) = \int_T a_x\left(f_p, \tau\right) a_x^*\left(f_p, \tau\right) d\tau \tag{11.5}$$

where $a_x(f_p, \tau)$ is the GHWT of the signal and T is the finite time interval of the signal.

In an analogous fashion to the Fourier bispectrum, a wavelet bispectrum (van Milligen et al. 1995) is defined by

$$B_{xxx}\left(f_p, f_q\right) = \int_T a_x\left(f_p, \tau\right) a_x\left(f_q, \tau\right) a_x^*\left(f_p + f_q, \tau\right) d\tau \tag{11.6}$$

The peaks in the wavelet bispectrum indicate phase and/or frequency interaction at bifrequency (f_p, f_q) in the time interval T. The wavelet bispectrum, which is a complex value, may be expressed by its magnitude A and biphase φ_d:

$$B_{xxx}\left(f_p, f_q\right) = A\left(f_p, f_q\right) e^{j\varphi_d\left(f_p, f_q\right)} \tag{11.7}$$

where the biphase φ_d can be calculated by

$$\varphi_d\left(f_p, f_q\right) = \varphi\left(f_p\right) + \varphi\left(f_q\right) - \varphi\left(f_p + f_q\right) \tag{11.8}$$

The normalised squared wavelet bicoherence (termed as WBIC) is defined by (van Milligen et al. 1995)

$$\left(b_{xxx}\left(f_p, f_q\right)\right)^2 = \frac{\left|B_{xxx}\left(f_p, f_q\right)\right|^2}{\int_T \left|a_x\left(f_p, \tau\right) a_x\left(f_q, \tau\right)\right|^2 d\tau \int_T \left|a_x\left(f_p + f_q, \tau\right)\right|^2 d\tau} \tag{11.9}$$

which characterises the QPC between different frequency components of the signal, ranging from 0 to 1. If the signal to be analysed contains three components (whose frequencies f_p and f_q and $f_p + f_q$) and the corresponding phases satisfy the relationship $\varphi\left(f_p\right) + \varphi\left(f_q\right) = \varphi\left(f_p + f_q\right)$, or the biphase = 0, the wavelet bicoherence should be close to unity, and the three waves of the different frequencies are quadratic phase coupled; in contrast, if the relationship fails to hold, the wavelet bicoherence is equal to zero, and the three waves are not quadratic phase coupled.

11.2.3 Improved Wavelet Bicoherence

11.2.3.1 Phase Randomised Wavelet Bicoherence Method

The bicoherence-based QPC detector should meet the following requirements (Kim et al. 2007): (I) If a complete QPC exists in the signal $x(t)$ at bifrequency (f_p, f_q), then the normalised squared bicoherence is equal to 1, i.e. $(b_{xxx}(f_p,f_q))^2 = 1$, and the biphase is equal to zero, i.e. $\varphi_d\left(f_p,f_q\right) = 0$; (II) If no QPC in $x(t)$, then $(b_{xxx}(f_p,f_q))^2 = 0$ and $\varphi_d\left(f_p,f_q\right) \in (-\pi,\pi]$. Generally, the traditional bicoherence method does not meet the requirement II. In (Kim et al. 2007), a phase randomisation method was proposed to improve the detection of bicoherence. The phase randomisation for the bispectrum of each segment of a signal is defined as

$$\tilde{B}\left(f_p,f_q\right) = E\left[\left|X\left(f_p\right)X\left(f_q\right)X*\left(f_p+f_q\right)\right| e^{jR\varphi_d\left(f_p,f_q\right)}\right] \tag{11.10}$$

where $E[]$ denotes an expectation operator, $X(\cdot)$ is the discrete Fourier transform of the realisation of $x(t)$, $e^{jR\varphi_d\left(f_p,f_q\right)}$ is termed as the phase randomisation, and R is a random variable. If the QPC is present in the signal, namely, $\varphi_d\left(f_p,f_q\right) = 0$, then $e^{jR\varphi_d\left(f_p,f_q\right)} = 1$ regardless of the value of R; if the QPC is not present in the signal, $\varphi_d\left(f_p,f_q\right) \in [-\pi,\pi]$, then the $E\left[e^{jR\varphi_d\left(f_p,f_q\right)}\right]$ becomes close to zero, so the bispectrum to zero.

In the study, we tried to move this idea to wavelet bicoherence. A new term $e^{jR\varphi_d\left(f_p,f_q,\tau\right)}$ is added to wavelet bispectrum for each time point τ, so Eq. (11.6) can be written as

$$\widehat{B}_{xxx}\left(f_p,f_q\right) = \int_T a_x\left(f_p,\tau\right)a_x\left(f_q,\tau\right)a_x^*\left(f_p+f_q,\tau\right)e^{jR\varphi_d\left(f_p,f_q,\tau\right)}d\tau \tag{11.11}$$

where $R \in (-\pi,\pi]$ is a random variable. If the QPC occurs at the time τ, the biphase $\varphi_d\left(f_p,f_q,\tau\right) = 0$, and the random variable R has no effect on the bispectrum because of the term $e^{jR\varphi_d\left(f_p,f_q,\tau\right)} = 1$; in contrast, if the QPC does not occur at the time τ, i.e. the biphase $\varphi_d\left(f_p,f_q,\tau\right) \neq 0$, R considerably reduces the bispectrum because of $e^{jR\varphi\tau\left(f_p,f_q,\tau\right)} < 1$. Replacing the B_{xxx} in Eq. (11.9) by $\widehat{B}_{xxx}$, a new bicoherence can be obtained and denoted as $\left(\widehat{b}_{xxx}\left(f_p,f_q\right)\right)^2$ (termed as IWBIC). The estimated bicoherence is indeed close to the 'true' QPC value as the addition of the term $e^{jR\varphi_d\left(f_p,f_q,\tau\right)}$ can effectively keep the QPC information and reduce the spurious QPC information at the time τ.

11.2.3.2 Significance Test

To obtain a reliable measure of statistical significance for GHWT bicoherence, a surrogate method is employed. The computational steps are as follows. First, the biphase $\phi_d(f_p,f_q)$ is calculated based on the wavelet bispectrum, and the summation of both is used to generate a new biphase $\phi'_d\left(f_p,f_q\right) = \phi_d\left(f_p,f_q\right) + \theta$, where random variable $\theta \in (-\pi,\pi]$; this step damages the condition of biphase $\phi_d\left(f_p,f_q\right) = 0$. Replacing $\phi_d(f_p,f_q)$ in Eq. (11.11) with $\phi'_d(f_p,f_q)$, a surrogated bicoherence can be obtained, which only contains non-QPC due to the aggregation of random variables. The above procedure is run 100 times, and the bicoherence values of each of the 100 samples are calculated at bifrequency (f_p, f_q). The 95 % statistical threshold may be defined as the mean plus two standard deviations of all bicoherence values at bifrequency (f_p, f_q). Note that the statistical threshold is based on the normality assumption which may be verified using the Kolmogorov–Smirnov goodness-of-fit test (Zar 1999). When the bicoherence estimated from the original data is greater than the threshold, it means the QPC at bifrequency (f_p, f_q) is present and the value will be preserved, otherwise the value is set to zero. After this thresholding, a filtered bicoherence, $\tilde{b}_{xxx}\left(f_p,f_q\right)$ (termed as FIWBIC), can be obtained.

During the computation of the bicoherence, it is very hard to determine from one epoch whether a phase coupling is present in the signal. A segment-averaging approach (Hagihira et al. 2001) can still be used for GHWT bicoherence. It was reported that the BIS could be considered as a marker of depth of sleep (Sleigh et al. 1999), like the depth estimation of general anaesthesia. The commercial BIS monitor calculates the bispectral value from 120 epochs (61.5 s) and overlap of 75 %, at a sampling rate of 128 Hz and epoch length of 2 s (Rampil 1998). In the study, we utilised similar parameter values for GHWT bicoherence, with the length and overlapping of epochs 2 s and 75 %, respectively.

11.2.3.3 Simulation Analysis

To demonstrate the performance of this method, a simulation study is presented to show whether or not this method can effectively detect the QPC of a short-duration time series. The model employed (Kim and Powers 1979) is

$$\begin{aligned} y(t) = {} & \sin\left(2\pi f_1 t + \phi_1\right) + \sin\left(2\pi f_2 t + \phi_2\right) + \mathrm{w}\Big(\sin\left(2\pi\left(f_1 + f_2\right)t + \left(\phi_1 + \phi_2\right)\right) \\ & + (1-\mathrm{w})\sin\left(2\pi\left(f_1 + f_2\right)t + \phi_3\right)\Big) + \varepsilon(t) \end{aligned} \tag{11.12}$$

where $\phi_j \in U(-\pi,\pi]$ $(j = 1,2,3)$ is a uniformly distributed random phase, $\mathrm{w} \in [0,1]$ is the coupling coefficient, and $\varepsilon(t)$ is uncorrelated white noises with zero mean and unit variance. The proportion of coupled energy at the sum frequency $(f_1 + f_2)$ is called the true squared bicoherence $b^2_{\text{true}}(f_1,f_2)$, with $b^2_{\text{true}}(f_1,f_2) = \mathrm{w}^2/\left(\mathrm{w}^2 + (1-\mathrm{w})^2\right)$, which is a function of the w parameter. We conducted

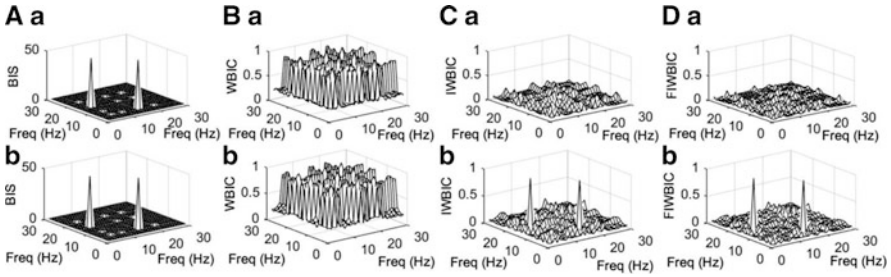

Fig. 11.1 Analysis of non-quadratic phase-coupled (*top panel*) and quadratic phase-coupled (*bottom panel*) signals in the presence of additive Gaussian noise (SNR = 5 dB). (Aa and b) The wavelet bispectrum, the peaks are at bifrequencies (6, 16 Hz) and (16, 6 Hz). The mixture of frequency and/or phase interaction is indistinguishable. (Ba and b) The WBIC, many spurious peaks appear in the quadratic phase-coupled signals and in the non-quadratic phase-coupled signals. (Ca and b) The IWBIC, nondistinct peak in the non-quadratic phase-coupled signals, and two significant peaks appear in the quadratic phase-coupled signals. (Da and b) The FIWBIC, two isolated distinct peaks are in the quadratic phase-coupled signals (Db)

simulation experiments with the following configuration: $f_1 = 6$ Hz, $f_2 = 16$ Hz, with the sampling rate of 256 Hz. The simulated signal has white noise added, denoted by signal to noise ratio (SNR).

Figure 11.1 shows the wavelet bispectrum and wavelet bicoherence for the non-phase-coupled (w = 0, SNR = 5) and phase-coupled signals (w = 1, SNR = 5). The wavelet bispectra for non-phase coupling and phase coupling signals of 20 epochs are shown in (A). Two peaks at bifrequency (6,16Hz) and (16,6Hz) can be found for both signals; the peak at bifrequency (16,6Hz) is derived from the symmetrical characteristics of bispectrum. This result illustrates the limitations of wavelet bispectral analysis as it is clearly not able to discriminate between peaks generated by frequency coupling, as against those generated by phase coupling. The normalised squared wavelet bicoherences (WBIC) of these two signals with or without phase coupling are shown in (B). Many spurious peaks can be found, so the direct application of the WBIC is also possible to generate some spurious results. In contrast, the wavelet bicoherence with phase randomisation (IWBIC) of these two signals is shown in (C). Two significant peaks can be found in (Cb), but not in (Ca). This indicates that the IWBIC can eliminate the spurious peaks in the bispectrum. Finally, the surrogate method is applied to filter the effect of noise in wavelet bicoherence (FIWBIC). The reduction of the effect of noise can be seen in (D), indicating the FIWBIC can effectively present the QPC in this simulation.

11.2.4 Characteristics of Bicoherence Matrix

There are a number of different possible approaches for *constructing* a measure that can optimally extract information from the bicoherence matrix.

An important characteristic of the bicoherence is the total bicoherence at the frequency bands (${f_p}^L \le f_p \le {f_p}^U$ and ${f_q}^L \le f_q \le {f_q}^U$) (van Milligen et al. 1995), which is defined as

$$b = \sum\sum b_{xxx}^2 (f_p, f_q) \tag{11.13}$$

where the summation is extended over all frequencies f_p and f_q at ${f_p}^L \le f_p \le {f_p}^U$ and ${f_q}^L \le f_q \le {f_q}^U$. This value is a measure of the degree of QPC between the oscillators of different frequency bands and the one of high frequency band, which is much more helpful for understanding the interaction dynamics of neuronal population, such as the phase coupling between the delta and theta waves.

Another important characteristic of the bicoherence is the summed bicoherence (van Milligen et al. 1995), and it is defined as

$$b(f) = \sum b_{xxx}^2 (f_1, f_2) \tag{11.14}$$

where the summation is overall frequencies f_1 and f_2 and satisfies $f = f_1 \pm f_2$. This value can be used to measure the distribution of phase coupling as a function of frequency *f*. To further compress this information into a unitary quantity, Shannon entropy could be applied to the normalised form of the *b(f)*, to quantify the flatness of distribution of phase coupling.

The bicoherence of one channel series is a symmetrical relative matrix to the main diagonal, denoted as $C = \{b_{xxx}(f_p, f_q)\}$. In accordance with the theory of linear algebra, the eigenvalue decomposition of *C* is given by

$$\mathbf{C}\mathbf{v}_i = \lambda_i \mathbf{v}_i \tag{11.15}$$

where λ_i is the eigenvalue and $\lambda_1 \le \lambda_2 \le \cdots \le \lambda_M$; $\mathbf{v}_i$ is the eigenvector corresponding to λ_i. The value of eigenvalue λ_i is proportional to the amount of correlation in the direction of their associated eigenvectors. The eigenvalues can provide information about the synchronisation between individual elements of the matrix (oscillators). Two indices could be considered: (1) the maximal eigenvalue (denoted as *maxEigen*) (Li et al. 2007) and (2) the S-estimator (denoted as *SI*). This is the Shannon entropy of the eigenvalue distribution (Cui et al. 2010; Dauwels et al. 2010), which is defined as follows:

$$SI = -\frac{\sum_{i=1}^{M} \tilde{\lambda}_i \log\left(\tilde{\lambda}_i\right)}{\log(M)} \tag{11.16}$$

where $\tilde{\lambda}_i = |\lambda_i| / \sum_{j=1}^{M} |\lambda_j|$ is the normalised absolute eigenvalue. These two indices can be regarded as global phase coupling indices for the whole bicoherence matrix.

11.3 Application of Wavelet Bicoherence to Sleep Analysis

The functional correlates of different sleep stages remain a topic of much debate (Marquet 2001; Stickgold and Walker 2005; Vertes and Siegel 2005). Current evidence suggests that different stages of sleep may promote different types of learning and memory (e.g. Gais and Born 2004; Pace-Schott and Hobson 2002; Ribeiro and Nicolelis 2004; Spencer et al. 2007; Walker and Stickgold 2006). For example, SWS may be associated with the consolidation of declarative memory, while REM may be associated with non-declarative memory formation (Gais and Born 2004; Rasch et al. 2006; Eschenko et al. 2008; Rasch et al. 2007). Exploration of neural oscillations and synchronisation using the method described may provide important tools for clarifying the unique neurophysiological functions of sleep (Wolansky et al. 2006; Womelsdorf et al. 2007). In this study, this improved wavelet bicoherence is applied to measure the comodulation of cerebral cortical oscillations recorded from rats at the transitions between slow-wave sleep (SWS), rapid eye movement (REM) sleep and awaking state (AWK).

11.3.1 Data Recordings

Four male Sprague–Dawley rats, weighting 300–400 g at the time of surgery, served as subjects. The rats were maintained on a 12:12 h light–dark cycle, were individually housed following surgery and had ad libitum access to food and water. Ethical approval for this study was granted by the Ruakura and University of Auckland Animal Ethics Committees.

Animals were anaesthetised with ketamine/xylazine (75/10 mg/kg, i.p.) and mounted in a stereotaxic instrument with the skull held level. Four holes were drilled in the exposed skull; three for stainless steel skull screws (positioned over the cerebellum and bilaterally over the parietal cortex) and one for implantation of a tungsten stereotrode (Micro Probe Inc., Potomac, USA) into the parietal cortex for two-channel LFP recording. The stereotrode consisted of two insulated microelectrodes (3 μm diameter) separated by 200 μm. The stereotrode was lowered into the cortex to a depth of 0.5 mm and cemented to one of the anchor screws with rapid setting glue. The skull screws also served as reference and ground electrodes for the cortical local field potential recordings. Insulated wires from the screws were terminated along with the stereotrode electrodes in a plastic nine-pin socket, the base of which was embedded in dental acrylic (GC Corporation, Tokyo, Japan). The animals were allowed to recover for at least seven days prior to testing.

The leads were connected to two differential amplifiers (A-M Systems Inc., Carisborg, USA) via a tether and electrical swivel (Stoelting Co, Illinois, USA), allowing free movement of the animal around the recording enclosure. The two cortical field potential channels were AD-converted at 10,000/s (CED Power 1401, Cambridge, England), high- and low-pass filtered at 1 and 2500Hz, respectively,

and 50Hz notch filtered. The data were displayed and recorded continuously on a computer using Spike2 software (CED, Cambridge, England). The animals were video recorded during all recording sessions to aid off-line sleep staging. The video was synchronised with the electrophysiological recordings. Data were collected for up to 6 h while the animals slept naturally. Sleep staging was performed off-line using accepted electrophysiological and behavioural criteria (van Betteray et al. 1991). Transitions from SWS to REM and from REM to AWK were identified off-line and 2 min of LFP spanning each transition point extracted for later analysis, respectively.

In the following section, we use the improved wavelet bicoherence (denoted as WBIC in the following) to describe the phase coupling dynamics of SWS to REM and REM to AWK. To calculate the degree of quadratic non-linear interaction, each LFP recording of 20 s during either SWS, REM or AWK is subdivided into epochs of 2 s with an overlap of 75 %.

11.3.2 Results and Discussions

The wavelet spectrum and WBIC of the LFPs during SWS and REM are calculated and plotted in Fig. 11.2a–b. As can be seen in the wavelet spectrum, a maximal peak lies at 2 Hz (a typical slow wave). The presence of interactions between neural activities during SWS can be observed by FIWBIC. The contour plot of WBIC in (A) shows that the slow-wave band (0.5–4 Hz) is synchronised with the theta (4–8 Hz) and alpha band (8–12 Hz), and a phase coupling occurs between the theta bands. A main peak at the wavelet spectrum of (B) lies at 4–8 Hz for REM sleep. A major difference between REM and SWS is that the waves at the theta band are strongly synchronised in REM, and the phase coupling of other waves is restricted to narrower bands during REM. The difference between the WBIC at the SWS and REM can be directly revealed by the summed WBIC.

To further resolve the details of the interactions during SWS and REM, the WBIC is divided into bands (delta 0–4 Hz, theta 4–8 Hz, alpha 8–12 Hz and beta 12–20 Hz). A statistical analysis of the estimated average synchronisation of WBIC values at the different bifrequency bands was conducted on the 11 samples from SWS and compared to REM. As is shown in (C), the strength of phase coupling between delta and theta/alpha/beta waves during SWS is significantly stronger than that during REM. Conversely, the phase coupling between theta bands during REM is higher compared to SWS. At the same time, it is found that the variances of phase coupling of the high frequency bands at the REM are smaller. The average of the summed WBIC in SWS is higher than in REM, except in the theta band. In addition, the global phase coupling strength at the frequency bands of 0–20 Hz is higher in SWS compared to REM ($p < 0.1$). This finding is consistent with data from human subjects, where the WBIC is higher during state II/III sleep compared to awake (Bullock et al. 1997). One possible explanation for the finding of greater

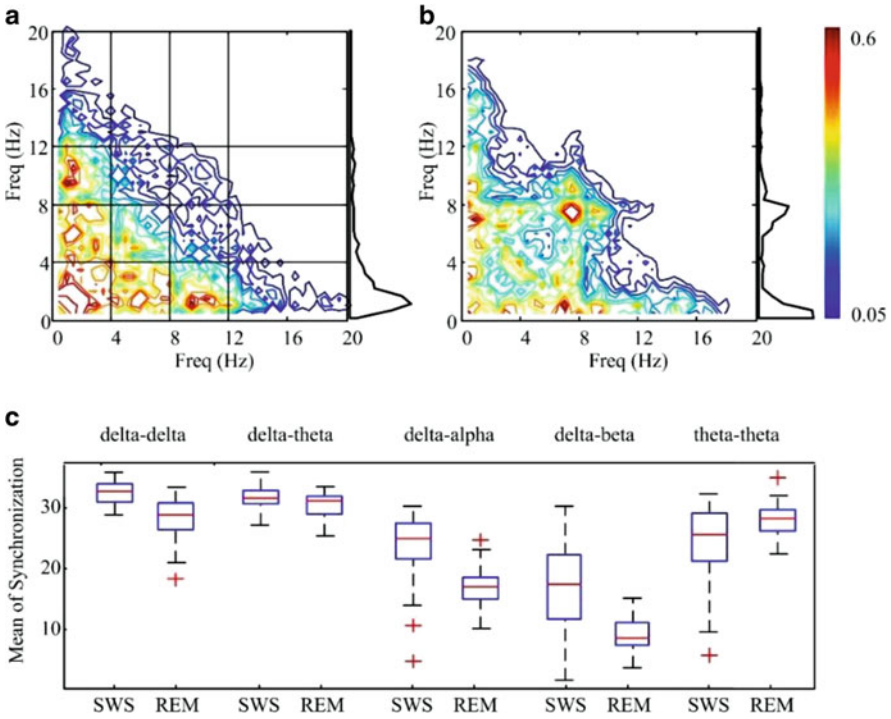

Fig. 11.2 The WBIC analysis of the transition from slow-wave sleep (SWS) to rapid eye movement (REM) sleep. (**a**–**b**) The FIWBIC and the wavelet spectrum at the SWS (**a**) and REM (**b**). (**c**) The statistical analysis of WBIC at the SWS versus REM at the local frequency bands (delta 0–4, theta 4–8, alpha 8–12 and beta 12–20 Hz.) (n = 11)

WBIC during SWS is an effective decrease in corticocortical connectivity as SWS progresses (Vyazovskiy et al. 2007). As a result, more oscillators with weak phase couplings could be generated, and these oscillators will have more chances to create 'resonance', so the number of bicoherent peaks increases during SWS.

Figure 11.3a–b show the wavelet spectrum and WBIC during REM and AWK have a high power of theta oscillations. However, it can be seen that there are small differences between REM and AWK. (c) presents the statistical results of REM compared to AWK at the different frequency bands for ten samples. The phase coupling of the delta–delta bands in AWK is higher than in REM ($p = 0.104$), and the variance of phase coupling at the AWK is smaller. The phase coupling of the delta–delta and delta–alpha bands may discriminate between REM and AWK. The total phase coupling in AWK is a little higher on average than in REM, but not statistically significant. This small total difference in WBIC between the REM and AWK indicates that the responsiveness to the outside world does not depend on the phase synchronisation of different bands; this finding is consistent with Massimini's work (Massimini et al. 2005).

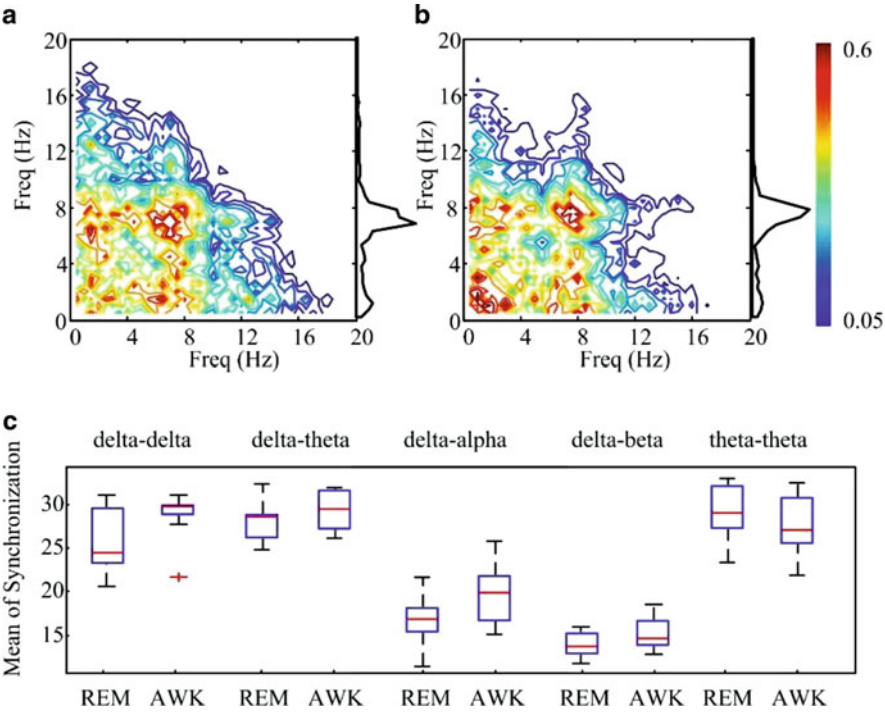

Fig. 11.3 The WBIC analysis of the transition from REM to awake (AWK). (**a**–**b**) The WBIC and the wavelet spectrum at the REM (**a**) and AWK (**b**). (**c**) The statistical analysis of WBIC at the REM versus AWK at the local frequency bands (n = 10)

In summary, real neuronal populations were investigated by the IWBIC. The main findings are as follows: (1) a phase coupling mechanism exists in the neuronal populations of rats at the SWS, REM and AWK, and (2) the degree of phase coupling in SWS is greater than in REM, and the degree in REM is less than in AWK. The improved wavelet bicoherence method described may provide a powerful tool to detect the QPC amongst the oscillations generated by neuronal populations.

11.4 Application of Wavelet Bicoherence to EEG During General Anaesthesia

The effects of general anaesthetics on the cerebral cortex and the thalamus (Musizza and Ribaric 2010) cause a multitude of different EEG oscillations (Steriade 2006). The EEG bicoherence has been found to be related to the concentration of anaesthetic drugs. Specifically, the bicoherence values in the alpha (at around 10 Hz) and

delta–theta (at around 4 Hz) band along the diagonal line of the bicoherence matrix were found to correlate well with the concentrations of isoflurane or sevoflurane (Hagihira et al. 2002; Morimoto et al. 2006). Hayashi et al. (Hayashi et al. 2008) found that sevoflurane caused bicoherence peaks in the alpha and delta–theta bands along the diagonal line, as well as a third peak at the pair of alpha basal frequency and its doubled frequency and that deeper anaesthesia shifted all peaks to lower frequencies and caused increased bicoherence in the delta–theta region. Recently Pritchett et al. (Pritchett et al. 2010) investigated bicoherence parameters across equal band (i.e. delta–delta) and unequal band (i.e. delta–theta) bifrequency regions, during different anaesthetic levels in routine clinical anaesthesia, and found that bicoherence estimates for the delta–theta region were more sensitive to anaesthetic changes. All these findings indicated that the bicoherence is a potential tool in the estimation of the effects of anaesthetic drugs on the brain (Hagihira et al. 2002; Hayashi et al. 2008). Here we applied the improved wavelet bicoherence method to analyse the EEG during isoflurane anaesthesia, examining how different isoflurane concentrations affected the bicoherence spectrum.

11.4.1 Data Recordings

The EEG signals (Hagihira et al. 2002) were obtained from 29 patients (9 men and 20 women, age 34–77 years, ASA physical status I–II) who underwent elective abdominal surgery under isoflurane general anaesthesia combined with epidural anaesthesia, after obtaining institutional approval (Osaka Prefectural Habikino Hospital, Osaka, Japan) and written informed consent from all participants. None of these participants had any neurologic or psychiatric disorders, nor were they receiving medication with any drugs known to influence anaesthetic or analgesic effects. Thirty minutes before the admission to the operating room, each patient received intramuscular premedication with 0.5 mg atropine. An epidural catheter was placed at the appropriate spinal location (T7/8, T8/9, T9/10 or T10/11). After confirming the effect of epidural analgesia, which was administered to minimise the influence of surgical stress on EEG during surgery, anaesthesia was induced with 3 mg/kg thiopental. After tracheal intubation, anaesthesia was maintained with isoflurane, oxygen and nitrogen. Vecuronium was given as required. Lidocaine 1 % (80–110 mg/h; initial dose, 90–100 mg) was administered epidurally. Patients received controlled ventilation to maintain adequate oxygenation and normocapnia. To keep mean blood pressure at 60 mmHg, as required, 2–5 $\mu g\ kg^{-1}\ min^{-1}$ dopamine was administered.

Five EEG electrodes (A_1, A_2, FP_1, FP_2 and FPz; according to the International 10–20 System) were attached to the patients before induction of anaesthesia. FPz was used as body ground. EEG data were collected from a single lead FP_1-A_1 using a 514X-2 EEG telemetry system (GE Marquette, Tokyo, Japan). EEG signals in the waking state were obtained before the induction of anaesthesia. Isoflurane was initially increased to 1.5 % and then stepped down to 0.7 %. To achieve a

steady state, the end-tidal concentration of isoflurane was purposely maintained at set levels (1.5 %, 1.3 %, 1.1 %, 0.9 %, 0.7 %) for 30 min, then changed to another concentration. The expired concentration of isoflurane was continuously monitored using Capnomac (Datex, Helsinki, Finland), and recorded simultaneously. The EEG segments with the 'burst suppression' pattern present were excluded from our analysis.

The EEG data were down-sampled at 128 Hz and preprocessed by the following steps: data points were rejected if the absolute amplitude values exceeded a threshold, which was selected as the mean plus c (5 7) times the standard deviation of the data analysed; a notch filter was used to remove the power signal of 50 Hz; the stationary wavelet transform was applied to the EEG signals, and the wavelet coefficients below 0.5 Hz were set to 0 to remove the effect of baseline drift.

11.4.2 Results and Discussions

Figure 11.4a shows the contour plots of wavelet bicoherence matrix at different isoflurane concentrations. The bicoherence patterns change with increasing isoflurane concentrations, and the changes are more distinct in the diagonal line and along the horizontal lines at slow frequencies. (B) shows the bicoherence values in the diagonal line (*diag_bic*) and the summed bicoherence values along the horizontal line at slow frequencies of 0.5 and 1 Hz (*low_bic*). In the *diag_bic*, it is obvious that isoflurane caused two main peaks at alpha and slow delta bands and that higher concentrations of isoflurane shifted the alpha peak to lower frequencies. These observations were consistent with the changes observed in the power spectrum with

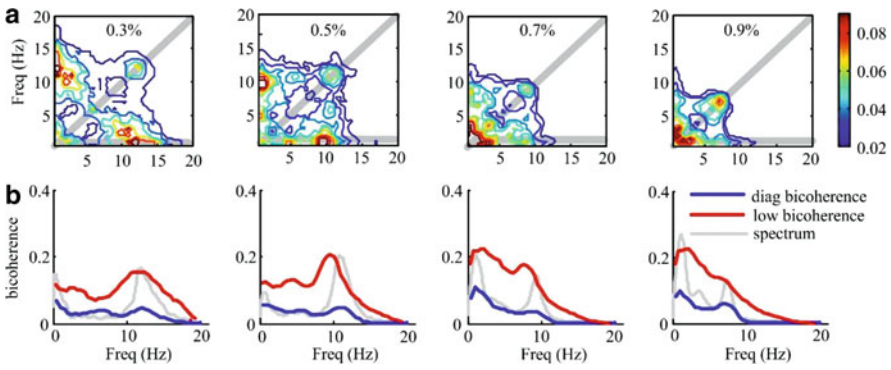

Fig. 11.4 Typical bicoherence patterns from a sample EEG with isoflurane anaesthesia. (**a**) Wavelet bicoherence matrix with increasing isoflurane concentrations of 0.3, 0.5, 0.7 and 0.9 %. (**b**) The bicoherence along the *diagonal line*, the summed bicoherence values at slow wave (0.5–1 Hz) along the *horizontal line* of the bicoherence matrix (*grey shadows* in (*a*)) and corresponding power spectra

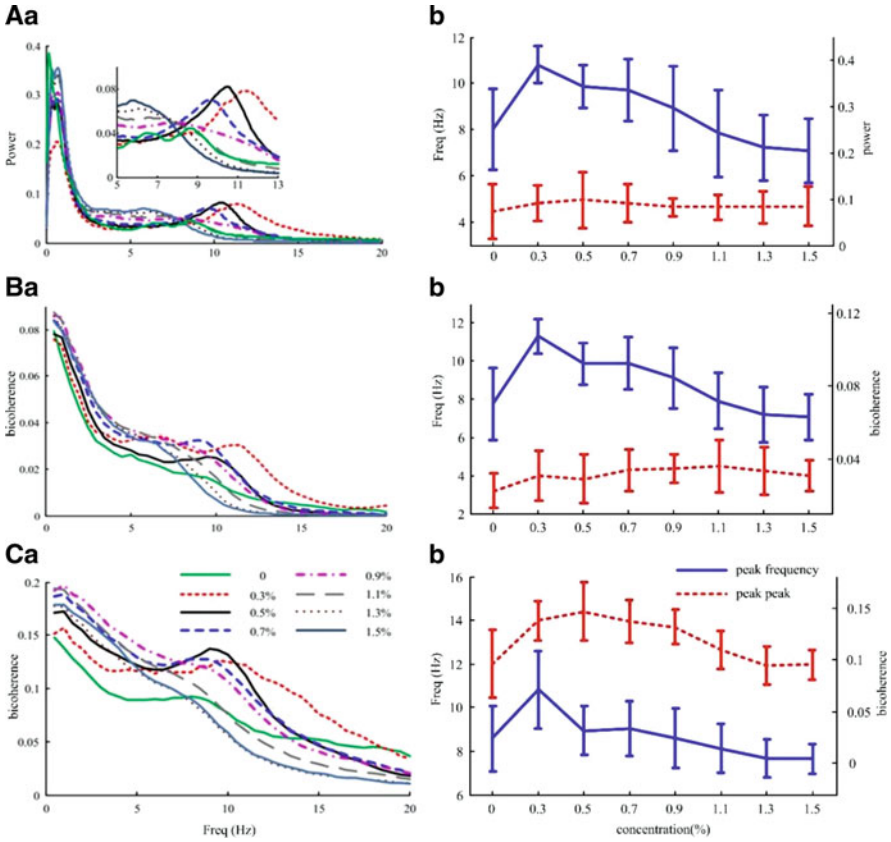

Fig. 11.5 (**a**) Averaged power spectra (*a*), the peak frequencies and peak power values at alpha band (*b*) for each study period from all the 29 subjects. (**b**) Averaged bicoherence values in the diagonal line ($f_p = f_q$) (*a*), the peak frequencies and peak bicoherence values (*b*). (**c**) Averaged summed bicoherence values at slow delta bands (0.5–1 Hz) (*a*), the peak frequencies and peak bicoherence values (*b*)

deeper isoflurane concentration. The shift of alpha peak also appeared in the plot of *low_bic*, and the summed bicoherence values at alpha peaks changes with drug concentration.

Figure 11.5a shows the mean power spectra from all the 29 subjects and the peak frequencies and peak power values in the alpha band for each study period. Isoflurane of 0.3 % caused a significant α peak at about 11 Hz, and when the isoflurane concentration increased, the peak moved to a lower region, resulting in peaks at about 7 Hz at 1.5 %. (B) summarises the mean bicoherence values in the diagonal line and the peak frequencies and peak bicoherence values with changes in isoflurane concentration. Consistent with the power spectra, the significant α peak at 11.3 ± 0.9 Hz tended to decrease to 7.1 ± 1.2 Hz, with increases in isoflurane concentration from 0.3 % to 1.5 % ($F(7114) = 12.416$, $p < 0.001$, one-way

ANOVA); the *diag_bic* alpha peak frequencies at lower isoflurane concentrations were significantly higher than those at deeper isoflurane concentrations and also than the no isoflurane condition ($p < 0.05$). These results indicated that the frequency shift in the *diag_bic* is coincident with the peak frequency shift in power spectrum. Bicoherence is a signal-processing technique capable of tracking changes in any reentry system. It is a method of investigating phase relations between two input signals with frequencies of f_1 and f_2 by examining an output signal with a frequency of $f_1 + f_2$ (Rampil 1998). With non-linear modulation – such as may be seen in the thalamocortical reverberating system – the output signal from the reverberating circuit is expected to reenter into the system as the input signal and cause self-modulated characteristics. Because this results in QPC between input signal components, bicoherence is expected to grow in these frequency components. Therefore, when a certain rhythm is dominantly formed in a thalamocortical reverberating network, a phase-coupled peak will often appear in the corresponding bicoherence (Hayashi et al. 2008).

Figure 11.5c shows the mean summed bicoherence values in the slow delta bands (*low_bic*), the peak frequencies and peak bicoherence values with changes in isoflurane concentration for each study period. The significant alpha peak appeared at a frequency of 10.8 ± 1.2 Hz at 0.3 % isoflurane, which slowed to 7.7 ± 0.7 Hz at 1.5 % isoflurane ($F(7114) = 6.767$, $p < 0.05$). As the isoflurane deepened, the summed bicoherence values tended initially to increase in amplitude, followed by a decrease ($F(7114) = 14.162$, $p < 0.001$). Post hoc analysis showed that the *low_bic* alpha peak frequencies at lower isoflurane concentrations (0.3–0.9 %) were significantly higher than those at deeper isoflurane concentrations (1.1–1.5 %) and also than during the period before induction (no isoflurane) ($p < 0.05$). This phase coupling between slow delta and alpha oscillations may point to some commonality between the states of natural sleep and general anaesthesia (Brown et al. 2010; Murphy et al. 2011). In natural sleep a number of studies (Steriade et al. 1993; Steriade et al. 1996; Mölle et al. 2002) have demonstrated that the cortically generated slow oscillation acts through corticocortical and corticothalamic drives to organise the faster rhythms; for example, spindle waves typically occur during the so-called 'up' states of the slow oscillation (Steriade 2006). During the depolarising phase of the slow oscillation, the synchronous firing of neocortical neurons impinges upon thalamic RE pacemaker neurons, thus creating conditions for the formation of spindles, which are transferred to TCR neurons and up to cortex, at which level the spindles shape the tail of the slow oscillatory cycle (Steriade 2006). This combination also results in the K-complex, and spectral analysis has shown the periodic recurrence of human K-complexes, with main peaks at 0.5–0.7 Hz and 12–15 Hz (Amzica and Steriade 1997).

In conclusion, we investigated the EEG wavelet bicoherence patterns under isoflurane general anaesthesia combined with epidural anaesthesia. In particular, the alpha and delta waves were coupled after isoflurane induction, and the coupling strength changed when the isoflurane concentration deepened. This phenomenon of alpha–delta coupling suggests that slow cortical oscillations organise the higher band activity, which is consistent with other studies in natural sleep.

References

Amzica F, Steriade M. The K-complex: its slow (<1Hz) rhythmicity and relation to delta waves. Neurology. 1997;49:952–9.

Brown EN, Lydic R, Schiff ND. General anesthesia, sleep, and coma. N Engl J Med. 2010;363:2638–50.

Bullock TH, Achimowicz JZ, Duckrow RB, Spencer SS, Iragui-Madoz VJ. Bicoherence of intracranial EEG in sleep, wakefulness and seizures. Electroencephalogr Clin Neurophysiol. 1997;103:661–78.

Chung J, Powers J. The statistics of wavelet-based bicoherence. In: Proceedings of the IEEE-SP international symposium on time-frequency and time-scale analysis. Pittsburgh; 1998. p. 141–144.

Cui D, Liu X, Wan Y, Li X. Estimation of genuine and random synchronization in multivariate neural series. Neural Netw. 2010;23:698–704.

Dauwels J, Vialatte F, Musha T, Cichocki A. A comparative study of synchrony measures for the early diagnosis of Alzheimer's disease based on EEG. Neuroimage. 2010;49:668–93.

Eschenko O, Ramadan W, Mölle M, Born J, Sara SJ. Sustained increase in hippocampal sharp-wave ripple activity during slow-wave sleep after learning. Learn Mem. 2008;15:373–7.

Gais S, Born J. Low acetylcholine during slow-wave sleep is critical for declarative memory consolidation. Proc Natl Acad Sci U S A. 2004;101:2140–4.

Hagihira S, Takashina M, Mori T, Mashimo T, Yoshiya I. Practical issues in bispectral analysis of electroencephalographic signals. Anesth Analg. 2001;93(4):966–70.

Hagihira S, Takashina M, Mori T, Mashimo T, Yoshiya I. Changes of electroencephalographic bicoherence during isoflurane anesthesia combined with epidural anesthesia. Anesthesiology. 2002;97(6):1409–15.

Hagihira S, Takashina M, Mori T, Ueyama H, Mashimo T. Electroencephalographic bicoherence is sensitive to noxious stimuli during isoflurane or sevoflurane anesthesia. Anesthesiology. 2004;100(4):818–25.

Hayashi K, Sawa T, Matsuura M. Anesthesia depth-dependent features of electroencephalographic bicoherence spectrum during sevoflurane anesthesia. Anesthesiology. 2008;108(5):841–50.

Hayashi K, Tsuda N, Sawa T, Hagihira S. Ketamine increases the frequency of electroencephalographic bicoherence peak on the alpha spindle area induced with propofol. Br J Anesthesiol. 2007;99(3):389–95.

Isler JR, Grieve PG, Czernochowski D, Stark RI, Friedman D. Cross-frequency phase coupling of brain rhythms during the orienting response. Brain Res. 2008;26(1232):163–72.

Jensen O, Colgin LL. Cross-frequency coupling between neuronal oscillations. Trends Cogn Sci. 2007;11:267–9.

Johansen JW, Sebel PS. Development and clinical application of electroencephalographic bispectrum monitoring. Anesthesiology. 2000;93(5):1336–44.

Kim YC, Powers EJ. Digital bispectral analysis and its applications to nonlinear wave interactions. IEEE Trans Plasma Sci. 1979;7:120–31.

Kim T, Powers EJ, Grady WM, Arapostathis A. A novel QPC detector for the health monitoring of rotating machines. In: Proceedings of IEEE instrumentation and measurement technology conference. Warsaw; 2007. p. 1–6.

Koronovskii AA, Khramov AE. Wavelet bicoherence analysis as a method for investigating coherent structures in an electron beam with an overcritical current. Plasma Phys Rep. 2002;28(8):666–81.

Larsen Y, Hanssen A, Pecseli HL. Analysis of non-stationary mode coupling by means of wavelet-bicoherence. IEEE international conference on acoustics, speech, and signal processing. Salt Lake City. 2001; p. 3581–3584.

Li X, Cui D, Jiruska P, Fox JE, Yao X, Jefferys JGR. Synchronization measurement of multiple neuronal populations. J Neurophysiol. 2007;98:3341–8.

Mallat S. A wavelet tour of signal processing. 2nd ed. New York: Academic Press; 1999.

Marquet P. The role of sleep in learning and memory. Science. 2001;294:1048–52.
Massimini M, Ferrarelli F, Huber R, Esser SK, Singh H, Tononi G. Breakdown of cortical effective connectivity during sleep. Science. 2005;309(5744):2228–32.
Morimoto Y, Hagihira S, Yamashita S, Iida Y, Matsumoto M, Tsuruta S, Sakabe T. Changes in electroencephalographic bicoherence during sevoflurane anesthesia combined with intravenous fentanyl. Anesth Analg. 2006;103(3):641–5.
Mölle M, Marshall L, Gais S, Born J. Grouping of spindle activity during slow oscillations in human non-rapid eye movement sleep. J Neurosci. 2002;22:10941–7.
Murphy M, Bruno MA, Riedner BA, et al. Propofol anesthesia and sleep: a high-density EEG study. Sleep. 2011;34:283–91A.
Musizza B, Ribaric S. Monitoring the depth of anaesthesia. Sensors. 2010;10:10896–935.
Newland DE. Harmonic wavelet analysis. Proc R Soc Lond A. 1993;443:203–25.
Newland DE. Harmonic and musical wavelets. Proc R Soc Lond A. 1994a;444:605–20.
Newland DE. Wavelet analysis of vibration, part 1: theory, part 2: wavelet maps. J Vib Acoust Trans ASME. 1994b;116:409–25.
Nikias CL, Raghuveer MR. Bispectrum estimation: a digital signal processing framework. Proc IEEE. 1987;75:869–91.
Pace-Schott EF, Hobson JA. The neurobiology of sleep: genetics, cellular physiology and subcortical networks. Nat Rev Neurosci. 2002;3(8):591–605.
Pritchett S, Zilberg E, Xu Z, Myles P, Brown I, Burton D. Peak and averaged bicoherence for different EEG patterns during general anaesthesia. BioMed Eng OnLine. 2010;9:76.
Rampil IJ. A primer for EEG signal processing in anesthesia. Anesthesiology. 1998;89:980–1002.
Rasch BH, Born J, Gais S. Combined blockade of cholinergic receptors shifts the brain from stimulus encoding to memory consolidation. J Cogn Neurosci. 2006;18:793–802.
Rasch B, Buchel C, Gais S, Born J. Odor cues during slow-wave sleep prompt declarative memory consolidation. Science. 2007;315:1426–9.
Ribeiro S, Nicolelis MAL. Reverberation, storage, and postsynaptic propagation of memories during sleep. Learn Mem. 2004;11:686–96.
Schack B, Vath N, Petsche H, Geissler HG, Moller E. Phase-coupling of thetagamma EEG rhythms during short-term memory processing. Int J Psychophysiol. 2002;44:143–63.
Schanze T, Eckhorn R. Phase correlation among rhythms present at different frequencies: spectral methods, application to microelectrode recordings from visual cortex and functional implications. Int J Psychophysiol. 1997;26:171–89.
Shils JL, Litt M, Skolnick BE, Stecker MM. Bispectral analysis of visual interactions in humans. Electroencephalogr Clin Neurophysiol. 1996;98:113–25.
Simonovski I, Boltezar M. The norms and variances of the Gabor, Morlet and general harmonic wavelet functions. J Sound Vib. 2003;264:545–57.
Sleigh JW, Andrzejowski J, Steyn-Ross A, Steyn-Ross M. The bispectral index: a measure of depth of sleep? Anesth Analg. 1999;88(3):659–861.
Spencer RMC, Gouw AM, Ivry RB. Age-related decline of sleep-dependent consolidation. Learn Mem. 2007;14:480–4.
Steriade M. Impact of network activities on neuronal properties in corticothalamic systems. J Neurophysiol. 2001;86:1–39.
Steriade M. Grouping of brain rhythms in corticothalamic systems. Neuroscience. 2006;137:1087–106.
Steriade M, Nunez A, Amzica F. A novel slow (<1 Hz) oscillation of neocortical neurons in vivo: depolarizing and hyperpolarizing components. J Neurosci. 1993;13:3252–65.
Steriade M, Contreras D, Amzica F, Timofeev I. Synchronization of fast (30–40 Hz) spontaneous oscillations in intrathalamic and thalamocortical networks. J Neurosci. 1996;16:2788–808.
Stickgold R, Walker MP. Sleep and memory: the ongoing debate. Sleep. 2005;28:1225–7.
Torrence C, Compo GP. A practical guide to wavelet analysis. Bull Am Meteorol Soc. 1998;79:61–78.
van Betteray JN, Vossen JM, Coenen AM. Behavioural characteristics of sleep in rats under different light/dark conditions. Physiol Behav. 1991;50:79–82.

van Milligen BP, Sánchez E, Estrada T, Hidalgo C, Brañas B, Carreras B, García L. Wavelet bicoherence: a new turbulence analysis tool. Phys Plasmas. 1995;2(8):3017–32.
Vertes RP, Siegel JM. Time for the sleep community to take a critical look at the purported role of sleep in memory processing. Sleep. 2005;28:1228–9.
von Stein A, Chiang C, Konig P. Top-down processing mediated by interareal synchronization. Proc Natl Acad Sci USA. 2000;97:14748–53.
Vyazovskiy VV, Riedner BA, Cirelli C, Tononi G. Sleep homeostasis and cortical synchronization: II. A local field potential study of sleep slow waves in the rat. Sleep. 2007;30(12):1631–42.
Walker MP, Stickgold R. Sleep, memory, and plasticity. Annu Rev Psychol. 2006;57:139–66.
Wolansky T, Clement EA, Peters SR, Palczak MA, Dickson CT. Hippocampal slow oscillation: a novel EEG state and its coordination with ongoing neocortical activity. J Neurosci. 2006;26:6213–29.
Womelsdorf T, Schoffelen J-M, Oostenveld R, Singer W, Desimone R, Engel AK, Fries P. Modulation of neuronal interactions through neuronal synchronization. Science. 2007;316:1609–12.
Zar JH. Biostatistical analysis. 4th ed. Upper Saddle River: Prentice-Hall; 1999.

Chapter 12
Multivariate EEG Synchronization Strength Measures

Dong Cui and Xiaoli Li

12.1 Introduction

The brain is a complex, nonlinear, nonstationary, massively interconnected dynamical system (McKenna et al. 1994; Friston 2000; Breakspear and Terry 2002; Le Van Quyen 2003). Electroencephalogram (EEG), local field potentials (LFP), magnetoencephalogram (MEG), or calcium imaging can precisely describe the dynamics of brain signals. Multivariate synchronization analysis is the technology for giving the information of the interrelations in the dynamics between different brain structures and synchronization phenomena of neural populations from these multivariate brain signals (Lawrence 2003; Womelsdorf et al. 2007). The assessment of the interdependence between signals can give new insights into the mechanisms underlying pathophysiological diseases and primarily improve treatment strategies especially for severe diseases (Lytton 2008; Van Albada and Robinson 2009; Van Albada et al. 2009). It has been proposed to play an essential role in cognition too. They are important approaches for understanding the overall dynamical properties in the brain (Buzsáki 2004; Buzsáki and Draguhn 2004; Engel et al. 2001; Rosso et al. 2001; Traub et al. 1998).

D. Cui
School of Information Science and Engineering, Yanshan University, Qinhuangdao, People's Republic of China
e-mail: cuidong@ysu.edu.cn

X. Li (✉)
State Key Laboratory of Cognitive Neuroscience and Learning & IDG/McGovern Institute for Brain Research, Beijing Normal University, Beijing 100875, People's Republic of China

Center for Collaboration and Innovation in Brain and Learning Sciences, Beijing Normal University, Beijing 100875, People's Republic of China
e-mail: xiaoli@bnu.edu.cn

X. Li (eds.), *Signal Processing in Neuroscience*, DOI 10.1007/978-981-10-1822-0_12

Existing linear and nonlinear methods to measure synchronization of neuronal population activity include cross correlation, spectrum-based coherence (Clifford Carter 1987; Gevins and Schaffer 1980), Granger causality (Granger 1969, 1980; Buchel and Friston 2000; Brovelli et al. 2004), synchronization likelihood (SL) (Stam and van Dijk 2002; Ferri et al. 2007; Stam and Reijneveld 2007; Micheloyannis et al. 2006), mutual information (Shannon 1948; Steuer et al. 2002; Kraskov et al. 2004; Darbellay and Vajda 1999; Min et al. 2003; Shabunin et al. 2002; Palus and Stefanovska 2003), nonlinear interdependence (Arnhold et al. 1999; Quian Quiroga et al. 2000, 2002; Schmitz 2000; Gandrzejak et al. 2003), generalized synchronization ((Rulkov et al. 1995; Schiff et al. 1996; Abarbanel et al. 1996; Quian Quiroga et al. 2000; Kramer et al. 2004), phase synchronization (Rosenblum et al. 1996; Pikovsky et al. 1996, 2001; Osipov et al. 1997; David et al. 2003; Engel et al. 2001; Varela et al. 2001; Lachaux et al. 1999; Tass et al. 1998; Shabunin et al. 2002; Palus and Stefanovska 2003; Mormann et al. 2000; Bruns 2004; Rosenblum et al. 2001; Fine et al. 2010; Quian Quiroga et al. 2002; Jamal et al. 2015) (where the phase of the time series is extracted by using the Hilbert or the wavelet transform, respectively), and correntropy coefficient (Xu et al. 2008). But these synchronization analyses have been constrained to the bivariate case. The examination of empirical multivariate data then was accomplished by the simple repeated application of bivariate synchronization measures. A picture of the bivariate synchronization measures of the ensemble can be obtained by estimating the pairwise synchronization between every possible pair of channels and then connecting the corresponding sites with lines of different thickness or color according to the strength of their interaction (Rodriguez et al. 1999; Bhattacharya et al. 2001). This approach gives detailed information on the topographic structure of synchronization relations, but it has some drawbacks: The representation of pairwise lines will get incomprehensible if the number of lines is large, and this picture in itself gives no information on a common integrating structure among the ensemble of electrodes. Another method is averaging the bivariate synchronization index for all the possible pairs of electrodes of the ensemble (van Putten 2003; Haig et al. 2000). But it cannot give the synchronization or topographic details and lose the spatial resolving power.

Multivariate data contain more information than those inferable from multiple bivariate examinations. In most neurological studies, it is interesting to investigate the interactions in a group of multivariate channels such as the degree of overall synchronization and the contribution of each channel. Moreover, bivariate techniques are also hampered by their inability to differentiate direct and indirect interactions, even when observing all important signals. It even shows the misleading results (Schelter et al. 2006). So the multivariate synchronization analysis aiming at the global information has been paid much more attention recently. It is a useful technique for studying the interactions in a group of multivariate channels for the understanding of overall dynamical properties in the brain.

This chapter describes several multivariate synchronization analyses including phase synchronization cluster analysis (Allefeld and Kurths 2004; Osipov and Kurths 2001; Osipov et al. 1997; Kim et al. 2008; Bialonski and Lehnertz 2006), S-estimator (Carmeli et al. 2005; Knyazeva et al. 2005; Boccaletti et al. 2002; Bialonski and Lehnertz 2006; Jalili et al. 2007) and extended method correlation matrix analysis (Gandrzejak et al. 2003; Allefeld et al. 2007; Seba 2003; Müller and Baier 2005; Müller et al. 2006a, b; Schreiber and Schmitz 1996; Seba 2003), omega complexity (Yoshimura et al. 2004), partial coherence (Bendat and Piersol 2000; Gersch and Goddard 1970; Cohen et al. 1995; Kocsis et al. 1999; Lopes da Silva et al. 1980; Mirski et al. 2003; Liberati et al. 1997; Tucker et al. 1986; Sun et al. 2004; Winterhalder et al. 2005, 2006; Albo et al. 2004) partial directed coherence (PDC) and direct tranfer function (DTF) (Sameshima and Baccalá 1999; Baccalá and Sameshima 2001a, 2001b; Kaminski and Blinowska 1991; Kus et al. 2004; Fanselow et al. 2001; Schelter et al. 2005; Astolfi et al. 2005; Thuraisingham 2007; Ding et al. 2000; Wu et al. 2011; Haufe et al. 2013), and complex network analysis (Stam et al. 2007; Ponten et al. 2007; Stam and van Dijk 2002; Ferri et al. 2007; Stam and Reijneveld 2007; Micheloyannis et al. 2006; Jamal et al. 2015). Throughout we introduce the processing of these multivariate synchronization analyses and their applications in neurophysiology. We compare the concept and methods and indicate their advantages and disadvantages.

12.2 Multivariate Synchronization Algorithm

12.2.1 Phase Synchronization Cluster Analysis

The basic idea of phase synchronization cluster analysis (PSCA) is a single cluster having a common rhythm, which is an average of the oscillations of each oscillator, and its dynamics is described by a cluster phase Φ. It conceives of the oscillators as constituting a cluster in which they participate in different degrees c_i ranging from no to perfect agreement with the cluster dynamics, where the degree of participation of each individual channel can be checked by assessing the phase synchronization (PS) between the global and the individual phases:

$$\Phi_k = \arg \sum_j c_j \exp\left(i\phi_{jk}\right) \tag{12.1}$$

$$c_i = f\left(\overline{R}_{iC}\right) \tag{12.2}$$

$$\overline{R}_{iC} = \left| \frac{1}{n} \sum_k \exp\left(i\left(\varphi_{ik} - \Phi_k\right)\right) \right| \tag{12.3}$$

where Φ_k is the cluster phase of each realization. The participation indices c_i are calculated as a function of the synchronization strength between the oscillator and the cluster $\overline{R}_{iC}$.

By introducing this mean field into the model equations, the dynamics of the phase differences of each oscillator to the cluster phase can be formally decoupled, assuming each oscillator is driven by noise independent of that acting on the other oscillators. In this sense, the factorization of the matrix of bivariate synchronization indices $\overline{R}_{ij}$ is an empirical estimate of $\rho_{ij} = \rho_{iC}\rho_{jC}$ which can be shown to be asymptotically normally distributed $\overline{R}_{ij} \sim N\left(\rho_{ij}, \sigma_{ij}^2\right)$ where ρ_{iC} is the synchronization strengths of the *ith* signal to the cluster. The work of estimating ρ_{iC} can be regarded as the generally applicable multivariate phase synchronization analysis. The maximum likelihood estimation of the ρ_{iC} then reduces to minimizing the sum of square weighted errors:

$$\sum_{i,j>i} {E_{ij}}^2, \; E_{ij} = \frac{\overline{R}_{ij} - \rho_{iC}\rho_{jC}}{\sigma_{ij}} \tag{12.4}$$

where $\sigma_{ij} = \frac{1}{2n}\left(1 - {\rho_{iC}}^2{\rho_{jC}}^2\right)$.

This generic multivariate analysis in the field of phase synchronization is useful in EEG studies where the assessment of overall synchronization of multivariate data is the main goal. It is in contrast to other studies concerning the dynamics and stability of clusters of perfect (phase) synchronization and the coexistence and interaction of multiple clusters (Osipov and Kurths 2001; Osipov et al. 1997). However, this method only can describe the form of a single statistical cluster assuming the dynamics of the oscillators can be decoupled by introducing a mean field. Its feasibility and decoupling are the most important. But even in cases where the conditions are not perfectly adequate, it may serve as a first approximation and specific deviations from the applied model and can be detected by large values of the residual errors E_{ij}.

12.2.2 S-estimator and Correlation Matrix Analysis

12.2.2.1 S-estimator

S-estimator is a new and simple measure based on the PCA embedding technique (Carmeli et al. 2005; Knyazeva et al. 2005; Bialonski and Lehnertz 2006). It can measure the amount of synchronization over a region of the cortex by an information theory-inspired measure defined as the complement of the entropy of the normalized eigenvalues of the corresponding correlation matrix. Such quantity is proportional to the embedding dimension of the dynamical phenomenon.

First we perform PCA meaning that we eigendecompose the covariance matrix of the data. From the diagonal elements λ_i of the eigenvalue matrix Λ, we compute the normalized eigenvalues $\lambda_i^{'}$ as follows:

$$\lambda_i{}' = \frac{\lambda_i}{\sum_{i=1}^{M} \lambda_i} = \frac{\lambda_i}{tr(C)} \tag{12.5}$$

where $\lambda_i{}'$ is the corresponding normalized eigenvalue and $tr(C)$ is the trace. Then we can compute the S-estimator:

$$S = 1 + \frac{\sum_{i=1}^{M} \lambda_i{}' \log\left(\lambda_i{}'\right)}{\log(M)} \tag{12.6}$$

S-estimator is a measure inversely proportional to the embedding dimension of the observed dynamical phenomenon, thus proportional to the amount of synchronization.

Applications to simulated coupled oscillators and to EEG data indicated that S appears at least as reliable and robust as other nonlinear measures of synchronization (Boccaletti et al. 2002). S-estimator is spectrum wide and not frequency specific. It addresses the investigations of broadband synchronization phenomena. More importantly, S is naturally multivariate, which makes it particularly suitable for high-density surface sampling EEG analysis, currently replacing conventional EEG methods, both in research laboratories and in clinics. However, it can only give the global synchronization index without the details. The contributions of each channel to the group are not acquired.

12.2.2.2 Correlation Matrix Analysis

This novel method correlation matrix analysis (CMA) is based on random matrix theory (RMT) (Seba 2003; Müller and Baier 2005; Müller et al. 2006a, b), equal-time correlation, correlation matrix analysis (Allefeld et al. 2007), and surrogate resampling (Schreiber and Schmitz 1996). It is able to quantify and describe properties of synchronization of population neuronal activity recorded simultaneously from multiple sites such as number and composition of clusters, global synchronization, and how synchronization patterns change with time.

Firstly, to provide the same scale for all of neuronal population activity, the data set is normalized and an equal-time correlation matrix $\boldsymbol{C}$ is constructed. The eigenvalue decomposition of $\boldsymbol{C}$ is given by

$$\mathbf{C}\mathbf{v}_i = \lambda_i \mathbf{v}_i \tag{12.7}$$

Secondly, we randomize all channels of the time series, thereby destroying all the equal-time correlations that exist. In the present work, we randomize the phase relationship using the amplitude-adjusted Fourier transform (AAFT) (Schreiber and Schmitz 1996) and get a surrogate correlation matrix **R**; the eigenvalues of this matrix **R** can be obtained as $\lambda_k^{'}$, $k = 1, \ldots, M$. Repeating this randomization by N, the mean and standard deviation of eigenvalues are $\overline{\lambda}_k^{'}$ and SD_k.

Then the normalized synchronization can be computed by the following equation:

$$\text{Syn\_Index}_k = \begin{cases} \left(\lambda_k - \overline{\lambda}_k^{'}\right) / \left(M - \overline{\lambda}_k^{'}\right), \lambda_k > \left(\overline{\lambda}_k^{'} + K \times SD_k\right) \\ 0, \qquad\qquad \text{otherwise} \end{cases} \tag{12.8}$$

Syn_Index ranges from 0 to 1, where 0 denotes no synchrony, and 1 denotes perfect synchrony among the time series. The maximal value is called the synchronization index (SI) and gives an indication of global synchronization throughout the population of neurons from which recordings have been made. The value of $K = 3$ is for an overall significance of 0.01.

The equation to compute the number of clusters is expressed as

$$\text{NoCluster} = \sum_k \text{sgn}\left(\lambda_k > \left(\overline{\lambda}_k^{'} + K \times SD_k\right)\right) \tag{12.9}$$

where sgn is a sign function.

The eigenvalue can indicate the strength of a cluster. Corresponding to the eigenvalue, the eigenvector can describe its internal structure. Thus, qualification of the structure of synchronized clusters should be described by combining the eigenvalues and eigenvectors, in a variable called the *participation index* (Allefeld et al. 2007), which is defined as

$$PI = \lambda_k v_{ik}^2 \tag{12.10}$$

We have therefore tested the procedure using the chaos system of coupled Lorenz-type oscillators and low-calcium in vitro model of epilepsy (Li et al. 2007). The results show that the technique can successfully identify synchronization of activity in small groups of neurons consisting of independent clusters of synchronous activity. Moreover, the participation index can be used to demonstrate how the distribution of clusters changes with time. The transition to an electrographic seizure is shown by an increase in the synchronization index as progressively more regions in the hippocampal slice are activated simutaneously.

CMA can be applied to the analysis of neurophysiological data recorded simultaneously from multiple sites. In principle, application of the method to neuronal data is very simple: A high eigenvalue indicates a high level of correlation, and a low level indicates poor correlation based on RMT. It is thus possible to identify clusters

of local synchrony in which activity is synchronized and to determine whether that activity is independent of activity in other subpopulations within the recording area.

The matrix $\boldsymbol{C}$ could, however, be composed from very different correlations, such as phase synchronization, linear cross correlation, or event synchronization, depending on the nature of the activity being analyzed (Pereda et al. 2005).

Based on the description of the SI method, global synchronization index (GSI) for measuring global synchronization of multiple time series was proposed (Cui et al. 2010). We used the equal-time correlation method to get the correlation matrix C, the surrogate correlation matrix R, and their eigenvalues, like the SI method. In the GSI method, the eigenvalues of matrix C are normalized by dividing the eigenvalues of matrix R to reduce the influence of random component. The GSI is defined as

$$\mathrm{GSI} = 1 + \frac{\sum_{i=1}^{M} \lambda_i \log(\lambda_i)}{\log(M)} \tag{12.11}$$

where λ_i is the normalized eigenvalues and computed as

$$\lambda_i = \frac{\lambda_i / \overline{\lambda}_i^s}{\sum_{i=1}^{M} \lambda_i / \overline{\lambda}_i^s} \tag{12.12}$$

where $\overline{\lambda}_i^s$ represents the mean values of the eigenvalues of matrix $\boldsymbol{R}$. M represents the number of time series like the SI mentioned. To understand how this estimator works, two cases should be considered. If there is no genuine correlation, the normalized eigenvalues are all equal to $1/M$, so $\mathrm{GSI} = 0$; on the contrary, if all the time series are correlated completely, the largest normalized eigenvalue should be M, and the others are equal to zero; at this point, $\mathrm{GSI} = 1$.

12.2.3 Omega Complexity

Omega complexity is a measurement based on principal component analysis (Yoshimura et al. 2004), which is similar to S-estimator. Firstly, eigenvalue decomposition is made on the covariance matrix C of the data matrix. Then the obtained eigenvalues are normalized. Omega complexity is defined as

$$\Omega = \exp\left(-\sum_{i=1}^{M} \lambda_i' \log\left(\lambda_i'\right)\right) \tag{12.13}$$

If a signal $x_i(k)$ was completely synchronized, having the largest eigenvalue M and other eigenvalue 1, then $\Omega = 1$. On the other hand, if all the eigenvalues were 1, then $\Omega = M$. Therefore, omega complexity is a nonsimilarity measurement, and its value is not normalized. Because the algorithm of omega complexity is similar to S-estimator, the performance of them is also similar.

12.2.4 Partial Directed Coherence and Directed Transfer Function

12.2.4.1 Partial Coherence

The first extension of bivariate analysis was made by a nonparametric analysis technique: partial coherence (PC), which introduced a third signal into the estimation of a new coherence measure. It was introduced to differentiate direct and indirect linear relationship.

For signals X, Y, and Z, the underlying idea of PC is to subtract linear influences from other processes to obtain the partial cross spectrum between X and Y:

$$S_{xy|z}(f) = S_{xy}(f) - S_{xz}(f){S_{zz}}^{-1}(f)S_{yz}(f) \tag{12.14}$$

Then the squared partial coherence is estimated as follows (Bendat and Piersol 2000):

$$\kappa^2_{xy|z}(f) = \frac{\left|\left\langle S_{xy|z}(f)\right\rangle\right|^2}{\left|\left\langle S_{xx|z}(f)\right\rangle\right|\left|\left\langle S_{yy|z}(f)\right\rangle\right|} \in [0,1] \tag{12.15}$$

where $S_{xx|z}(f)$ and $S_{yy|z}(f)$ are partial auto-spectra and $\langle\cdot\rangle$ indicates average over data segments. The $\kappa^2_{xy|z}(f)$ represents the partial coherence between X and Y that is not shared with Z.

And the partial phase spectrum is

$$\Phi_{xy|z}(f) = \arg\left(S_{xy|z}(f)\right) \tag{12.16}$$

The direction of interrelations can be inferred from the partial phase spectrum if there is a strict linear phase relation.

PC measure is a nonparametric method which is robust in detecting relationships in multivariate systems. The statistical properties are well known and critical values for a given significance level can be calculated (Winterhalder et al. 2005, 2006). This is an important fact especially in applications to noisy neural signal transfer as measured by, e.g., EEG recordings. But recent study demonstrates that PC measure is very sensitive to noise contamination (Albo, et al. 2004). It must be noted that PC is based on the assumption of linearity. Although direct and indirect influences

can be distinguished in the example of the nonlinear stochastic Roessler system (Winterhalder et al. 2005), but in other nonlinear system (e.g., some neural signals) might cause errors in its applications. Furthermore the direction of interrelations can be inferred if and only if there is a strict linear phase relation. A shortcoming of PC and partial phase spectrum is that reliable assessment of the phase spectrum has rigorous conditions such as highly significant coherence value and broad range of frequencies (Winterhalder et al. 2006). So the ability to distinguish direction of PC is weak.

12.2.4.2 Partial Directed Coherence and Directed Transfer Function

Partial directed coherence (PDC) is a frequency domain description of Granger causality between multivariate time series. This linear and parametric method was introduced by Baccalá and Sameshima (Sameshima and Baccalá 1999; Baccalá and Sameshima 2001a, b). PDC is based on modeling time series by multivariate autoregressive (MAR) process. Consider an m-dimensional MAR model with order p as follows:

$$\begin{pmatrix} x_1(n) \\ x_2(n) \\ \vdots \\ x_m(n) \end{pmatrix} = \sum_{r=1}^{p} \mathbf{A}_r \begin{pmatrix} x_1(n-r) \\ x_2(n-r) \\ \vdots \\ x_m(n-r) \end{pmatrix} + \begin{pmatrix} \varepsilon_1(n) \\ \varepsilon_2(n) \\ \vdots \\ \varepsilon_m(n) \end{pmatrix} \tag{12.17}$$

where

$$\mathbf{A}_r = \begin{bmatrix} a_{11}(r) & a_{12}(r) & \cdots & \cdots & a_{1m}(r) \\ \vdots & \vdots & \vdots & \vdots & \vdots \\ \vdots & \vdots & \vdots & a_{ij}(r) & \vdots \\ \vdots & \vdots & \vdots & \vdots & \vdots \\ a_{m1}(r) & \cdots & \cdots & \cdots & a_{mm}(r) \end{bmatrix} \tag{12.18}$$

In this model, time series $x_i(n)$ depends on its own past values $x_i(n-r)$ through the coefficients $a_{ii}(r)$ of A_r, while $x_i(n)$ dependence on the past values of other series $x_j(n-r)$ is through coefficients $a_{ij}(r)$. As such, the time series $x_j(n)$ only Granger-causes $x_i(n)$ if we can statistically show that $a_{ij}(r) \neq 0$ for some values of r. Or equivalently rejecting the null hypothesis of $a_{ij}(r) = 0$ means that $x_j(n)$ does Granger-cause $x_i(n)$.

Let $\mathbf{A}(f)$ be essentially the Fourier transform of the coefficients $\mathbf{A}_r$

$$\mathbf{A}(f) = \sum_{r=1}^{p} \mathbf{A}_r z^{-r} \big|_{z=e^{j2\pi f}} \tag{12.19}$$

Let $\overline{\mathbf{A}}(f) = \mathbf{I} - \mathbf{A}(f) = [\bar{\mathbf{a}}_1(f)\bar{\mathbf{a}}_2(f)\cdots\bar{\mathbf{a}}_m(f)]$. $\bar{\mathbf{a}}_i(f)$ is the ith column of the matrix, and $\bar{a}_{ij}(f)$ expresses the i,jth element of $\bar{\mathbf{A}}(f)$:

$$\bar{a}_{ij}(f) = \begin{cases} 1 - \sum_{r=1}^{p} a_{ij}(r)e^{-j2\pi rf}, & \text{if } i = j \\ -\sum_{r=1}^{p} a_{ij}(r)e^{-j2\pi rf}, & \text{otherwise} \end{cases} \tag{12.20}$$

The PDC measure from signal j to signal i at frequency f is defined as

$$\pi_{ij}(f) = \frac{\bar{a}_{ij}(f)}{\sqrt{\bar{\mathbf{a}}_j^H(f)\bar{\mathbf{a}}_j(f)}} \tag{12.21}$$

The PDC $\pi_{ij}(f)$ represents the direct frequency domain Granger causality test (relative coupling strength) from j to i channels. For $i = j$ the PDC represents how much of x_i's own past contributes to the evolution on itself that is not explained by other signals.

Directed transfer function (DTF) which is a very similar measure of causal influence was introduced as follows (Kaminski & Blinowska 1991):

$$\mathrm{DTF}_{ij}(f) = \theta_{ij}(f) = \frac{H_{ij}(f)}{\sqrt{\mathbf{h}_i^H(f)\mathbf{h}_i(f)}} \tag{12.22}$$

where the superscript $(\cdot)^H$ indicates the Hermitian transpose. $\mathbf{H}(f) = \overline{\mathbf{A}}^{-1}(f) = [\mathbf{I} - \mathbf{A}(f)]^{-1}$ is called the transfer function matrix.

DTF provided a physiologically interesting frequency domain picture as well. But due to intrinsic aspects of DTF's definition, structural inference based on its computation did not always agree with the result of Granger causality tests (GCT) (Baccalá and Sameshima 2001a). DTF can't differentiate the interactions between direct or indirect. On the contrary, PDC can clearly indicate the direct interactions and expose the feedback structure. At this point, DTF can provide complementary information for PDC. PDC and DTF causality measures are meaningful only in statistical sense. The statistical properties of PDC and significance level for testing nonzero PDC at a given frequency were proposed (Schelter et al. 2005). But there is no analytical significance level for testing for nonzero DTF. Thus, interpretation of the results obtained by the DTF is more complicated than PDC. Furthermore the computation of PDC does not involve any matrix inversion. It is computationally more efficient and more robust than DTF for avoiding numerical imprecision that results from possible ill-conditioning of $\bar{\mathbf{A}}(f)$ at some frequencies in DTF estimation. An important difference between DTF and PDC since DTF $\theta_{ij}(f)$ is normalized with respect to the structure that receives the signals (the total inflow of information), whereas PDC $\pi_{ij}(f)$ is normalized with respect to the structure that

sends the signals (the total outflow of the information). So the PDC is in much common use than DTF. The comparative results between the two methods can also be seen (Baccalá and Sameshima 2001a, b; Kus et al. 2004).

In practice, the successful estimation of them depends primarily on the reliability of the MAR model, since all the necessary information depends completely on the estimated model parameters. The parameter estimation methods for coefficient matrices $\mathbf{A}_r$ in common use are multivariate Yule-Walker equations, least squares estimates, or fast maximum entropy methods.

The order in an autoregressive process is the number of immediate previous values that have a direct effect on the current value. The studies (Thuraisingham 2007) indicated that coherence provides an accurate estimate of the order unlike the spectral density, which underestimated the value of the order leading to inaccurate values for the PDC. The order of the model p can also be inferred using Akaike's AIC criterion. But the choice of an optimal model order is awfully difficult now.

How to choose the window size properly is another crucial difficulty. The length of the data has a statistically significant influence on the accuracy of PDC connectivity pattern estimation (Astolfi et al. 2005). However, the data in neurophysiology usually are nonstationary signals. The window of signal was limited and influenced the accuracy of PDC. Furthermore if the signals are found to be nonstationary, time-varying MAR model parameter estimation must be adopted such as the recursive least squares algorithm (RLS) and short-window-based adaptive MAR approach (Ding et al. 2000). The ability of PDC to deal with the nonstationary data has not been validated well.

Another problem is the ability of PDC in dealing with nonlinear system; as we all know PDC was based on linear VAR model. Winterhalder applied PDC to the nonlinear coupled stochastic Roessler system with pronounced frequencies. PDC was found to be sensitive in detecting interactions in nonlinear multivariate systems. But a higher order of the model is required, and followed by a larger amount of computation (Winterhalder et al. 2006). And the performance of PDC to other nonlinear system and real neurophysiology has not been studied.

Furthermore the PDC or DTF can only give the information of causality for one signal to another. If we want to obtain the interaction details in M channels, we must give M^2 pictures of PDC or DTF. It is seemed deduced to the bivariate measure case. The global interaction information which is our motive is not obtained directly too. How the preprocessing gives the influence to PDC is not solved as well.

12.2.5 Complex Network Analysis

The first step in applying complex network analysis (CNA) is to use the bivariate synchronization measures to construct a matrix, which describe details of the brain function connection. Given a threshold the synchronization matrix converts to a binary graph. Then the graph theoretic analysis and complex network analysis

are used to find the network connection characteristic and give the details of synchronization information (Stam et al. 2007; Ponten et al. 2007).

The matrix is mostly constructed by the synchronization likelihood (SL), which is a recently introduced measure of statistical interdependencies within a dynamical systems framework (Stam and van Dijk 2002), and other bivariate synchronization index can be used as well. The cluster coefficient C and the characteristic path length L are computed with a different threshold. The cluster coefficient C is the ratio of all existing edges between the neighbors and the maximum possible number of edges between the neighbors which range between 0 and 1. It is a measure for the tendency of network elements to form local clusters. The characteristic path length L is the average shortest path connecting any two vertices of the graph; the length of a path is indicated by the number of edges it contains. It is an emergent property of the graph, which indicates how well its elements are integrated/interconnected.

CNA is quite general and could also be applied to connectivity matrices based upon reconstructed sources in future studies. It can characterize the whole network in terms of local and global integration and to determine which aspect might be affected. However, there is no unique way how to determine threshold, and only one cluster can be described by this approach.

12.3 Applications

Multivariate EEG synchronization measures have been widely used for studying the relationship among neural signals at present. Partial coherence (PC) is the first attempt to analyze the signals more than two channels and has been applied popularly in neurophysiology. In neurophysiology, PC was first applied to identify epileptic focus with three electrodes (Gersch and Goddard 1970). To this date, it has been used to study the nature of connectivity and causal information in various neural signals from spike trains (Cohen et al. 1995), hippocampal field oscillations (Kocsis et al. 1999), intracortical EEG (Lopes da Silva et al. 1980; Mirski et al. 2003), scalp EEG (Liberati et al. 1997; Tucker et al. 1986), and functional magnetic resonance imaging (fMRI) data (Sun et al. 2004).

PDC was defined by Baccalá and Sameshima ((Sameshima and Baccalá 1999; Baccalá and Sameshima 2001a, b). It was first used to neural spike train data (Sameshima and Baccalá 1999). The spike trains are convolved with a Gaussian kernel and are sampled, leading to discrete time series. The author observed short-lived and frequency-altering feedback from the thalamus to cortex. Another PDC study showed a clear directional preference from somatosensory cortex to medial thalamic nucleus during whisker twitching than other behaviors in freely moving rats (Fanselow et al. 2001); Winterhalder et al. used the data obtained from experimental recordings of deep sedation with burst suppression patterns (BSP) to analyze electrophysiological signals from thalamic and cortical brain structures. A clear depiction of the system generating such burst patterns is given (Winterhalder et al. 2005). Baccalá and Sameshima illustrate PDC in connection to local field

potentials recorded from a rat in exploratory behavior. The simultaneously processed structures comprise the hippocampal CA1 field, somatosensory (A3) and motor (A10) cortical areas, and the dorsal raphe (DR), where rhythmic oscillations in the theta range are observed during desynchronized sleep and alert states. The experiment portrays the distinct and potentially interesting functional connectivity patterns that characterize different behavioral states and indicate that DR is possibly an important role (source reversal to an information sink) (Baccalá and Sameshima 2001a). In the application to essential tremor, directions of the interrelations are determined using partial directed coherence analysis. Both directions from the cortex to the muscles and vice versa are observed. It could be shown that the cortex imposes its oscillatory activity on the contralateral muscles via the corticospinal tract and that additionally muscle activity is reflected to the contralateral cortex via proprioceptive afferences (Schelter et al. 2005). Astolfi used PDC to actual event-related recordings: The activity noted in the supplementary and primary motor areas in the present study is consistent with the role that such cortical areas have in the organization and in the performance of simple foot movements (Astolfi et al. 2005).

The DTF was defined by Kaminski and Blinowska (Kaminski and Blinowska 1991). Babiloni et al. applied DTF to study the direction of information flux within EEG functional coupling at electrode pairs in normal elderly, amnesic MCI, and mild AD subjects at rest condition (closed eyes). They found that parietal to frontal direction of the information flux within EEG functional coupling was stronger in normal elderly than in MCI and/or AD subjects, namely, alpha and beta rhythms (Babiloni et al. 2009).

Phase synchronization cluster analysis (PSCA) is a genuine multivariate synchronization analysis method which is essentially different with partial coherence and partial directed coherence (PDC). It was introduced by Allefeld and Kurths in 2004, who introduced the concept of a statistical phase synchronization cluster and derive a method to identify this structure in a given data set (Allefeld and Kurths 2004). PSCA has been applied to different experimental situations in some fields. Allefeld and Kurths applied it to human EEG data from a visual attention psychological experiment in a time- and frequency-specific way, resulting in a common topography of synchronized behavior, but showing differences in the overall strength of synchronization between experimental conditions (Allefeld and Kurths 2004). Based on the theory of multivariate phase synchronization, it is feasible to propose the strategy to find groups of genes according to the specific biological process by analyzing cell cycle-specific gene expression data (Kim et al. 2008).

S-estimator was proposed by Carmeli et al. (2005). It was applied to high-density EEG recordings of nine adult with two different vision stimuli in wide spectrum or specified spectrum. S-estimator appeared to cause a complex rearrangement of synchronous neuronal assemblies distributed over the cortex, in particular over the visual cortex (Carmeli et al. 2005). Jalili et al. applied S-estimator to reveal a whole-head synchronization topography in schizophrenia to the resting dense array (128 channels) EEG obtained from 14 patients and 14 controls; they found bilaterally increased synchronization over temporal brain regions and decreased

synchronization over the postcentral/parietal region neighboring the midline. Its application to schizophrenia research shows that schizophrenia can be explained within the concept of neural disconnection across and within large-scale brain networks (Jalili et al. 2007).

Based on equal-time correlation, correlation matrix analysis, and surrogate resampling, Li et al. develop a new method called correlation matrix analysis (CMA) at 2007, which is able to quantify and describe properties of synchronization of population neuronal activity recorded simultaneously from multiple sites. They applied CMA to the data recorded from an in vitro model of epileptic seizures. The results demonstrate that this novel method can be successfully used to analyze synchronization between multiple neuronal population series (Li et al. 2007). Cui et al. developed the CMA method to estimate the genuine and random synchronization, denoted as GSI (genuine synchronization index) and RSI (random synchronization index) in multivariate neural series by means of a correlation matrix analysis and surrogate technique. The proposed method is applied to analyze a 21-channel scalp electroencephalographic recording of a 35-year-old male who suffers from medial temporal lobe epilepsy. The GSI and the RSI at different frequency bands during the epileptic seizure were shown (Cui et al. 2010). Lee et al. analyzed the EEG of AD patients by using the SI method. They found that the global SI values in the beta1 (12–18 Hz), beta2 (19–21 Hz), beta3 (22–30 Hz), and gamma (30–50 Hz) bands were significantly lower in AD patients than in normal control. The global SI values in the beta and gamma bands were positively correlated with the MMSE scores in all participants (AD and normal control) (Lee et al. 2010). Cui et al. applied S-estimator, synchronization index (SI), and global synchronization index (GSI) to analyze the synchronization in five ROIs of sLORETA sources of resting eyes-closed EEG data which were recorded in eight aMCI subjects and 11 age-matched controls in T2DM. They found that aMCI group had lower synchronization values than control groups in parietal delta and beta2 bands, temporal delta and beta2 bands, and occipital theta and beta2 bands significantly (Cui et al. 2014).

In this chapter, an example of analyzing the epileptic data is used to illustrate the application of CMA method. The multiple field potentials (MFP) were recorded, in vitro, from the CA1 region of the hippocampus. Transverse hippocampal slices (400 μm) were prepared from male Sprague-Dawley rats (150–300 g). Spontaneous seizure-like events were induced by perfusion with low-calcium, high-potassium artificial cerebrospinal fluid consisting of (in mM) 125NaCl, 26$NaHCO_3$, 5KCl, 0.2$CaCl_2$, 1.0$MgCl_2$, 1.25NaH_2PO_4, and10 glucose, bubbled with 95%O_2-5%CO_2 mixture. Extracellular field potentials were recorded using nine Pt/Ir wire electrodes (25 μm in diameter), positioned individually on the surface of stratum pyramidale along the long axis of CA1. The spacing of adjacent electrodes was about 200 μm. Signals were amplified ($\times$500), low-pass filtered (3 kHz), and digitized with sampling frequency of 2.5 kHz (Li et al. 2007).

The signal waveform is shown in Fig. 12.1. The data length is 40s. The different states in epilepsy seizures are shown in Fig. 12.1. Rat data in vitro slicing is very clear, noise and delay are small, and so the simple cross correlation method is selected to construct the synchronization matrix. Surrogate data are obtained by

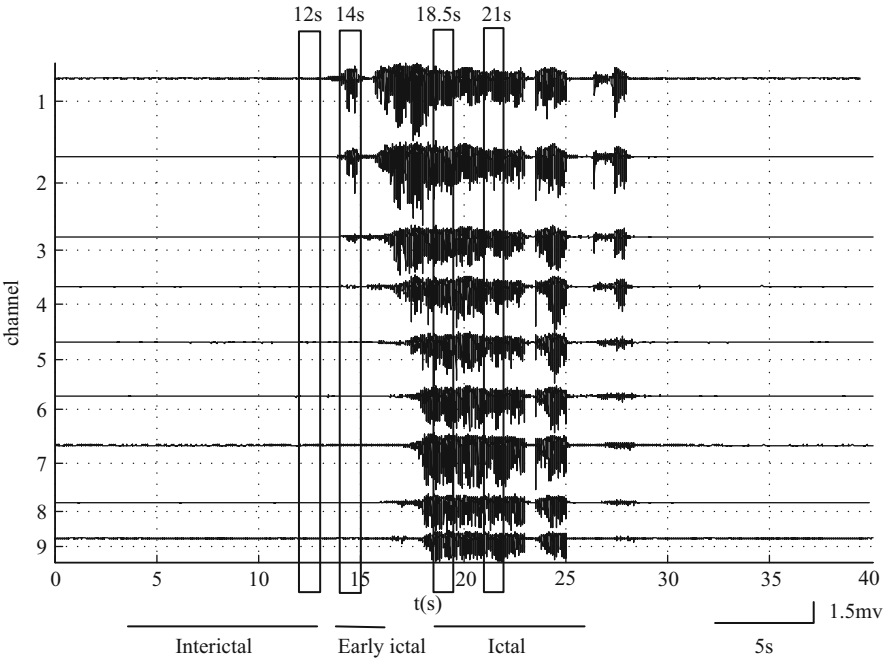

Fig. 12.1 Multiple field potential recordings of nine channels. The different stages including interictal state, pre-ictal state, and ictal state in epilepsy seizures are shown

using the AAFT method. After repeating 50 times, the surrogate eigenvalues and their mean values are obtained.

In order to analyze epileptic seizures synchronizing characteristics and typical correlation structure at different stages in detail, we extract and analyze the 1 s EEG data recording at interictal state (12 s), pre-ictal state (14 s) and ictal state 1 (18.5 s), and ictal state 2 (21 s). Data waveform, correlation matrix, data eigenvalues, and surrogate eigenvalues of correlation matrix at the four states are displayed, respectively, in Fig. 12.2. During the interictal state (Fig. 12.2a), the multichannel field potential performs low-amplitude high-frequency behavior, and the correlation matrix shows no obvious synchronization, also any significant eigenvalue. The global synchronization index of interictal state is 0.0019.

During the pre-ictal state of epileptic seizures (Fig. 12.2b), the high-amplitude rhythmic activity is clearly visible on former several channels. The synchronization matrix shows a synchronization cluster composed of the channels 1–4. The biggest eigenvalue of data correlation significantly exceeds the means of surrogate eigenvalues. The GSI of pre-ictal state is 0.181. 1–4 channels can be thought as the main area that causes seizures.

Figure 12.2c, d show two different correlation structures in epileptic ictal state. High-amplitude activity and two significant eigenvalues are shown at both ictal states. GSI is 0.2314 and 0.2535, respectively. The synchronization is more obvious

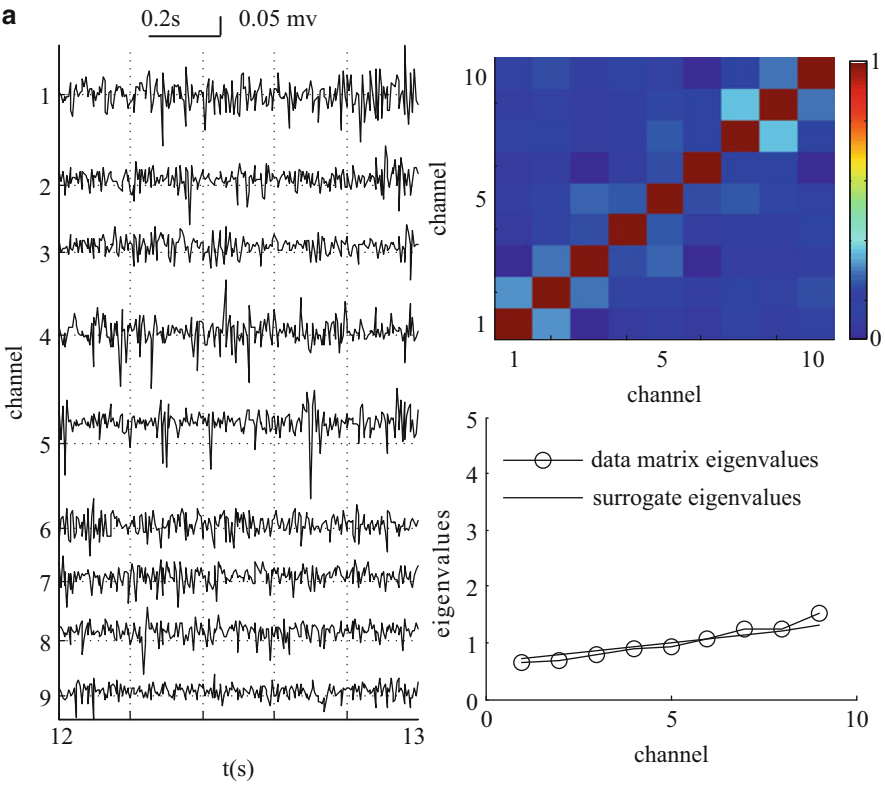

Fig. 12.2 The signal waveform and correlation structure during the different ictal states: (**a**) interictal state, (**b**) pre-ictal state, (**c**) ictal state 1, and (**d**) ictal state 2

than the interictal and pre-ictal stage. The two different correlation matrixes show different synchronization clusters, which show the propagation of epilepsy.

In order to trace the synchronization of the MFP series over time, a moving window technique is applied. The width of the moving window is 1 s with the overlap of 0.5 s. Figure 12.3a shows the number of clusters that varies at different state. There is zero or one cluster during interictal state, but two or three clusters during the pre-ictal and ictal stage and one or two clusters during late ictal stage. Figure 12.3b shows GSI changes over time. The GSI values obviously increase from interictal to ictal state, which showed greater synchronization at ictal state. Figure 12.3c, d show the first and second participation index PI9 and PI8. The red color indicates the greater PI values, and blue indicates smaller values. The former channels and latter channels form two different synchronization clusters at the ictal state, and the strengths of the two synchronization clusters alternate, which show the propagation of epilepsy.

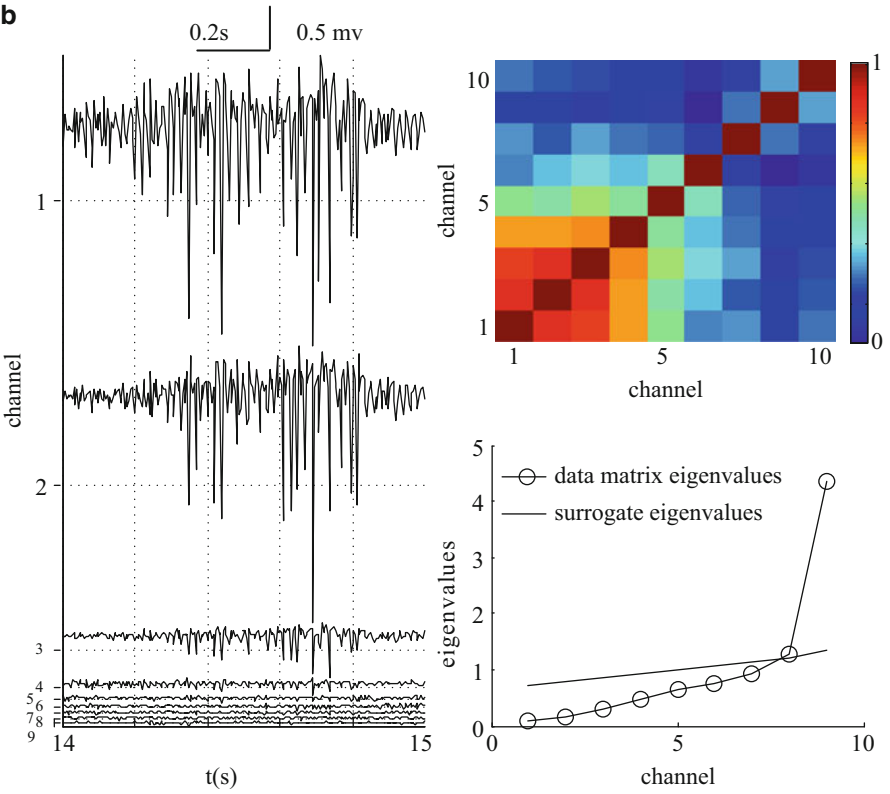

Fig. 12.2 (continued)

Omega complexity was applied to help early diagnosis of Alzheimer's disease. Results showed that omega complexity showed significantly higher values than the control group. The omega complexity values were highly correlated with the Mini-Mental State Examination scores and the full IQ and performance IQ scores of the Japanese Wechsler Adult Intelligence Scale-Revised (Yoshimura et al. 2004).

Complex network analysis has been used in the study of models of neural networks, anatomical connectivity, and functional connectivity based upon fMRI, EEG, and MEG. There is also increasing evidence that various types of brain disease such as Alzheimer's disease, schizophrenia, brain tumors, and epilepsy may be associated with deviations of the functional network topology from the optimal small-world pattern (Stam et al. 2007; Ponten et al. 2007; Ferri et al. 2007; Stam and Reijneveld 2007; Jamal et al. 2015). Kim et al. applied SL-based graph theoretic analysis over the electrode array to assess network properties. They found that the clustering coefficient and global efficiency were decreased in bipolar disorder (BD) patients, whereas the characteristic path length increased, and the normalized

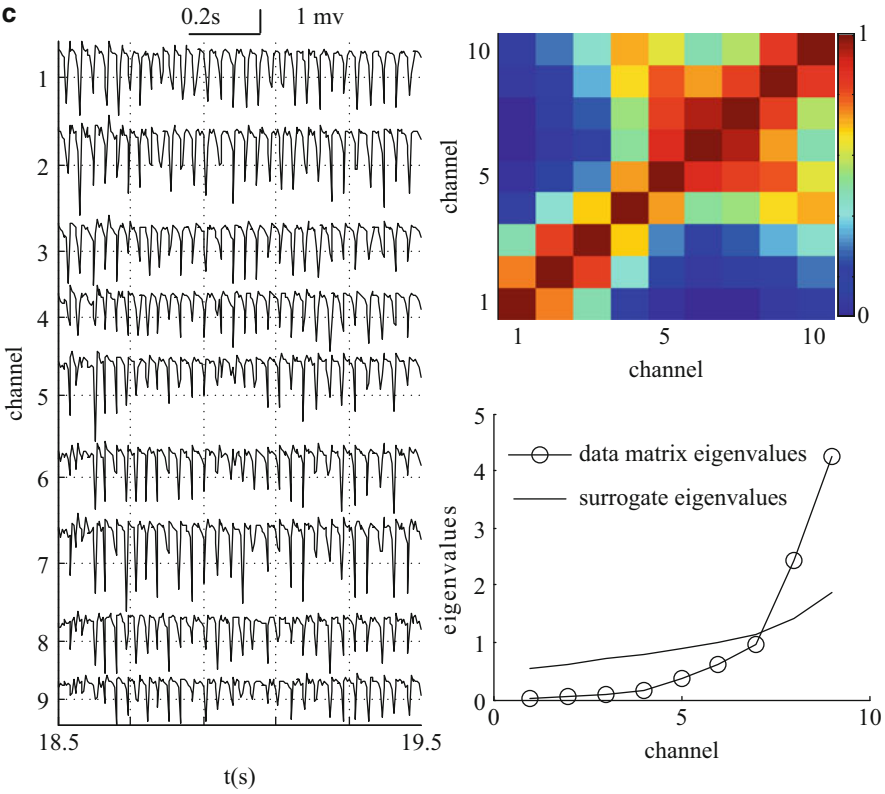

Fig. 12.2 (continued)

characteristic path length and small worldness were significantly correlated with depression scores in BD patients (Kim et al. 2013).

12.4 Conclusions

Synchronization is an important feature for communication in the brain. Multivariate synchronization algorithms provide us a new and global perspective to understand the synchronization mechanism, whether it is in the normal human brain cognitive state or under pathological conditions.

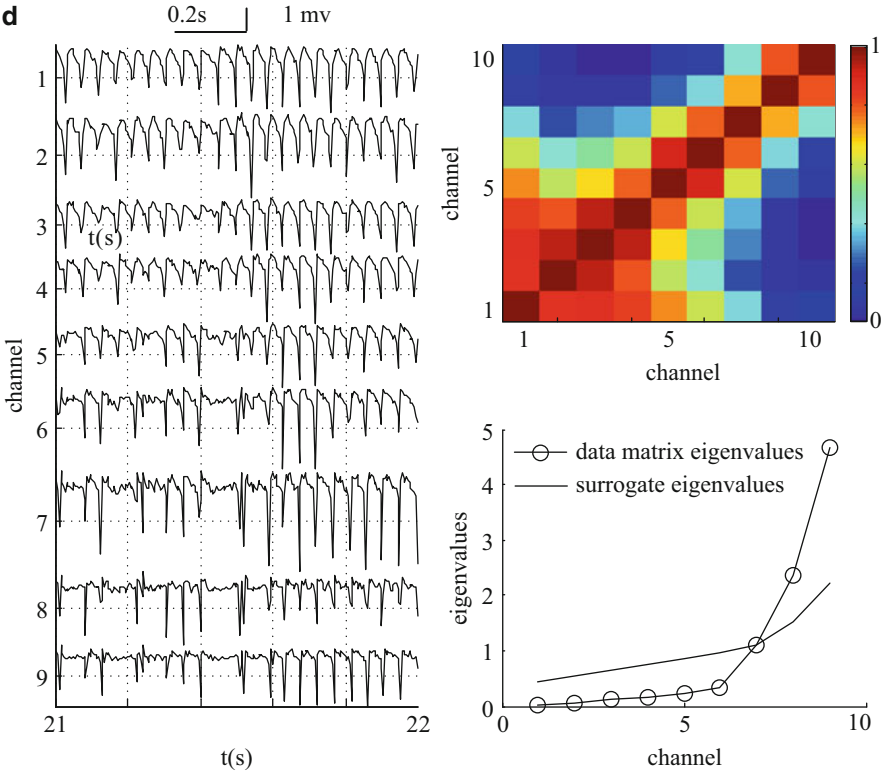

Fig. 12.2 (continued)

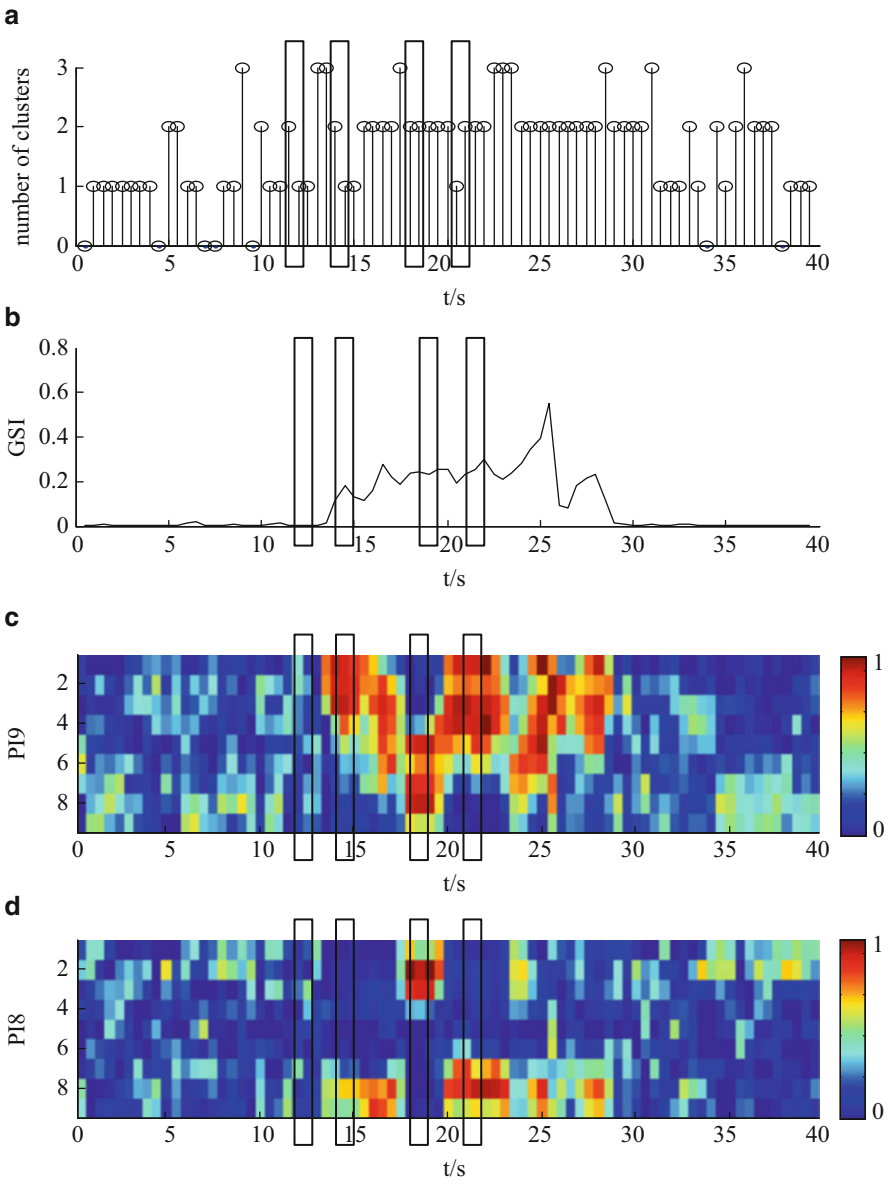

Fig. 12.3 (**a**) The number of synchronization clusters, (**b**) GSI values, (**c**) PI9, (**d**) PI8 during the different ictal states

References

Abarbanel HDI, Rulkov NF, Sushchik MM. Generalized synchronization of chaos: the auxiliary system approach. Phys Rev E Stat Phys Plasmas Fluids Relat Interdiscip Topics. 1996;53(5):4528–35.

Albo Z, Di Prisco GV, Chen Y, et al. Is partial coherence a viable technique for identifying generators of neural oscillations? Biol Cybern. 2004;90(5):318–26.

Allefeld C, Kurths J. An approach to multivariate phase synchronization analysis and its application to event-related potentials: synchronization cluster analysis. Int J Bifurcation Chaos. 2004;14:417–26.

Allefeld C, Müller M, Kurths J. Eigenvalue decomposition as a generalized synchronization cluster analysis. Int J Bifurcation Chaos. 2007;17(10):3493–7.

Arnhold J, Lehnertz K, Grassberger P, et al. A robust method for detecting interdependences: application to intracranially recorded EEG. Physica D Nonlinear Phenomena. 1999;134(4):419–30.

Astolfi L, Cincotti F, Mattia D, et al. Causality estimates among brain cortical areas by partial directed coherence: simulations and application to real data. Int J Bioelectromagnetism. 2005;7(1):1–4.

Babiloni C, Ferri R, Binetti G, et al. Directionality of EEG synchronization in Alzheimer's disease subjects. Neurobiol Aging. 2009;30(1):93–102.

Baccalá LA, Sameshima K. Overcoming the limitations of correlation analysis for many simultaneously processed neural structures. Prog Brain Res. 2001a;130(1):33–47.

Baccalá LA, Sameshima K. Partial directed coherence: a new concept in neural structure determination. Biol Cybern. 2001b;84(6):463–74.

Bendat JS, Piersol AG. Random data analysis and measurement procedures. Mea Sci Technol. 2000;11(12):1825–6.

Bhattacharya J, Petsche H, Pereda E. Long-range synchrony in the gamma band: role in music perception. J Neurosci Off J Soc Neurosci. 2001;21(16):6329–37.

Bialonski S, Lehnertz K. Identifying phase synchronization clusters in spatially extended dynamical systems. Phys Rev E Stat Nonlin Soft Matter Phys. 2006;74(5 Pt 1):051909.

Boccaletti S, Kurths J, Osipov G, et al. The synchronization of chaotic systems. Phys Rep. 2002;366:1–101.

Breakspear M, Terry JR. Topographic organization of nonlinear interdependence in multichannel human EEG. Neuroimage. 2002;16(3 Pt 1):822–35.

Brovelli A, Ding M, Ledberg A, et al. Beta oscillations in a large-scale sensorimotor cortical network: directional influences revealed by Granger causality. Proc Natl Acad Sci U S A. 2004;101(26):9849–54.

Bruns A. Fourier-, Hilbert- and wavelet-based signal analysis: are they really different approaches? J Neurosci Methods. 2004;137:321–32.

Büchel C, Friston K. Assessing interactions among neuronal systems using functional neuroimaging. Neural Netw. 2000;13(8):871–82.

Buzsáki G. Large-scale recording of neuronal ensembles. Nat Neurosci. 2004;7(5):446–51.

Buzsáki G, Draguhn A. Neuronal oscillations in cortical networks. Science. 2004;304(1):1926–9.

Carmeli C, Knyazeva MG, Innocenti GM, et al. Assessment of EEG synchronization based on state-space analysis. Neuroimage. 2005;25(2):339–54.

Clifford Carte G. Coherence and time delay estimation. Proc IEEE. 1987;75(2):236–55.

Cohen MI, Yu Q, Huang WX. Preferential correlations of a medullary neuron's activity to different sympathetic outflows as revealed by partial coherence analysis. J Neurophysiol. 1995;74(1):474–8.

Cui D, Liu XZ, Wan Y, et al. Estimation of genuine and random synchronization in multivariate neural series. Neural Netw. 2010;23:698–704.

Cui D, Liu J, Bian Zh J, et al. Cortical source multivariate EEG synchronization analysis on amnestic mild cognitive impairment in type 2 diabetes. Scientific World Journal. 2014;523216:1–9.

Darbellay GA, Vajda I. Estimation of the information by an adaptive partitioning of the observation space. IEEE Trans Inf Theory. 1999;45(4):1315–21.
David O, Cosmelli D, Lachaux JP, et al. A theoretical and experimental introduction to the non-invasive study of large-scale neural phase synchronization in human beings. Int J Comput Cogn. 2003;1(4):53–77.
Ding M, Bressler SL, Yang W, et al. Short-window spectral analysis of cortical event-related potentials by adaptive multivariate autoregressive modeling: data preprocessing, model validation, and variability assessment. Biol Cybern. 2000;83:35–45.
Engel AK, Fries P, Singer W. Dynamic predictions: oscillations and synchrony in top-down processing. Nat Rev Neurosci. 2001;2(10):704–16.
Fanselow EE, Sameshima K, Baccala LA, et al. Thalamic bursting in rats during different awake behavioral states. Proc Natl Acad Sci. 2001;98(26):15330–5.
Ferri R, Rundo F, Bruni O, et al. Small-world network organization of functional connectivity of EEG slow-wave activity during sleep. Clin Neurophysiol Off J Int Fed ClinNeurophysiol. 2007;118(2):449–56.
Fine AS, Nicholls DP, Mogul DJ. Assessing instantaneous synchrony of nonlinear nonstationary oscillators in the brain. J Neurosci Methods. 2010;186(1):42–51.
Friston KJ. The labile brain. I. Neuronal transients and nonlinear coupling. Philos Trans Royal Soc Lond. 2000;355(1394):215–36.
Gandrzejak R, Kraskov A, Stögbauer H, et al. Bivariate surrogate techniques: necessity, strengths, and caveats. Phys Rev E Stat Nonlin Soft Matt Phys. 2003;68:1855–62.
Gersch W, Goddard GV. Epileptic focus location: spectral analysis method. Science. 1970;169(3946):701–2.
Gevins AS, Schaffer RE. A critical review of electroencephalographic (EEG) correlates of higher cortical functions. Crit Rev Bioeng. 1980;4(2):112–64.
Granger CWJ. Investigating causal relations by econometric models and cross-spectral methods. Econometrica. 1969;37:424–38.
Granger CWJ. Testing for causality: a personal viewpoint. J Econ Dyn Control. 1980;2(1):329–52.
Haig AR, Gordon E, Wright JJ, et al. Synchronous cortical gamma-band activity in task-relevant cognition. Neuroreport. 2000;11(4):669–75.
Haufe S, Nikulin VV, Müller KR, et al. A critical assessment of connectivity measures for EEG data: a simulation study. Neuroimage. 2013;64:120–33.
Jalili M, Lavoie S, Deppen P, et al. Disconnection topography in schizophrenia revealed with state-space analysis of EEG. PLoS One. 2007;2(10):e1059.
Jamal W, Das S, Maharatna K, et al. Brain connectivity analysis from EEG signals using stable phase-synchronized states during face perception tasks. Physica A. 2015;434:273–95.
Kamiński MJ, Blinowska KJ. A new method of the description of the information flow in the brain structures. Biol Cybern. 1991;65(3):203–10.
Kim CS, Bae CS, Tcha HJ. A phase synchronization clustering algorithm for identifying interesting groups of genes from cell cycle expression data. BMC Bioinformatics. 2008;9(1):56.
Kim DJ, Bolbecker AR, Howell J, et al. Disturbed resting state EEG synchronization in bipolar disorder: a graph-theoretic analysis. NeuroImage Clin. 2013;2:414–23.
Knyazeva MG, Innocenti GM, Carmeli C, et al. Assessment of EEG synchronization based on state-space analysis. Neuroimage. 2005;25(2):339–54.
Kocsis B, Bragin A, Buzsáki G. Interdependence of multiple theta generators in the hippocampus: a partial coherence analysis. J Neurosci Off J Soc Neurosci. 1999;19(14):6200–12.
Kramer MA, Edwards E, Soltani M, et al. Synchronization measures of bursting data: application to the electrocorticogram of an auditory event-related experiment. Phys Rev E Stat Nonlin Soft Matter Phys. 2004;70:127–50.
Kraskov A, Stőgbauer H, Grassberger P. Estimating mutual information. Phys Rev E Stat Nonlin Soft Matter Phys. 2004;69:279–307.
Kus R, Kaminski M, Blinowska KJ. Determination of EEG activity propagation: pair-wise versus multichannel estimate. IEEE Trans Bio-Med Eng. 2004;51(9):1501–10.

Lachaux J, Rodriguez E, Martinerie J, et al. Measuring phase synchrony in brain signals. Hum Brain Mapp. 1999;8(4):194–208.

Lawrence W. Synchronous neural oscillations and cognitive processes. Trends Cogn Sci. 2003;7(12):553–9.

Le Van Quyen M. Disentangling the dynamic core: a research program for a neurodynamics at the large scale. Biol Res. 2003;36:61–82.

Lee SH, Park YM, Kim DW, et al. Global synchronization index as a biological correlate of cognitive decline in Alzheimer's disease. Neurosci Res. 2010;66(4):333–9.

Li XL, Cui D, Jiruska P, et al. Synchronization measurement of multiple neuronal populations. Neurosci Lett. 2007;98(6):3341–8.

Liberati D, Cursi M, Locatelli T, et al. Total and partial coherence analysis of spontaneous and evoked EEG by means of multi-variable autoregressive processing. Med Biol Eng Comput. 1997;35(35):124–30.

Lopes da Silva FH, Vos JE, Mooibroek J, et al. Relative contributions of intracortical and thalamocortical processes in the generation of alpha rhythms, revealed by partial coherence analysis. Electroencephalogr Clin Neurophysiol. 1980;50:449–56.

Lytton WW. Computer modelling of epilepsy. Nat Rev Neurosci. 2008;9(8):626–37.

Mckenna TM, Mcmullen TA, Shlesinger MF. The brain as a dynamic physical system. Neuroscience. 1994;60(3):587–605.

Micheloyannis S, Pachou E, Stam CJ, et al. Using graph theoretical analysis of multi channel EEG to evaluate the neural efficiency hypothesis. Neurosci Lett. 2006;402(3):273–7.

Min BC, Jin SH, Kang IH, et al. Analysis of mutual information content for EEG responses to odor stimulation for subjects classified by occupation. Chem Senses. 2003;28(9):741–9.

Mirski MA, Tsai YC, Rossell LA, et al. Anterior thalamic mediation of experimental seizures: selective EEG spectral coherence. Epilepsia. 2003;44(3):355–65.

Mormann F, Lehnertz K, David P, et al. Mean phase coherence as a measure for phase synchronization and its application to the EEG of epilepsy patients. Physica D Nonlinear Phenomena. 2000;144:358–69.

Müller M, Baier G. Detection and characterization of changes of the correlation structure in multivariate time series. Phys Rev E. 2005;71:046116.

Müller M, Lopez Y, Rummel C, et al. Localized short-range correlations in the spectrum of the equal-time correlation matrix. Phys Rev E Stat Nonlin Soft Matter Phys. 2006a;74:159–63.

Müller M, Wegner K, Kummer U, et al. Quantification of cross correlations in complex spatiotemporal systems. Phys Rev E Stat Nonlin Soft Matter Phys. 2006b;73:046106.

Osipov GV, Kurths J. Regular and chaotic phase synchronization of coupled circle maps. Phys Rev E. 2001;65:016216.

Osipov GV, Pikovsky AS, Rosenblum MG, et al. Phase synchronization effects in a lattice of nonidentical Rössler oscillators. Phys Rev E Stat Nonlin Soft Matter Phys. 1997;55(3):2353–61.

Palus M, Stefanovska A. Direction of coupling from phases of interacting oscillators: an information-theoretic approach. Phys Rev E Stat Nonlin Soft Matter Phys. 2003;67:055201.

Pereda E, Quiroga EQ, Bhattacharya J. Nonlinear multivariate analysis of neurophysiological signals. Prog Neurobiol. 2005;77:1–37.

Pikovsky AS, Rosenblum MG, Kurths J. Synchronization in a population of globally coupled chaotic oscillators. Epl. 1996;34(3):165–70.

Pikovsky A, Rosenblum M, Kurths J. Synchronization: a universal concept in nonlinear sciences. Am J Phys. 2001;70(6):655–5.

Ponten SC, Bartolomei F, Stam CJ. Small-world networks and epilepsy: graph theoretical analysis of intracerebrally recorded medial temporal lobe seizures. Clin Neurophysiol. 2007;118(4):918–27.

Quian Quiroga R, Arnhold J, Grassberger P. Learning driver-response relationships from synchronization patterns. Phys Rev E Stat Phys Plasmas Fluids Relat Interdiscip Topics. 2000;61:5142–8.

Quian Quiroga R, Kraskov A, Kreuz T, et al. Performance of different synchronization measures in real data: a case study on electroencephalographic signals. Phys Rev E. 2002;65:041903.
Rodriguez E, George N, Lachaux JP, et al. Perception's shadow: long-distance synchronization of human brain activity. Nature. 1999;397(6718):430–3.
Rosenblum MG, Pikovsky AS, Kurths J. Phase synchronization of chaotic oscillators. Phys Rev Lett. 1996;1(11):1804–7.
Rosenblum M, Pikovsky A, Kurths J. Phase synchronization: from theory to data analysis. Handb Biol Phys. 2001;4:93–4.
Rosso OA, Blanco S, Yordanova J, et al. Wavelet entropy: a new tool for analysis of short duration brain electrical signals. J Neurosci Methods. 2001;105(1):65–75.
Rulkov NF, Sushchik MM, Tsimring LS, et al. Generalized synchronization of chaos in directionally coupled chaotic systems. Phys Rev E Stat Phys Plasmas Fluids Relat Interdiscip Topics. 1995;51(2):980–94.
Sameshima K, Baccalá LA. Using partial directed coherence to describe neuronal ensemble interactions. J Neurosci Methods. 1999;94(1):93–103.
Schelter B, Winterhalder M, Eichler M, et al. Testing for directed influences among neural signals using partial directed coherence. J Neurosci Methods. 2005;152:210–9.
Schelter B, Winterhalder M, Hellwig B, et al. Direct or indirect? Graphical models for neural oscillators. J Physiol Paris. 2006;99(1):37–46.
Schiff SJ, So P, Chang T, et al. Detecting dynamical interdependence and generalized synchrony through mutual prediction in a neural ensemble. Phys Rev E Stat Phys Plasmas Fluids Relat Interdiscip Topics. 1996;54(6):6708–24.
Schmitz A. Measuring statistical dependence and coupling of subsystems. Phys Rev E Stat Phys Plasmas Fluids Relat Interdiscip Topics. 2000;62:7508–11.
Schreiber T, Schmitz A. Improved surrogate data for nonlinearity tests. Phys Rev Lett. 1996;77(4):635–8.
Seba P. Random matrix analysis of human EEG data. Phys Rev Lett. 2003;91(19):198104.
Shabunin A, Demidov V, Astakhov V, et al. Information theoretic approach to quantify complete and phase synchronization of chaos. Phys Rev E. 2002;65:634–4.
Shannon CE. A mathematical theory of communication. Bell Syst Technic J. 1948;27(3):379–423.
Stam CJ, Reijneveld JC. Graph theoretical analysis of complex networks in the brain. Nonlinear Biomed Phys. 2007;1(1):3.
Stam CJ, van Dijk BW. Synchronization likelihood: an unbiased measure of generalized synchronization in multivariate data sets. Physica D Nonlinear Phenomena. 2002;163:236–51.
Stam CJ, Jones BF, Nolte G, et al. Small-world networks and functional connectivity in Alzheimer's disease. Cereb Cortex. 2007;17(1):92–9.
Steuer R, Kurths J, Daub CO, et al. The mutual information: Detecting and evaluating dependencies between variables. Bioinformatics. 2002;18:231–40.
Sun FT, Miller LM, D'Esposito M. Measuring interregional functional connectivity using coherence and partial coherence analyses of fMRI data. Neuroimage. 2004;21(2):647–58.
Tass P, Rosenblum MG, Weule J, et al. Detection of n: m phase locking from noisy data: application to magnetoencephalography. Phys Rev Lett. 1998;81:3291–4.
Thuraisingham RA. A new method using coherence to obtain the model order in the evaluation of partial directed coherence. Comput Biol Med. 2007;37(9):1361–5.
Traub RD, Spruston N, Soltesz I, et al. Gamma-frequency oscillations: a neuronal population phenomenon, regulated by synaptic and intrinsic cellular processes, and inducing synaptic plasticity. Prog Neurobiol. 1998;55(6):563–75.
Tucker DM, Roth DL, Bair TB. Functional connections among cortical regions: topography of EEG coherence. Electroencephalogr Clin Neurophysiol. 1986;63(3):242–50.
Van Albada SJ, Robinson PA. Mean-field modeling of the basal ganglia-thalamocortical system. I: firing rates in healthy and parkinsonian states. J Theor Biol. 2009;257(4):642–63.
Van Albada SJ, Gray RT, Drysdale PM, et al. Mean-field modeling of the basal ganglia-thalamocortical system. II: dynamics of parkinsonian oscillations. J Theor Biol. 2009;257(4):664–88.

Van Putten MJAM. Proposed link rates in the human brain. J Neurosci Methods. 2003;127(1):1–10.
Varela F, Lachaux JP, Rodriguez E, et al. The brainweb: phase synchronization and large-scale integration. Nat Rev Neurosci. 2001;2(4):229–39.
Winterhalder M, Schelter B, Hesse W, et al. Comparison of time series analysis techniques to detect direct and time-varying interrelations in multivariate, neural systems. Signal Process. 2005;85:2137–60.
Winterhalder M, Schelter B, Hesse W, et al. Detection of directed information flow in biosignals. Biomed Tech. 2006;51(5-6):281–7.
Womelsdorf T, Schoffelen JM, Oostenveld R. Modulation of neuronal interactions through neuronal synchronization. Science. 2007;316(5831):1609–12.
Wu MH, Frye RE, Zouridakis G. A comparison of multivariate causality based measures of effective connectivity. Comput Biol Med. 2011;41:1132–41.
Xu JW, Bakardjian H, Cichocki A, et al. A new nonlinear similarity measure for multichannel signals. Neural Netw Off J Int Neural Netw Soc. 2008;21:222–31.
Yoshimura M, Isotani T, Yagyu T, et al. Global approach to multichannel electroencephalogram analysis for diagnosis and clinical evaluation in mild Alzheimer's disease. Neuropsychobiology. 2004;49(3):163–6.

Chapter 13
Cross-Frequency Coupling in Neural Oscillations

Juan Wang and Xiaoli Li

13.1 Introduction

Electrophysiology is typically described in terms of rhythmic activity. The rhythmic activity is divided into bands by frequency, known as delta (<4 Hz), theta (4–7 Hz), alpha (8–13 Hz), beta (13–30 Hz), and gamma (>30 Hz). Within the brain network research, a general principle of the functional role of oscillations in various frequency bands was considered—slow oscillations (e.g., delta/theta) are involved in further distance information transformation, and fast oscillation (e.g., alpha/beta/gamma) are more likely to be restricted to local circuits (Moran and Hong 2011). Many known brain functions are associated with activities from different brain regions; it is natural to spur researchers to investigate the cross-frequency coupling between different frequency oscillations.

Previous studies have proposed some theories to model the interaction between the slow and fast oscillations, and they formed based on perspectives of either network or coding. The former one suggested that fast oscillations synchronize cell assemblies over relatively short spatial scales representing functional networks while slow oscillations synchronize network over long distances; the integration of different functional networks or spatial integration involved slower oscillations (von Stein and Sarnthein 2000; Buzsaki and Draguhn 2004). The latter assumed that slow

J. Wang
Center for Cognitive Neuroscience, Neuroscience and Behavioral Disorders Program, Duke-NUS Medical School, Singapore, Singapore

X. Li (✉)
State Key Laboratory of Cognitive Neuroscience and Learning & IDG/McGovern Institute for Brain Research, Beijing Normal University, Beijing 100875, China

Center for Collaboration and Innovation in Brain and Learning Sciences, Beijing Normal University, Beijing 100875, China
e-mail: xiaoli@bnu.edu.cn

X. Li (eds.), *Signal Processing in Neuroscience*, DOI 10.1007/978-981-10-1822-0_13

oscillation is a carrier for the fast oscillation as active brain representations involving fast oscillations are encoded at different phase of the slow oscillations (Mc 1959), and it has been supported by some experiments (Lisman and Idiart 1995).

13.2 Background

13.2.1 The Phase of Neural Oscillations

Oscillations can be described in terms of phase, frequency, and amplitude. The phase of neural oscillations represents the timing of neuronal activity (Klimesch et al. 2007). Differences in phase are related to differences in the excitability of neurons and, thus, to differences in the probability of the generation of action potential. A directly founding is that CA1 cells fire when an animal is at a particular place in its environment, and these place cells fire at a particular sequence in time that is related to the phase of the ongoing theta rhythm (O'Keefe and Dostrovsky 1971). Not only in animal studies, but also in many human event-related potential (ERP) studies, the phase reset is an important mechanism of brain cognitive function (Hanslmayr et al. 2007; Yin Fen and Daniel 2009).

13.2.2 The Amplitude of Neural Oscillation

The amplitude of neural oscillation plays an important role in characterization of the extent of task involvement (Klimesch et al. 2007). Large amplitudes reflect a pronounced influence of an oscillation for a certain kind of neural process that is related to certain aspects in the processing of a task. Small amplitudes reflect minimal involvement in processing of a task. It is important to emphasize that the influence of amplitude also is related to the timing of neural activity.

13.3 Cross-Frequency Coupling Methods Review

According to the wording of "cross-frequency coupling," the oscillations in a lower and a higher frequency band consequently were involved in the interaction process. How do the oscillations in these frequency bands interact?

Recently, three types of cross-frequency interaction, including power-to-power, phase-to-phase, phase-to-frequency, and phase-to-power were involved in brain mechanism investigation. Previous studies have done neurophysiological research by estimating the above analysis. However, according to Canolty et al. (Canolty

et al. 2006), the phase-to-power coupling, also named as phase-amplitude coupling (PAC), is sensible from a physiological perspective. They argued that, if high-frequency oscillations in a network are modulated by the low-frequency oscillations and the low-frequency oscillation is produced from the network or another network, the excitability and the dynamics of the cells producing high-frequency oscillations in the network can be guaranteed by the low-frequency oscillations phase modulation even if there are no fluctuations in the low-frequency oscillations. The above inference has been supported by the network model which occurred in slow and fast GABAergic feedback (White et al. 2000).

Recently, much neurophysiological research has revealed that the PAC between slow and fast oscillations is involved in the cognitive processes, such as memory processes (Canolty et al. 2006; Jensen and Colgin 2007) and speech perception (Wang et al. 2014). PAC can be used a marker for clinical diagnosis of memory-related psychiatric disorders (Jelic and Kowalski 2009). In these studies, the cognitive model, allowing for top-down modulation of bottom-up sensory inputs, is involved in the information process in the brain. Brain oscillation has typically been divided into specific frequency ranges that are associated with different cognitive processes. Indeed, previous studies have suggested that feed-forward bottom-up information is indexed through high-frequency cortical activity (above 30 Hz), whereas top-down feedback information is marked by low-frequency cortical activity (Wang 2010; Arnal et al. 2011). There is growing evidence that perception involves the coordination of slow and fast brain oscillations, typically theta-gamma coupling (Buzsaki and Draguhn 2004; Canolty et al. 2006). How oscillations in low- and high-frequency bands interact with each other has received an increasing amount of attention in recent years, and a number of methods have been developed to measure the PCA.

In order to estimate the coupling strength between the high- and low-frequency oscillations, the corresponding components should be extracted from the brain neuronal activity. In this step, the band-filter, Hilbert transform, and complex wavelet methods were commonly used. When the phase of neural oscillations was analyzed, the two-way, least-squared finite impulse response filter (e.g., eegfilt.m included in EEGLAB toolbox (Delorme and Makeig 2004)) was used to avoid distortions of the phase value during filtering. Then, the Hilbert transform was performed to compute the phase time series and amplitude envelope time series corresponding low- and high-frequency oscillations. The next step was to estimate the coupling strength between the high- and low-frequency oscillations. According to the present research, four types of method have been proposed.

We firstly review the method based on quantization of the phase-amplitude distribution (Tort et al. 2010), and this method can be briefly described as follows. Step 1: A complex-valued signal composited by phase time series of low-frequency oscillations and amplitude time series of high-frequency oscillations was constructed as $[\phi_L(n), a_H(n)]$. Step 2: The phase time series ϕ_L was binned into M intervals, and the mean amplitude $\langle a_H \rangle_{\phi_L}(j)$ in each bin $(p(j), j = 1, 2, \ldots, M)$ was derived, and the phase-amplitude distribution was constructed. Step 3: The normalized values were obtained by dividing each bin value by sum across all bins. Step 4: The

asymmetry degree of the distribution was estimated as the mutual information shared by phase and amplitude time series, and this parameter was defined as the coupling strength between the low-frequency phase and high-frequency amplitude as follows: $MI_{KL} = \frac{\log(M)-H}{\log(M)}$, in which $H = \sum_{j=1}^{M} p(j) \log [p(j)]$.

The second method is based on the average vector length of the composite signals (Canolty et al. 2006). Similarly, a complex-valued signal $z(n) = a_H(n)e^{i\phi_L(n)}$ composited by phase time series of low-frequency oscillations ϕ_L and amplitude time series of high-frequency oscillation a_H is constructed. Then the composite signal takes on some particular values in the complex plane. If the probability density function of the composite signal is not radially symmetric, the phase and the amplitude time series will share mutual information, or the distribution of the phase time series will be nonuniform. Accordingly, the degree of asymmetry of the probability density function was estimated by computing the mean of the composite signal as coupling strength between the phase and amplitude time series.

The third method is based on the quantization of the low-frequency oscillation and amplitude from the high-frequency oscillation synchronization. Cohen (2008) and Mormann et al. (2005) have proposed the phase locking value (PLV) estimation; this method computes the two phase time series obtained from the low-frequency oscillation and the envelope of high-frequency oscillation. And another method computes the correlation between low-frequency oscillation and envelope of high-frequency oscillation. Furthermore, Colgin proposed that instead of the low-frequency oscillation, using its cosine transform of phase time series can remove the effect of amplitude from low frequency to the coupling estimation (Colgin et al. 2009).

The fourth method is based on the general linear model to quantify the coupling strength between the low-frequency phase time series and high-frequency amplitude time series (Penny et al. 2008). In this measure, high-frequency amplitude is modeled by a multiple regression, and the design matrix is comprised of three columns, in which these first and second columns correspond to the cosine and sine transforms of low-frequency phase, respectively, and the third column is a column of 1 s. Then the proportion of variance explained by the model is defined as the coupling strength between the low-frequency phase and the high-frequency amplitude.

In actual application, the surrogate method was performed to reduce the effect of artifacts and the marginal distributions of low-frequency phase and the high-frequency amplitude on the above coupling estimation, especially for the first and second method. So we can obtain a set of surrogate coupling estimations. Then raw coupling estimations were normalized by the mean and the standard of the surrogate coupling estimation, and this normalized value was used to estimate the coupling strength between the low-frequency phase and high-frequency amplitude. One way to accomplish this is to shuttle the corresponding time point of the phase and amplitude time series in the composite signal; another way is to randomize the phase or amplitude time series blocks for tasking-state signals; this performance ensures the phase and amplitude time series come from different recording blocks.

Some studies have compared the performance of the above methods. The paper (Penny et al. 2008) performed comparatively overall analysis by using sigmoidal coupling model. In this paper, four variables participated in the comparison, including the coupling strength, noise intensity, the length of signal, and the coupling phase. The result suggested that when the coupling strength changed, the above all methods can distinguish the coupled and uncoupled mode; however, only the first and second type of methods can distinguish the different coupling strength; the second type of method has better noise immunity than the other methods; all methods are sensitive to the signal length, and the surrogate method was recommended to reduce the effect of signal length; lastly, only the envelope-signal correlation method was effected by the coupling phase.

13.4 Application

13.4.1 Data Recording and Analysis

We investigate how the interaction of different brain oscillations (particularly theta-gamma coupling) modulates the bottom-up and top-down processes during speech perception. A speech perception paradigm was employed that manipulated the congruency between a visually presented picture and an auditory stimulus, and participants were asked to judge whether they matched or mismatched. Seventeen children ($N = 17$; 12 female, mean age 10 years 5 months, $SD = 1$ year 2 months) participated in this study, and their electroencephalographic (EEG) data were recorded while performing a picture-word matching task. In each trial, a fixation cross was followed by a picture of an object that appeared on a screen for 1500 ms. While this item remained on the screen, subjects heard an auditory word that either matched or mismatched the picture. They were asked to judge, indicating their response via button press, whether the auditory word matched or mismatched the picture present on the screen. We derived mismatches that were different in tone, onset, rhyme, all segments but not tone, or all segments and tone. The data were amplified at gain of 500 using a SynAmps2 amplifier and filtered online using 50 Hz notch and 0.1–100 Hz band-pass filters. The EEG data were then segmented into epochs spanning from 250 ms pre-stimulus to 3000 ms post-stimulus onset and time locked to the onset of the visual picture stimulus. The detailed description can be seen (Wang et al. 2014).

For the coupling of theta phase and gamma amplitude, briefly, five steps were needed. Step 1: A FIR filter was applied to obtain the real-value band-pass gamma component $x_{fA}(t)$ (see Fig. 13.1b) and theta component $x_{fP}(t)$ (Fig. 13.1c) from epochs $x_{raw}(t)$ (see Fig. 13.1a). Step 2: The amplitude envelope of $A_{fA}(t)$ (see Fig. 13.1f) and phase $\varphi_{fP}(t)$ (see Fig. 13.1g) at each time point was estimated by the Hilbert transform, with values between [0, <2*pi>] radians. Step 3: The phase $\varphi_{fP}(t)$ was binned into eighteen 20° intervals, and the mean $A_{fA}(t)$ in each bin

was derived (see Fig. 13.1h). Step 4: The normalized values $\{p_i, i = 1 \ldots 18\}$ were obtained by dividing each bin value by the sum across all bins; then, the entropy measure H was calculated by $H = -\sum_{i=1}^{n=18} p_i \log p_i$ and normalized by the maximum entropy value $H_{\max}$, defined as MI ($MI = \frac{H_{\max} - H}{H_{\max}}$), in which $H_{\max} = \log n$ (see Fig. 13.1j). To reduce the effect of artifacts on the MI, 100 surrogated MI values were obtained by shuffling trials (see Fig. 13.1i). Step5: The significant threshold $MI_{\text{surr}} = \text{mean} + 1.96 * \text{std}$ ($p < 0.05$) was used to then post-process MI (termed as true MI: MI_{true}) as defined by $MI_{\text{true}} = MI - MI_{\text{surr}}$ (see Fig. 13.1k). Finally, the true MI values were summed together in the frequency bands of 30–70 Hz and 4–8 Hz within the segmented time window of each trial for further analysis (see Fig. 13.1l). An example of theta phase and gamma power modulation in the 1000 ms EEG signal from channel F8 of one subject was given in Fig. 13.1 to demonstrate its flow path of computation process. The normalized time-frequency instantaneous power of the gamma activity was illustrated in Fig. 13.1d, e indicated phase convergence between the theta and gamma activity to a certain extent. In addition, the coupling strength between the oscillations was the highest in the frequency band of 3–8 Hz and the 30–70 Hz, as can be seen in Fig. 13.1l.

For statistical analysis, the mean and the standard deviation of the whole brain for the baseline were used to convert the MI after stimulus into normalized values for each person to eliminate the variance between subjects. In addition, once the coupling strength below the average value of the whole brain, it was marked negatively, while it was marked positively. The MI values were averaged within five brain regions (frontal, parietal, occipital, left temporal, and right temporal). Five time windows (pre-visual ($-250 - 0$ ms), visual_1 (0–1000 ms), visual_2 (500–1500 ms), auditory_1 ($1500 - 2500$ ms), and auditory_2 ($2000 - 3000$ ms)) were chosen for further analysis. To investigate the role of each brain region at different time windows during the visual stimulus interval, a two-way repeated measures analysis of variance (ANOVA) with the factors Brain Region (frontal, parietal, occipital, left temporal, right temporal) and Time Window (pre-visual, visual_1, visual_2) was applied. A similar two-way repeated ANOVA analysis with the factors Brain Region (the same 5 regions as the above) and Time Window (auditory_1, auditory_2) was also applied to the auditory stimulus interval. In addition, a three-way repeated measures ANOVA was performed during the auditory interval with the factors Condition (2 conditions: match and mismatch), Brain Region (the same 5 regions as the above), and Time Window (2 windows: $1500 - 2500$ ms, $2000 - 3000$ ms) used to investigate the condition effect according to brain region and time. Post-hoc two-tailed t-tests were used to compare different brain areas, time windows, or conditions when a simple effect was significant. The Bonferroni correction was applied to correct for multiple comparisons.

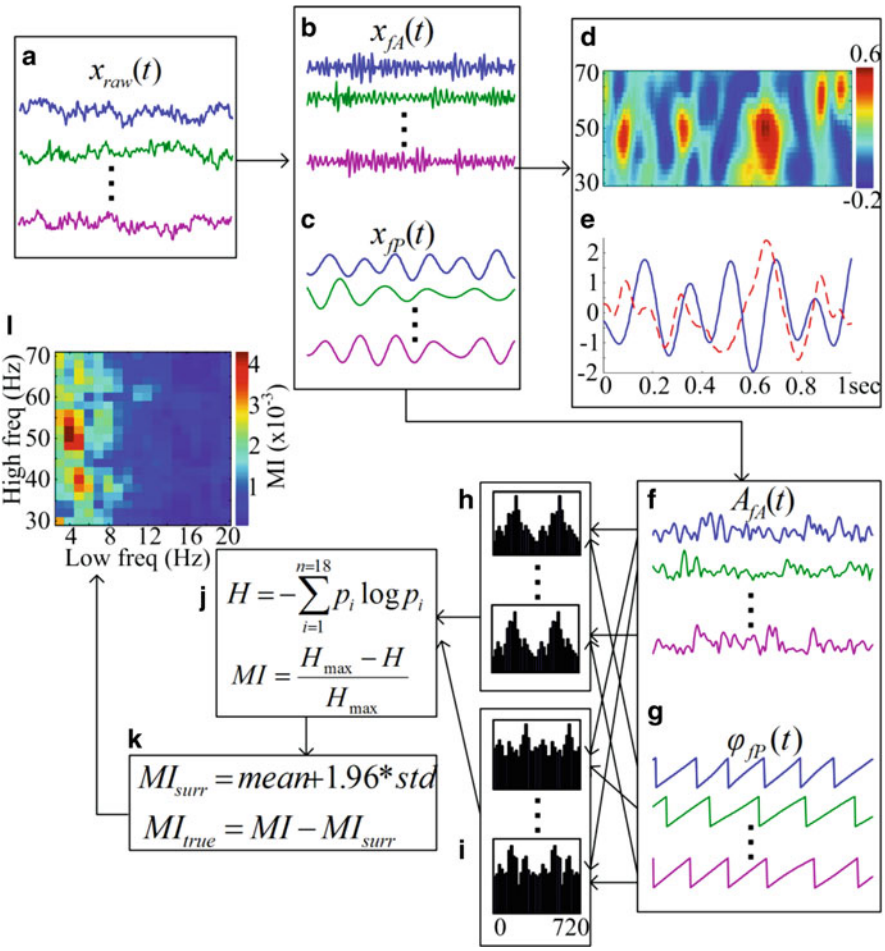

Fig. 13.1 Steps in the computation of the modulation index (*MI*). The raw signals (**a**) were filtered at the amplitude (**b**) and phase (**c**) frequency ranges of interest. The spectral distribution of the high-frequency component was illustrated in (**d**), and the relation of the gamma envelope (*red*) and the theta component (*blue*) was shown in plot (**e**). Next, the gamma amplitude (**f**) and the theta phase (**g**) time series were calculated from the filtered signals by using the Hilbert transform. Then a composite time series was constructed and used to obtain the mean amplitude values at each 20° phase bin (**h**), and the same calculation was for the surrogate composite time series (**i**). The MI was finally obtained by applying a normalized entropy measure to the mean amplitude vector (**j**). Finally, the significant threshold MI was obtained, and true MI value was defined as the difference between the *MI* and the MIsurr (**k**). The statistically significant modulation plot of low-frequency phase and high-frequency amplitude showed an evident coupling between the oscillation in 3–8 Hz and in 30–70 Hz (**l**)

13.4.2 Results of EEG Data

A two-way repeated measures ANOVA on the theta-gamma coupling (i.e., *MI* values) revealed significant main effects of Brain Region ($F4,64 = 9.494$, $p < 0.001$) and Time Window ($F2,32 = 4.601$, $p < 0.05$) as well as a significant interaction effect of Brain Region × Time Window ($F8,128 = 3.542$, $p < 0.01$).

To further understand the interaction effect, an analysis of the simple main effects was performed, revealing a significant difference in the level of coupling across the three time windows in the frontal ($F2,32 = 9.06$, $p < 0.01$) and left temporal ($F2,32 = 17.99$, $p < 0.01$) areas but not in the occipital, parietal, and right temporal areas. Further post-hoc t-tests (Fig. 13.2a) showed that the modulation level in the frontal area for the pre-visual interval was significantly lower than for the first time window in the visual interval (pre-visual vs. visual_1: $t16 = -4.764$, $p < 0.003$ Bonferroni corrected). For the left temporal area, the modulation level in the first time window of the visual interval was significantly higher than in the pre-visual interval ($t16 = 4.232$, $p < 0.003$ Bonferroni corrected) as well as in the second time window of the visual interval ($t16 = 6.064$, $p < 0.003$ Bonferroni corrected).

We next examined the theta-gamma phase-amplitude coupling levels during the auditory interval. A two-way repeated measures ANOVA on MI values revealed a significant main effect of Brain Region ($F4,64 = 3.976$, $p = .006$) and a significant interaction of Brain Region × Time Window ($F4,64 = 3.913$, $p < 0.01$). To further understand the interaction effect, an analysis of the simple effect (see Fig. 13.2b) was performed, which showed that the theta-gamma coupling was significantly lower for the first time window compared to the second time window in the frontal ($F1,16 = 6.23$, $p < 0.05$) and occipital areas ($F1,16 = 4.56$, $p < 0.05$). The increase of theta-gamma coupling was mainly driven by match condition in the frontal area while mainly driven by mismatch condition in the occipital area (see Fig. 13.2d). Alternatively, the left temporal area showed significantly higher coupling strength for the first time window compared to the second time window ($F1,16 = 5.60$, $p < 0.05$). The increase of theta-gamma coupling for the first time window in the left temporal area was mainly driven by mismatch condition (see Fig. 13.2c).

To investigate the theta-gamma coupling difference for the match vs. mismatch conditions, a three-way repeated measures ANOVA for MI values was performed, which showed a significant three-way interaction of Condition × Brain Region × Time Window ($F4,64 = 4.218$, $p < 0.01$) and a significant two-way interaction of Condition × Brain area ($F4,64 = 3.742$, $p < 0.01$). An analysis of the simple effect was performed to further understand the three-way interaction effect. As shown in Fig. 13.2c, in the first time window, the theta-gamma coupling in the right temporal region was significantly higher for the match than for the mismatch condition ($F1,16 = 6.44$, $p < 0.05$), and the left temporal region showed significantly higher coupling strength for the mismatch compared to the match condition ($F1,16 = 20.08$, $p < 0.001$), whereas in the second time window, as shown in Fig. 13.2d, a coupling difference between conditions was only shown in the frontal area ($F1,16 = 4.88$, $p < 0.05$).

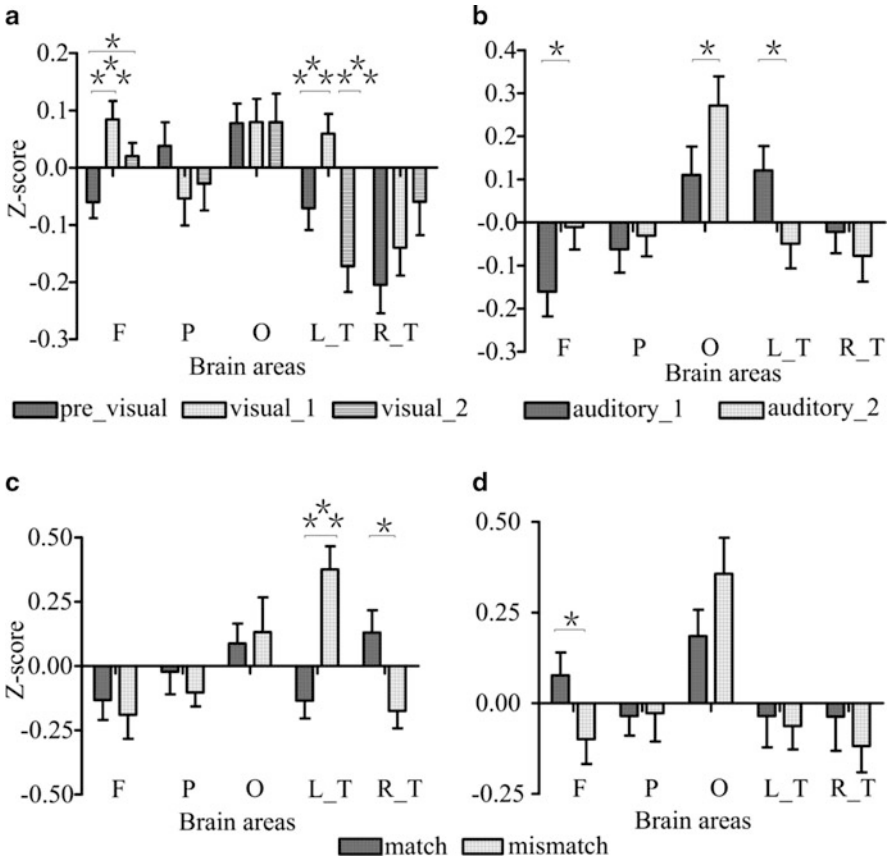

Fig. 13.2 The statistical differences among the brain areas for the pre-auditory interval (**a**) (including pre-visual: −250 − 0 ms, visual_1: 0 − 1000 ms, visual_2: 500–1500 ms) and auditory interval (**b**) (including auditory_1: 1500 − 2500 ms, auditory_2: 2000 − 3000 ms) were given. Then, the statistical differences in theta-gamma coupling levels in different brain areas between the match and mismatch conditions during the auditory_1 (**c**) and auditory_2 (**d**) intervals were presented. The statistical results were reported as the mean Z-score of theta-gamma coupling with respect to the average values across all electrodes. Brain region labels: *F* frontal, *P* parietal, *O* occipital, *L_T* left temporal, *R_T* right temporal (*: $p < 0.05$,***: $p < 0.001$)

As can be seen In Fig. 13.3a, the brain-behavior correlation analysis revealed significantly negative correlation between RT difference and the theta-gamma coupling difference between the match and mismatch conditions in the frontal ($r = -0.5764$, $p = 0.0154$), but not in the left and right temporal areas. However, the RT is negatively correlated with the coupling in the left temporal area for the mismatch condition ($r = -0.547$, $p = 0.023$) (see Fig. 13.3b), but not match condition, while the RT is negatively correlated with the coupling in the right temporal for the match condition ($r = -0.688$, $p = 0.002$) (see Fig. 13.3c), but not mismatch condition.

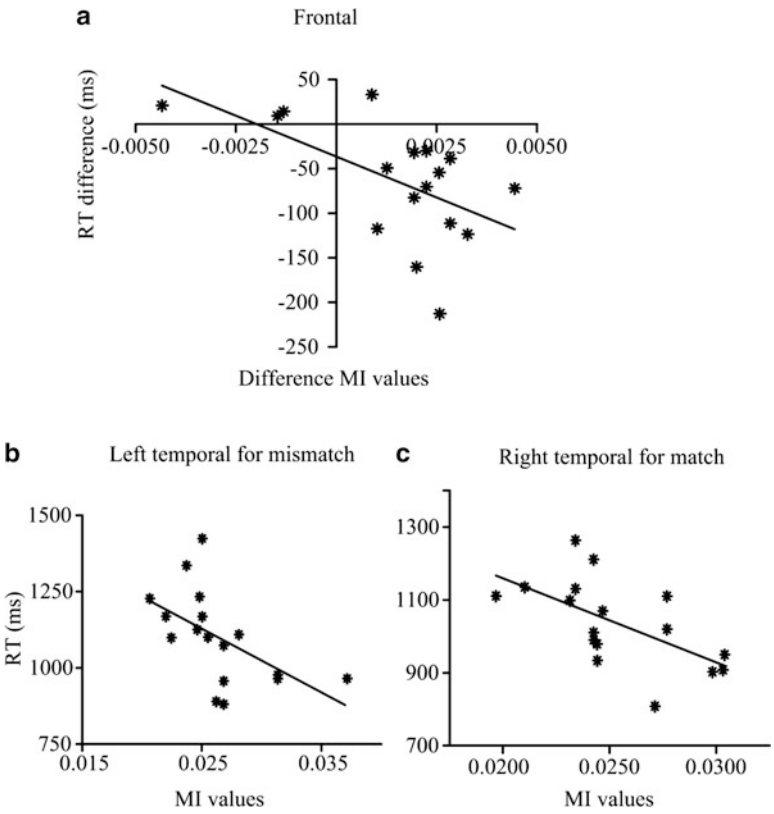

Fig. 13.3 The correlation between the theta-gamma coupling difference in frontal and the response time (*RT*) difference between the match and mismatch conditions during the auditory_2 interval was presented in (**a**), and the correlation between the coupling strength in the left temporal and the RT for the mismatch condition during the auditory_1 interval was depicted in (**b**), and the correlation between the coupling strength in the right temporal and the RT for the match condition was demonstrated in (**c**)

To investigate whether there is a symmetry pattern across hemispheres between the match and mismatch conditions, the distribution of theta-gamma coupling between the hemispheres for the two conditions was calculated. In this process, the relative distribution between hemispheres was calculated in order to reduce the amount of calculation. That is, the mean MI values of each channel in the right hemisphere were subtracted from the mean MI values of the corresponding channel in the left hemisphere, and the resulting MI values (rMI) were used to assess the strength of the hemisphere lateralization effect. As shown in Fig. 13.4a, a two-way repeated measures ANOVA revealed a significant interaction of Condition × Electrode Pair ($F10,160 = 2.456$, $p < 0.01$) and a significant main effect of Condition ($F1,16 = 24.078$, $p < 0.001$) in the first time window. Further analyses of the simple main effects revealed significant

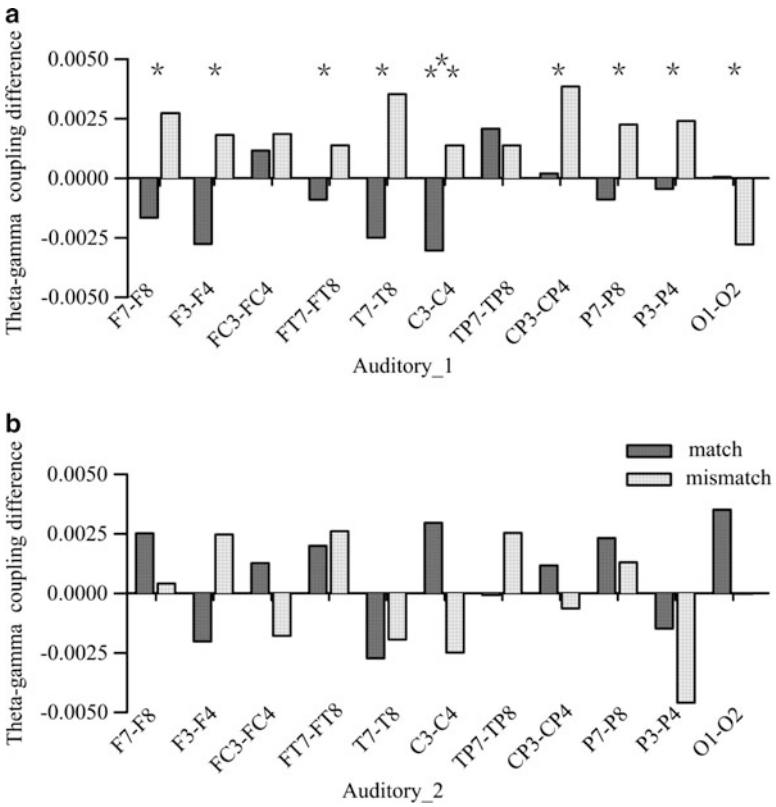

Fig. 13.4 The hemispheric asymmetry in theta-gamma coupling level (left electrode and right electrode) for the match and mismatch conditions averaged over 17 subjects for the auditory_1 (**a**) and auditory_2 (**b**) intervals. Positive values depict higher coupling levels for the left electrodes than the right electrodes, and negative values depict higher coupling levels for the right electrodes. The *bar plots* show the trend from an obvious divergence between match and mismatch conditions in the 1500–2500 ms window to a convergence in the 2000–3000 ms window. Note that significant differences (labeled by *stars*) are located in frontal, temporal and parietal areas (*: $p<0.05$, ***: $p<0.001$)

difference in hemisphere lateralization between conditions, mainly in the frontal (F7–F8: $F1,16=5.40$, $p<0.05$; F3–F4: $F1,16=5.25$, $p<0.05$), temporal (FT7–FT8: $F1,16=8.31$, $p<0.05$; T7–T8: $F1,16=6.97$, $p<0.05$), parietal (C3–C4: $F1,16=24.15$, $p<0.001$; CP3–CP4: $F1,16=6.31$, $p<0.05$; P7–P8: $F1,16=7.28$, $p<0.05$; P3–P4: $F1,16=5.35$, $p<0.05$), and occipital areas (O1–O2: $F1,16=6.87$, $p<0.05$). Higher coupling was found in the right hemisphere for the match compared to the mismatch condition. However, a higher left-hemispheric coupling level was shown in the mismatch condition compared to the match condition. In the second time window, a similar two-way repeated measures ANOVA analysis showed no significant effects. As shown in Fig. 13.4b, for these two conditions, the lateralization tendency vanished.

13.5 Conclusion

In this chapter, the relative knowledge on cross-frequency coupling was briefly overviewed. The interaction of top-down and bottom-up processes based on the coupling of theta phase and gamma amplitude in speech perception in a group of children was demonstrated. These findings challenge previous studies indicating weak top-down modulation in children (Bitan et al. 2006, 2009; Cao et al. 2011). Specifically, in comparison with mismatch, prior information match facilitated speech perception by eliciting stronger theta-gamma coupling in the frontal compared to the left temporal area. In addition, different hemispheric patterns were revealed with higher theta-gamma coupling in the match condition in the right hemisphere, compared to higher theta-gamma coupling in the mismatch condition in the left hemisphere. This asymmetry indicates that a fast global processing strategy and a slow detailed processing strategy were adopted in the congruent and incongruent conditions, respectively. These results provide neuroanatomical evidence for theories of speech perception allowing for top-down feedback connections and also provide insight into children's speech perception development. In addition, our findings indicate that the interaction of different oscillatory activities could be exploited to investigate the bottom-up and top-down mechanisms in speech perception.

References

Arnal LH, Wyart V, Giraud AL. Transitions in neural oscillations reflect prediction errors generated in audiovisual speech. Nat Neurosci. 2011;14(6):797–801.

Bitan T, Burman DD, Lu D, Cone NE, Gitelman DR, Mesulam MM, Booth JR. Weaker top-down modulation from the left inferior frontal gyrus in children. NeuroImage. 2006;33(3):991–8.

Bitan T, Cheon J, Lu D, Burman DD, Booth JR. Developmental increase in top-down and bottom-up processing in a phonological task: an effective connectivity, fMRI study. J Cogn Neurosci. 2009;21(6):1135–45.

Buzsaki G, Draguhn A. Neuronal oscillations in cortical networks. Science. 2004;304(5679):1926–9.

Canolty RT, Edwards E, Dalal SS, Soltani M, Nagarajan SS, Kirsch HE, Berger MS, Barbaro NM, Knight RT. High gamma power is phase-locked to theta oscillations in human neocortex. Science. 2006;313(5793):1626–8.

Cao F, Khalid K, Lee R, Brennan C, Yang Y, Li K, Bolger DJ, Booth JR. Development of brain networks involved in spoken word processing of Mandarin Chinese. Neuroimage. 2011;57(3):750–9.

Cohen MX. Assessing transient cross-frequency coupling in EEG data. J Neurosci Methods. 2008;168(2):494–9.

Colgin LL, Denninger T, Fyhn M, Hafting T, Bonnevie T, Jensen O, Moser M-B, Moser EI. Frequency of gamma oscillations routes flow of information in the hippocampus. Nature. 2009;462(7271):353–7.

Delorme A, Makeig S. EEGLAB: an open source toolbox for analysis of single-trial EEG dynamics including independent component analysis. J Neurosci Methods. 2004;134(1):9–21.

Hanslmayr S, Klimesch W, Sauseng P, Gruber W, Doppelmayr M, Freunberger R, Pecherstorfer T, Birbaumer N. Alpha phase reset contributes to the generation of ERPs. Cereb Cortex. 2007;17(1):1–8.

Jelic V, Kowalski J. Evidence-based evaluation of diagnostic accuracy of resting EEG in dementia and mild cognitive impairment. Clin EEG Neurosci. 2009;40(2):129–42.

Jensen O, Colgin LL. Cross-frequency coupling between neuronal oscillations. Trends Cogn Sci. 2007;11(7):267–9.

Klimesch W, Sauseng P, Hanslmayr S, Gruber W, Freunberger R. Event-related phase reorganization may explain evoked neural dynamics. Neurosci Biobehav Rev. 2007;31(7):1003–16.

Lisman JE, Idiart MA. Storage of 7 +/− 2 short-term memories in oscillatory subcycles. Science. 1995;267(5203):1512–5.

Mc LT. Hippocampal formation of brain as detector-coder of temporal patterns of information. Perspect Biol Med. 1959;2(4):443–52.

Moran LV, Hong LE. High vs low frequency neural oscillations in schizophrenia. Schizophr Bull. 2011;37(4):659–63.

Mormann F, Fell J, Axmacher N, Weber B, Lehnertz K, Elger CE, Fernandez G. Phase/amplitude reset and theta-gamma interaction in the human medial temporal lobe during a continuous word recognition memory task. Hippocampus. 2005;15(7):890–900.

O'Keefe J, Dostrovsky J. The hippocampus as a spatial map. Preliminary evidence from unit activity in the freely-moving rat. Brain Res. 1971;34(1):171–5.

Penny WD, Duzel E, Miller KJ, Ojemann JG. Testing for nested oscillation. J Neurosci Methods. 2008;174(1):50–61.

Tort AB, Komorowski R, Eichenbaum H, Kopell N. Measuring phase-amplitude coupling between neuronal oscillations of different frequencies. J Neurophysiol. 2010;104(2):1195–210.

von Stein A, Sarnthein J. Different frequencies for different scales of cortical integration: from local gamma to long range alpha/theta synchronization. Int J Psychophysiol. 2000;38(3): 301–13.

Wang XJ. Neurophysiological and computational principles of cortical rhythms in cognition. Physiol Rev. 2010;90(3):1195–268.

Wang J, Gao D, Li D, Desroches AS, Liu L, Li X. Theta-gamma coupling reflects the interaction of bottom-up and top-down processes in speech perception in children. Neuroimage. 2014;102(Pt 2):637–45.

White JA, Banks MI, Pearce RA, Kopell NJ. Networks of interneurons with fast and slow gamma-aminobutyric acid type A (GABAA) kinetics provide substrate for mixed gamma-theta rhythm. Proc Natl Acad Sci U S A. 2000;97(14):8128–33.

Yin Fen L, Daniel JS. EEG phase reset due to auditory attention: an inverse time-scale approach. Physiol Meas. 2009;30(8):821.

Chapter 14
Nonnegative Matrix and Tensor Decomposition of EEG

Fengyu Cong

Nonnegative matrix factorization (NMF) and nonnegative tensor factorization (NTF) are multichannel source separation algorithms with the constraints of nonnegativity and sparsity on signals (Cong et al. 2010). They can be used in many disciplines, including image recognition, language modeling, speech processing, gene analysis, biomedical signal extraction and recognition, and so on. Researchers from various research fields are interested in different, usually very diverse, aspects of NMF and NTF. We applied NMF and NTF into EEG feature extraction. In fact, in the past few years, researchers have used NMF and NTF to extract or separate useful information from superimposed biomedical data corrupted by a large level of noise and interference and, then, by using noninvasive recordings of human brain activities targeted at understanding the ability of the brain to sense, recognize, store, and recall patterns and comprehending crucial elements of learning: association, abstraction, and generalization (Cichocki et al. 2009).

14.1 Introduction of Nonnegative Matrix Factorization

Signal processing, data analysis, and data mining are pervasive throughout science and engineering. Extracting interesting knowledge from experimental raw datasets, measurements, and observations and understanding complex data have become an important challenge and objective. Often datasets collected from complex phenomena represent the integrated result of several interrelated variables, or they are combinations of underlying latent components or factors. Such datasets can be

F. Cong (✉)
Department of Biomedical Engineering, Faculty of Electronic Information and Electrical Engineering, Dalian University of Technology, Dalian, China
e-mail: cong@dlut.edu.cn

X. Li (eds.), *Signal Processing in Neuroscience*, DOI 10.1007/978-981-10-1822-0_14

first decomposed or separated into the components that underlie them in order to discover structures and extract hidden information (Cichocki et al. 2009).

In many cases, the primitive datasets or observations are organized as data matrices and described by linear combination models, whereupon the formulation of dimensionality reduction can be regarded as, from the algebraic perspective, decomposing the original data matrix into two factor matrices. The canonical methods, such as principal component analysis (PCA), linear discriminant analysis (LDA), independent component analysis (ICA), vector quantization (VQ), etc., are the exemplars of such low-rank approximations. They differ from one another in the statistical properties attributable to the different constraints imposed on the component matrices and their underlying structures; however, they have something in common that there is no constraint in the sign of the elements in the factorized matrices. In other words, the negative component or the subtractive combination is allowed in the representation.

Often the data to be analyzed is nonnegative, and the low-rank data are further required to be comprised of nonnegative values in order to avoid contradicting physical realities. Classical tools cannot guarantee to maintain the nonnegativity. The approach of finding reduced rank nonnegative factors to approximate a given nonnegative data matrix thus becomes a natural choice. This is the so-called nonnegative matrix factorization (NMF) problem which can be stated in generic form as follows:

NMF Problem *Given a nonnegative matrix* $V \in R^{m\times n}$ *and a positive integer* $r < min\{m,n\}$, *find nonnegative matrices* $W \in R^{m\times r}$ *and* $H \in R^{r\times n}$ *to minimize the functional*

$$f(\boldsymbol{W},\boldsymbol{H}) = \frac{1}{2} \parallel \boldsymbol{V} - \boldsymbol{WH}\parallel_{\boldsymbol{F}}^2 \tag{14.1}$$

The product $\boldsymbol{WH}$ is called an NMF of $\boldsymbol{V}$, although $\boldsymbol{V}$ is not necessarily equal to the product $\boldsymbol{WH}$, Clearly the product $\boldsymbol{WH}$ is an approximate factorization of rank at most $\boldsymbol{r}$. An appropriate decision on the value of $\boldsymbol{r}$ is critical in practice, but the choice of $\boldsymbol{r}$ is very often problem dependent. In most cases, however, $\boldsymbol{r}$ is usually chosen such that $r \ll min\{m,n\}$ in which case $\boldsymbol{WH}$ can be thought of as a compressed form of the data in $\boldsymbol{V}$. The algorithms construct approximate factorization of the form

$$V_{m\times n} \approx W_{m\times r}H_{r\times n}, W \geq 0,\ H \geq 0. \tag{14.2}$$

As a matter of fact, the notion of NMF has a long history under the name "self-modeling curve resolution" in chemometrics, where the vectors are continuous curves rather than discrete vectors. NMF was first introduced by Paatero and Tapper (1994; Paatero 1997) as the concept of positive matrix factorization, which concentrated on a specific application with Byzantine algorithms. These shortcomings limit both the theoretical analysis, such as the convergence of the algorithms or the properties of the solutions, and the generalization of the algorithms in other

applications. Fortunately, NMF was popularized by Lee and Seung (1999, 2001) due to their contributing work of a simple yet effective algorithmic procedure and more importantly the emphasis on its potential value of part-based representation.

14.1.1 Classic Basic NMF Optimization Framework

The prototypical multiplicative update rules originated from Lee and Seung. Their multiplicative update algorithm with the mean squared error objective function is provided below:

$$W_{mr} \leftarrow W_{mr} \sum_n \frac{V_{mn}}{(WH)_{mn}} H_{rn} \tag{14.3}$$

$$W_{mr} \leftarrow \frac{W_{mr}}{\sum_j W_{jr}} \tag{14.4}$$

$$H_{rn} \leftarrow H_{rn} \sum_m W_{mr} \frac{V_{mn}}{(WH)_{mn}} \tag{14.5}$$

The iterative algorithm for nonnegative matrix factorization is as the following. Starting from nonnegative initial condition for W and H, iteration of these update rules for nonnegative V finds an approximate factorization $V \approx WH$ by converging to a local maximum of the objective function. The fidelity of the approximation enters the updates through the quotient $V_{mn}/(WH)_{mn}$. Monotonic convergence can be proven using techniques similar to those used in proving the convergence of the EM algorithm (Dempster 1977; Saul and Pereira 1997). The update rules preserve the nonnegativity of W and H, and also contrain the columns of W to sum to unity. This sum constraint is a convenient way of eliminating the degeneracy associated with the invariance of WH under the transformation $W \rightarrow \lambda W$, $H \rightarrow \lambda^{-1} H$, where λ is a scalar.

14.1.2 Applications of Nonnegative Matrix Factorization (NMF) of EEG Signals

We apply NMF to process and analyze EEG signals, and the purpose is often source localization of brain activity (Becker et al. 2014), research questions of cognitive neuroscience (Cong et al. 2012), or clinical neuroscience.

The EEG data was collected at the First Affiliated Hospital of Dalian Medical University. The dataset included 48 people with mean age of 46 years, 23 patients with insomnia, and 25 normal as contrast. They were collected as resting state of EEG, and frequency range was 13 to 80Hz. The sampling frequency was 500 Hz

and an analog band-pass of 0.1–80 Hz was performed on the raw data. Sixty-four electrodes were placed over the standard sites. Electrodes included frontal (F3, Fz, F4, etc.), central (C3, Cz, C4, etc.), parietal (Pz, etc.), and mastoid (M1 and M2) placements. After the preprocessing, the power spectrum of each channel's data was calculated, and the data were stacked in the space mode for the group-level EEG spectral analysis.

14.1.2.1 Group Component Analysis and Feature Extraction

For this nonnegative matrix, the row is for the channel/space component, and the column corresponds to the frequency bins of the power spectrum. It could be factorized into two parts: one represents power spectrum and another represents space information, i.e., brain topographic map.

When low-rank NMF HALS (lraNMF_HALS) (Zhou et al. 2012) was applied on the EEG data, we could use principal component analysis method to calculate the variance below. Through Fig. 14.1, we chose the number of components to extract as eight. So the dataset was factorized into two parts. One contained eight frequency components and another eight spatial components.

Figure 14.2 shows the result of lraNMF_HALS. Every row shows the same component. The first column shows frequency waveforms that were factorized. The second column shows brain map of people with insomnia (PI, people with insomnia). The third column shows normal people brain map. We can find the differences in brain areas on the same frequency band.

For group analysis, we could use analysis of variance (ANOVA) to compare the difference between different groups. ANOVA is a collection of statistical models used to analyze the difference among group means and their associated procedures. First, we should select power spectrum from spectrum components, for example, γ band. And then choose interesting locations of electrodes from space components for statistical analysis.

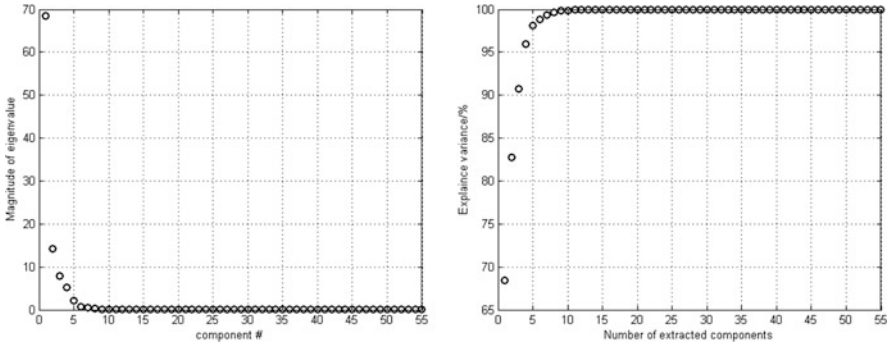

Fig. 14.1 Eigenvalue of the data

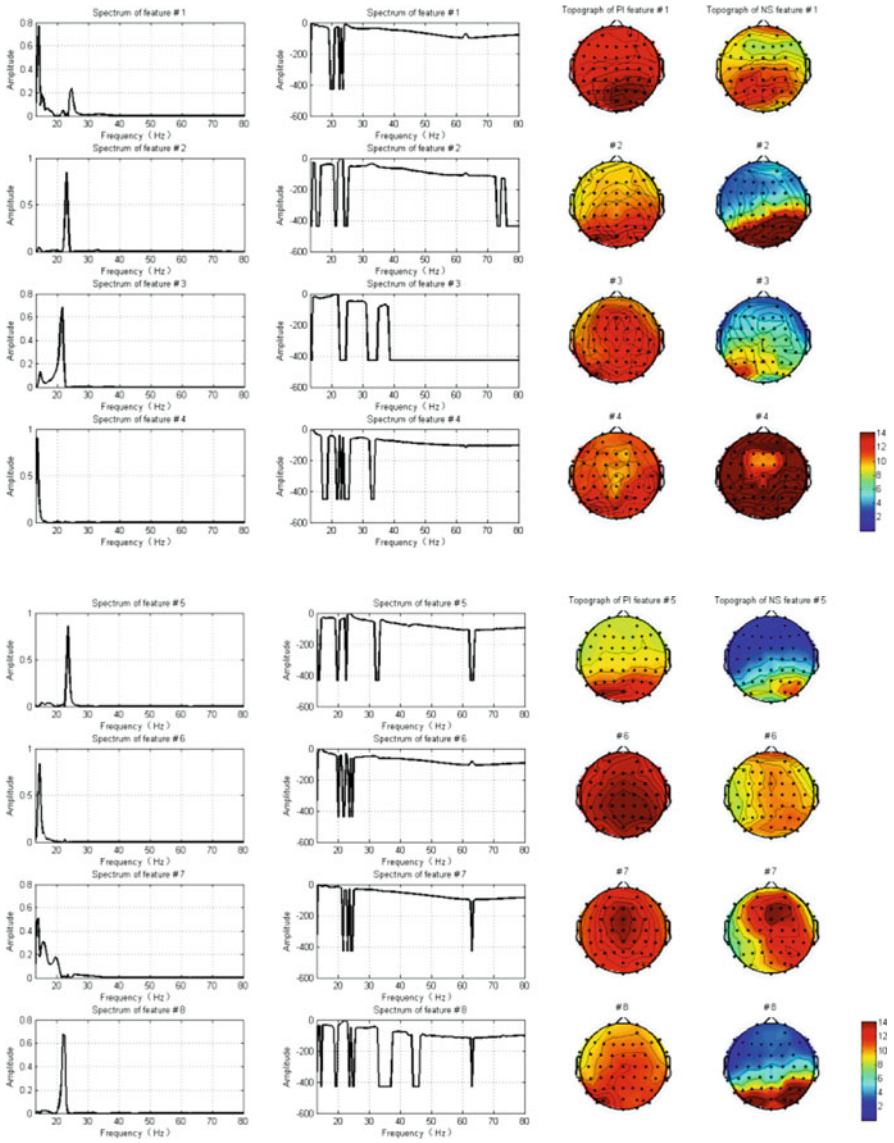

Fig. 14.2 Example of lraNMF_HALS of EEG includes 23 insomniac and 25 normal people. The *first column* shows eight spectral components and the *second column* shows eight spectral components taking the logarithm. The *third column* shows eight spatial components of insomniac (average overall subjects), and the *fourth column* shows eight spatial components of normal people (average overall subjects)

14.2 Introduction of the Tensor Decomposition

14.2.1 Introduction to Tensor

A multi-way data array is called a tensor. Tensors are usually denoted by capital boldface letters with underline, e.g., $\underline{\boldsymbol{Y}} \in \mathbb{R}^{I_1 \times I_2 \times \cdots \times I_N}$. A third-order tensor (or three-way array) has three modes as shown in Fig. 14.3 (Cichocki et al. 2009).

Tensor decomposition has been used in many fields such as chemistry (Bro 1998; Kroonenberg 2008), psychometrics (Harshman 1969; Carroll and Chang 1970), and brain science (Beckmann et al. 2005; Cichocki 2013). Canonical polyadic (CP) model and Tucker model are two mainly tensor decomposition methods. Canonical polyadic model could be traced back to 1927, and Tucker model was proposed in 1966 (Tucker 1966). For the electroencephalograph (EEG) data in event-related potential (ERP) experiments, there are many modes, including stimulus, time, space, frequency, trial, and participant, so the ERP data could be assembled as tensor, and tensor decomposition method could be used to analyze ERP data.

14.2.1.1 Basis of Tensor Algebra

14.2.1.1.1 Inner Product

For two-column vectors $\mathbf{a} = [a_1, a_2, a_3]^T$ and $\mathbf{b} = [b_1, b_2, b_3]^T$, the inner product is defined as

$$\mathrm{x} = \mathbf{a}^T \cdot \mathbf{b} = a_1 \cdot b_1 + a_2 \cdot b_2 + a_3 \cdot b_3 \tag{14.6}$$

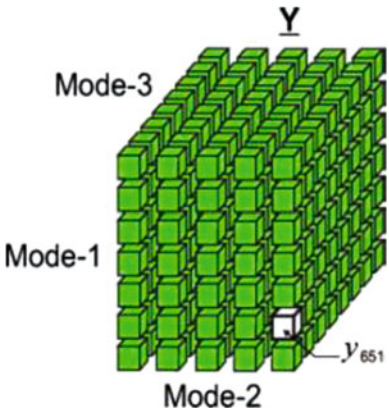

Fig. 14.3 Third-order tensor (Cichocki 2009)

14.2.1.1.2 Outer Product

For two tensors $\underline{\mathbf{Y}} \in \mathbb{R}^{I_1 \times I_2 \times \cdots \times I_N}$ and $\underline{\mathbf{X}} \in \mathbb{R}^{J_1 \times J_2 \times \cdots \times J_M}$, the outer product is defined as

$$\underline{\mathbf{Z}} = \mathbf{Y} \circ \mathbf{X} \in \mathbb{R}^{I_1 \times I_2 \times \cdots \times I_N \times J_1 \times J_2 \times \cdots \times J_M}, \tag{14.7}$$

where

$$z_{i_1, i_2, \ldots i_N, j_1, j_2, \ldots j_M} = y_{i_1, i_2, \ldots i_N} x_{j_1, j_2, \ldots j_M}.$$

The outer product of two vectors $\mathbf{a} \in \mathbb{R}^I$ and $\mathbf{b} \in \mathbb{R}^J$ yields a rank-one matrix:

$$\mathbf{A} = \mathbf{a} \circ \mathbf{b} = \mathbf{a}\mathbf{b}^T \in \mathbb{R}^{I \times J} \tag{14.8}$$

and the outer product of three vectors $\mathbf{a} \in \mathbb{R}^I$, $\mathbf{b} \in \mathbb{R}^J$, and $\mathbf{c} \in \mathbb{R}^I$ yields a third-order rank-one tensor:

$$\underline{\mathbf{Z}} = \mathbf{a} \circ \mathbf{b} \circ \mathbf{c} \in \mathbb{R}^{I \times J \times Q} \tag{14.9}$$

where

$$z_{ijq} = a_i b_j c_q. \tag{14.10}$$

14.2.1.1.3 Kronecker Product

The Kronecker product of two matrices $\mathbf{A} \in \mathbb{R}^{I \times J}$ and $\mathbf{B} \in \mathbb{R}^{T \times R}$ is denoted as $\mathrm{A} \otimes \mathrm{B} \in \mathbb{R}^{IT \times JR}$ and defined as

$$\mathbf{A} \otimes \mathbf{B} = \begin{bmatrix} a_{11}B & a_{12}B & \cdots & a_{1J}B \\ a_{21}B & a_{22}B & \cdots & a_{2J}B \\ \vdots & \vdots & \ddots & \vdots \\ a_{I1}B & a_{I2}B & \cdots & a_{IJ}B \end{bmatrix}$$

$$= [a_1 \otimes b_1 \; a_1 \otimes b_2 \; a_1 \otimes b_3 \; \cdots a_J \otimes b_{R-1} \; a_J \otimes b_R] \tag{14.11}$$

14.2.1.1.4 Hadamard Product

The Hadamard product of two equal-size matrices is denoted by $\circledast$ and defined as

$$\mathbf{A} \circledast \mathbf{B} = \begin{bmatrix} a_{11}a_{11} & a_{12}a_{12} & \cdots & a_{1J}a_{1J} \\ a_{11}a_{21} & a_{22}a_{22} & \cdots & a_{2J}a_{2J} \\ \vdots & \vdots & \ddots & \vdots \\ a_{I1}a_{I1} & a_{I2}a_{I2} & \cdots & a_{IJ}a_{IJ} \end{bmatrix} \tag{14.12}$$

14.2.1.1.5 Khatri-Rao Product

The Khatri-Rao product of two matrices $\mathrm{A} \in \mathbb{R}^{I \times J}$ and $\mathrm{B} \in \mathbb{R}^{T \times J}$ with the same number of column is denoted by $\odot$ and is defined as

$$\mathrm{A} \odot \mathrm{B} = [a_1 \otimes b_1 \, a_2 \otimes b_2 \cdots \, a_J \otimes b_J] \tag{14.13}$$

14.2.1.1.6 Mode-n Tensor-Matrix Product

The mode-n tensor-matrix product $\underline{\mathrm{X}} = \underline{\mathrm{G}} \times_n \mathrm{A}$ of tensor $\underline{\mathrm{G}} \in \mathbb{R}^{J_1 \times J_2 \times \cdots \times J_N}$ and matrix $\mathrm{A} \in \mathbb{R}^{I_n \times J_n}$ is tensor $\underline{\mathrm{X}} \in \mathbb{R}^{J_1 \times J_2 \times \cdots \times J_{n-1} \times I_n \times J_{n+1} \times \cdots \times J_N}$ with the following elements:

$$\mathrm{x}_{j_1 j_2 \ldots j_{n-1} i_n j_{n+1} \ldots j_N} = \sum_{j_n=1}^{J_n} \mathrm{g}_{j_1 j_2 \ldots j_N} a_{i_n, j_n}.$$

14.2.2 Canonical Polyadic Decomposition (CPD) Model

Generally, for an nth-order tensor $\underline{\mathrm{X}} \in \mathbb{R}^{I_1 \times I_2 \times \cdots \times I_N}$, the CPD is defined as

$$\underline{\boldsymbol{X}} = \sum_{r=1}^{R} u_r^{(1)} \circ u_r^{(2)} \circ \cdots \circ u_r^{(N)} + \underline{\boldsymbol{E}} = \sum_{r=1}^{R} \underline{\boldsymbol{X}}_r + \underline{\boldsymbol{E}} = \hat{\underline{\boldsymbol{X}}} + \underline{\boldsymbol{E}} \tag{14.14}$$

where $\underline{\boldsymbol{X}}_r = u_r^{(1)} \circ u_r^{(2)} \circ \cdots \circ u_r^{(N)}, r = 1, 2, \ldots, \mathrm{R}$ $\hat{\underline{\boldsymbol{X}}}$ approximates to $\underline{\boldsymbol{X}}$, $\underline{\boldsymbol{E}} \in \mathbb{R}^{I_1 \times I_2 \times \cdots \times I_N}$ is residual, and $\| u_r^{(n)} \|_2 = 1$,for $n = 1, 2 \ldots, N-1$.

For the ERP data, channel, time, and frequency could be assembled as three-order tensor as in Fig. 14.4. For two-component CPD, it could be shown in Fig. 14.5 (Bro 1998).

$$\underline{\boldsymbol{X}} \approx a_1 \circ b_1 \circ c_1 + a_2 \circ b_2 \circ c_2 = \underline{\boldsymbol{X}}_1 + \underline{\boldsymbol{X}}_2 \tag{14.15a}$$

In this application, the first temporal component a_1, the first spectral component b_1, and the first spatial component c_1, their outer product produces rank-one tensor $\underline{X}_1$ means the component #1. The second component in the time, frequency, and space modes is associated with one another, and their outer product generates rank-one tensor $\underline{X}_2$. The sum of rank-one tensor $\underline{X}_1$ and $\underline{X}_2$ approximates original tensor $\underline{X}$.

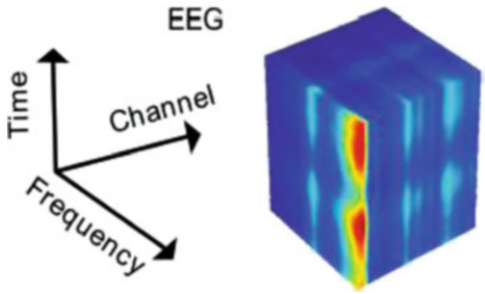

Fig. 14.4 Three-order tensor by channel, time, and frequency

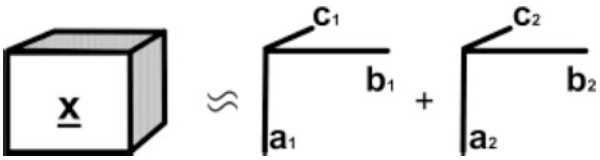

Fig. 14.5 Model of two-component CPD (Bro 1998)

14.2.3 Tucker Decomposition Model

For an nth-order tensor $\underline{\boldsymbol{X}} \in \mathbb{R}^{I_1 \times I_2 \times \cdots \times I_N}$, the Tucker decomposition is defined as follows:

$$\underline{\boldsymbol{X}} = \sum_{r_1=1}^{R_1} \sum_{r_2=1}^{R_2} \cdots \sum_{r_N=1}^{R_N} g_{r_1 r_2 \ldots r_N} u_{r_1}^{(1)} \circ u_{r_2}^{(2)} \circ \cdots \circ u_{r_N}^{(N)}$$

$$+ \underline{\boldsymbol{E}} = \sum_{r_1=1}^{R_1} \sum_{r_2=1}^{R_2} \cdots \sum_{r_N=1}^{R_N} g_{r_1 r_2 \ldots r_N} \underline{\boldsymbol{X}}_{r_1 r_2 \ldots r_N} + \underline{\boldsymbol{E}} \tag{14.15b}$$

where rank-one tensor $\underline{\boldsymbol{X}}_{r_1 r_2 \ldots r_N} = u_{r_1}^{(1)} \circ u_{r_2}^{(2)} \circ \cdots \circ u_{r_N}^{(N)}$, and $g_{r_1 r_2 \ldots r_N}$ denotes the core tensor $\underline{\boldsymbol{G}} \in \mathbb{R}^{I_1 \times I_2 \times \cdots \times I_N}$.

Therefore, the Tucker decomposition is the sum of rank-one tensors plus the error tensor. In the tensor-matrix form, the equation could be transformed into

$$\underline{\boldsymbol{X}} = \underline{\boldsymbol{G}} \times_1 \boldsymbol{U}^{(1)} \times_2 \boldsymbol{U}^{(2)} \times_3 \cdots \times_N \boldsymbol{U}^{(N)} + \underline{\boldsymbol{E}} = \hat{\underline{\boldsymbol{X}}} + \underline{\boldsymbol{E}} \tag{14.16}$$

where $\boldsymbol{U}^{(n)} = \left[u_1^{(n)}, u_2^{(n)}, \ldots u_{R_n}^{(n)} \right] \in \mathbb{R}^{I_n \times R_n}$ $(n = 1, 2, \ldots, N)$ denotes the component matrix.

We could understand Tucker decomposition clearly as shown in Fig. 14.6 (Zhao et al. 2013), if the tensor stands for ERP data, and each order means time, channel, frequency (Fig. 14.4). The matrix $U^{(1)}$ means all components at temporal courses, each column means a component. The matrix $U^{(2)}$ means all components at the

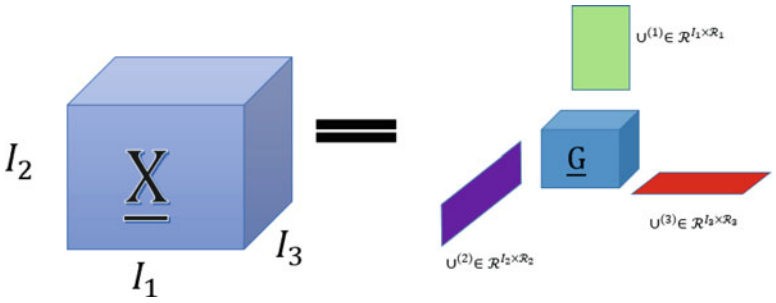

Fig. 14.6 Tucker decomposition (Zhao et al. 2013)

spatial domain, and each column means a component; we could draw a spatial map for each component. The matrix $U^{(3)}$ means all components at frequency domain, each column means a component at frequency domain.

14.2.4 Demo

When tensor decomposition is used to factorize a nonnegative tensor, nonnegative constraints are often applied. The CPD model with nonnegative constraints is called nonnegative CPD (NCPD) (Cong et al. 2013, 2014), and the Tucker model with nonnegative constraints is called nonnegative Tucker decomposition (NTD) (Cong et al. 2012; Phan and Cichocki 2011). One of the properties of time-frequency representations (TFR) of ERP data is nonnegative. The previous study (Cong et al. 2014) shows that more reasonable ERP components could be extracted, so we will mainly use nonnegative tensor decomposition later.

The size of the data is 71*60*9*42 that means each frequency course has 71 points, each time course has 60 points, and each spatial map has nine channels; there are 42 participants together, 21 of them with reading disability (RD) and 21 with attention deficit (AD). The tensor could be reshaped as a matrix (38340*42) that means time, frequency, and channel are merged; we could use principal component analysis method to calculate the variance below. Through the Fig. 14.7, we chose the number of components to be 36.

14.2.4.1 Canonical Polyadic Decomposition (CPD)

14.2.4.1.1 Feature Extraction

For a fourth-order ERP tensor assembled with course of time, frequency, space, and different participants, it could be decomposed by the following equation where $\boldsymbol{U}^{(t)}$, $\boldsymbol{U}^{(s)}$, $\boldsymbol{U}^{(c)}$ means time, spectrum, and channel component matrix, respectively.

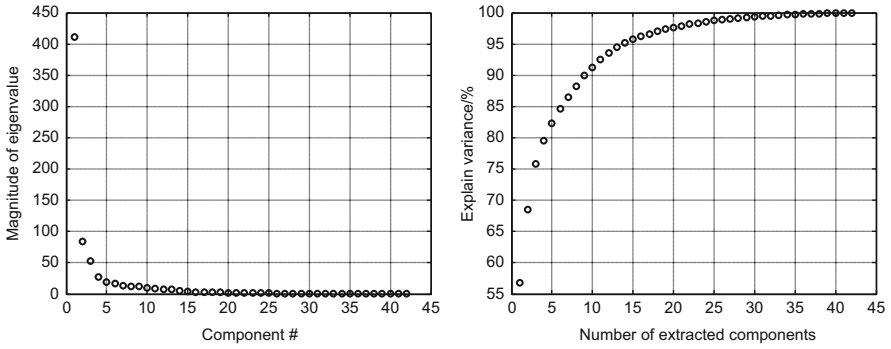

Fig. 14.7 Eigenvalue of the data

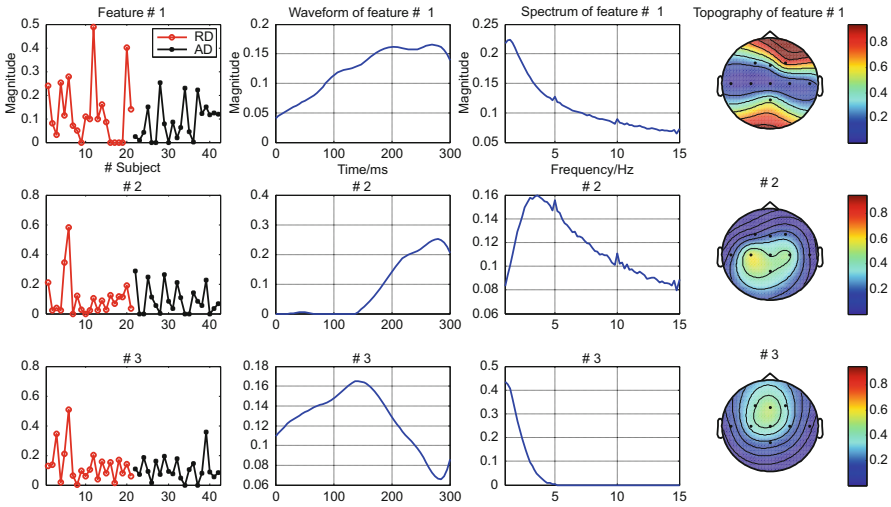

Fig. 14.8 Result of NCPD

$$\underline{\boldsymbol{X}} = \underline{\boldsymbol{I}} \times_1 \boldsymbol{U}^{(t)} \times_2 \boldsymbol{U}^{(s)} \times_3 \boldsymbol{U}^{(c)} \times_1 \boldsymbol{F} + \underline{E} = \sum_{r=1}^{R} \boldsymbol{u}_r^{(t)} \circ \boldsymbol{u}_r^{(s)} \circ \boldsymbol{u}_r^{(c)} \circ f_r + \underline{\boldsymbol{E}} \tag{14.17}$$

Figure 14.8 shows the result of NCPD. The first column shows the features of component of AD and RD, that also the difference of AD and RD. The second column shows the waveform of component, the third column shows the spectrum of component, and the last column shows the brain map. There has to be mentioned that for the same component, different participants share the same brain map, the same time course, and the same spectrum, and just the strengths of different subjects are different.

14.2.4.2 Tucker

14.2.4.2.1 Feature Extraction

Using the NTD to analyze the same data with the equation below:

$$\underline{\boldsymbol{X}} = \underline{F} \times_1 \boldsymbol{A}^{(t)} \times_2 \boldsymbol{A}^{(s)} \times_3 \boldsymbol{A}^{(c)} + \underline{\boldsymbol{E}} \tag{14.18}$$

we could get three component matrices as shown in Fig. 14.9. The components of different modes are interacted with each other. The number of spectral components is three, the number of temporal components is eight, and the number of spatial

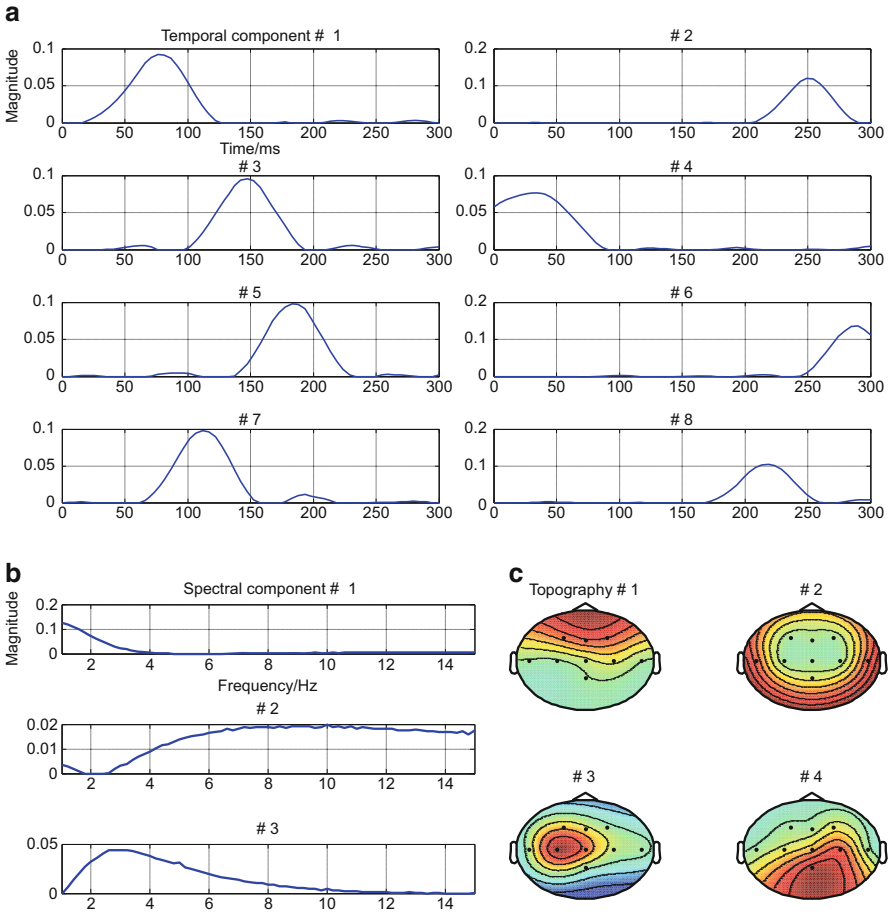

Fig. 14.9 Result of NTD. (**a**) Temporal components. (**b**) Spectral components. (**c**) Spatial components

components is four in this study. Choosing different numbers of components for different modes, the result could be different. Therefore, the number of components of Tucker decomposition for each mode is challenging, which should be solved in further study.

14.2.4.2.2 Feature Selection and Analysis

It is similar with matrix decomposition like ICA and PCA. After decomposition, we have to select components by their properties of each mode. For the data in the demo, we have to think about temporal, spectral, and spatial properties; when they meet the theoretical requirements of ERP, the corresponding feature could be further analyzed to find the difference between AD and RD.

For group analysis, we could use analysis of variance (ANOVA) to compare the difference between AR and RD. ANOVA is a collection of statistical models used to analyze the difference among group means and their associated procedures. For this case one-factor statistical analysis is applied because the feature mode includes just one factor.

Acknowledgement This work was supported by the Fundamental Research Funds for the Central Universities [DUT16JJ(G)03] in Dalian University of Technology, and National Natural Science Foundation of China (Grant No. 81471742).

References

Becker H, et al. EEG extended source localization: tensor-based vs. conventional methods. Neuroimage. 2014;96(8):143–57.

Beckmann CF, Smith SM, Beckmann CF, Smith SM. Tensorial extensions of independent component analysis for multisubject FMRI analysis. Neuroimage. 2005;25(1):294–311.

Bro R. Multi-way analysis in the food industry: theory, algorithms and applications. Doctoral Dissertation: University of Amsterdam; 1998.

Carroll JD, Chang JJ. Analysis of individual differences in multidimensional scaling via an N-way generalization of. Psychometrika. 1970;35(3):283–319.

Cichocki A. Tensor decompositions: a new concept in brain data analysis? 2013;7(2011).

Cichocki et al. Nonnegative matrix and tensor factorizations. 2009.

Cong F, et al. Extract mismatch negativity and P3a through two-dimensional nonnegative decomposition on time-frequency represented event-related potentials. Berlin/Heidelberg: Springer; 2010. p. 385–91.

Cong F, et al. Benefits of multi-domain feature of mismatch negativity extracted by non-negative tensor factorization from EEG collected by low-density array. Int J Neural Syst. 2012;22(6):1415–28.

Cong F, et al. Multi-domain feature extraction for small event-related potentials through non-negative multi-way array decomposition from low dense array EEG. Int J Neural Syst. 2013;23(2):1350006. 10.1142/S0129065713500068

Cong F, et al. Low-rank approximation based non-negative multi-way array decomposition on event-related potentials. Int J Neural Syst. 2014;24(8):1440005. 10.1142/S012906571440005X

Dempster AP. Maximum likelihood estimation from incomplete data via the EM algorithm (with discussion. in J R Stat Soc Ser B. 1977.

Harshman RA. Foundations of the PARAFAC procedure: model and conditions for an "explanatory" multi-mode factor analysis. In UCLA working papers in. 1969.

Kroonenberg PM. Applied multiway data analysis. Ppsw.rug.nl. 2008.

Lee DD, Seung HS. Learning the parts of objects by non-negative matrix factorization. Nature. 1999;401(6755):788–91.

Lee DD, Seung HS. Algorithms for non-negative matrix factorization. In: In NIPS. 2001.

Paatero P. Least squares formulation of robust non-negative factor analysis. Chemom Intell Lab Syst. 1997;37(96):23–35.

Paatero P, Tapper U. ‡, Positive matrix factorization: a non-negative factor model with optimal utilization of error estimates of data values †. Environmetrics. 1994;5(2):111–26.

Phan AH, Cichocki A. Extended HALS algorithm for nonnegative Tucker decomposition and its applications for multiway analysis and classification. Neurocomputing. 2011;74(11):1956–69.

Saul L, Pereira F. Aggregate and mixed-order Markov models for statistical language processing. eprint arXiv:cmp-lg/9706007, 1997;81–9.

Tucker LR. Some mathematical notes on three-mode factor analysis. Psychometrika. 1966;31(3):279–311.

Zhao Q, et al. Kernelization of tensor-based models for multiway data analysis: processing of multidimensional structured data. IEEE Signal Process Mag. 2013;30(4):137–48.

Zhou G, Cichocki A, Xie S. Fast nonnegative matrix/tensor factorization based on low-rank approximation. Signal Proces IEEE Transact. 2012;60(6):2928–40.